# Quantum Simulation of Abelian Gauge Fields with Ultracold Gases

Von der Fakultät für Mathematik und Physik der
Gottfried Wilhelm Leibniz Universität Hannover

zur Erlangung des Grades

**Doktor der Naturwissenschaften**
**Dr. rer. nat.**

genehmigte Dissertation von
M.Sc. Lorenzo Cardarelli

2019

Referent : Prof. Dr. Luis Santos
Korreferenten : Prof. Dr. André Eckardt
Prof. Dr. Matteo Rizzi
Tag der Promotion : 12.12.2019

*"Veramente l'immaginazione è bella,*
*solo gli manca il non essere*
*né dimostrata né dimostrabile."*

Galileo Galilei, on the sphericity of the moon.

# Abstract

Gauge theories are ubiquitous in physics. Many intriguing phenomena in condensed matter physics owe to the action of the electromagnetic field, which is an Abelian gauge theory. The numerical treatment of many-body systems is inherently complex due to the exponentially growing size of the Hilbert space. While in one dimension an area law guarantees that numerical methods on classical computers can deal with strongly correlated systems, in higher dimensions the quantum simulation comes as the panacea for the many-body problem. The present thesis comprises the elaboration of experimentally feasible methods for the quantum simulation of dynamical Abelian gauge fields with ultra-cold gases of neutral atoms and the theoretical analysis of the related model Hamiltonians. As neutral atoms do not interact with external vector potentials like charged particles would do, the gauge fields have to be artificially engineered.

The elements of a gauge theory that need to be replicated on a quantum simulator vary depending on the subject of investigation. The key ingredient at the root of many condensed matter phenomena, from the quantum Hall effect to superconductivity and chiral topological insulators, is the Berry phase. Whilst artificial static gauge fields have been widely explored, much remains to do regarding the realization of artificial dynamical gauge fields. In Chapter 3 we present a method based on the amplitude modulation of a one-dimensional optical lattice, which allows for an unprecedented degree of control over a wide range of parameters. The method also comprises the generation of a density-dependent complex phase, fundamental to the creation of anyonic pseudo-particles. The anyons are amenable of observation through interferometric measurement, realizable with the same experimental set-up.

With regard to gauge theories, the Berry phase is just the visible tip of the iceberg. Below the waterline, there is more to consider in order to comprehensively reproduce a gauge theory, like the electric and magnetic fields in quantum electrodynamics. Moreover, a full account for the inherent symmetry is crucial to investigate phenomena proper of non-Abelian gauge theories in the context of high-energy physics, such as confinement. For this collection of topics, one can turn to lattice gauge theories. In Chapter 5, we consider a class of lattice gauge theories particularly suitable for quantum simulation, the Quantum Link Model. The study of the Abelian U(1) Quantum Link Model on a ladder geometry reveals a highly non-trivial phase diagram, featuring a symmetry-protected topological phase.

In both Chapters, innovative solutions for the experimental realization of the model Hamiltonians are designed and proposed. To gain numerical access to the ground-state properties and the dynamics of the systems investigated we make use of state-of-the-art numerical methods based on Tensor Networks. The elements of the numerical analysis carried out throughout this thesis are presented in Chapter 6.

In the last part we offer an outlook on research perspectives related to the topics discussed in the thesis.

# Schlagwörter

- Abelsche Eichfelder
- Quantum Link Model
- Quantensimulation

# Keywords

- Analogue quantum simulation
- Ultracold gases
- Optical lattices
- Abelian gauge fields
- Density-dependent gauge fields
- Lattice Gauge Theories
- Quantum Link Model
- Tensor Networks
- DMRG
- Matrix Product States

# Contents

**1 Introduction** **1**
- 1.1 Quantum simulation of many-body systems . . . . . . . . . . . . . . . 1
- 1.2 Ultracold gases of neutral atoms . . . . . . . . . . . . . . . . . . . . . . 3
- 1.3 Neutral atoms in optical lattices . . . . . . . . . . . . . . . . . . . . . . 4

**2 Berry-like dynamical gauge fields** **15**
- 2.1 The Berry phase . . . . . . . . . . . . . . . . . . . . . . . . . . . . . . 15
- 2.2 Artificial gauge fields in cold gases . . . . . . . . . . . . . . . . . . . . 17
  - 2.2.1 Raman-assisted tunnelling . . . . . . . . . . . . . . . . . . . . 17
  - 2.2.2 Periodically driven optical lattices . . . . . . . . . . . . . . . . . 21
- 2.3 Anyons . . . . . . . . . . . . . . . . . . . . . . . . . . . . . . . . . . . 27
  - 2.3.1 Abelian Anyons in 1-D lattices . . . . . . . . . . . . . . . . . . 29
  - 2.3.2 Experimental realization of density-dependent gauge fields . . 33

**3 Dynamical gauge fields with three-color modulation** **35**
- 3.1 Multi-color modulation of a 1-D optical lattice . . . . . . . . . . . . . 35
  - 3.1.1 The model . . . . . . . . . . . . . . . . . . . . . . . . . . . . . 35
  - 3.1.2 The effective Hamiltonian . . . . . . . . . . . . . . . . . . . . . 37
- 3.2 Non-equilibrium dynamics . . . . . . . . . . . . . . . . . . . . . . . . . 40
- 3.3 Phases of the effective Hamiltonian . . . . . . . . . . . . . . . . . . . . 41
  - 3.3.1 Metal-insulator phase diagram . . . . . . . . . . . . . . . . . . 41
  - 3.3.2 Multi-component phase . . . . . . . . . . . . . . . . . . . . . . 42
  - 3.3.3 Intersite interactions . . . . . . . . . . . . . . . . . . . . . . . . 44
- 3.4 Two-component anyon-Hubbard model . . . . . . . . . . . . . . . . . . 46
- 3.5 Anyons interferometry . . . . . . . . . . . . . . . . . . . . . . . . . . . 47
  - 3.5.1 Scheme for an effective periodic anyon model . . . . . . . . . . 47
  - 3.5.2 Dynamical probing of the exchange statistics . . . . . . . . . . . 49
  - 3.5.3 Dynamical probing of pairing . . . . . . . . . . . . . . . . . . . 51
- 3.6 Conclusions . . . . . . . . . . . . . . . . . . . . . . . . . . . . . . . . 53

**4 Quantum simulation of Abelian Quantum Link Models** **55**
- 4.1 Quantum field theories . . . . . . . . . . . . . . . . . . . . . . . . . . . 55
- 4.2 The Kogut-Susskind Hamiltonian . . . . . . . . . . . . . . . . . . . . . 57
  - 4.2.1 Truncated Kogut-Susskind Hamiltonian . . . . . . . . . . . . . 61
- 4.3 QLMs numerical analysis and quantum simulation . . . . . . . . . . . 65
  - 4.3.1 Experimental proposals . . . . . . . . . . . . . . . . . . . . . . 66
  - 4.3.2 Numerical studies . . . . . . . . . . . . . . . . . . . . . . . . . 68
- 4.4 Conclusions . . . . . . . . . . . . . . . . . . . . . . . . . . . . . . . . 70

**5 Quantum link model on a ladder geometry** **73**
- 5.1 Introduction to the model . . . . . . . . . . . . . . . . . . . . . . . . . 73
  - 5.1.1 The Quantum Link Ladder model . . . . . . . . . . . . . . . . . 73
  - 5.1.2 Analysis of the one-dimensional QLM . . . . . . . . . . . . . . . 74

5.2 Analysis of the quantum link ladder model . . . . . . . . . . . . . . . . 75
5.3 Experimental realization with cold gases . . . . . . . . . . . . . . . . . . . 83
5.4 Multi-leg ladders . . . . . . . . . . . . . . . . . . . . . . . . . . . . . . 86
5.5 Conclusions . . . . . . . . . . . . . . . . . . . . . . . . . . . . . . . . 91

**6 Numerical methods** **93**
6.1 Tensor networks . . . . . . . . . . . . . . . . . . . . . . . . . . . . . . 93
6.1.1 Density Matrix Renormalization Group . . . . . . . . . . . . . . 93
6.1.2 Matrix Product States . . . . . . . . . . . . . . . . . . . . . . . . 94
6.1.3 The DMRG algorithm with MPS . . . . . . . . . . . . . . . . . . 98
6.2 MPSs for the Quantum Link Model . . . . . . . . . . . . . . . . . . . . . 103

**7 Conclusions and Outlook** **107**

**A Derivation of the effective model via Magnus expansion** **109**

**B Multi-component phase** **111**

**Bibliography** **119**

**Acknowledgements** **133**

# Chapter 1

# Introduction

## 1.1 Quantum simulation of many-body systems

### The many-body problem

The ultimate purpose of physics is to unveil the universal rules governing Nature, to express them in a mathematical language and to be able to make predictions. The set of equations to consider in order to characterize a certain physical phenomenon depends on the length or energy scale at which that phenomenon occurs. While the equations of classical mechanics fail at describing the fundamental constituents of matter on the atomic and molecular scale or at a relativistic speed, adopting quantum mechanics on the Euclidean regime is at least redundant. Nonetheless, striking features of macroscopic many-body systems do find their origins in the quantum world, preeminent examples being superfluidity and superconductivity.

The description of physical systems involving multiple particles interacting with one another is an ubiquitous task in physics and takes the name of many-body problem. In a quantum system with many particles, the solutions to the equations of interest rarely come in elegant closed form expressions. Mostly, they are grounded on some form of approximation or they are obtained with numerical methods on classical computers. The difficulty that makes the many-body problem hard to tackle with numerical methods lies in the exponential scaling of the possible configurations space dimension. For instance, a system with only two relevant local states such as a gas of $N$ half-integer spin particles spans a full configuration space of size $2^N$. It is sufficient that $N$ be larger than fifty to practically become impossible for the most powerful modern supercomputer to even just store a full representation of the many-body state; searching its ground state eigenvector or following its evolution in real time is something inconceivable. That means, an elementary square grid of spins 1/2 with eight sites per side ($2^{64}$ configurations) is already a utopia, and yet it is far away from earning the title of many-body system.

The many-body problem appears in a number of different contexts, ranging from condensed matter physics, where the processes underlying high-temperature superconductivity still lack a comprehensive description, to the high-energy physics, where expected phenomena of the fundamental particles are experimentally hard to access and verify. Quantum computation and quantum simulation are currently acknowledged as the right strategy to pursue in order to crack and solve any many-body problem.

### Quantum computation and quantum simulation

"Quantum simulation fights fire with fire" [1]. This evocative quote is a catchy reinterpretation of the most renowned seminal concept proposed by Feynman [2] in

1982: if we want the resources required by a computer to simulate a large quantum system to be of the same order of the system itself, there is no other way for the computer than to undergo the laws of quantum mechanics.

The realization of a universal digital quantum computer is arguably the lighthouse in quantum information and certainly a major long-term goal in the field of atomic physics. Generally speaking, the quantum computer shall be used to study both steady properties of a certain physical system (the energy spectrum, the ground state, etc.) and the dynamics. The hindrance arising from the continuity of time was early identified by Feynman himself, who proposed the discretization of the time variable as a problem workaround. Already in 1996 it was proven [3] that the simulation of the real-time evolution in discrete steps of generic many-body Hamiltonians with local interactions is indeed correct and efficient, since the time grows polynomially and not exponentially with the number of particles. The existence of a theoretical edge gave hopes and stimulated the experimental efforts seen in the last decades, however a universal quantum computer able to deliver when it comes to non-trivial many-body systems does not exist yet.

While the digital quantum computer could be a long way to come, the experimental community also pursued the road of analogue quantum simulation: a target model Hamiltonian can be directly emulated on a physically different though mathematically equivalent quantum system instead of converting it onto a quantum digital form, and by means of that the ground state properties and the dynamics can be directly addressed cooling the system to the lowest temperatures or letting it evolve. Furthermore, analogue quantum simulators are in some cases prone to scalability. In the last decades analogue quantum simulators have seen a thriving development: the joint action of constant refinements in controlling and manipulating simulation platforms and the proposals of novel, simpler experimental techniques, allowed for the successful implementation and simulation of a number of relevant model Hamiltonians.

### Quantum simulation platforms: superconductors and ions

On-chip superconducting circuits stand as a preminent quantum hardware platform at the interface between quantum computation and quantum simulation [1]. With those, milestone goals of quantum computation have been achieved: single- and two-qubit operations, entangled state preparation, protocols for fault tolerance and quantum error correction have been faithfully realized [4]. Yet the most sound achievements attained so far have come from the field of quantum simulations, which is still the branch more amenable to scalability. Designed with lithography techniques, these nanofabricated systems allow for a large flexibility in the range of geometries realizable and in the tunability of nearly every parameter involved. A peculiarity lies in the fact that the simulated particles are in fact circuit excitations, not necessarily conserved, which makes the superconducting circuits eligible for investigations in the grand canonical ensemble.

Along with superconducting circuits, trapped ions represent a leading platform for first-generation quantum computers. The respective advantages and drawbacks of these two technologies might lead to a complementary use for scaling special-purpose quantum computers (not yet universal nor fully-programmable) to an interesting number of qubits [5]. Like superconducting circuits, ions too are established as a useful platform for analogue simulations. The Jaynes–Cummings model, a two-level atom in a bath of resonant photons, is a preminent model straightforwardly realizable with ions, which makes them suitable for faithful simulations of the dynamics of cavity QED [6], the quantum-Rabi model [7] and its quantum phase transition [8] or quantum spin models [9].

## 1.2 Ultracold gases of neutral atoms

It is safe to say that the experimental platform that has attracted the largest part of the atomic, molecular and optical (AMO) physics community and which has inspired and driven the work of many theorists in the past quarter century is that of ultracold gases of neutral atoms [10, 11]. Cooling and trapping neutral atomic gases to quantum degeneracy took a long journey, decades long, to become nowadays a standard practice in physics laboratories. As intense coherent light beams with a narrow bandwidth (lasers) became available, people used them to guide the motion of particles. It is well known that light exerts a radiation pressure on any substance it scatters with. Ashkin pioneered the field from the early 70s, achieving first the deflection of a chosen isotopic species of an atomic beam from a circular orbit using a laser in resonance with an atomic transition [12]. In 1975, seminal proposals based on the Doppler effect arose to selectively address and slow down incoming atoms [13, 14], which grounded and inspired the work of many in the following years [15]. Ions could be straightforwardly trapped, the traps being deep enough to easily keep particles even at room temperature. Significant cooling is instead required before neutral particles can be trapped.

### Sub-doppler cooling

Common cooling procedures for neutral atoms begin funnelling a hot gas of some alkali-atoms species onto a vacuum chamber through a Zeeman slower, where the gas is slowed down by a counter-propagating laser beam near-resonant to one atomic transition. The laser is set to account for the re-pumping and the Doppler shifts. Atoms in an optically excited state return to the ground state in a few nanoseconds and are ready to absorb again. Each absorption-emission process corresponds to a deceleration by a recoil momentum unit. Let us consider Sodium atoms interacting through the familiar yellow D-line: the recoil velocity is $v_{\text{rec}} = 2.9$ cm/s [16], while a typical atomic beam velocity is about $10^5$ cm/s, which gives the scale of the number of scattering events needed to bring an atom to a velocity of the order of $v_{\text{rec}}$. Out of the Zeeman slower, the atoms can be temporarily confined (not stored) in a spatial region at the intersection of three mutually orthogonal, retro-reflected, counter-propagating, near-resonant lasers, that provide a viscous damping to the atoms, again exploiting the principle underlying the Doppler effect. Typically, the spatial region has a width of a few millimeters. At this stage, Sodium atoms should have a temperature close to the Doppler temperature $T_D = 235\mu K$. To their surprise, Phillips and his group found out in 1989 that the actual temperature was pleasantly well below the predicted limit: only 40 $\mu K$ [17]. First hints of an unpredicted behaviour had already appeared in 1987 [15], when the same group observed a large discrepancy between the 1-D theory and the 3-D experiment on the molasses lifetime spectrum. Their guesswork was "It remains to consider whether the multiple levels and sublevels of Na [...] can explain the surprising behavior of optical molasses [18]" and contained an element of truth. The puzzle was soon solved by Dalibard and Cohen-Tannoudji [19]. The mechanism of Sysyphus cooling, already described for two-level atoms in 1985, explains why an atom with various ground and excited sublevels allows for an additional absorption-emission process that saturates at a sub-Doppler temperature.

### Evaporative cooling

The production of samples of atoms with sub-millikelvin temperatures made it possible to trap neutral atoms. Evaporative cooling, the adiabatic opening of the trap and expulsion of the most energetic particles, is the last step to take in order to further decrease the temperature. Initially, a severe loss mechanism known as Majorana flopping hindered the realization of an abundant quantum degenerate gas. Spending a lot of time in the centre of the trap, where the magnetic field is null, the particles may undergo a spin flip and by that free themselves from the trap. A modification of the magnetic potential in the central region that lifted the minimum potential to a finite magnetic field fixed the problem.

Magnetic and optical traps share an analogous operating principle, based on conservative dipole interaction; both are used for confinement in a continuous geometry. In magnetic traps, the magnetic dipole moment $\mu$ of the atoms couples with an externally produced field **B** as $U_{\text{mag}} = -\boldsymbol{\mu} \cdot \mathbf{B}$; when $U_{\text{mag}} > 0$ ($U_{\text{mag}} < 0$) the atoms are attracted towards the minimum (maximum) of the external field and are called low (high) field seekers. Typical depths of magnetic traps are on the order of 100 mK, which makes them excellent for evaporative cooling purposes.

Optical traps rely on the electric dipole interaction between induced atomic dipole moment and the intensity gradient of the far-detuned light field. Red (blue) detuned traps make the atoms high (low) field seekers. Focused Gaussian laser beams in red detuning (far below an atomic resonance frequency) represent the simplest way to create a dipole trap providing three-dimensional confinement. Typical depths of optical traps are in the range below 1 mK [20], hence they are much weaker than their magnetic counterpart but deep enough to trap atoms previously cooled in optical molasses and bring them to quantum degeneracy [21]. The relatively shallow trap requires to ensure that the gravitational force does not exceed the confining dipole force. Focused-beam traps are therefore mostly aligned along the horizontal axis. However, the Majorana flopping problem is eliminated and moreover external magnetic fields can be used at will for various purposes.

The development of evaporative cooling led to the realization and observation of the first degenerate Bose-Einstein condensate, in 1995 [22, 23]. With BECs at disposal, experimentalists got the chance to explore phenomena proper of coherent gases, such as solitons [24] and vortices in Abrikosov arrays [25, 26], as well as to use the BEC as a laboratory for the investigation on generic coherent phenomena like Kibble-Zurek mechanism [27] and supersolid properties [28].

## 1.3 Neutral atoms in optical lattices

A major branch of research in neutral cold gases regards atomic lattices. A milestone experiment, the observation of a Mott to superfluid phase transition of a BEC on a 3-D lattice [29], came only a few years after the first BEC to breach the barriers between AMO and condensed matter physics, demonstrating that long-envisaged quantum phase transitions could be experimentally realized and observed in a pristine and largely controllable environment. That was a significant breakthrough which untapped the florid and thriving stream of quantum simulation experiments seen in the last two decades.

### Lattices of ultracold gases

Let us briefly recall how cold gases can be arranged onto a discrete spatial geometry. Neutral atoms are trapped in optical lattices after the usual cooling step in a continuous trap. A one-dimensional standing wave field is realized with counter-propagating optical lasers, which imposes on the atoms gas a lattice structure by means of the dipole force. When an electromagnetic field is close to resonance with an atom transition frequency, the light field induces on the atom an oscillating electric dipole, which in turn interacts again through a dipole-dipole force with the laser. This makes the atom see a potential proportional to the intensity of the laser beam. For sufficiently deep lattice potentials $V_0$, with respect to the recoil energy $E_{\text{rec}}$ (about $V_0 \gtrsim 5E_{\text{rec}}$ [30]), the physics of the gas is well captured by the tight-binding approximation. The particles basically sit on the lattice potential minima with a finite probability of tunnelling proportional by the kinetic energy and dependent on the finite overlap between the wavefunctions on two neighboring sites. Furthermore, a single band approximation is valid as long as the particles interaction remains small with respect to the separation between the two lowest energy bands.

The degrees of control offered by optical lattice traps are numerous. For instance, light crystals permit to explore a broad variety of higher dimensional lattices by simply overlapping more optical standing waves, along the wished directions. This is a major advantage compared to solids, where the self-imposed binding structure of atoms determines the lattice geometry. The tunnelling rate, or kinetic energy, can be reduced by increasing the lattice depth instead of lowering the temperature, which is a challenging task at the quantum degeneracy regimes. The caveat is to not make the ratio between kinetic energy and temperature too small otherwise the system becomes essentially classical [31]. Historically, as for gases in continuous traps, atomic lattices were first realized in labs with bosonic particles since fermions are harder to bring to degeneracy with evaporative cooling as they lack s-wave scattering [32]. Nowadays, atomic lattices are realized with a variety of bosonic and fermionic isotopes.

### Tight-binding approximation

Atoms in an optical dipole trap with red-detuned light are subject to a force pointing towards the regions with higher beam intensity. Therefore, atoms in a red-detuned standing-wave optical lattice experience a sinusoidal external potential of the form

$$V_{\text{ext}}(x) = V_0 \sin^2(k_{\text{OL}} x).$$

with $k_{\text{OL}}$ being the wave number and $V_0$ the potential depth, proportional to the laser intensity. In absence of interactions, the atoms obey the free Schrödinger equation with an external potential

$$E\psi(x) = -\frac{\hbar}{2m}\frac{\partial^2}{\partial x^2}\psi(x) + V_0 \sin^2(k_{\text{OL}} x)\psi(x). \tag{1.1}$$

The Bloch theorem prescribes stationary periodic solutions of the form

$$\psi_{qn} = u_{qn}(x)e^{\mathrm{i}qx}, \tag{1.2}$$

where $u_{qn}(x)$ is a periodic function, $q$ is the quasi-momentum (a good quantum number but not the momentum) and the index $n$ denotes the Bloch band. These solutions are de-localized. The Bloch bands describe the dispersion relation, the gap between the bands being larger as the trapping potential increases. For sufficiently deep lattices ($V_0 \gtrsim 5E_{\rm rec}$ [30]), the tight-binding approximation becomes valid and a particle wave-function is rather localized on a site than spread across the lattice. In this regime, the Wannier functions are a preferable set of eigensolutions. They form a complete set of orthogonal functions strongly localized at a given site $x = jd$,

$$W_j^{(n)}(x) = \frac{1}{\sqrt{N}} \sum_q e^{-\mathrm{i}qjd} \psi_{qn}(x), \tag{1.3}$$

where $d$ is the lattice parameter. In the limit of very deep lattice, the Wannier functions tend to the eigenstates of the harmonic oscillator. The wells are faithfully approximated by a harmonic potential, $V_0 \sin^2(k_{\rm OL} x) \simeq V_0 k_{\rm OL}^2 x^2$, whose effective frequency $\tilde{\omega}$ depends on the recoil energy and on the amplitude $V_0$:

$$\frac{m\tilde{\omega}^2}{2} = V_0 k_{\rm OL}^2 \quad \rightarrow \quad (\hbar\tilde{\omega})^2 = 4V_0 \frac{\hbar^2 k_{\rm OL}^2}{2m} \quad \rightarrow \quad \hbar\tilde{\omega} = 2\sqrt{s}E_{\rm rec}, \tag{1.4}$$

where $s = \sqrt{V_0/E_{\rm rec}}$. The recoil frequency reads

$$E_{\rm rec} = \frac{\hbar^2 k_{\rm OL}^2}{2m} = \frac{\omega_0^2}{m} \frac{\hbar^2}{2c^2} \quad \rightarrow \quad \omega_{\rm rec} = 2\pi \cdot \frac{\nu_0^2}{m} \frac{h}{2c^2} \simeq 2\pi \cdot 2.22 \frac{\nu_0^2}{m}, \tag{1.5}$$

where $\nu_0$ is expressed in THz units and the mass in a.m.u.

To put some numbers, let us consider the $^{87}$Rb isotope of Rubidium, with mass of 86.91 u [16], used in the experiment by Greiner *et al.* [29]. The optical lattice lasers operated at wavelength $\lambda = 852$ nm, to $\omega_0 = 2\pi \cdot 351.9$ THz, corresponding to a recoil frequency

$$\omega_{\rm rec} = 3.163 \text{ kHz}. \tag{1.6}$$

Although the lasers are far detuned from all atomic resonances, it is safe to pick as a scale the recoil energy at the $D_1$ line, centered at $\lambda = 795$ nm, $\omega_0 = 2\pi \cdot 377.1$ THz, for which $\omega_{\rm rec} = 3.633$ kHz [16]. Typical lasers reach a max intensity of 1 mK [20]: this corresponds to about 20 MHz, $s \sim 1000$, thousands of recoil energy units. The superfluid to Mott-insulator transition (see in Section 1.3) occurs at a depth of about $s = 13$ recoil energy units, whence

$$\tilde{\omega} = 22.805 \text{ kHz}, \tag{1.7}$$

which gives the energy scale of lowest band gap. Lightest atoms have higher recoil energy, yet the tight-binding regime is attainable: for instance, the composite boson $^7$Li has $\omega_{\rm rec} = 63.164$ kHz, thus a 1 mK trap is about $s = 300$ recoil energy units deep.

In second quantization, the continuous kinetic energy operator is mapped to a discrete hopping operator coupling nearest-neighbouring sites, the overlap between next-nearest neighbours being negligible. The hopping amplitude reads

$$t = -\int d\mathbf{r} W_{\vec{j}}^{(0)}(\mathbf{r}) \left[ -\frac{\hbar^2}{2m} \nabla^2 + V_{\rm ext}(\mathbf{r}) \right] W_{\vec{j}+\vec{\delta}}^{(0)}(\mathbf{r}), \tag{1.8}$$

where $\vec{j} + \vec{\delta}$ are the nearest neighbours of the site $\vec{j}$. The kinetic energy term reads

$$\hat{H}_{\rm kin} = -t \sum_i \left( \hat{c}_{i+1}^\dagger \hat{c}_i + \hat{c}_i^\dagger \hat{c}_{i+1} \right). \tag{1.9}$$

The on-site interaction energy depends on the particle statistics: for Bose gases it reads

$$\hat{H}_{\text{int}} = \frac{U}{2} \sum_i \hat{n}_i(\hat{n}_i - 1), \tag{1.10}$$

while for Fermi gases on-site interactions are only non-zero in the presence of more than one component, due to the Pauli exclusion principle:

$$\hat{H}_{\text{int}} = U \sum_i \hat{n}_{i\uparrow} \hat{n}_{i\downarrow}. \tag{1.11}$$

The coefficient $U$ accounts for the on-site $s$-wave contact interaction:

$$U = g \int d\mathbf{r} \left| W_{\vec{j}}^{(0)}(\mathbf{r}) \right|^4 . \tag{1.12}$$

In tight-binding approximation, the hopping rate decreases exponentially with the lattice depth,

$$\frac{J}{E_{\text{rec}}} = \frac{4}{\sqrt{\pi}} s^{3/4} e^{-2\sqrt{s}} \tag{1.13}$$

while $U$ increases with a power law that depends on the dimensionality $D$ of the lattice:

$$\frac{U}{E_{\text{rec}}} \sim s^{D/4}; \tag{1.14}$$

For instance, at the Mott-insulator phase transition ($s = 13$) for $^{87}$Rb the energy scales are $J \simeq 0.01 E_{\text{rec}} \simeq 36$ Hz and $U \simeq 6.85 E_{\text{rec}} \simeq 25$ kHz.

The nearest-neighbours hopping term, the on-site and inter-site interaction terms are the basic ingredients of a vast class of models, the Hubbard-type Hamiltonians, which are extensively investigated:

$$\hat{H}_{\text{Hubbard}} = -J \sum_i \left( \hat{a}_{i+1}^\dagger \hat{a}_i + \hat{a}_i^\dagger \hat{a}_{i+1} \right) + U \sum_i f(\hat{n}_i^{(a)}, \hat{n}_i^{(b)}). \tag{1.15}$$

Analogously to the Ising and Heisenberg models for spin systems, these models succeed in faithfully capturing a wealth of physics of complex many-body real systems, despite their elementariness.

### The Bose-Hubbard model

Let us now describe the above-mentioned experiment by Greiner *et al.* [29], forerunner of quantum simulations with atomic lattices. The Bose-Hubbard model is defined as follows:

$$\hat{H}_{\text{BH}} = -J \sum_i \left( \hat{b}_i \hat{b}_{i+1}^\dagger + \hat{b}_i^\dagger \hat{b}_{i+1} \right) + \frac{U}{2} \sum_i \hat{n}_i(\hat{n}_i - 1). \tag{1.16}$$

At zero temperature thermal fluctuations are suppressed. Quantum fluctuations, due to the Heisenberg principle, drive the phase transitions. A prominent example is the Mott-insulator to superfluid phase transition The superfluid state occurs in Bose-Einstein condensates, which exhibit long-range phase coherence. When the on-site atom-atom repulsive interaction $U$ becomes larger than $J$, the fluctuations in the atom number per site is reduced. Accordingly, the fluctuations in the phase increase and coherence is lost. The interplay between the two competing Hamiltonian terms is inherent in quantum phase transitions and fundamentally distinct from the

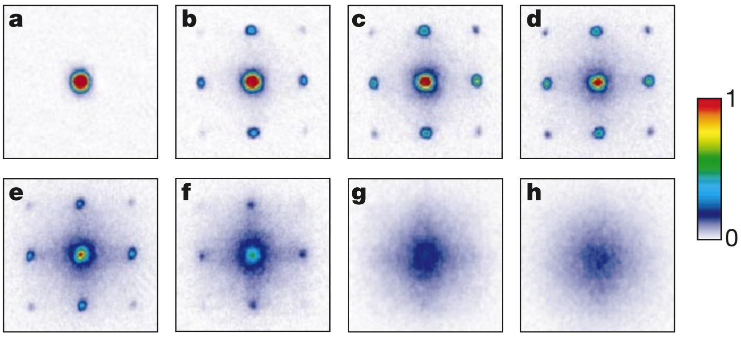

FIGURE 1.1: From $a$ to $h$: single interference peak from a coherent superfluid state, degrading coherence giving rise to interference patterns, incoherent localized Mott insulating state. Imaging in time of flight, 15 ms after release from the trap. Figure from Greiner *et al.* [29].

competition between inner energy and entropy, which drives classical phase transitions.

Owing to a different scaling (see Eqs. (1.13) and (1.14)), the ratio $U/J$ can be controlled by varying the lattice depth. To probe the phase of the gas, the trapping potential is suddenly turned off and the gas wavefunctions are let free to evolve and interfere. The momentum distribution of a Bose gas in a lattice is the convolution of the Fourier-transformed Wannier function and the quasi-momentum distribution. The hallmark of the superfluid phase is the sharp central interference peak in Fig. 1.1. As one increases the lattice depth, the Wannier function becomes narrower so that the envelope function broadens and hence one sees peaks appear, due to the periodic array of phase-coherent matter-wave sources. When the system starts to localize, the quasi-momentum distribution broadens too, the coherence between different sites decreases and the peaks get thicker and thicker until, in the Mott regime, the momentum distribution blurs. This and the existence of an energy gap where clearly identified and shown by Greiner *et al.* [29] and represent the smoking gun of the transition to a Mott insulating phase.

### The Fermi-Hubbard model

The Fermi-Hubbard model is defined as

$$\hat{H}_{\mathrm{FH}} = -J \sum_{<i,j>} \sum_{\sigma=\uparrow,\downarrow} \left( \hat{c}^{\dagger}_{i,\sigma} \hat{c}_{j,\sigma} + \hat{c}^{\dagger}_{j,\sigma} \hat{c}_{i,\sigma} \right) + U \sum_{i} \hat{n}_{i\uparrow} \hat{n}_{i\downarrow}, \tag{1.17}$$

where $< i,j >$ are nearest-neighbouring sites. With a single spin component $\sigma$ the system lacks on-site interaction, since the Pauli exclusion principle forbids two fermions of the same spin to co-exist in the same lattice site. In local density approximation, the Hamiltonian models well a Fermi gas a in a real deep optical lattice. To also account for the inhomogeneous lattice depth, which is higher in the centre where the beam is focused and decreases outwards, one can introduce a chemical potential term $\sum_i \varepsilon_i \hat{n}_i$. We consider hereafter a balanced two-components Fermi gas: for each particle with spin down there is another one with spin up. A fundamental assumption in the Fermi-Hubbard model is that thermal and quantum fluctuations are not sufficient to cause excitations above the lowest Bloch band. As a consequence, the gas behaves as a band insulator at unit filling. The single-band Hubbard model

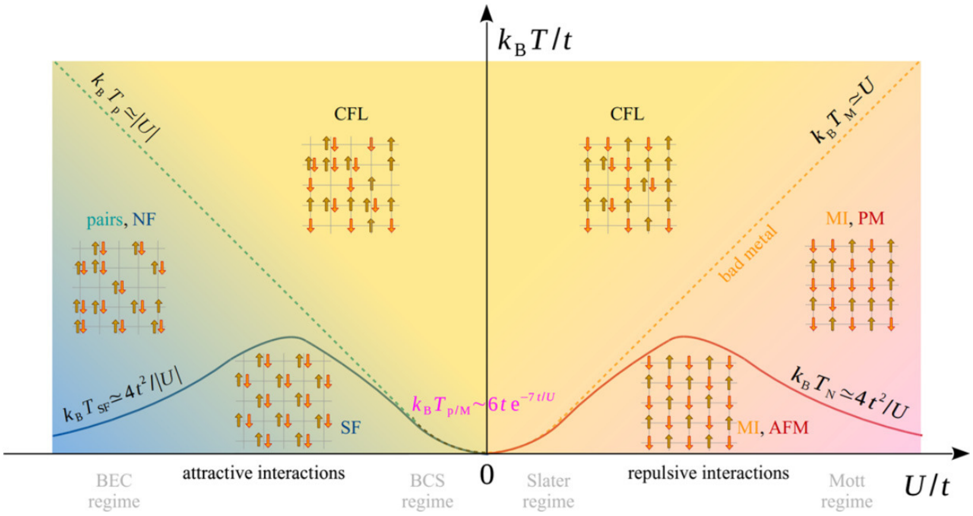

FIGURE 1.2: Phase diagram of the Fermi–Hubbard model, at half filling, for a three-dimensional cubic lattice. The dashed lines indicate the smooth crossovers between the correlated Fermi liquid (CFL) phase and the normal fluid or paramagnetic phases. Solid lines are second order phase transitions. Figure from Tarruell [33].

ceases to be correct when the scattering length approaches the size of the Wannier function.

The ground-state phases at half filling are recapitulated in Figure 1.2 and can be analysed in terms of charge and spin sectors. In the charge sector, three regimes can be identified:

- the Mott insulator, with a vanishing compressibility. Large repulsive interaction $U \gg t$ and low temperature make it unfavourable for the particles to hop and form an itinerant metallic state;
- the correlated Fermi liquid, at finite temperature, for weak repulsive or attractive interactions. It has a metallic character, with density fluctuations;
- the pairing regime for attractive interactions and low temperature, characterized by itinerant stable bosonic pairs.

These phases are separated by smooth crossovers. In the deep Mott phase, whilst the charge distribution is classical, a large entropy remains in the spin degree of freedom. In the limit of strong interactions the Fermi-Hubbard model can be mapped to an isotropic antiferromagntic Heisenberg model, characterized by the onset of Néel staggered magnetization:

$$H^{(2)} = 4\frac{t^2}{U}\vec{S}_i\vec{S}_{i+1}, \tag{1.18}$$

where $\hat{S}_i^{(z)} = \frac{1}{2}(c^\dagger_{i\uparrow}c_{i\uparrow} - c^\dagger_{i\downarrow}c_{i\downarrow})$, $\hat{S}_i^{(-)} = c^\dagger_{i\downarrow}c_{i\uparrow}$ and $\hat{S}_i^{(+)} = c^\dagger_{i\uparrow}c_{i\downarrow}$. In intermediate regions, the competition of interactions, Pauli principle and tunnelling drives the phases of the spin sector, separated by second-order phase transitions: the solid red and blue lines in Figure 1.2. For repulsive interactions, the transition separates the disordered paramagnetic phase from the anti-ferromagnetic phase. In the limit of weak repulsive interaction $0 < U/t \ll 1$ , mean field theory arguments suggest a spin density wave as the ground state [33]. Through Hartree-Fock decoupling, one

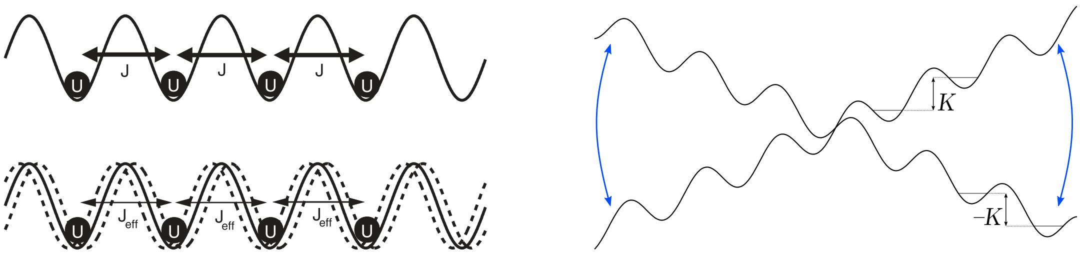

FIGURE 1.3: The tunnelling of an ultra cold gases on a 1-D lattice is dynamically suppressed by strong longitudinal driving of the optical trap: the bare tunnelling matrix element $J$ becomes a renormalized, smaller $J_{\text{eff}}$. Figure from Lignier *et al.* [41].

obtains the Hamiltonian

$$H \simeq -J\sum_{i}\sum_{\sigma}\left(\hat{c}^{\dagger}_{i+1,\sigma}\hat{c}_{i,\sigma}+\hat{c}^{\dagger}_{i,\sigma}\hat{c}_{i+1,\sigma}\right)+\frac{U}{4}N(1+n_s^2)-\frac{Un_s}{2}\sum_{i}(-1)^i(\hat{n}_{i\uparrow}-\hat{n}_{i\downarrow}); \tag{1.19}$$

here, $N$ is the number of particles and $n_s = (-1)^i \langle \hat{n}_{i\uparrow} - \hat{n}_{i\downarrow} \rangle$ is an order parameter: for $n_s = 0$ the spin components at every site on average balanced, for $n_s = 1$ there is a maximally staggered magnetization. The ground state is thus a spin density wave, namely a very small modulation or long wavelength. For attractive interactions, the transition is from a normal to superfluid phase, this last characterized by the crossover from Bose–Einstein condensate to the BCS regime.

Analytical solutions of the Fermi–Hubbard model are known solely in one dimension, where the ground state can be obtained by Bethe ansatz. Exotic FH model in 1-D can be solved numerically with tensor network methods. In higher dimensions, numerical simulations are hindered by the well-known sign problem [34] or unfavourable computational resources scaling with increasing lattice size [35]. One of the motivations to investigate the Fermi-Hubbard model lies in the belief that the Fermi-Hubbard model might capture the fundamental ingredients of the high-temperature superconductivity [36–38], unexplained within the frame of the BCS theory.

### Tunnelling coherent control

Independent coherent control on $J$, $U$ and on additional terms appearing in extended Hubbard-type models is crucial to explore the various phases of the Hamiltonian investigated. Tuning the on-site interaction $U$ is a standard and well-known practice, based on the use of Feshbach resonances. Coherent control of the tunnelling has been the subject of fruitful investigations. Tunnelling control was first proposed with far-infrared strong photon dressing on semiconductors super-lattices [39]. By the same token, coherent control of $J$ on cold gases in lattices was proposed [40], which allowed a group of experimentalists in Pisa to reversibly induce the superfluid to Mott-insulator phase transition [41, 42].

To realize collective tunnelling control with photon dressing, one can add a periodic perturbation to the optical lattice, either by mechanical vibration or by varying the frequency. In the first case, the laser mirrors are mounted on piezoelectric actuators that sinuisoidally shake the lattice in the longitudinal direction. A system globally accelerated by a homogeneous force experiences a linear potential; the sinusoidal acceleration of the lattice echoes in a linear tilting with amplitude and

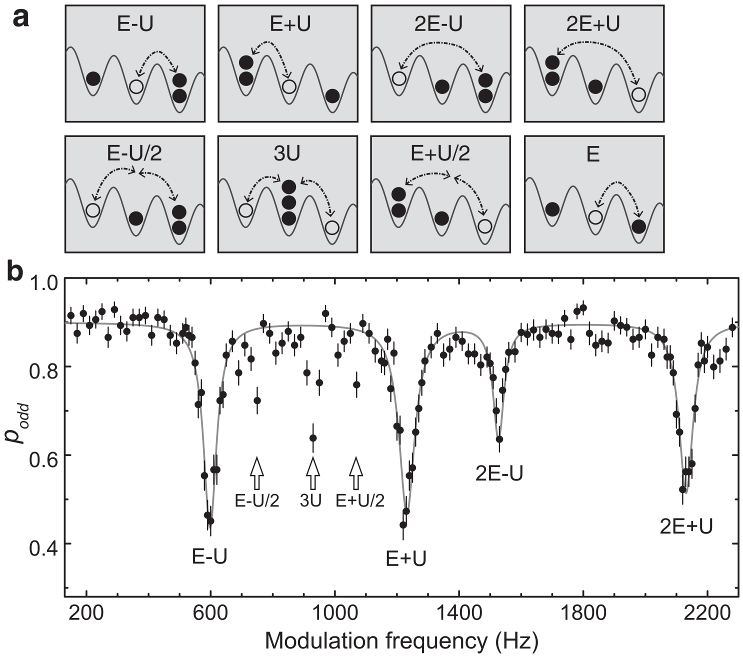

FIGURE 1.4: Amplitude modulation spectroscopy on a 1-D optical lattice. (a) Schematic of the tunnelling channels connecting to a deep Mott state - all but the hopping between two empty wells in the last panel, added by way of example. (b) Odd-number occupation probability vs modulation frequency, dropping when doublon-hole pairs are resonantly created. Figure from Ma *et al.* [43].

direction modulation, see Figure 1.3:

$$\hat{H} = -J \sum_i \left( \hat{b}_i \hat{b}_{i+1}^\dagger + \text{h.c.} \right) + K \cos(\omega t) \sum_i i \hat{n}_i, \tag{1.20}$$

Periodically shaking the lattice induces inhibition, suppression and eventually change of sign of the tunnelling amplitude, steered by the zeroth-order Bessel function of the driving strength. The driving frequency is not bound to any energy scale, as long as it does not cause undesired interferences, such as inter-band excitations. The effective tunnelling $J_{\text{eff}}$ is measured by letting the BEC freely expand in the lattice. A negative $J_{\text{eff}}$ flips the energy band upside down, favouring the occupation of states with larger quasi-momentum. This can be evidenced by looking at the interference peaks in time-of-flight, shifted by half a Brilluoin zone.

### Amplitude modulation

A more selective control of the tunnelling rate can be obtained by modulating the lattice amplitude. On a tilted lattice, with linear bias $E$, the bare hopping couples two neighbouring wells off-resonantly with probability $P \sim 4\,(J/\Delta)^2$. The energy gap $\Delta$ depends on the on-site interaction and on the two wells occupation number. An amplitude modulation of intensity $\delta J$ with frequency $\omega = E$ provides photons with the required energy for an atom to resonantly be transferred between the two wells, with an effective Rabi frequency given by $\delta J/2$. Figure 1.4(a) displays the states reachable from the deep Mott configuration at unit filling of a Bose gas; the last board depicts the case of a single particle in two empty wells. The validity of the

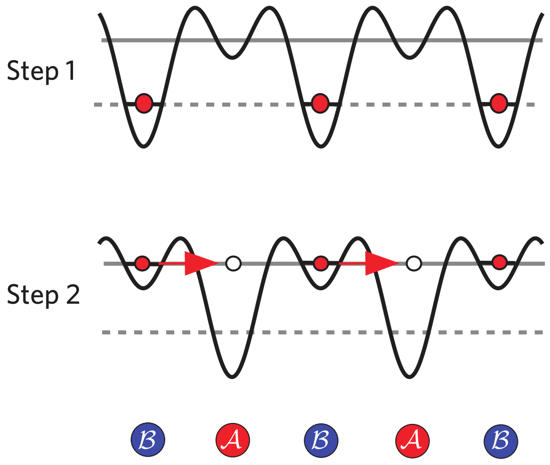

FIGURE 1.5: A superlattice in its ground states hosts particles on the $s$-band of the deep sites, step 1. A quench swaps the sites, step 2, bringing the $s$- and $p$-bands of the $\mathcal{B}$ and $\mathcal{A}$ sublattices to energetic degeneracy. Figure from Wirth *et al.* [44].

method was demonstrated by Ma *et al.* [43]. As shown in Figure 1.4(b), they swept the frequency spectrum and revealed the resonances by in situ fluorescence imaging, sensitive to the parity of site occupation.

### Populating the $p$-band states

Up to now, we have restricted our considerations to a single band. The outweighing amplitude of the lowest gap compared to the energy scale of quantum fluctuations, on-site interactions or the frequency of external modulations guarantees the exclusive occupation of the lowest $s$-orbital in optical lattices. In bare Hubbard models, higher orbitals population is unwelcome and has generally only marginal effects. However, one can look at the hybridization with excited states, primarily $p$-orbitals, as a route towards extended models.

Orbital effects play a fundamental role in metal oxides. In several instances, novel quantum phases emerge due to the coupling of the orbital degree of freedom to the charge, spin, or lattice degrees of freedom. In the context of cold gases, multi-orbital physics can lead to unconventional superfluid states, Haldane phases, graphene-like physics and models with no prior analogues in solid state electronic materials [45]. Several groups have now achieved selectively loading and manipulating ultracold atoms in $p$-bands. In hexagonal lattices, the graphene-like band-structure features $s$- and $p$-bands separated by a gap of the order of the tunnelling energy [46], hence the hybridization is spontaneous.

In square lattices, the formation of a superfluid state in resonant $s$- and $p$-bands of a bipartite lattice was achieved by the group of Hemmerich [44]. A Bose gas was loaded on the lowest band of the deepest sublattice $A$, the hopping being negligible due to the high energy gap between those and the intermediate sublattice $B$, as in Figure 1.5. From this Mott state, a rapid (faster than the hopping time scale) ramping of the lattice beam intensity swaps the sublattices, so that $B$ is deeper and the energy of its $p$-band equals that of the $A$ sites $s$-band. Note that, the solutions of the isotropic harmonic oscillator in 3-D are the spherical harmonics, stretched or compressed in case of anisotropic frequencies: irrespective of that and independently from energy degeneracies, the tunnelling along the $x$-direction is most likely between $p_x$-band states (same for $y$, $z$), owing to a larger overlap of the wavefunctions. The quench eventually scrambles the system and populates up to the fourth Brillouin zone. However, in an intermediate time interval of about 20 ms, a cross-dimensional coherence is observed, marked by a momentum spectrum featuring condensation at the corners of the Brillouin zone, characteristic of the concave $p$-band.

# Chapter 2

# Berry-like dynamical gauge fields

Gauge fields are ubiquitous in physics. In condensed matter physics, gauge fields lie at the roots of a number of fundamental or emergent physical phenomena. The signature of gauge fields in non-relativistic physics is often identifiable in a non-trivial complex phase, inherent or acquired by the wave-function. A complex phase is picked up during the evolution of a charged particle encircling a region of space permeated by a magnetic field, the Aharonov-Bohm effect, or after the exchange of two identical particles in lower dimensions, the anyonic statistics. In particular, complex phases embedded in the anyonic quasi-particles of a many-body system determine non-trivial macroscopic behaviours, such as the plateaus in the conductivity of the fractional quantum Hall effect. A unifying mathematical framework that encompasses these and other phenomena in classical and quantum physics is built upon the notions of Berry curvature, connection and complex phase.

In this chapter, we give a brief introduction to the Berry theory. We discuss the panoply of physical phenomena related to the Berry phase and recently investigated with experiments in cold gases, in one- and two-dimensional atomic lattices. Concurrently, we discuss the experimental techniques engineered to enforce an artificial gauge field. Then, we move to the anyonic statistics and the significance of anyon quasi-particle in emergent phenomena on strongly coupled many-body systems. We present the state-of-the-art experimental methods to quantum simulate a dynamical gauge field, focusing on the work done so far on 1-D anyons.

## 2.1 The Berry phase

The notion of Berry phase is present in many branches of physics. Introduced in 1984, it encompasses and generalizes a number of phenomena whose explanation requires the presence of a non-gaugeable complex phase. To outline the topic, we follow the review by Xiao, Chang and Niu [47]. Consider a Hamiltonian that depends on time through a set of parameters $\boldsymbol{R}$,

$$H = H(\boldsymbol{R}), \qquad \boldsymbol{R} = \boldsymbol{R}(t), \tag{2.1}$$

and suppose to follow the time evolution of an initial eigenstate through a closed path $\mathcal{C}$ in the parameter space $\mathcal{P}(\boldsymbol{R})$. At each instant we can define a set of eigenstates of $H(\boldsymbol{R})$:

$$H(\boldsymbol{R}) \left| n(\boldsymbol{R}) \right\rangle = \varepsilon_n(\boldsymbol{R}) \left| n(\boldsymbol{R}) \right\rangle . \tag{2.2}$$

In the absence of degeneracy and if the energy manifold $\varepsilon_n(\boldsymbol{R})$ is well isolated by a gap along the entire path, the quantum adiabatic theorem tells that the eigenstate will surely come back to itself at the end of a closed path. Each state $|n(\boldsymbol{R})\rangle$ is obviously defined up to a complex phase. We can assume that the instantaneous global phase is smooth and single valued along the path $\mathcal{C}$. The global phase can be expressed as the sum of a dynamical and a geometric phase. The geometrical phase is defined as the integral of the *Berry connection* $\mathcal{A}_{\text{geom}}(\boldsymbol{R})$ over a path $\mathcal{C}$,

$$\gamma_{\text{geom}} = \int_{\mathcal{C}} d\boldsymbol{R} \cdot \mathcal{A}_{\text{geom}}(\boldsymbol{R}), \tag{2.3}$$

where the Berry connection is defined as

$$\mathcal{A}_{\text{geom}}(\boldsymbol{R}) = \mathrm{i} \left\langle n(\boldsymbol{R}) \middle| \frac{\partial}{\partial \boldsymbol{R}} \middle| n(\boldsymbol{R}) \right\rangle. \tag{2.4}$$

Using the Green's theorem, $\gamma_{\text{geom}}$ is equal to the integral of the curl of the connection over the relative surface $\Sigma$,

$$\gamma_{\text{geom}} = \int_{\Sigma} d\boldsymbol{S} \cdot \Omega_{\text{geom}}(\boldsymbol{R}), \tag{2.5}$$

where $\Omega_{\text{geom}} = \nabla_{\boldsymbol{R}} \times \mathcal{A}_{\text{geom}}(\boldsymbol{R})$ is named the *Berry curvature*. The geometric phase was long deemed unimportant as, on an open path, it can be cancelled out by a gauge transformation:

$$\begin{aligned} &|n(\boldsymbol{R})\rangle \to e^{\mathrm{i}\xi(\boldsymbol{R})} |n(\boldsymbol{R})\rangle, \\ &\mathcal{A}_{\text{geom}}(\boldsymbol{R}) \to \mathcal{A}_{\text{geom}}(\boldsymbol{R}) - \frac{\partial}{\partial \boldsymbol{R}} \xi(\boldsymbol{R}). \end{aligned} \tag{2.6}$$

Since the gauge adds to the geometric phase a term $\xi(\boldsymbol{R}(0)) - \xi(\boldsymbol{R}(T))$, exclusively dependent on the initial and final points of the path, it is always possible to find one gauge transformation that offsets $\gamma_{\text{geom}}$. However, Berry showed that this changes in a closed path: since the gauge needs to be single valued, $\xi(\boldsymbol{R}(0)) - \xi(\boldsymbol{R}(T))$ can only take values multiples of $2\pi$, hence the geometric phase can not be gauged out. Furthermore, it only depends on the geometric aspect of the closed circuit, the explicit time path being thus irrelevant.

Note that the geometric phase acquired by the evolving state has a gauge structure, as it is invariant under a local transformation of the connection, as in Eq. (2.6). The local transformation can be recognized as the same gauge transformation on the vector potential that leaves the classical electrodynamics Lagrangian invariant. The analogy with electromagnetism extends to the Berry curvature that takes the form of a magnetic field in parameter space. In fact, the Berry phase is readily recognized as a generalization of the Aharonov-Bohm phase, acquired by a charged particle moving along a circuit in real (and parameter) space that encloses a region with a finite external magnetic field. To summarize, the following schematic equivalence links the Berry formalism to the electromagnetic potential:

$$\text{Berry phase} \leftrightarrow \text{Aharonov} - \text{Bohm phase}$$

$$\text{Berry connection} \leftrightarrow \text{Vector potential}$$

$$\text{Berry curvature} \leftrightarrow \text{Magnetic field}$$

In order to study Berry-related physics in ultracold gases it is necessary to generate an artificial Berry phase: we will see later in this Chapter how the goal can be achieved.

## 2.2 Artificial gauge fields in cold gases

Finding stratagems to generate artificial gauge fields in quantum simulators with cold gases has attracted major interest. In this section, we describe the main solutions conceived and the milestone experiments in which those were adopted.

### 2.2.1 Raman-assisted tunnelling

**Minimal coupling** The coupling between a generic electric charge distribution and an electromagnetic field can be expressed in terms of a multi-pole series. The first-order, isotropic term is known as minimal-coupling,

$$\hat{H} = \frac{(\mathbf{p} - e\mathbf{A})^2}{2m} + e\Phi, \tag{2.7}$$

and it is exact for a point-like charged particle. The minimal coupling suggests that the electromagnetic potential enters the Hamiltonian acting on the momentum; we will discuss in this Chapter how constant and dynamical gauge fields cause drift and reshaping of the momentum distribution.

**The Peierls phase** In the presence of a lattice, the electromagnetic field enters the Hamiltonian as a phase factor on the hopping term,

$$J \to J e^{-\mathrm{i}e \int_{\mathcal{P}} d\mathbf{r}\cdot\mathbf{A}(\mathbf{r})}, \tag{2.8}$$

where the $\mathcal{P}$ is the hopping path, generally limited to two nearest-neighbouring sites. In this context, the complex phase is also known as Peierls phase.

#### Engineering complex phases

Raman-assisted tunnelling is one of the methods available to realize controlled phase-dependent tunnelling [48, 49]. This technique requires the inhibition of the bare tunnelling with a strong linear potential offset $\Delta$, realized by accelerating the 1-D optical lattice along the longitudinal direction or by applying an inhomogeneous external electric or magnetic field. The linear tilt suppresses the Hamiltonian translation symmetry, so that the Wannier functions $W_n(x)$ of Equation (1.3) are not a proper description of the localized states. The Hamiltonian can be instead diagonalized in the basis of the Wannier-Stark states,

$$\Psi_n(x) = \sum_m J_{m-n}\left(\frac{2J}{\Delta}\right) W_m(x), \tag{2.9}$$

where $J_m$ are Bessel functions. When the energy gap between neighbouring sites is large compared to the band width (while still being small compared to the first band gap), the tunnelling probability vanishes as $J_{\mathrm{eff}} \sim 4\left(\frac{J}{\Delta}\right)^2$. Likewise the Bessel functions with $m \neq n$ become negligible, so that $\Psi_n(x)$ is faithfully and conveniently described by the sole nearest contributions,

$$\Psi_n(x) \simeq W_n(x) + \frac{J}{\Delta}\left[W_{n+1}(x) - W_{n-1}(x)\right]. \tag{2.10}$$

Tunnelling is restored with two far-detuned Raman beams of Rabi frequency $\Omega$, Figure 2.1. The lasers have a frequency shift $\delta\omega = \omega_1 - \omega_2$ and the transfer rate is

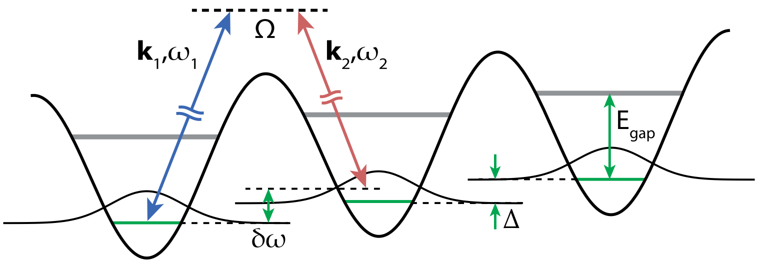

FIGURE 2.1: Raman-assisted tunnelling in a tilted lattice with energy bias between neighbouring sites $\Delta$, quasi-resonant two-photons offset $\delta\omega \simeq \Delta$ and Rabi frequency $\Omega$. Figure from Miyake *et al.* [50].

maximized at resonance with the linear gap, $\delta\omega = \Delta$. The atom also experiences an impulse $\delta\mathbf{k} = \mathbf{k}_1 - \mathbf{k}_2$. The effective tunnelling amplitude is given by

$$J_{\text{eff}} = \frac{\Omega}{2} \int d\mathbf{r}\, \Psi_n^*(\mathbf{r})\, e^{\mathrm{i}\delta\vec{\mathbf{k}}\cdot\mathbf{r}}\, \Psi_{n+1}(\mathbf{r}) \tag{2.11}$$

We consider now a 2-D lattice, tilted along the $x$-direction. Let us assume that the impulse is finite also in the $y$-direction, although the Raman-assisted tunnelling occurs along $x$. Then

$$\begin{aligned} J_{\text{eff}} =& \frac{\Omega}{2} \int dx\, \Psi_n^*(x)\, e^{\mathrm{i}\delta k_x x}\, \Psi_{n+1}(x) \int dy\, W_n^*(y)\, e^{\mathrm{i}\delta k_y y}\, W_n(y) \qquad (2.12) \\ \simeq& \frac{\Omega}{2} \int dx\, \left\{ W_n(x) W_{n+1}(x) + \frac{J}{\Delta}\left[W_{n+1}^2(x) - W_n^2(x)\right] \right\} e^{\mathrm{i}\delta k_x x} \int dy\, W_n^2(y)\, e^{\mathrm{i}\delta k_y y}. \end{aligned}$$

The first term of the integral over the variable $x$ is null due to the orthogonality of the Wannier functions. Typically, the energy offset $\Delta$ is on the order of the kHz, way below the optical lattice frequency; correspondingly, the impulse wavelength $\lambda_k$ is large compared to the lattice parameter $a$. Thus, the phase $e^{\mathrm{i}\delta k_x x}$ is practically constant $\simeq e^{\mathrm{i}\delta k_x n a}$ over the integration range of the Wannier function $W_n(x)$, and likewise along the $y$-direction. The effective hopping amplitude then reads

$$\begin{aligned} J_{\text{eff}} \simeq& \frac{\Omega J}{2\Delta} \left( e^{\mathrm{i}\delta k_x (n+1) a} - e^{\mathrm{i}\delta k_x n a} \right) e^{\mathrm{i}\delta k_y n a} \\ =& \mathrm{i}\frac{\Omega J}{\Delta} \sin\left(\frac{\delta k_x a}{2}\right) e^{\mathrm{i}\delta k_x (n+\frac{1}{2}) a}\, e^{\mathrm{i}\delta k_y n a} \\ =& J_{\text{eff}}^{(0)}\, e^{\mathrm{i}\Phi_x n}\, e^{\mathrm{i}\Phi_y n}, \end{aligned} \tag{2.13}$$

where $\Phi_{x,y} = \delta k_{x,y} a$. According to Equation (2.8), the vector potential amplitude $A$ relates to the complex phase as

$$A = \phi / a = \delta k_y n. \tag{2.14}$$

As one can see in Figure 2.2, a particle taking a minimal closed path of one plaquette picks up no phase along $y$ and two phases $-\delta k_y n$ and $\delta k_y (n+1)$ along $x$. Note that:

- without a momentum kick $\delta k_x$ the Raman-assisted hopping $J_{\text{eff}}$ is null;

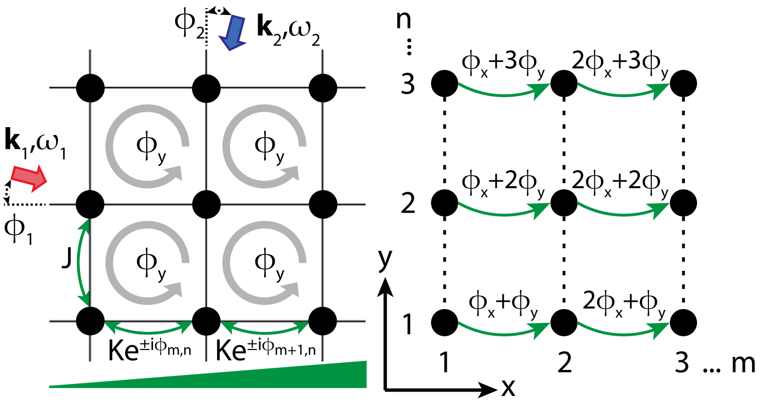

FIGURE 2.2: Schematic of the experimental arrangement to generate uniform magnetic fields. The bare hopping amplitude $J$ drives the dynamics along $y$. An energy gradient along $x$ inhibits the tunnelling, which is restored with amplitude $K$ by a pair of far-detuned laser beams: note that at least one beam must carry momentum along $y$ in order to induce a $y$-dependent phase. The equivalent number of flux quanta per unit cell is $\alpha = \phi_y/2\pi$. Figure from Miyake *et al.* [50].

- without a momentum kick $\delta k_y$ the overall phase picked up on a closed path is null.

Other schemes exist to add a complex phase to the hopping, primarily lattice shaking. The one just introduced is particularly favourable as it requires only far-off-resonant lasers and a single internal state. Previous analogous proposals explored coupling of different hyperfine states, requiring near-resonant light that causes heating.

**Harper–Hofstadter model** In the continuum, the eigenstates of a charged particle in a strong magnetic field are the highly-degenerate Landau levels. On periodic potentials, the energy spectrum is defined by the Bloch bands. Electron gases on a 2-D lattice exposed to strong magnetic fields see the interplay between the two characteristics length scales, the lattice constant and the magnetic length $l_B = \sqrt{\hbar/eB}$. This is called the Harper-Hofstadter model. This gives rise to a complex energy spectrum known as Hofstadter's butterfly. A confirmation of such phenomenology on solid state samples would require extremely large magnetic fields of several thousands Tesla.

In 2013, the Harper-Hofstadter model was successfully reproduced with cold gases [50, 51]. There, Raman-assisted hopping along the $x$ direction of a 2-D lattice imprinted a $y$-dependent complex phase. The Peierls phase accumulated as particle hops around a close loop corresponds to the geometric Berry phase picked up by a charged particle encircling a (effective) magnetic field.

**Chiral Meissner currents** Another landmark experiment was the simulation of the Meissner to vortex phase transition, fingerprints of type-II superconductors exposed to magnetic fields [52]. The experiment involved a Bose gas loaded on ladder traps, the simplest 2-D geometry hosting orbital magnetic fields. A super-lattice in the $x$-direction, as in Figure 2.3, decouples the wells separated by the larger energy bias, while the smaller tilting is functional to the laser assisted tunnelling. The chiral Meissner currents can be identified by observing the average current on either leg of

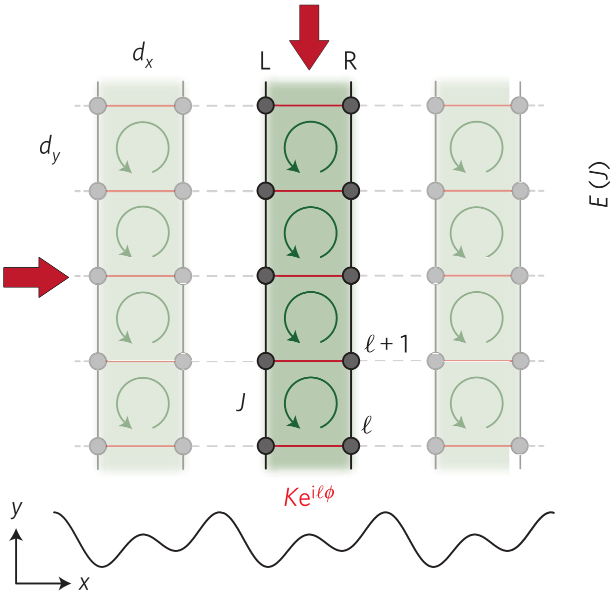

FIGURE 2.3: The experimental setup of Atala *et al.* [52] corresponds to the one in Figure 2.2, with an additional strong energy offset every two sites along the $x$-direction to decouple the two-dimensional lattice onto an array of ladders.

one ladder. Technically, the magnetic flux is kept fixed and the transition is induced by changing $K$ and thus the rung-to-leg coupling ratio $K/J$. The global current is observed to increase in response to small but growing $K/J$, until a critical flux is reached beyond which the system adapts fractionalizing into local, regularly distributed, vortices.

### Synthetic dimensions and edge properties

The works on rotating BECs, the Meissner to vortex phase transition, the Hofstadter butterfly and the Harper Hamiltonian all addressed bulk properties of the systems. Edge states with their topological character represent an appealing frontier of research. Besides the fundamental interest on the intriguing properties of 2-D topological materials, the robustness of edge states against perturbations makes them desirable for quantum computation aims. Basic quantum Hall physics has been recently investigated using synthetic gauge fields in synthetic dimensions [53].

A group at LENS realized that on a 1-D optical lattice loaded with a gas of $^{14}$Yt fermions, which effectively behaves as a 2-D lattice when a constant magnetic field Zeeman lifts the degeneracy of the sub-levels of the hyperfine manifold [54]. The internal nuclear spin degree of freedom becomes the synthetic $y$-direction; the virtual dimension is topped by the manifold degeneracy and can be controlled by the Zeeman splitting. Analogously to the Raman-assisted tunnelling in real space coordinates, the hyperfine states are coupled via two-photon Raman transitions including a complex phase. Setting the synthetic coordinate to two states defines a ladder geometry, leading back to the Meissner-vortex phase transition. Three or more synthetic legs can host chiral edge states, a macroscopic evidence of micro cyclotron orbits induced by strong magnetic fields. The chiral edge states are indicated by a clear asymmetric momentum distribution on the synthetic direction, detected via time-of-flight imaging. Note that, in the limit of blurred or non-existing border, one can only observe the Hofstadter butterfly spectrum, which is a bulk property, but not the chiral currents. Indeed, the key point in using the synthetic dimension is to enforce a robust edge on the $y$-direction, which is not the case when $y$ is a real-space coordinate.

A similar work was carried out at NIST [55], using a bosonic $^{87}$Rb gas, obtaining equivalent results. Note that, despite the quantum Hall effect does involve fermions (the electrons), the key feature is the Lorentz force and not the statistics: since the gauge field is artificial and ultimately determined by the momentum kick in the Raman-assisted tunnelling, whether the atomic species is bosonic or fermionic becomes irrelevant.

### 2.2.2 Periodically driven optical lattices

We mentioned in the previous section a few examples of laser-assisted controlled tunnelling. Let us see now a different class of methods, based on Floquet theory.

#### Theory of periodic Hamiltonians

The time evolution of a quantum state is governed by the Schrödinger equation. If the Hamiltonian is time independent, the time-evolution operator reads

$$\hat{U}(t) \equiv \exp\left(-\frac{\mathrm{i}}{\hbar}\hat{H}t\right). \tag{2.15}$$

This is in general not true if the Hamiltonian has a time-dependent component. In that case, a formal solution is provided in interaction (or Dirac) picture by the Dyson's series, which is amenable of approximate solutions in perturbation theory:

$$\begin{aligned} U(t_1,t_0) =& \exp\left(-\frac{\mathrm{i}}{\hbar}\int_{t_0}^{t_1} H(t)dt\right) && (2.16)\\ =& \mathbb{1} + ... + (-\mathrm{i})^n \int_0^t dt' ... \int_0^{t^{(n-1)}} dt^{(n)} V_I(t')...V_I(t^{(n)}) + ... && (2.17)\end{aligned}$$

If the time-dependent Hamiltonian satisfies $\hat{H}(t) = \hat{H}(t+\tau)$, there exists methods to tackle the problem more thoroughly than with perturbative approaches, taking advantage of the periodicity property. It can be shown [56] that the time evolution operator is equivalent to

$$\hat{U}(t_1,t_0) = \hat{U}_F(t_1)\exp\left(-\frac{\mathrm{i}}{\hbar}(t_1-t_0)\hat{H}_F\right)\hat{U}_F^\dagger(t_0). \tag{2.18}$$

The unitary operator $\hat{U}_F(t)$ is assumed to be periodic, $\hat{U}_F(t) = \hat{U}_F(t+T)$, and to describe the micromotion. $\hat{H}_F$ is a time-independent effective Hamiltonian. The set of eigenvectors of the effective Hamiltonian are the Floquet modes and the eigenvalues are called quasi-energies:

$$\hat{H}_F\left|\tilde{u}_n\right\rangle = \varepsilon_n\left|\tilde{u}_n\right\rangle. \tag{2.19}$$

The Floquet states are defined as

$$\left|\psi_n(t)\right\rangle = e^{-\mathrm{i}t\varepsilon_n/\hbar}\hat{U}_F(t)\left|\tilde{u}_n\right\rangle, \tag{2.20}$$

which are eigenstates of the evolution operator over one time period T:

$$|\psi_n(t+T)\rangle = \hat{U}(t+T,t)\,|\psi_n(t)\rangle = e^{-\mathrm{i}T\varepsilon_n/\hbar}\,|\psi_n(t)\rangle\,. \tag{2.21}$$

Ultimately, $\hat{U}(t_1, t_0)$ operates a dual time evolution: the linear phase evolution over large time scales is determined by the quasi-energies $\varepsilon_n$ of the initial coherent superposition of Floquet modes; within a time period T, the dynamics is driven by the micromotion operator.

One can easily verify that any unitary transformation can gauge the micromotion operator and the effective Hamiltonian to equivalent pairs of $\hat{U}_F(t)$ and $\hat{H}_F$. This degree of freedom is most evident if one takes the Floquet Hamiltonian, a particular case of the effective Hamiltonian, defined as:

$$\hat{U}(t_0+T,t_0) = \exp\left(-\frac{\mathrm{i}}{\hbar}T\hat{H}^F_{t_0}\right). \tag{2.22}$$

The multivalued solutions of the logarithm suggests that the effective Hamiltonian is not uniquely defined. For instance, considering the Fourier decomposition of the time-periodic Hamiltonian,

$$\hat{H}(t) = \hat{H}(t+T) = \sum_{m=-\infty}^{\infty} e^{\mathrm{i}m\omega t}\hat{H}_m, \qquad \hat{H}_m \equiv \frac{1}{T}\int_0^T dt e^{-\mathrm{i}m\omega t}\hat{H}(t) = \hat{H}^\dagger_{-m}, \tag{2.23}$$

a valid transformation of the micromotion operator and the effective Hamiltonian is given by

$$\hat{U}'_F(t) = \hat{U}_F(t)\exp\left(\mathrm{i}m\omega t\,|\tilde{u}_n\rangle\langle\tilde{u}_n|\right), \qquad \hat{H}'_F = \hat{H}_F + m\hbar\omega\,|\tilde{u}_n\rangle\langle\tilde{u}_n|\,, \tag{2.24}$$

which leaves the spectrum and the Floquet modes unaltered, except for a shift $m\hbar\omega$:

$$\varepsilon_{nm} = \varepsilon_n + m\hbar\omega. \tag{2.25}$$

One can see this by writing the Schrödinger equation in the Floquet basis:

$$[H(t) - \mathrm{i}\hbar\partial_t]\,|u_n(t)\rangle = \varepsilon_n\,|u_n(t)\rangle\,; \tag{2.26}$$

if $|u_n(t)\rangle$ is a solution, then

$$|u_{nm}(t)\rangle = e^{\mathrm{i}m\omega t}\,|u_n(t)\rangle \tag{2.27}$$

is a valid state too, associated to the quasi-energy $\varepsilon_{nm}$.

A prerequisite of any Floquet analysis is the definition of the effective Hamiltonian and the micro-motion operator, be it an exact expression or a faithful approximation. For a time period $T$ much shorter than any time scale of the system, or equivalently for $\hbar\omega$ large compared to the matrix elements of the Hamiltonian, a systematic approximation is given by the Floquet expansion [56]:

$$\hat{H}^{(1)}_F = \hat{H}_0, \qquad \hat{H}^{(2)}_F = \sum_{m\neq 0}\frac{\hat{H}_m\hat{H}_{-m}}{m\hbar\omega}, \tag{2.28}$$

$$\hat{H}^{(3)}_F = \sum_{m\neq 0}\left[\frac{[\hat{H}_{-m},[\hat{H}_0,\hat{H}_m]]}{2(m\hbar\omega)^2} + \sum_{m'\neq 0,m}\frac{[\hat{H}_{-m'},[\hat{H}_{m'-m},\hat{H}_m]]}{3mm'(\hbar\omega)^2}\right] \tag{2.29}$$

From this, one can build an alternative expansion, known as Floquet-Magnus expansion:

$$\hat{H}_M^{(1)} = \hat{H}_0, \qquad \hat{H}_M^{(2)} = \hat{H}_F^{(2)} - \left[\hat{H}_F^{(1)}, G^{(1)}(t_0)\right] = \sum_{m\neq 0} \frac{\hat{H}_m \hat{H}_{-m} + \mathrm{e}^{\mathrm{i}m\omega t_0}[H_0, H_m]}{m\hbar\omega}. \tag{2.30}$$

**Hopping amplitude coherent control with lattice shaking**

If the periodic time-dependent part of the Hamiltonian consists of a single-frequency sinusoidal modulation, the framework simplifies. Let us consider the driven Bose-Hubbard Hamiltonian describing the driven system introduced in Section 1.3:

$$\hat{H}_{\mathrm{BH}} = -J \sum_i \left(\hat{b}_i \hat{b}_{i+1}^\dagger + \mathrm{h.c.}\right) + \sum_i \hat{V}_i + \hat{H}_{\mathrm{os}}. \tag{2.31}$$

Here, $\hat{H}_{\mathrm{os}}$ accounts for on-site terms such as interactions $\frac{U}{2}\sum_i \hat{n}_i(\hat{n}_i - 1)$ and trapping potentials $\sum_i \mu_i \hat{n}_i$. An homogeneous inertial force $F(t) = -m\ddot{x}(t) = -ma(t)$ is associated to a time-dependent linear potential of the kind $V_i(t) = -iF(t)$. In this classical picture, we can define the potential as

$$\hat{V}_i = a_i(t)\hat{n}_i, \tag{2.32}$$

where $a_i(t) = iK\cos(\omega t) = ia(t)$ and, apart from dimensional factors, $a(t)$ is an acceleration with harmonic driving.

In analogy with the transformation mapping between Schrödinger and Dirac picture, we can gauge out the time-dependent chemical potential with the unitary transformation,

$$\hat{U}(t) = \exp\left(-\mathrm{i}\sum_j v_j(t)\hat{n}_j\right), \tag{2.33}$$

acting on the state and on the operators as

$$\left|\psi'(t)\right\rangle = \hat{U}^\dagger(t)\left|\psi(t)\right\rangle, \qquad \hat{H}'(t) = \hat{U}^\dagger(t)\hat{H}(t)\hat{U}(t) - \mathrm{i}\hbar\hat{U}^\dagger(t)[\partial_t\hat{U}(t)],$$

and where the time-dependence resides on the velocity $v(t)$:

$$v_i(t) = \frac{1}{\hbar}\int_0^t a_i(t')dt' = iK\frac{\sin(\omega t)}{\hbar\omega} = iv(t). \tag{2.34}$$

Recall the (anti-)commutation rules for indistinguishable particles:

$$\hat{a}_i\hat{a}_j = \pm\hat{a}_j\hat{a}_j, \qquad \hat{a}_i\hat{a}_j^\dagger = \delta_{ij} \pm \hat{a}_j^\dagger\hat{a}_i;$$

the Bose/Fermi statistics is associated to the sign +/-. The commutation relation between the particle density and the annihilation operator reads

$$\hat{a}_i\hat{n}_j = \hat{a}_i\hat{a}_j^\dagger\hat{a}_j = (\delta_{ij} \pm \hat{a}_j^\dagger\hat{a}_i)\hat{a}_j = \delta_{ij}\hat{a}_j \pm \hat{a}_j^\dagger(\pm\hat{a}_j\hat{a}_i) = (\hat{n}_j + \delta_{ij})\hat{a}_j,$$

which, in turn, gives

$$\hat{a}_i e^{\alpha_j\hat{n}_j} = e^{\alpha_j(\hat{n}_j+\delta_{ij})}\hat{a}_i, \qquad \hat{a}_i^\dagger e^{\alpha_j\hat{n}_j} = e^{\alpha_j(\hat{n}_j-\delta_{ij})}\hat{a}_i^\dagger. \tag{2.35}$$

Note that $\hat{H}_{\mathrm{os}}$ depends only on the particle density and therefore commutes with $\hat{U}$, and so the time derivative of the unitary transformation, cancels with the driving term:

$$-\mathrm{i}\hbar\hat{U}^{\dagger}(t)[\partial_t\hat{U}(t)] = -\sum_i a_i(t)\hat{n}_i. \tag{2.36}$$

The hopping term acquires a complex phase in the interaction picture,

$$\hat{U}^{\dagger}\hat{b}_k\hat{b}^{\dagger}_{k+1}\hat{U} = \hat{U}^{\dagger}\hat{b}_k\hat{U}e^{-\mathrm{i}v_{k+1}(t)}\hat{b}^{\dagger}_{k+1} = e^{\mathrm{i}v_k(t)k}\hat{b}_k e^{-\mathrm{i}v_{k+1}(t)}\hat{b}^{\dagger}_{k+1} = \hat{b}_k e^{-\mathrm{i}v(t)}\hat{b}^{\dagger}_{k+1}.$$

We see that the broken translational invariance in real space is necessary for the time-dependent phase in the hopping to not be null. The gauged Hamiltonian reads

$$\hat{H}'_{\mathrm{BH}}(t) = -J\sum_i\left(\hat{b}_i e^{-\mathrm{i}v(t)}\hat{b}^{\dagger}_{i+1} + \mathrm{h.c.}\right) + \frac{U}{2}\sum_i \hat{n}_i(\hat{n}_i - 1). \tag{2.37}$$

Since $\omega$ is larger than $U$ and $J$, the periodic rapid oscillations of the Peierls phase can be integrated out to a constant value. The averaging of fast periodic modulations to obtain an effective time-independent system is an ubiquitously adopted tool, from NMR probes in solid state physics to atom-light interactions or Raman-dressed states. By this, we define an effective time-independent Floquet Hamiltonian $\hat{H}^{F}_{\mathrm{BH}}$:

$$\hat{H}^{F}_{\mathrm{BH}} = \frac{1}{T}\int_0^T dt\hat{H}'_{\mathrm{BH}}(t). \tag{2.38}$$

The integral of the time-dependent part corresponds to the definition of the $0$th-order Bessel function:

$$\mathcal{J}_0\left(x\right) = \frac{1}{2\pi}\int_{-\pi}^{\pi} e^{\mathrm{i}x\sin\theta}d\theta, \qquad \mathcal{J}_0\left(\frac{K}{\hbar\omega}\right) = \frac{1}{T}\int_0^T e^{-\mathrm{i}\frac{K}{\hbar\omega}\sin(\omega t)}dt. \tag{2.39}$$

This defines the effective hopping amplitude $J_{\mathrm{eff}} = J\mathcal{J}_0\left(\frac{K}{\hbar\omega}\right)$ of the Floquet Hamiltonian driven by $K$; the effect was first experimentally verified by the group of Arimondo in Pisa [41]:

$$\hat{H}^{F}_{\mathrm{BH}} = -J_{\mathrm{eff}}\sum_i\left(\hat{b}_i\hat{b}^{\dagger}_{i+1} + \mathrm{h.c.}\right) + \frac{U}{2}\sum_i \hat{n}_i(\hat{n}_i - 1). \tag{2.40}$$

#### Heating in Floquet engineering

Many experimental results confirmed that the time evolution of a periodically driven system largely coincides with that portrayed by the corresponding effective time-independent Hamiltonian $\hat{H}_F$, plus the micromotion. However, the periodic driving obviously violates energy conservation. In the long time scale, this leads to heating in the form of undesirable excitations, such as higher bands or large collective intraband states, as in Figure 2.4. This is related to the nature of the spectrum of the effective Hamiltonian which is determined modulo a quantum of energy $\hbar\omega$, Eq. (2.25), analogously to the Bloch dispersion relation. The absorption of one or multiple phonons couples different spectrum sectors, leading to the hybridization between Floquet modes with quasi-energies shifted by $m\hbar\omega$, corresponding to or in the proximity of high-energy excited states of the bare system.

The absorption of a phonon occurs along the tunnelling. The Hamiltonian off-diagonal matrix terms are thus arranged in different sectors, associated to the $n$

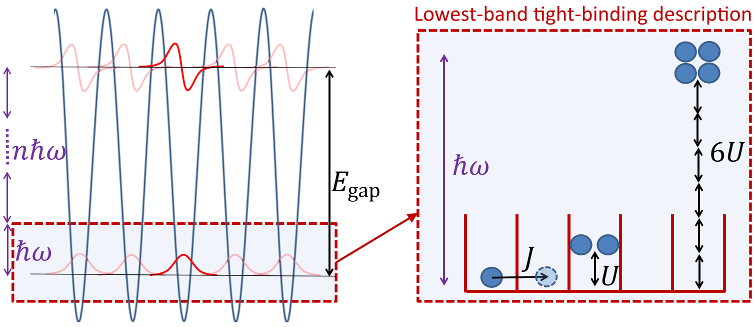

FIGURE 2.4: Possible high-energy resonant excitations causing heating: multiple photon absorption may lead to interband excitations (left), collective intraband excitations may be resonant with the driving frequency. Figure from Eckardt [56].

phonons exchanged. As shown in Eq. (2.27), the bath of $m$ phonons enters the Floquet state as a complex phase dressing. Thus, the photon absorption ultimately reduces to adding a further complex phase in the hopping term. The integral over one period defines the $n$-th order Bessel function:

$$\mathcal{J}_n\left(\frac{K}{\hbar\omega}\right) = \frac{1}{T}\int_0^T \exp\left(-\mathrm{i}\frac{K}{\hbar\omega}\sin(\omega t) + in\omega\right) dt. \tag{2.41}$$

In general, the high-frequency approximation holds as long as the heating time is large compared to the lifetime of the experiment. In particular, for lattice systems with a bound local state space as Fermi-Hubbard or spin systems, the heating time increases exponentially with the driving frequency [56].

### Generating static complex phases

In order to induce a non-trivial phase $\theta$, the periodic amplitude modulation $a_i(t)$ introduce above needs to break both a global reflection symmetry $a_i(-t-\tau) = a_i(t-\tau)$ and a shift antisymmetry $a_i(t-T/2) = -a_i(t)$ [57]. An interval $T_2$ between two consecutive sine pulses, as in Figure 2.5, makes up a valid modulation of the homogeneous force meeting the time-reversal symmetry breaking requirements,

$$a_j(t) := j\begin{cases} K\sin(\omega_1 t) & \text{for } 0 < t < T_1 = \frac{2\pi}{\omega_1}, \\ 0 & \text{for } \mathrm{T_1 < t < T}, \end{cases} \tag{2.42}$$

corresponding, see Eq. (2.34), to the velocity

$$v_j(t) := -j\begin{cases} c_0 + \frac{K}{\hbar\omega_1}\left[\cos(\omega_1 t) - 1\right] & \text{for } 0 < t < T_1 = \frac{2\pi}{\omega_1}, \\ c_0 & \text{for } \mathrm{T_1 < t < T}. \end{cases} \tag{2.43}$$

As in Eq. (2.38), integrating the Hamiltonian over a time period $T$ yields an effective hopping amplitude $J_{\text{eff}} = J\left\langle e^{-\mathrm{i}v(t)}\right\rangle_T$, provided with a non gaugeable complex

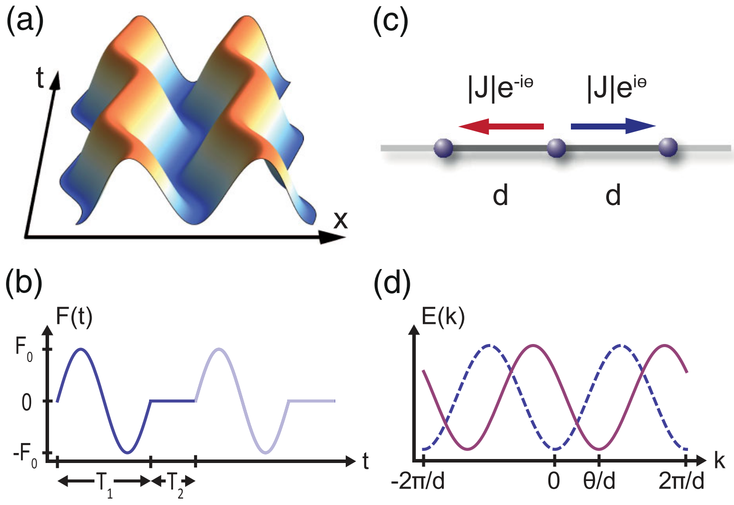

FIGURE 2.5: Periodic driving of a 1-D lattice generating a complex phase. (a) Time-periodic movement of the lattice in real space. (b) Resulting periodic inertial force of zero mean. (c) Effective complex tunnelling elements. (d) Effective single-particle dispersion relation. A complex phase induces a shift of $\theta/d$. Figure from Struck *et al.* [57].

phase $\theta$:

$$J_{\mathrm{eff}} = \frac{J}{T}\left[\int_0^{T_1} e^{\mathrm{i}\frac{K}{\hbar\omega_1}\cos(\omega_1 t)} e^{\mathrm{i}\frac{K}{\hbar\omega_1}} e^{\mathrm{i}c_0} dt + \int_{T_1}^{T} e^{\mathrm{i}c_0} dt\right] \tag{2.44}$$

$$= J\left[\frac{T_1}{T}\mathcal{J}_0\left(\frac{K}{\hbar\omega_1}\right) e^{\mathrm{i}\frac{K}{\hbar\omega_1}} + \frac{T_2}{T}\right] e^{\mathrm{i}c_0} = |J_{\mathrm{eff}}|e^{\mathrm{i}\theta}. \tag{2.45}$$

The Peierls phase can be read out from the quasi-momentum distribution, revealed in the time of flight. The phase is deduced from the observed shifts of the interference patterns.

### Modulated interactions

The modulation of the magnetic field in a Feshbach resonance [58–60] results in a time-dependent on-site interaction that makes it possible to engineer a class of correlated-hopping models. Consider the modulated Fermi-Hubbard Hamiltonian

$$\hat{H}_{\mathrm{FH}} = -J\sum_{<i,j>}\sum_{\sigma=\uparrow,\downarrow}\left(\hat{c}_{i,\sigma}\hat{c}^{\dagger}_{j,\sigma} + \mathrm{h.c.}\right) + U(t)\sum_i \hat{n}_{i\uparrow}\hat{n}_{i\downarrow}, \tag{2.46}$$

where $U(t) \equiv U_0 + U_1\cos(\omega t)$. Adopting the Floquet formalism, the system can be described by an effective one-band model Hamiltonian with density-dependent tunnelling rates:

$$\hat{H}_{\mathrm{eff}} = -J\sum_{<i,j>}\sum_{\sigma=\uparrow,\downarrow}\left(\hat{c}_{i,\sigma}\hat{c}^{\dagger}_{j,\sigma} + \mathrm{h.c.}\right)\mathcal{J}_0\left[K(n_{i,\bar{\sigma}} - n_{j,\bar{\sigma}})\right] + U_0\sum_i \hat{n}_{i\uparrow}\hat{n}_{i\downarrow}, \tag{2.47}$$

where the usual 0th-order Bessel function presents here a density dependence. Analogous modulation of the interaction on a Bose gas leads to a rich physics featuring pair superfluid phases, also to defect-free Mott states and holon and doublon superfluids [61].

For sole lattice shaking or sole modulating interactions, hops are mirror symmetric since $\mathcal{J}_0$ is even. As shown by Greschner *et al.* [62], a double modulation combining lattice shaking and modulated interactions allows to engineer a much broader class of models with correlated hopping and to investigate otherwise unreachable regimes, such as insulating 1-D phases with both parity and string order. Fine-tuning the modulation frequencies and amplitudes in atomic lattices with bosons grants precise control of selected hopping processes that break the mirror symmetry $J_{(1,1)\leftrightarrow(2,0)} \neq J_{(1,1)\leftrightarrow(0,2)}$ and allows to tune the relative amplitudes of low-density hopping elements $J_{(1,1)\leftrightarrow(2,0)}/J_{(0,1)\leftrightarrow(1,0)}$. The same scheme applied to fermions leads to a much richer phase diagram than the one of the bare Fermi-Hubbard model.

### Honeycomb Haldane model

Coherent control on the tunnelling allows to explore Landau-like quantum phase transitions in Hubbard-type models. Quantum phase transitions may also have a topological character, which is associated to symmetry breaking but does not come with a variation of any local order parameter. Topological phases have a characteristic Chern number instead, encoded in the band structure. The Chern number of the $n$-th band is calculated integrating the Berry curvature of that band over the first Brillouin zone

$$C_n = -\frac{1}{2\pi} \int_{\mathrm{BZ}} \Omega^{(n)}(\mathbf{k}) d\mathbf{k}. \tag{2.48}$$

The Haldane Hamiltonian on a honeycomb is a paradigmatic model, expected to have topologically distinct phases of matter, exhibiting non-zero Hall conductance. Differently from quantum-Hall-like physics, no external factor drives the phase transition, rather it appears as an intrinsic property of the band structure associated to broken time-reversal and inversion symmetry. The topological phase transition distinguishes between a trivial band insulator (when a symmetry breaks and a gap opens) and a Chern insulator, occurring when both symmetries are broken. In cold gases, the model was realized by Jotzu and coworkers [63], by shaking an atomic lattice of $^{40}$K. A honeycomb lattice is designed by tweaking a square lattice. A sinusoidal modulation of the trap along the $x$ and $y$ directions, with a relative phase $\phi$, sets the honeycomb in linear ($\phi = 0$), circular ($\phi = \pi/2$) or elliptic oscillation. By means of Floquet analysis, one can verify that the time-dependent Hamiltonian is well described by an effective Haldane model

$$\hat{H} = \sum_{<i,j>_{\mathrm{nn}}} t^{(1)}_{ij} \left( \hat{c}^\dagger_i \hat{c}_j + \mathrm{h.c.} \right) + \sum_{<i,j>_{\mathrm{nnn}}} t^{(2)}_{ij} \left( \hat{c}^\dagger_i \hat{c}_j + \mathrm{h.c.} \right) + \Delta_{AB} \sum_{i \in A} \hat{c}^\dagger_i \hat{c}_i, \tag{2.49}$$

where $< i,j >$ nn ($< i,j >$ nnn) stands for (next-) nearest-neighbouring sites. The modulation has thus two effects: it splits the honeycomb onto two sublattices A and B, which breaks the inversion symmetry, and generates real $t^{(1)}$ and complex $t^{(2)}$ tunnelling amplitudes, that break the time-reversal symmetry.

## 2.3 Anyons

Anyons are quasi-particles obeying a fractional statistics, intermediate between the Bose-Einstein and the Fermi-Dirac. The existence of anyons was originally postulated in two-dimensional systems, where the deep connection to peculiar 2-D and

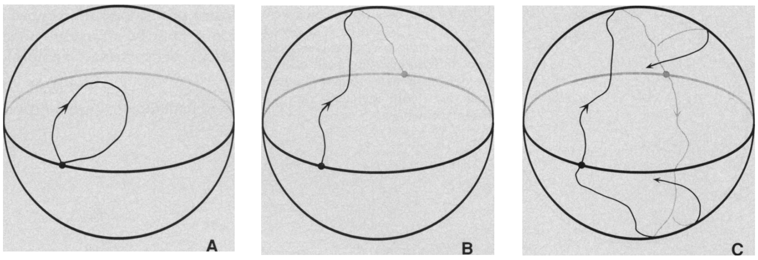

FIGURE 2.6: Paths of the relative coordinate $\mathbf{r}$ of two identical particles, as they move around in a three-dimensional space and at fixed distance $|\mathbf{r}| = r_0$. A) a path which does not involve an exchange, B) a path with an exchange, C) a path with two consecutive exchanges, equivalent to A). Figure from Canright *et al.* [69].

topological phenomena was readily recognized [64–66]. Later, Haldane and Wu [67, 68] proposed the concept of fractional exclusion statistics, that generalizes the notion of anyons without specific reference to the spatial dimension.

**Fractional statistics** The easiest way to discuss the notion of complex phases and statistics under exchange of particles is by making use of Feynamn's path integrals formalism [69]. The probability amplitude $A$ to evolve a quantum system between two space-time points is equal to the sum over all the possible paths $A = \sum_{\text{paths}} e^{iS}$, weighted by the action $S = \int dt\mathcal{L}$. When we consider the evolution in time of two identical particles that move from and return to two points $(\boldsymbol{r}_1, \boldsymbol{r}_2)$, the possible paths can be divided in two classes: direct and exchange. To show the topological distinction between the two classes of paths, we can parametrize the configuration space of the relative coordinates of the two particles $\boldsymbol{r} = \boldsymbol{r}_1 - \boldsymbol{r}_2$ on the surface of a sphere: an exchange path corresponds to a string stretching between two antipodes, while a direct path corresponds to a closed string (see Figure 2.6). Whether or not the particles have been exchanged, the probability density of the wave function can not vary: however, the two distinct classes of paths can be defined up to a relative phase $\phi$. Two exchanges correspond to an open string closing on itself, which is topologically equivalent to a direct path: this requires the wave-function to be single valued under double exchange and constrains $\phi$ to be $[0, \pi]$, which identifies bosons and fermions.

In two dimensions, the topology changes. The relative coordinates configuration space can be represented on a circle: any direct path is topologically equivalent and can be shrunk to a point, while the two exchanges paths reaching the antipodes moving counter- or clockwise are topologically distinct. Two exchange paths are no longer topologically equivalent to a direct one since the string looping around the circle can no longer be mapped to the point-like string of a direct path. Hence, no constraint on the complex phase can be set. Mathematically, the braid group [69] offers a more solid and finer classifications of anyons in 2-D than the complex phase attribute: it distinguishes between counter- and clockwise exchanges and keeps track of this properties across all particles swaps.

**Fractional quantum Hall effect** Anyons have been the subject of intense studies, as connections were found to lower-dimensional physical phenomena, in particular the fractional quantum Hall effect. Whilst the integer quantum Hall effect can be described simply in terms of non-interacting fermions occupying the lowest Landau levels, it is crucial to include the interaction between particles and magnetic flux in order to explain the fractional quantum Hall effect (FQHE). A theory that successfully predicts the Hall resistivity plateaus in the FQHE is based on composite fermions, defined as fermions with an even number of vortices or flux quanta attached. The composite fermions have anyonic fractional statistics and correspond to the true quasi-particle excitations of the system. The strongly coupled ensemble of fermions and flux quanta can be described as a gas of anyons: this quasi-particle gas turns out to be weakly interacting, so that the key physical features of the FQHE can be obtained in mean field approximation.

In the last decades, there has been an enormous progress in our theoretical understanding of the FQHE, crucially in intertwine with both Abelian and non-Abelian anyonic quasi-particles. Nevertheless, while theoretically settled, an unambiguous detection of the anyonic character of excitations, e.g. by interferometric measurements [70], is still an open challenge and the object of active research [71, 72]. Eventually it would be interesting to realize and investigate anyons in two-dimensional quantum simulators, for the purpose of interrogating regimes and phases otherwise inaccessible in solid state systems. The challenge is all but trivial and realizing artificial fractional statistics in 2-D will require to come up with some brilliant technical artifice.

### 2.3.1 Abelian Anyons in 1-D lattices

Anyons emerged as a new two-dimensional category of particles, originally defined in terms of the braiding group. Haldane [67] gave a general definition of fractional exchange statistics, which extends to 1-D and is considered as a generalization of the Pauli exclusion principle. The definition proposed by Haldane requires that the single-particle Hilbert space dimension be extensive. In general, the particle has the character of an excitations in condensed matter, i.e. it can only exist in the interior of a region of condensed matter and not in the vacuum outside with an arbitrarily large momentum. With regard to 2-D, the FES coincides with the previous definition in terms of the braiding group, although the two are not equivalent. In 1-D this can be thought of as a long-tail-dressed particle, formalized by a Jordan-Wigner transformation. The FES disentangled anyons from their role in the FQHE, strictly related to dimensionality and to the presence of an external magnetic flux.

A wealth of intriguing properties associated to the fractional exchange statistics emerges in one-dimensional geometries, which stimulated large interest on the subject in the last decades [73–80]. The exotic properties of 1-D abelian anyon models include asymmetric momentum distributions [81–86], particle dynamics [87–89], entanglement properties [90–92] and statistically induced Mott insulator to superfluid quantum phase transitions [93–96]. Moreover, in one dimension, the quantum simulation of fractional statistics seems to be viable and is encouraged by the existence of solid numerical methods with which it is possible to cross-check and assess the experimental results.

The realization of artificial quasi-particles with anyonic character require a non-constant, density-dependent gauge, which effectively realizes a first degree of back-action of the atoms distribution on the gauge field. We have seen in previous sections how a constant artificial Berry phase can be realized in 1-D and 2-D atomic lattice, which led to the simulation of the Harper model. In what follows, we will present in summary the state of the art of density-dependent gauge fields in cold gases.

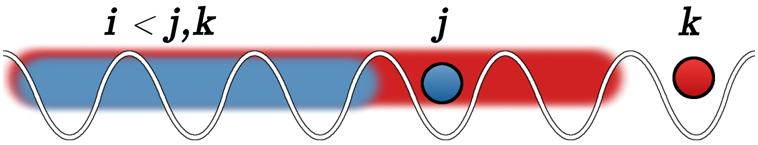

FIGURE 2.7: The fractional Jordan-Wigner transformation, Eq. (2.52), defines anyons in one dimension as hard-core bosons dressed with a tail of density-dependent complex phases (the coloured stripes).

### The Jordan-Wigner transformation

The commutation rules defining the two classical statistics in lattice geometries are

$$\hat{a}_j\hat{a}_k^\dagger + \mathcal{F}_{j,k}\hat{a}_k^\dagger\hat{a}_j = \delta_{jk}, \tag{2.50a}$$

$$\hat{a}_k\hat{a}_j + \mathcal{F}_{j,k}\hat{a}_j\hat{a}_k = 0, \tag{2.50b}$$

with $\mathcal{F}_{j,k} = 1$ for fermions, $\mathcal{F}_{j,k} = -1$ for bosons. Remind that, assuming the single band approximation, the site indices uniquely identify one state. In 1-D, it implies that spinless fermions can not undergo a spatial position exchange, owing to the Pauli principle, while bosons can penetrate through.

We now introduce the (currently) common definition of anyons in 1-D lattices [93], trying to offer a justification a posteriori of that. We address the attention of the interested reader to the following pieces of literature, for further reading: [78, 79]. The anyons statistics in 1-D is defined as

$$\mathcal{F}_{j,k} := \pm \begin{cases} e^{-\mathrm{i}2\phi}, & j > k, \\ 1, & j = k, \\ e^{\mathrm{i}2\phi}, & j < k, \end{cases} \tag{2.51}$$

The different sign of the phase is obvious if one looks at (2.50b). The phase swap suggests that for $j = k$ the phase is 0, hence $\mathcal{F}_{j,k} = \pm 1$. Therefore, the so-defined 1-D pseudo-anyons behave locally as (and actually are extensive dressed-states of) either fermions or bosons, which set the overall sign in front of $\mathcal{F}_{j,k}$ (irrelevant to the anyon character for $j \neq k$).

In order to define operators satisfying the fractional statistics commutation relations, we need them to be able to distinguish between two inverted orders of action. In other words, the operator $\hat{a}_j$ needs to know the state (in particular, the particle density) of the site $k$ where $\hat{a}_k$ acted upon, and vice-versa for the commuted pair. One way to obtain this, in 1-D, is to define non-local operators made of a local creation/destruction operator acting on site $j$ and a product of density-dependent phases related to the tail of sites $i < j$, as depicted in Figure 2.7. The tail is arbitrarily placed on one side of site $j$. As said, the actual particle can be either a boson or fermion, the type of the species being reflected in the sign of $\mathcal{F}_{j,k}$: when the induced phase $\phi$ is set back to 0, $\mathcal{F}_{j,k}$ must regain the sign of the underlying gas species.

Let us consider a gas of single-species bosons, so that the local occupation number is not trivial. In what follows, we fix $j < k$. We define anyonic operators $\hat{a}_j$, $\hat{a}_j$ through a Jordan-Wigner transformation,

$$\hat{a}_j = \hat{b}_j \exp\left(-\mathrm{i}\phi \sum_{k<j} \hat{n}_k\right), \qquad \hat{a}_j^\dagger = \hat{b}_j^\dagger \exp\left(\mathrm{i}\phi \sum_{k<j} \hat{n}_k\right). \tag{2.52}$$

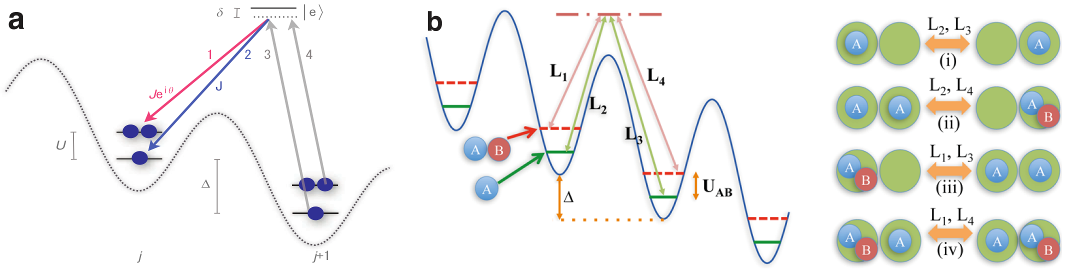

FIGURE 2.8: Raman-assisted hopping inducing a density-dependent complex phase. a) Interacting bosons allow to resolve states with different occupation number. Figure from Keilmann *et al.* [93]. b) Two non degenerate hyperfine states realize a more flexible doubly occupancy. A frequency offset in the channel $L_{2,4}$ between $\omega_2 - \omega_4$ and the energy gap $\Delta - U_{AB}$ reflects in an effective on-site interaction $U$. Figure from Greschner *et al.* [98].

Note that the exponential operator commutes with the creation/annihilation operator, as the tail does not include site $j$. The sign of the phase is arbitrary. We can verify that the density operators are invariant

$$\hat{n}_j = \hat{a}_j^\dagger \hat{a}_j = \hat{b}_j^\dagger \exp\left(\mathrm{i}\phi \sum_{k<j} \hat{n}_k\right) \exp\left(-\mathrm{i}\phi \sum_{k<j} \hat{n}_k\right) \hat{b}_j = \hat{b}_j^\dagger \hat{b}_j, \tag{2.53}$$

and, reminding Eq. (2.35), that the fractional exclusion statistics is satisfied:

$$\hat{a}_j \hat{a}_k = \hat{b}_j \exp\left(-\mathrm{i}\phi \sum_{i<j} \hat{n}_i\right) \hat{b}_k \exp\left(-\mathrm{i}\phi \sum_{i<k} \hat{n}_i\right) = e^{\mathrm{i}\phi} \hat{a}_k \hat{a}_j. \tag{2.54}$$

Methods exist to generalize the Jordan-Wigner transformation to two dimensions [97], but the subject goes beyond the scope of this work.

In practical scenarios, the realization of non-local operators as those in Eq. (2.52) is in fact not feasible, but neither is it necessary. Crucially, the anyon-Hubbard is a local Hamiltonian featuring nearest-neighbours hopping elements

$$\hat{a}_j^\dagger \hat{a}_{j+1} = \hat{b}_j^\dagger e^{-\mathrm{i}\phi \hat{n}_j} \hat{b}_{j+1},$$

therefore the key is to realize hopping terms with a phase shift dependent on the occupation of the left-hand site. We will see a few major instances in the following paragraphs.

### Raman-assisted density-dependent hopping

In a seminal proposal, Keilmann *et al.* [93] suggested a Raman-assisted hopping scheme analogous to that discussed in Sec. 2.2.1 to create pseudo-anyons with bosons. Four lasers couple singly and doubly occupied sites to a virtual state, see Fig. 2.8(a). The excited state could be the minimum of a blue-detuned lattice, spatially localized between the left and right wells of the original lattice [99]; alternatively, one can use a different hyperfine virtual state. The latest option has the advantage that the external driving fields are in the radio-frequency regime, which favours the resolution of the typical energy scales $U$ and $\Delta$, of the order of the kHz; in the first case we are in the optical lattice (THz) frequency regime, which would demand a rather narrow linewidth (see Sec. 1.3). The local Hilbert space is truncated, for simplicity, to a max of two particles per site, although higher local occupations are possible. The density-dependent hopping is achieved by selectively inducing a phase shift on the hopping of a particle onto an already occupied site, on the left-hand side

The density distribution in momentum space for bosons is peaked at the centre of the Brillouin zone. As the statistical phase increases, the peak shifts and is increasingly smeared out, until it is completely spread in the pseudo-fermions limit $\phi = \pi$. The density-dependent picked phase is local and uncorrelated. As it grows, it induces destructive interference and yields localization in real-space coordinates. This property is proper of spinless Fermi gases and of the Mott phase of Bose gases, phenomenologically equivalent to the pseudo-fermions regime. The Mott and superfluid phases of the Bose-Hubbard model present characteristic peaked lobes. Simulations with DMRG show that the Mott region expands with increasing statistical angle $\phi$. Adding a harmonic potential should render a wedding-cake-like real-space density distribution at integer filling; remarkably, in the pseudo-fermions limit there are Mott plateaus at fractional filling.

**Hard-core two-body constraint** A precondition to realize a non trivial anyon gas hopping is to have multiple particles per site. A clear energy gap between singly and doubly occupied states is crucial to resolve those state and target them separately. Interacting bosons fulfil both requirements but are limited to have repulsive interactions, to avoid three-body collisions that lead to particle losses.

An analogous scheme (Fig. 2.8(b), [98]) considering two hyperfine states of one single species per site (no matter if bosons or fermions) permits instead to enforce a two-body hard-core constraint. In the first proposal the target state is uniquely determined by the occupation number: lasers 1 or 4 in Fig. 2.8(a) do not induce hopping if the destination site is empty. In the scheme of Fig. 2.8(b), unwanted driven hopping can occur but are avoided by properly tuning the interactions within the hyperfine states to be larger than the width of the Raman resonances. The anyon-Hubbard model presents a boson-like interaction $U$ associated to the off-resonant frequencies of the Raman lasers coupling an empty with a doubly occupied site. The frequency detuning can be regulated at will, allowing to explore effective attractive couplings, which is not possible with the previous scheme. A rich phase diagram emerges in the region of negative $U$, including a pair superfluid, a dimerized gapped phase and an exotic partially paired phase.

### Density-dependent gauge with lattice shaking

As noted by Sträter *et al.* [100], Floquet-type methodologies to selectively control the hopping amplitude and to create an artificial constant phase (see Secs. 1.3 and 2.2.2) have already been successfully employed in experiments; this constitutes a solid basis and indicates that artificial occupation-dependent gauge fields may be generated with time-periodic forcing as well. The shaking protocol follows the scheme illustrated in Sec. 2.2.2, breaking the time-reversal symmetry with a driving term

$$i\hat{n}_i \Delta F(t), \qquad F(t) \sim A\sin(\omega t) + B\sin(2\omega t)$$

but crucially abandons the far off-resonant principle in favour of frequencies in resonance with the hopping gaps. In fact, the tilting is set equal to the on-site interaction $U$ (a single-species bosonic gas is considered), so that for a particle hopping uphill onto an empty site the gap is $\Delta$ while it is twice as much when hopping onto a singly occupied site, $\Delta + U$. In the latter hopping event, the atom absorbs a $2\omega$ phonon, receiving thus a different momentum kick and related phase. The tunnelling parameter reads

$$J_{\mathrm{eff}}(n) = \frac{J}{T}\int_0^T dt \exp\left(\mathrm{i}\omega t n - \mathrm{i}v(t)\right) \tag{2.55}$$

where the Floquet sector element $\mathrm{i}\omega t n$ provides the occupation-dependency. As mentioned in the previous subsection, a resonant driving suppresses the hindrance of the tilting but a little frequency off-resonance detuning is reflected in an effective on-site coupling $U'$, resulting in an anyon-Hubbard model with effective Bose-like on-site interaction:

$$\hat{H}_{\mathrm{eff}} = -J\sum_j \left(\hat{b}_j^\dagger \hat{b}_{j+1} e^{\mathrm{i}\phi \hat{n}_j} + \mathrm{h.c.}\right) + U\sum_j \hat{n}_j(\hat{n}_j - 1). \tag{2.56}$$

### 2.3.2 Experimental realization of density-dependent gauge fields

The efforts towards the experimental realization of density-dependent gauge fields in optical lattices has just recently begun to show promising results. Görg and coworkers [101] engineered a non-constant Peierls phase using fermions in a Hubbard dimer. A balanced mixture of two internal states, labelled as $|\uparrow\rangle$ and $|\downarrow\rangle$, is initially loaded in a tilted lattice with $\Delta = 660$ Hz. The on-site repulsive interaction $U_{\uparrow,\downarrow}$ is tuned using a magnetic Feshbach resonance to a magnitude of about 6 kHz. The time-reversal symmetry is broken by driving the optical lattice simultaneously at two frequencies, $\omega = 2.75$ kHz and $2\omega$. The splitting of a dimer $|0, \uparrow\downarrow\rangle$ sitting on the lower site of a double well onto the singlet state $|\uparrow, \downarrow\rangle - |\uparrow, \downarrow\rangle$ occurs according to the principle of single or multiple photons resonant absorption given that $n\hbar\omega = U_{\uparrow,\downarrow} \pm \Delta$, as discussed in Sec. 1.3. Since $\omega \gg \Delta$, the single-particle hopping is driven by off-resonant shaking process. The hopping amplitude is complex and differs between dimer and single-particle tunnel coupling. Differently from [57], Sec. 2.2.2, the Peierls phase is not deduced from quasi-momentum interference patterns in time of flight but from Ramsey fringes generated by applying an RF pulse that convert the $|\downarrow\rangle$ atoms to an ancillary $|\rightarrow\rangle$ spin state. Another recent experiment demonstrated density-dependent gauge fields induced by coherent shaking in 2-D quantum gases [102]. We will not commented in details here the rather different methodology utilised, based on the synchronous interaction strength modulation and lattice shaking, which allowed the experiment to equivalently achieve the goal of a density-dependent gauge field.

# Chapter 3

# Dynamical gauge fields with three-color modulation

In Chapter 1 we discussed how the Fermi-Hubbard model is simulated with neutral cold gases trapped in optical lattices and we presented the main experimental techniques that can be used to create static and dynamical gauge fields, mainly relying on Floquet engineering or Raman transitions. In the present chapter we introduce a method for the quantum simulation of the one-dimensional Fermi-Hubbard Hamiltonian based on the multi-color modulation of the depth of a tilted optical lattice. Our proposal allows to achieve a separate flexible control of correlated hopping, effective on-site interactions without need of Feshbach resonances, nearest-neighbours interactions and above all a density-dependent gauge field heralding the creation of anyonic quasi-particles.

## 3.1 Multi-color modulation of a 1-D optical lattice

### 3.1.1 The model

We consider two-components fermions in an optical lattice, or likewise two species of spinless fermions: we distinguish the two components with the index $\sigma = \uparrow, \downarrow$. The optical lattice is identical for both components and its depth is modulated in time:

$$V(t) = V_0 + \delta V(t).$$

As shown by Ma et al. [43], lattice-depth modulations may be employed to realize different occupation-dependent assisted hopping. We assume the modulation amplitude to be small compared to the lattice depth, $\delta V \ll V_0$, and the optical lattice to be deep enough for the gas to be faithfully described in tight-binding approximation. The hopping rate is thus

$$\frac{J(s)}{E_{\text{rec}}} = \frac{4}{\sqrt{\pi}} s^{3/4} \exp\left(-2\sqrt{s}\right),$$

where $E_{\text{rec}}$ is the recoil energy associated to the laser that creates the optical lattice and

$$s(t) = \frac{V_0 + \delta V(t)}{E_{\text{rec}}} = s_0 + \delta s(t)$$

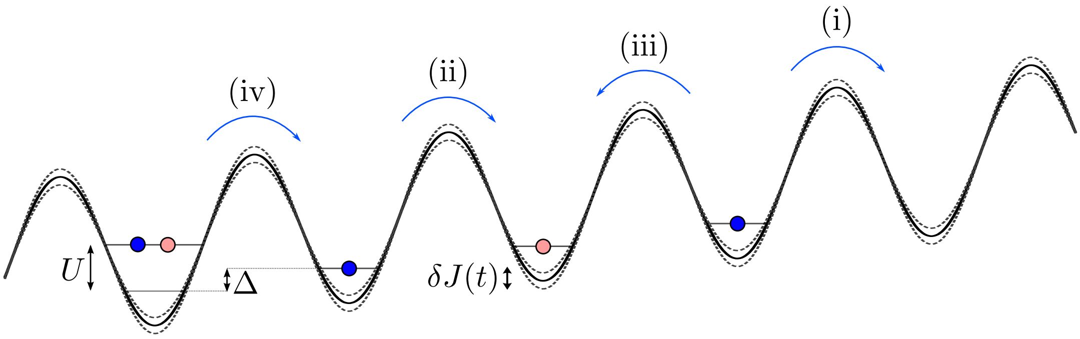

FIGURE 3.1: Sketch of the three-color modulation experimental scheme and the relevant tunnelling processes.

is the time-dependent lattice depth in recoil energy units. Since $\delta s \ll s_0$, it is valid to approximate the time-dependent hopping to first order:

$$J(t) \simeq \frac{4}{\sqrt{\pi}} e^{-2\sqrt{s_0}} s_0^{3/4} - \frac{e^{-2\sqrt{s_0}}(-3+4\sqrt{s_0})}{\sqrt{\pi}\sqrt[4]{s_0}} \delta s(t)$$

$$= J_0 + \delta J(t).$$

Thus, the lattice modulation maps linearly onto a modulation of the hopping rate as

$$\frac{\delta J(t)}{J_0} = -\left(\sqrt{s_0} - \frac{3}{4}\right) \frac{\delta s(t)}{s_0},$$

the tight binding approximation regime being valid for $V_0 \gtrsim 5E_r$ [30]. We choose two-component fermions for simplicity, but similar ideas may be applied to bosons, and multi-component fermions. We assume the lattice to be strongly tilted (see Figure 3.1): the tilting can be realized in gravity or by means of linearly space dependent magnetic fields. The energy shift $\Delta$ between neighbouring sites is larger than any other energy scale in the Hubbard model and yet much smaller than the lattice depth. The system is described by a Fermi-Hubbard-type Hamiltonian:

$$\hat{H}(t) = -J(t) \sum_{i,\sigma} \left[\hat{c}^\dagger_{i+1,\sigma} \hat{c}_{i,\sigma} + \text{h.c.}\right] + U \sum_i \hat{n}_{i\uparrow} \hat{n}_{i\downarrow} + \Delta \sum_{i,\sigma} i \hat{n}_{i,\sigma}$$

$$= -J(t)\hat{H}_{\text{hop}} + U\hat{H}_{\text{int}} + \Delta \hat{H}_{\text{tilt}}, \tag{3.1}$$

where $\hat{c}_{i,\sigma}$ is the annihilation operator of a fermion with spin $\sigma$ at site $i$, $U$ characterizes the on-site interactions and $\Delta$ the tilting. Four different hopping events are possible:

- (i) a single atom, alone at a given site, hops to an empty site, leading to an energy shift $\Delta E_I = \pm\Delta$;
- (ii) an atom with spin $\sigma$, initially alone at a given site, tunnels to the site on the right side already occupied by a single atom with $\bar{\sigma} \neq \sigma$, resulting in a shift $\Delta E_{II} = \Delta + U$;
- (iii) the same event as (ii) but the hopping is to the left. In this case $\Delta E_{III} = U - \Delta$;

- (iv) an atom of component $\sigma$ sharing a site with a $\bar{\sigma}$ atom, tunnels into the site at its right already occupied by a single atom with $\bar{\sigma}$ leading to $\Delta E_{IV} = \Delta$ (i.e. (iv) and (i) are resonant)

We assume $J(t) \ll \Delta, |\Delta \pm U|$, so that the direct hopping is negligible: under these conditions the dynamics of the system is frozen. The amplitude modulation at frequency $\omega_s$ can be equivalently regarded as the act of populating the system with quanta of energy $\hbar\omega_s$. Therefore, it appears intuitive and plausible that, if the modulation frequency is tuned to match the energy difference $\Delta E$ associated to a hopping process, the particle may absorb the phonon-like resonant quantum of energy and tunnel [43]. The dynamics is thus restored in an assisted and controlled way.

The key point of our proposal is to address the three hopping energy deltas separately but simultaneously, using a three-color modulation of the laser intensity:

$$\delta V(t) = \sum_{k=1,2,3} \delta V_k \cos(\omega_k t + \phi_k). \tag{3.2}$$

The frequencies $\omega_{1,2,3}$ match the three hopping energies $\Delta E_{1,2,3}$ and $V_k$, $\phi_k$ are the associated modulation amplitude and dephasing. As mentioned above, the amplitude modulation translates in an equivalent modulation of the hopping rates:

$$\delta J(t) = \sum_{k=1,2,3} \delta J_k \cos(\omega_k t + \phi_k). \tag{3.3}$$

Crucially, processes (i), (ii) and (iii) are characterized by energy shifts typically separated by several kHz (see 3.1.2); hence, the different hopping events may be individually laser-assisted without these modulations affecting one another (at least for the time span in which the linear regime remains valid). Note that the amplitude $\delta J_s$ and dephase $\delta\phi_s$ of each component of the modulation may be independently controlled.

### 3.1.2 The effective Hamiltonian

The Hamiltonian consists of a time-independent, exactly solvable (diagonal) part $\hat{H}_0$, and a time-dependent, smaller, coupling term $\hat{H}_I$:

$$\hat{H}_0 = \Delta\hat{H}_{\text{tilt}} + U\hat{H}_{\text{int}}, \qquad \hat{H}_I = -J(t)\hat{H}_{\text{hop}}. \tag{3.4}$$

The relevant physics of the Hamiltonian just introduces is adequately described by an effective, time-independent Hamiltonian that we derive and comment upon hereafter. To do that, we switch from the Schrödinger to the Dirac interaction picture, where the quantum state is exclusively evolved by the coupling part of the Hamiltonian, and subsequently use the rotating wave approximation to get rid of micromotion terms:

$$\hat{H}_{\text{Dir}} = \hat{\mathcal{O}}^{\dagger}\hat{H}_{\text{Sch}}\hat{\mathcal{O}}. \tag{3.5}$$

We invite the reader less familiar with this techniques to study the simpler, analogous case of the rotating wave approximation applied to the quantum Rabi-model [103]. For an alternative derivation based on Magnus expansion, see Appendix A The unitary operator $\hat{\mathcal{O}}$ mapping the two representations is the time evolution operator of the diagonal part $\hat{H}_0$,

$$\hat{\mathcal{O}} = \exp\left(-\mathrm{i}t\hat{H}_0\right).$$

By using the commutation rule (2.35), one can explicitly derive the Dirac form of the interacting part of the Hamiltonian:

$$\begin{aligned}\hat{H}_I &= -J(t)e^{\mathrm{i}t\hat{H}_0}\hat{H}_{\mathrm{hop}}e^{-\mathrm{i}t\hat{H}_0} \qquad (3.6)\\ &= -J(t)\sum_{k,\sigma} e^{\mathrm{i}t\sum_j\left[\Delta j(\hat{n}_{j\uparrow}+\hat{n}_{j\downarrow})+U\hat{n}_{j\uparrow}\hat{n}_{j\downarrow}\right]}\left(\hat{c}_{k,\sigma}\hat{c}^{\dagger}_{k+1,\sigma}+\mathrm{h.c.}\right)e^{-\mathrm{i}t\sum_j\left[\Delta j(\hat{n}_{j\uparrow}+\hat{n}_{j\downarrow})+U\hat{n}_{j\uparrow}\hat{n}_{j\downarrow}\right]}.\end{aligned}$$

As the only relevant terms in the Dirac representation are those that do not commute with the unitary operator $\hat{\mathcal{O}}$, $\hat{H}_I$ reduces to

$$\begin{aligned}\hat{H}_I &= -J(t)\sum_{k,\sigma}\prod_{j\neq k,k+1} e^{\mathrm{i}t\left(\Delta j\hat{n}_{j,\sigma}+U\hat{n}_{j,\sigma}\hat{n}_{j,\bar{\sigma}}\right)}\hat{c}_{k,\sigma}\hat{c}^{\dagger}_{k+1,\sigma}\prod_{j\neq k,k+1} e^{-\mathrm{i}t\left(\Delta j\hat{n}_{j,\sigma}+U\hat{n}_{j,\sigma}\hat{n}_{j,\bar{\sigma}}\right)}\\ &= -J(t)\sum_{k,\sigma}\hat{c}_{k,\sigma}e^{\mathrm{i}t\{\Delta[k(1+\hat{n}_{k,\sigma})+(k+1)\hat{n}_{k+1,\sigma}]+U[(1+\hat{n}_{k,\sigma})\hat{n}_{k,\bar{\sigma}}+\hat{n}_{k+1,\sigma}\hat{n}_{k+1,\bar{\sigma}}]\}}\\ &\qquad e^{-\mathrm{i}t\{\Delta[(k+1)\cdot(1+\hat{n}_{k+1,\sigma})+k\hat{n}_{k,\sigma}]+U[(1+\hat{n}_{k+1,\sigma})\hat{n}_{k+1,\bar{\sigma}}+\hat{n}_{k,\sigma}\hat{n}_{k,\bar{\sigma}}]\}}\hat{c}^{\dagger}_{k+1,\sigma}\\ &= -J(t)\sum_{k,\sigma}\hat{c}_{k,\sigma}e^{-\mathrm{i}t(\Delta+U(\hat{n}_{k+1,\bar{\sigma}}-\hat{n}_{k,\bar{\sigma}})]}\hat{c}^{\dagger}_{k+1,\sigma} \qquad (3.7)\end{aligned}$$

One can easily verify that the Hamiltonian in Dirac picture has the following form:

$$\begin{aligned}\hat{H}_I(t) =& J(t)\sum_i\hat{c}_{i,\uparrow}\mathrm{e}^{-\mathrm{i}t\left[\Delta+U(\hat{n}_{i+1,\downarrow}-\hat{n}_{i,\downarrow})\right]}\hat{c}^{\dagger}_{i+1,\uparrow}\\ &+J(t)\sum_i\hat{c}_{i,\downarrow}\mathrm{e}^{-\mathrm{i}t\left[\Delta+U(\hat{n}_{i+1,\uparrow}-\hat{n}_{i,\uparrow})\right]}\hat{c}^{\dagger}_{i+1,\downarrow}+\mathrm{H.c.} \qquad (3.8)\end{aligned}$$

Note that the complex phase associated to the tunnelling of the ↑ component depends on the density imbalance between the two neighboring sites of the other component ↓, and vice versa. This constitutes already a main achievement of the proposed scheme, heralding an interesting form of dynamical, density-dependent gauge field. The three-color modulation introduces a number of oscillating terms. By using the substitution $\cos(x) = (e^{\mathrm{i}x}+e^{-\mathrm{i}x})/2$, one obtains

$$J(t) = J_0 + \frac{\delta J_1}{2}(e^{i(\omega_1 t+\phi_1)}+e^{-i(\omega_1 t+\phi_1)}) + \frac{\delta J_2}{2}(...) + \frac{\delta J_3}{2}(...) \qquad (3.9)$$

and therefore

$$\begin{aligned}\hat{H}_I(t) =& J_0\sum_i\hat{c}_{i,\uparrow}\mathrm{e}^{-\mathrm{i}t\left[\Delta+U(\hat{n}_{i+1,\downarrow}-\hat{n}_{i,\downarrow})\right]}\hat{c}^{\dagger}_{i+1,\uparrow}\\ &+\frac{\delta J_1}{2}\sum_i\hat{c}_{i,\uparrow}\mathrm{e}^{-\mathrm{i}t\left[\Delta+U(\hat{n}_{i+1,\downarrow}-\hat{n}_{i,\downarrow})\pm\omega_1\right]\pm\mathrm{i}\phi_1}\hat{c}^{\dagger}_{i+1,\uparrow}\\ &+\frac{\delta J_2}{2}\sum_i\hat{c}_{i,\uparrow}\mathrm{e}^{-\mathrm{i}t\left[\Delta+U(\hat{n}_{i+1,\downarrow}-\hat{n}_{i,\downarrow})\pm\omega_2\right]\pm\mathrm{i}\phi_2}\hat{c}^{\dagger}_{i+1,\uparrow}\\ &+\frac{\delta J_3}{2}\sum_i\hat{c}_{i,\uparrow}\mathrm{e}^{-\mathrm{i}t\left[\Delta+U(\hat{n}_{i+1,\downarrow}-\hat{n}_{i,\downarrow})\pm\omega_3\right]\pm\mathrm{i}\phi_3}\hat{c}^{\dagger}_{i+1,\uparrow}+\mathrm{s.s.}+\mathrm{H.c.}, \qquad (3.10)\end{aligned}$$

where the acronym s.s. refers to the set of terms with the spin components swapped and H.c. indicates the Hermitian conjugate of all the previous terms. Recalling that the particles are fermions, the density imbalance $\hat{n}_{i,\sigma}-\hat{n}_{i+1,\sigma}$ can take the values

$[0, \pm 1]$, which sets $\Delta + U(\hat{n}_{i+1,\downarrow} - \hat{n}_{i,\downarrow})$ equal to one of the three energy deltas introduced above $\Delta E_{I,II,III}$. Now the rotating wave approximation can be applied, which simplifies $\hat{H}_I$. Reminding that $|\Delta - U|, U \gg J_0$, all the terms are averaged out except for those (quasi-) resonant with the modulation frequency $\omega_k$.

As anticipated, we set the three modulation frequencies at resonance or close to resonance with the hopping energy barriers,

$$\omega_1 = \Delta, \qquad \omega_2 = \Delta + U - \tilde{U}, \qquad \omega_3 = -\Delta + U - \tilde{U}, \tag{3.11}$$

and consider below the particular case with $\delta J_{2,3} = \beta \delta J_1$, $\phi_1 = 0$, $\phi_{2,3} = \phi$. By neglecting the fast-oscillating terms and undoing the unitary transformation, we obtain the effective time-independent Hamiltonian:

$$\hat{H}_{\text{eff}} = -\frac{\delta J_1}{2} \sum_{i,\sigma} \hat{c}_{i,\sigma} F\left[|\hat{n}_{i+1,\bar{\sigma}} - \hat{n}_{i,\bar{\sigma}}|\right] \hat{c}^{\dagger}_{i+1,\sigma} + \tilde{U}\hat{H}_{\text{int}}, \tag{3.12}$$

where $F[0] = 1$ and $F[1] = \beta e^{\mathrm{i}\phi}$. The detuning $\tilde{U}$ results in an effective on-site interaction, which allows to control the interactions even in those systems where Feshbach resonances are not available: this is particularly the case of alkaline-earth fermions in the lowest $^1\mathrm{S}_0$ state [104]. Since three-color modulation may also be used with multi-component fermions, this opens a novel way of controlling the properties of $SU(N)$ fermions [104].

**Effective nearest neighbour interaction** Although for $J(t) \ll \Delta, |\Delta \pm U|$ direct hopping is energetically forbidden, virtual hopping - second order processes in which a particle tunnels to its neighbouring site and back - may induce effective interactions between nearest-neighboring sites (for the derivation, see Appendix A) of the form

$$\begin{aligned}\hat{H}_{\text{NN}} = \sum_{\langle i,j \rangle} \Bigg[ & \frac{2J_0^2}{\Delta + U} P_i^0 P_j^2 - \frac{2J_0^2}{\Delta - U} P_i^2 P_j^0 \\ & + \frac{J_0^2}{\Delta}\Big((1-n_i)P_j^1 - P_i^1(1-n_j)\Big) \\ & + \frac{2UJ_0^2}{\Delta^2 - U^2}\big(P_i^{1\uparrow}P_j^{1\downarrow} + P_i^{1\downarrow}P_j^{1\uparrow} - S_i^+ S_j^- - S_i^- S_j^+\big)\Bigg],\end{aligned} \tag{3.13}$$

where $S_i^+ = \hat{c}^{\dagger}_{i,\uparrow}\hat{c}_{i,\downarrow}$ and $S_i^- = \hat{c}^{\dagger}_{i,\downarrow}\hat{c}_{i,\uparrow}$ are spin operators, $\hat{n}_i = \hat{n}_{i,\downarrow} + \hat{n}_{i,\uparrow}$, and we introduce the projector of zero, one and two particles per site

$$\begin{aligned} & P_i^0 = (1 - \hat{n}_{i,\downarrow})(1 - \hat{n}_{i,\uparrow}) \\ & P_i^{1\sigma} = (1 - \hat{n}_{i,\bar{\sigma}})\hat{n}_{i,\sigma}, \quad P_i^1 = P_i^{1\downarrow} + P_i^{1\uparrow} \\ & P_i^2 = \hat{n}_{i,\downarrow}\hat{n}_{i,\uparrow}. \end{aligned} \tag{3.14}$$

The peculiar nearest-neighbours interactions depend on $J_0^2/\Delta$ and $J_0^2/(U \pm \Delta)$, whereas the effective hopping is given by $\delta J_i$, hence they may be separately controlled. For sufficiently small $J_0 \ll \Delta, |U \pm \Delta|$ we may neglect $\hat{H}_{\text{NN}}$. However, as shown below, $\hat{H}_{\text{NN}}$ opens additional interesting possibilities.

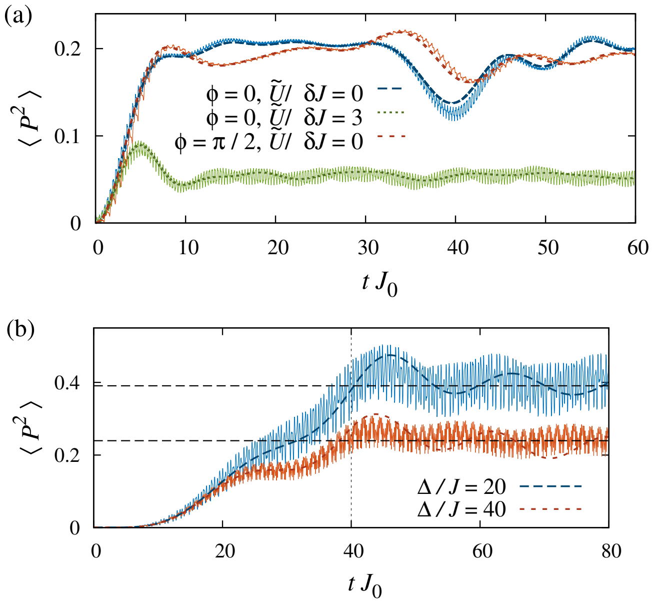

FIGURE 3.2: Time-evolution of the average double occupancy $\langle P^2 \rangle$. Dashed (solid) curves represent the effective (full) model. a) The two models show a good match, robust across different values of the phase $\phi$; for higher repulsive on-site interaction, $\tilde{U}/\delta J = 3$, the probability to find two particles on the same site is reduced. b) The tilting enters the effective model as a nearest-neighbour interaction term. Larger $\Delta$ favours configurations with less doubly occupied sites (see Figure 3.5 for ground-state phases).

**A feasible model ready for the lab** The rotating-wave approximation requirements necessary for the three-color modulation are readily achievable experimentally. As an example, let us consider the Ytterbium isotope $^{173}$Yb, with scattering length $a_0 = 199.4 a_B$, a lattice with spacing $d = 380$nm [54, 105] and depth $s_0 = 6.9$, tilted in gravity. By virtue of the tight confinement, the on-site interaction may be quantified in harmonic approximation. In this case, one has a hopping rate $J_0/h = 100$Hz, and $U = 23J_0$, $\Delta = 16J_0$, $|\Delta - U| = 7J_0$, well within the RWA requirements. For $\delta J/J_0 = 0.2$, the typical effective-tunnelling time is $\tau = \hbar/\delta J \simeq 8$ ms.

## 3.2 Non-equilibrium dynamics

We employ numerical simulations to examine the properties of the time-dependent Hamiltonian of Eq. (3.1) and the effective description given in Eq. (3.12), including the second order corrections of Eq. (3.14). Figure 3.2 depicts our results for the dynamics of the averaged probability of double occupancy, $\langle P^2 \rangle = \frac{1}{2} \sum_i \langle P_i^2 \rangle$.

In Figure 3.2(a), we present the evolution of a small system of 6 particles distributed on 6 sites, simulated with exact diagonalization methods. We initially set $\delta V = 0$ and prepare a Mott-insulator (MI) state at $U \gg J_0$, assuming an initial temperature $T = J_0$ and hence negligible initial double occupancy $\langle P^2 \rangle \simeq 0$. At time $t = 0$ we abruptly turn on the modulation $\delta J(t)$, with $\Delta/J_0 = 40$, $U/J_0 = 20$, $\delta J_1/J_0 = 0.2$ and $\beta = 1$ (where $\beta = \delta J_{2,3}/\delta J_1$) and let the system evolve. The results show a very good agreement between the effective model $\hat{H}_{\text{eff}} + \hat{H}_{\text{NN}}$, and the full model of Eq. (3.1). Non-equilibrium experiments should be able to reveal both the occupation-dependent gauge, and the suppression of $\langle P^2 \rangle$ resulting from the repulsive effective on-site interactions $\tilde{U}$.

Similar agreement between the dynamics of the full and the effective model is obtained in the thermodynamic limit, see Figure 3.2 (b), employing infinite time evolving block decimation (iTEBD) simulations [106], which are possible using the translational invariant formulation of Eq. (3.8). The analysis of ground-state properties requires a quasi-adiabatic ramping of $\delta V$. Starting again from an initial MI state (lattice filling factor $\rho = 1$) with $\delta V = 0$, we studied the quasi-adiabatic preparation of different MI ground states of our effective Hamiltonian with second order corrections. While linearly increasing $\delta V(t)$ from zero to its final value in the time-interval $0 < t < t_{\text{ramp}} = 40/J_0$, we monitored $\langle P^2 \rangle$. We consider $U/J_0 = 5$, $\delta J_1/J_0 = 0.1$, $\tilde{U}/\delta J_1 = 2$, $\beta = 1$. For computational simplicity we restrict the initially prepared state to $\chi = 40$ matrix-states, limiting its entanglement. Again $\hat{H}_{\text{eff}} + \hat{H}_{\text{NN}}$ reproduces very well the dynamics of the full model (3.1). In fact, after the ramp, $\langle P^2 \rangle(t)$ (the dashed line concealed in the micromotion) oscillates around the expected value for the ground state of the effective model (horizontal lines), the oscillations due to the heating induced by the quasi-adiabatic character of the finite ramping time.

## 3.3 Phases of the effective Hamiltonian

At this point we focus on the ground-state physics of $\hat{H}_{\text{eff}}$, at first assuming that $J_0 \ll \Delta, |\Delta \pm U|$, and hence that the inter-site interaction $\hat{H}_{\text{NN}}$ may be neglected, recovering it when it occurs to analyze how it affects the phase diagram. For $\beta \neq 1$ (in-phase and out-of-phase modulations have different amplitudes, as $\beta = \delta J_{2,3}/\delta J_1$), $\hat{H}_{\text{eff}}$ realizes a broad class of Hubbard models with correlated hopping extensively studied in the context of cuprate superconductors [107–111], and recently revisited for ultra-cold gases with modulated interactions [60, 62]. For $\phi \neq 0$, the occupation-dependent gauge gives rise to a particularly intriguing physics.

### 3.3.1 Metal-insulator phase diagram

We comment hereafter on Figure 3.3, which shows the ground-state phase diagram of Eq. (3.19) as a function of $\beta$ and the chemical potential $\mu$, in the limit of hard-core bosons $\phi = \pi/2$, with balanced population of the two components and for $\tilde{U} = 0$. The result is obtained by means of density matrix renormalization group (DMRG) [112] simulations, in finite-size open-boundary systems of up to 80 sites, keeping up to 600 Schmidt states. The Hamiltonian in Eq. (3.12) is symmetric under particle-hole exchange, and hence the region $\mu > 0$ ($\rho > 1$) is mirror symmetric to that depicted for $\mu < 0$ ($\rho < 1$) in Figure 3.3(a).

We refer henceforth only to the range $\mu < 0$. The case $\beta = 0$ deserves particular attention. In this limit, the hopping processes (ii) and (iii) are not activated and doubly-occupied sites (doublons) and empty ones (holons) become mutually impenetrable. The ground state is a metal without doublons (holons, for $\mu > 0$), that tends to a lattice half-filling $\rho = 1/2$ for $\mu \to 0$ (quarter-filling of the energy band for each component). If existing, two doublons confine a localized metallic region within their sites, due to the doublon-holon mutual impenetrability; this results in a non-conducting metal with a vanishing Drude weight (Kohn-metal) [108] for lattice fillings within $\rho = 1/2$ and $\rho = 3/2$: all these states lie in the point of infinite compressibility $\mu = 0$.

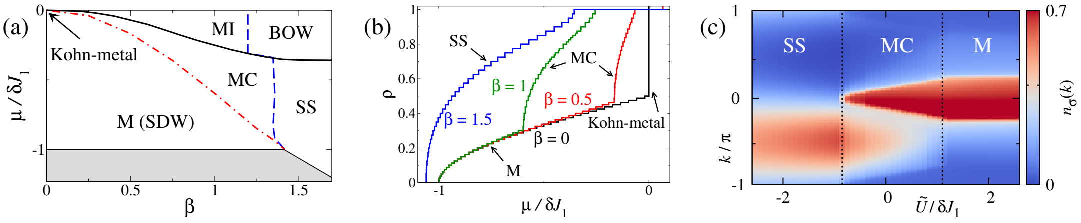

FIGURE 3.3: (a) Phase diagram of $\hat{H}_{\text{eff}}$ as a function of $\mu/\delta J_1$ and $\beta$ for $\phi = \pi/2$ and $\tilde{U} = 0$. The dash-dotted lines mark the commensurate-incommensurate metal-MC transition. The dashed (blue) lines denote the opening of $\Delta_S$ that marks the MC-SS and MI-BOW transitions. Shaded regions depict the vacuum. (b) Equation of state $\rho = \rho(\mu)$ for $\beta = 0, 0.5, 1$, and $1.5$ for the parameters of Figure (a). (c) Momentum distribution $n_\sigma(k)$ of Eq. (3.19) as a function of the for $\rho = 0.5$ and $\phi = \pi/2$ ($L = 60$).

For $0 < \beta < 1$, in the absence of occupation-dependent gauge [62], the system undergoes a smooth phase transition from a metal (M) with dominant spin-density wave (SDW) correlations, $(-1)^j \langle n_{0-} n_{j-} \rangle$, with $n_{j-} = n_{j,\uparrow} - n_{j,\downarrow}$, to a triplet superconductor. On the contrary, for $\phi = \pi/2$, the metallic phase undergoes for $\beta \lesssim 1.4$ a commensurate-incommensurate phase transition, marked by a kink in the $\mu(\rho)$ curve, Figure 3.3(b), to a peculiar gapless multi-component (MC) phase. We evaluate the central charge of different phases from the conformal expression of the von-Neumann entropy,

$$S_{vN,L}(l) = \frac{c}{3} \ln \left[ \frac{L}{\pi} \sin \left( \frac{\pi}{L} l \right) \right] + \gamma, \tag{3.15}$$

for a subsystem of length $l$ in a systems of L sites, with $\gamma$ a constant [113, 114]. The MC phase presents a central charge $c \approx 3$; in contrast, the metallic phase has $c = 2$. The MC phase smoothly connects to the Kohn-metal for $\beta \to 0$.

For $\beta \gtrsim 1.4$ and $\rho \neq 1$, a spin gap $\Delta_S$ opens and the kink in $\mu(\rho)$ disappears, marking the transition to a phase with dominant singlet-superconducting (SS) correlations, $\langle \mathcal{Q}^\dagger_{0-} \mathcal{Q}_{j-} \rangle$, with $\mathcal{Q}_{j-} \equiv \hat{c}_{j+1,\downarrow} \hat{c}_{j,\uparrow} - \hat{c}_{j+1,\uparrow} \hat{c}_{j,\downarrow}$. Finally, at $\rho = 1$ we find a MI with dominant SDW correlations, and a totally gapped phase with bond-ordering wave (BOW) order $\mathcal{O}_D(j) = \sum_\sigma T_\sigma(j) - T_\sigma(j+1)$, with $T_\sigma(j) = \hat{c}^\dagger_{j,\sigma} \hat{c}_{j+1,\sigma} + \text{H.c.}$.

### 3.3.2 Multi-component phase

The multi-component phase, which occurs even for $\beta = 1$ and $\tilde{U} = 0$, is a direct consequence of the occupation-dependent gauge. The nature of this phase is best understood for $\phi = \pi/2$ and $\beta = 1$. In that case, the two-particle problem, with a $\uparrow$ particle and a $\downarrow$ one, presents for any $\tilde{U}$ an exact bound eigenstate,

$$|P\rangle = \cos\theta |D\rangle + \mathrm{i} \sin\theta |S\rangle, \tag{3.16}$$

with eigenenergy

$$E_P = \frac{\tilde{U}}{2} - \sqrt{\frac{\tilde{U}^2}{4} + 2\delta J_1{}^2}, \tag{3.17}$$

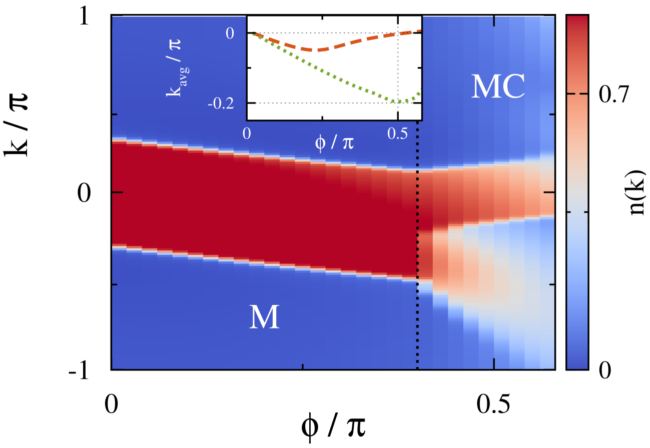

FIGURE 3.4: Momentum distribution $n(k)$ of one component as a function of the Peierls phase. We used DMRG with $L = 80$, filling $\rho = 0.6$, $\tilde{U} = 0$ and $\delta J = 0.4$. The inset shows the centre of the momentum distribution as a function of $\phi$ for different fillings $\rho = 0.6$ (dashed line) and $\rho = 0.2$ (dotted line). We included nearest-neighbours interactions, with $J = 1$, $\Delta = 10$, $U = 20$.

where

$$\begin{aligned} \tan\theta &= \frac{\tilde{U} - E_P}{\sqrt{2}\delta J_1}, \\ |D\rangle &= \sum_j (-1)^j |\uparrow,\downarrow\rangle_j, \\ |S\rangle &= \sum_j (-1)^j (|\uparrow\rangle_j |\downarrow\rangle_{j+1} - |\downarrow\rangle_j |\uparrow\rangle_{j+1})/\sqrt{2}. \end{aligned} \tag{3.18}$$

The existence of this bound state even for $\tilde{U} > 0$ results from the occupation-dependent gauge (see Appendix B). For sufficiently large $\tilde{U} > 0$, the eigenenergy $E_P$ is larger than $E_F$ (the Fermi energy of the metal) and the metallic phase is stable. For decreasing $\tilde{U}$, the system enters the regime where $E_P < 2E_F$ and part of the Fermi sea forms pairs that quasi-condense in $|P\rangle$, until the new Fermi energy $E'_F = E_P/2$. The MC phase results from the coexistence of a partially depleted Fermi sea and bound pairs. When $E'_F$ reaches the bottom of the lattice band, the Fermi sea is fully depleted marking the onset of the SS phase. The MC phase has a characteristic momentum distribution of both components, $n_\sigma(k)$, and it can be thus easily revealed in time-of-flight measurements. The momentum distribution as a function of $\tilde{U}/\delta J$ is conveniently analyzed in the simple case $\beta = 1$, for which the hopping processes share the same hopping rate $\delta J_1/2$:

$$\hat{H}_{\text{eff}} = -\frac{\delta J_1}{2} \sum_{j,\sigma} \hat{c}^\dagger_{j+1,\sigma} e^{i\phi|\hat{n}_{j+1,\bar{\sigma}} - \hat{n}_{\bar{\sigma},j}|} \hat{c}_{j,\sigma} + \tilde{U} H_{\text{int}}. \tag{3.19}$$

Figure 3.3(c) shows our results for $\hat{n}_\sigma(k)$, at $\phi = \pi/2$. For large-enough $\tilde{U}$, the metallic phase presents a slab-like Fermi sea. In the MC phase, the slab shrinks due to partial pairing. The latter results in a blurred contribution to $n_\sigma(k)$,

$$\frac{1}{2\pi}\left[1 - \sqrt{2}\sin(2\theta)\sin(k/2) - \sin^2\theta\cos(2k)\right], \tag{3.20}$$

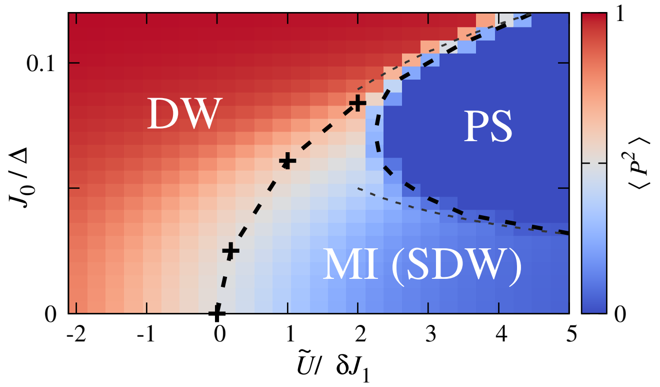

FIGURE 3.5: Phase diagram of $\hat{H}_{\mathrm{eff}} + \hat{H}_{\mathrm{NN}}$ for $\rho = 1$, $U = 5J_0$, $\delta J = 0.1J_0$, $\beta = 1$, and $\phi = 0$. The MI-DW transition is given by $K_S = 1$ (extrapolated from DMRG calculations of up to $L = 160$ sites. The coloring codes $\langle P^2 \rangle$ are obtained from iTEBD calculations (for 200 states results are consistent with our DMRG data of 160 sites).

as expected for $|P\rangle$ pairs (see Appendix B). The MC-SS transition is marked by the vanishing Fermi sea. Lastly, we show in Figure 3.4 how the MC phase enters the system as the Peierls phase increases, presenting numerical results on the momentum distribution. We set $\rho = 0.6$, $\tilde{U} = 0$ and $\delta J_1 = 0.4$; up to a threshold Peierls phase, we observe a metallic phase with drifted momentum distribution, and beyond it the momentum distribution splits into a blurred lower branch corresponding to the bound pairs, and a more definite upper branch, the metallic component. The centre of the momentum distribution $k_{\mathrm{avg}}$, in the inset, has a maximum in the drift which is more pronounced and occurs at larger phases when the lattice filling is smaller.

### 3.3.3 Intersite interactions

The nearest-neighbor interaction $\hat{H}_{\mathrm{NN}}$ becomes relevant for large-enough $J_0/\Delta$ and $J_0/|\Delta \pm U|$. Combining effective on-site and nearest-neighbours interactions constitutes an additional interesting control possibility resulting from the three-color modulation.

Figure 3.5 depicts for $\beta = 1$, $\phi = 0$ and $\rho = 1$ the phase diagram as a function of $\tilde{U}/\delta J$, and $J_0/\Delta$ (which controls the strength of the nearest-neighbours terms). For $J_0/\Delta \to 0$ the standard two-component 1-D Fermi-Hubbard model is recovered [115]: for any $\tilde{U} > 0$ there is a Mott-insulator (SDW) phase with a finite charge excitation gap $\Delta_c > 0$ and spin gap null $\Delta_S = 0$; in contrast, for $\tilde{U} < 0$, a spin gap $\Delta_S > 0$ opens, while $\Delta_c = 0$. For sufficiently large $J_0/\Delta$ the system is driven into a fully gapped density-wave (DW) phase, characterized by a non-vanishing DW order parameter $\mathcal{O}_{DW} = \sum_j (-1)^j \langle n_0 n_j \rangle$. For a dominant inter-site interactions, the first term of Eq. (3.14) favors the crystalline phase with - neglecting quantum fluctuations - an energy $\vec{S}$

$$E_{DW} \sim \tilde{U} - \frac{4U}{\Delta^2 - U^2}. \tag{3.21}$$

In this region, the condition $E_{DW} = 0$ gives a rough estimate of the DW phase boundary, which also marks the transition between the DW and the PS phase (dotted upper line). For $\tilde{U} > 0$ we observe two different MI phases with a suppressed doublon number: the above mentioned MI phase with antiferromagnetically ordered spin,

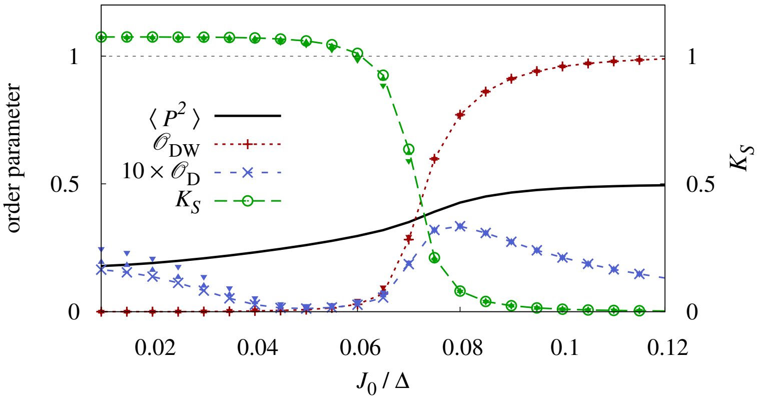

FIGURE 3.6: Average doublon density $\langle P^2 \rangle$, order parameters $\mathcal{O}_{DW}$, $\mathcal{O}_D = \mathcal{O}_D(L/2)$ and Luttinger-liquid parameter $K_S$ (cut of Figure(3.5) at $\tilde{U}/\delta J = 1$): DMRG simulations with $L = 180$ sites, small filled downwards- and upwards-pointing triangles depict results for $L = 80$ and $L = 120$ sites).

that means dominant SDW correlations and a vanishing spin gap $\Delta_S = 0$, and a region of phase separation of ferromagnetic domains (PS). The interplay between the two phases can be understood best from an expansion in the limit of strong interaction $\tilde{U} \gg \delta J$. In this limit, one can project out the doubly occupied sites and obtain an effective spin-1/2 model with superexchange interaction $H_{\mathrm{se}} \sim J_{\mathrm{eff}} \vec{S} \cdot \vec{S}$, with

$$J_{\mathrm{eff}} = \frac{2U}{\delta^2 - U^2} - \frac{\delta J^2}{4} \left( \frac{1}{\tilde{U} + \frac{2U}{U\Delta - \Delta^2}} + \frac{1}{\tilde{U} + \frac{2U}{U\Delta + \Delta^2}} \right). \tag{3.22}$$

At $1/\Delta \sim \delta J / \sqrt{4U\tilde{U}}$, $J_{\mathrm{eff}}$ changes sign and this marks the transition from the SDW phase ($J_{\mathrm{eff}} > 0$) to the PS region ($J_{\mathrm{eff}} < 0$), as shown in Figure (3.5) with a lower dashed line. In our DMRG and iTEBD calculations we could clearly characterize the first order transition to the PS-region by a marked drop of the doublon density, as illustrated by the color distribution in the figure. The MI-DW transition is associated to the opening of the spin gap $\Delta_S$, characterized by the Luttinger-liquid parameter in the spin sector $K_S = 1$ ("+" symbols in Figure 3.5). We extract $K_S$ from the long wavelength behavior of the static spin structure factor [116]:

$$S_{n_-}(k) = \frac{1}{L} \sum_{i,j} e^{\mathrm{i}(i-j)k} \langle n_{i-} n_{j-} \rangle. \tag{3.23}$$

Since $\hat{H}_{\mathrm{NN}}$ breaks the spatial reflection symmetry, we do not observe a separate BOW phase, as it is the case for Hubbard models with standard density-density nearest-neighbours interactions [117], but a non-vanishing BOW order $\mathcal{O}_D$ in the DW phase, due to the preferred creation of excitations in a particular spatial direction.

Several physical quantities and order parameters have been considered and numerically calculated in order to mark the phases and the phase transitions described so far. Figure 3.6 presents a plot of them on a vertical cut of the phase diagram of Figure(3.5): we fix $\tilde{U}/\delta J_1 = 1$ and vary $\Delta$ across the MI to DW phase transition. As already evident from the color scale in Figure 3.5, the average double occupancy $\langle P^2 \rangle$ increases rather smoothly from a finite value at zero nearest-neighbours interaction to the maximum $\langle P^2 \rangle = 0.5$ in the deep density-wave phase limit, already at $J_0/\Delta = 0.12$. In the same range, the DW order parameter ranges from zero in the MI

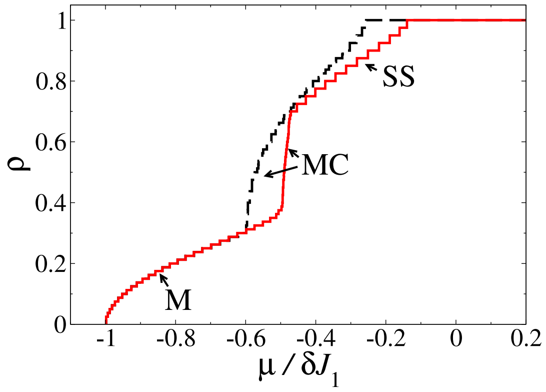

FIGURE 3.7: Comparison between the effective Hamiltonian of Eq. (3.19), black dashed line, and the anyon-Hubbard model of Eq. (3.25), red continuous line; $\tilde{U} = 0$ and $\phi = \pi/2$ and $\beta = 1$.

state to its maximum value on a narrower interval, which allows us to mark more precisely the MI-DW transition. Conversely, the Luttinger-parameter clearly characterizes the opening of a spin gap $\Delta_S$ and the simultaneous suppression of SDW correlations around the region $J_0/\Delta \simeq 0.6$, $J_0/\Delta \simeq 0.8$. The BOW-order is instead completely enclosed in the dominating DW curve, which does not allow to distinguish uniquely the BOW phase.

## 3.4 Two-component anyon-Hubbard model

At low lattice filling $\rho$, for which the processes in (iv) in Sec. 3.1.1 may be neglected, a Jordan-Wigner-like transformation [93],

$$f_{j,\sigma} = \mathrm{e}^{-\mathrm{i}2\phi \sum_{1\leq l<j} n_l} \mathrm{e}^{-\mathrm{i}\phi n_j} \hat{c}_{j,\sigma}, \tag{3.24}$$

maps (3.19) into a two-component anyon-Hubbard model (2AHM):

$$\hat{H}_{\mathrm{2AHM}} = -\frac{\delta J_1}{2} \sum_{j,\sigma} (f^\dagger_{j,\sigma} f_{j+1,\sigma} + \mathrm{H.c.}) + \tilde{U} H_{\mathrm{int}}. \tag{3.25}$$

The operators $f_{j,\sigma}$ and $f^\dagger_{j,\sigma}$ characterize anyon-like hardcore particles, that fulfil a fractional exchange statistics:

$$\begin{aligned} f_{j,\sigma} f^\dagger_{k,\sigma'} + \mathcal{F}_{j,k} f^\dagger_{k,\sigma'} f_{j,\sigma} &= \delta_{j,k}\delta_{\sigma,\sigma'}, \\ f_{j,\sigma} f_{k,\sigma'} + \mathcal{F}_{j,k} f_{k,\sigma'} f_{j,\sigma} &= 0. \end{aligned} \tag{3.26}$$

The complex-parameter $\mathcal{F}_{j,k}$ determines the statistics of the system:

$$\mathcal{F}_{j,k} := \begin{cases} e^{-\mathrm{i}2\phi}, & j > k, \\ 1, & j = k, \\ e^{\mathrm{i}2\phi}, & j < k, \end{cases} \tag{3.27}$$

where the condition $\mathcal{F}_{j,j} = 1$ sets the hard-core behaviour of the particles. For $\phi = 0$ one recovers the standard two-component Fermi-Hubbard model, while $\phi = \pi/2$ corresponds to the two-component hard-core Bose-Hubbard model.

In Figure 3.7 we present a comparison between the phase diagram of the effective Hamiltonian of Eq.(3.19), with $\beta = 1$, and the anyon-Hubbard model of Eq. (3.25),

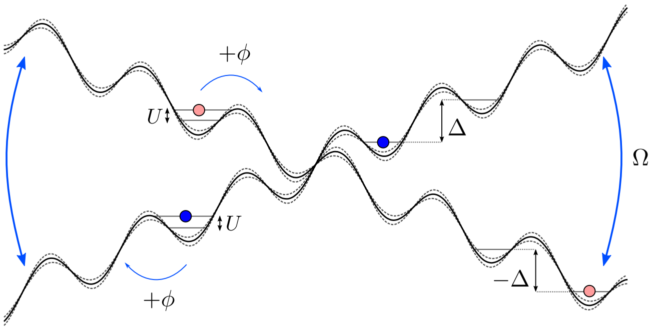

FIGURE 3.8: Lattice shaking schee with a magnetic field gradient for the realization of the hardcore anyon-Hubbard model. Microwave fields $\Omega$ couple the boundaries of the system.

for $\tilde{U} = 0$ and $\phi = \pi/2$. Both models provide identical results at low densities. Not unexpectedly they diverge when the density grows ($\rho \gtrsim 0.3$). As for the effective model, the anyon model shows as well a (narrower) MC phase. At larger densities close to $\rho = 1$, Model (3.25) presents an intermediate SS phase absent in the effective Hamiltonian (3.19). Specific cases of the have been studied in the context of exactly solvable models [118, 119]. In contrast, the non-integrable FES discussed here does strongly modify the spectrum of the 2AHM compared to the Fermi-Hubbard model.

## 3.5 Anyons interferometry

In the following, we will introduce a method that may be employed to reveal the anyonic exchange statistics of the 2AHM model.

### 3.5.1 Scheme for an effective periodic anyon model

We consider a spin dependent tilting of the optical lattice, realized in a magnetic field gradient, such as in Figure 3.8. Again, we may identify four hopping processes and three corresponding frequencies.

- (i) a single atom, alone at a given site, hops to an empty site leading to an energy shift $\Delta E_I = \pm\Delta$;
- (ii) an atom with spin ↑ (↓), initially alone at a given site, tunnels to its right (left) onto a site already occupied by a single atom with opposite spin ↓ (↑), resulting in a shift $\Delta E_{II} = \Delta + U$;
- (iii) the same event as (ii) but the hopping is to the left (right): $\Delta E_{III} = U - \Delta$;
- (iv) energy-degenerate doublon hopping: $\Delta E_{IV} = \Delta$

Hence, now the same three color-modulation scheme allows to realize opposite phases for the hopping of ↑ and ↓ particles of the anyon-Hubbard model:

$$H_{\text{eff}}^{\text{SD}} = \sum_{\substack{i=0\cdots L,\\ \zeta=0,1}} \hat{c}_{i,\zeta}^{\dagger} e^{i(-1)^{\zeta}\phi(n_i - n_{i+1})} \hat{c}_{i+1,\zeta} + \text{H.c.}\,. \tag{3.28}$$

Interestingly, the phase $\phi$, contrary to model (3.12), has no effect on the spectrum and can be gauged out in an open boundary conditions system by a simple redefinition

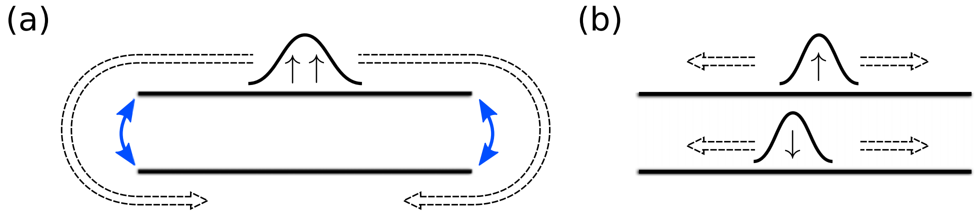

FIGURE 3.9: Scheme of the experimental protocol for interferometry with 2AHM. a) Interferometer scheme for the anyon model in PBC. b) Balanced-spin doublon expansion on a empty lattice, in OBC.

of the fermion operators. This, however, depends on the boundary conditions and is no longer possible if we couple the two components by means of a resonant laser or microwave field. If we assume the particles to be trapped in a steep box-shaped trap, such that the boundaries of the systems are well defined, we may couple the boundaries [120] through spin-flip terms:

$$H^{\rm SD}_{\rm eff} + \left(\hat{c}^\dagger_{0,1}\hat{c}_{0,0} + \hat{c}^\dagger_{L,1}\hat{c}_{L,0} + \text{H.c.}\right) . \tag{3.29}$$

For low densities we may now interpret the system as an anyon model with single-component particles in $2L$ sites and with periodic boundary conditions. Most importantly, two effective single-component particles pick up a phase $\phi$ when exchanging their position, i.e. by travelling once around the ring. In the low density limit, i.e. if we again neglect process (iv), we obtain a model, now spin-less, of hard-core anyons on a synthetic ring:

$$\hat{H}_{\rm 2AHM} = \sum_{i=0\cdots 2L} \alpha^\dagger_i \alpha_{i+1} + \alpha^\dagger_L \alpha_0 + \text{H.c.}. \tag{3.30}$$

The anyons $\alpha_i$ obey the hardcore constraint $(\alpha^\dagger_i)^2 \equiv 0$, and the fractional exchange relation,

$$\alpha_j \alpha^\dagger_k + e^{-i2\phi\,\text{sign}(j-k)} \alpha^\dagger_k \alpha_j = \delta_{jk} \tag{3.31a}$$

$$\alpha_j \alpha_k + e^{-i2\phi\,\text{sign}(j-k)} \alpha_k \alpha_j = 0 \tag{3.31b}$$

It is important to note that, without further interactions, Model (3.30) is integrable. For open boundary conditions a Jordan-Wigner transformation maps it to the case of free fermions and the spectrum, as well as those properties that depend on the density, are unaffected by the phase $\phi$ (see e.g. Ref. [83] and references therein for a detailed discussion on the Jordan-Wigner transformation in open boundary conditions and periodic boundary conditions). The quasi-momentum distribution and the single particle density matrix certainly exhibit a strong dependence on the statistics. However, an experiment will only measure the fermionic momentum distribution (since only local hoppings in the model are affected). This changes, however, for periodic boundary conditions. Certainly, the model is still integrable, but a mapping to free fermions leads to a density-dependent boundary term:

$$\hat{H}_{\rm AHM} = \sum_j \hat{c}_j \hat{c}^\dagger_{j+1} + e^{i\phi \sum_{0<j<L-1} \hat{n}_j} c^\dagger_L c_0 + \text{H.c.} \tag{3.32}$$

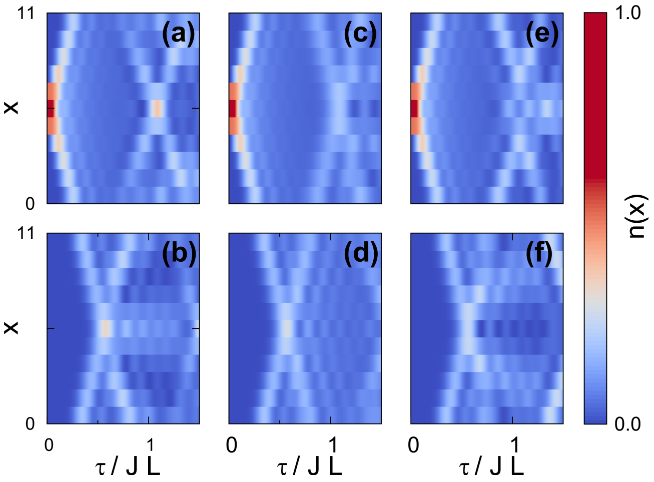

FIGURE 3.10: Time evolution of the local density for (a) and (b) fermions ($\phi = 0$, (c) and (d) anyons ($\phi = \pi/2$) and (e) and (f) hard-core bosons ($\phi = \pi/2$). Panels (a), (c) and (e) show the $\uparrow$ component (sites 0 to 5) while panels (b), (d) and (f) show the $\downarrow$ component (sites 6 to 11).

We will show in the following how this effective boundary term will affect the real space density during the time evolution after a quantum quench.

### 3.5.2 Dynamical probing of the exchange statistics

The experimental setup described above, allows for the engineering of 1-D anyons with an arbitrary statistical angle $0 \leq \phi \leq \pi/2$. In the following, we propose an interferometer scheme that reveals the anyonic character by means of an expansion experiment in a small lattice system. The general idea is sketched in Figure 3.9 (a). Initially, a spin polarized cloud of two or more particles is prepared in the centre of the lattice. For concreteness we first consider exactly two (spin $\uparrow$) particles tightly confined to the two adjacent central sites. After that, we discuss the case of a larger cloud with fixed average particle number.

#### Two particle interference

In Figure 3.10 we show the evolution of the density of two particles for different statistical angles $\phi = 0$, $\pi/4$ and $\pi/2$. The upper panels of Figure 3.10 show the evolution of the density of the spin-$\uparrow$ component $n_0$ and in the lower panels the spin-$\downarrow$ component $n_1$. Although the particle expansion is diffusive and we cannot monitor the position of single particles, one may observe the emergence of an interference pattern at the centre of the system after particles have in average traveled once through the whole lattice at $\tau \sim JL$.

Figure 3.11 depicts in detail the time evolution of the central density for both components for $\phi = 0$ (effective fermions) and $\phi = \pi/2$ (effective hardcore bosons). For $\tau/J \gtrsim L/2$ the curves noticeably depend on the statistical angle. In particular close to the classical point of return $\tau \sim JL$ the density $n_0(L/2)$ shows a strong dependence on the statistical angle. The inset of Figure 3.11 (a) depicts this central spin $\uparrow$ density $n_0$ for $\tau/J = L + 1$, where we observe a distinct peak for fermions and a local minimum for the bosonic case (dashed line in Figure 3.11). Figure 3.11 also compares the evolution of the full three-color modulation Model (3.1) and the

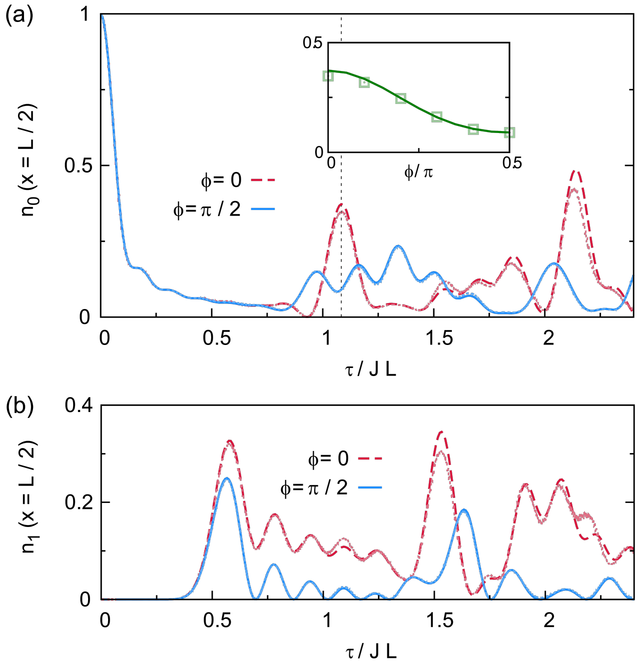

FIGURE 3.11: Time evolution of the central density for the two spin components: a) spin ↑, b) spin ↓. Dashed lines show the effective hard-core anyon model for fermions, the solid line for bosons. Dotted lines depict a comparison with the full three color modulation model with $\Delta/J_0 = 40$, $U/J_0 = 20$ (length $L = 12$ sites, two particles, $\delta J = 0.5 J_0$). The inset of (a) shows the density $n_0(x = L/2)$ for $\tau/J = L+1$ of the effective model (solid line) and the full three-color modulation simulation (symbols) as a function of the statistical angle $\phi$.

effective periodic boundary conditions anyon-Hubbard model (3.30). Due to higher order terms the two corresponding curves separate during the time evolution, however, for the given parameters the time evolution of model (3.1) recovers very well the hardcore anyon model over the full range of $\tau/J \lesssim 2L$ shown in Figure 3.11.

While Model (3.30) is integrable as discussed above, for the real time evolution of the interacting two component three-color modulated Fermi-Hubbard model we employ exact diagonalization techniques in combination with a higher order Runge-Kutta method.

### Fixed average particle density

Experiments with single site resolution [121–124] may allow for the controlled initial preparation of a two particle state and the subsequent observation of the time evolution of the (possibly spin-resolved) density [125] corresponding to Figure 3.11. In the following, we relax these conditions and analyze the possibility of an interferometrical measurement with a larger cloud with fixed average density. Initially we assume a fully polarized sample with all the particles prepared in a tight trap and ensemble-average over several realizations of the setting with fluctuating total particle densities with average density $n_{\text{avg}}$; for concreteness we choose an ensemble with $\rho(n) \sim \mathrm{e}^{-(n-n_{\text{avg}})^2}$.

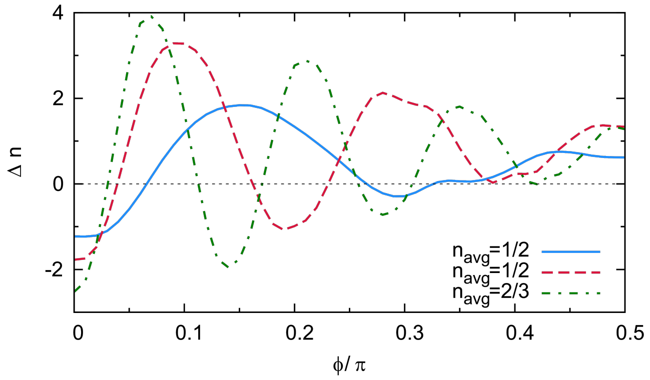

FIGURE 3.12: Spin polarization as a function of the statistical angle $\phi$ for various average fillings $n_{\text{avg}}$.

A measurement of the total spin-polarization,

$$\Delta n = \sum_x \langle n_0(x) - n_1(x) \rangle \,, \tag{3.33}$$

may be used as a indicator of the anyonic exchange statistics. As the particles travel to the other half of the chain, they start to interfere and differences in the average populations of the two components may be measured. After long enough waiting time this difference may be quite pronounced. In Figure 3.12 we show the ensemble averaged value of $\Delta n$ after a fixed time $\tau/J = 2L$ as a function of the statistical angle $\phi$ for different values of $n_{\text{avg}}$. The curves are not a monotonous function of the phase $\phi$ and depend on $n_{\text{avg}}$, however exhibit a strong dependence on the statistics of the particles.

### 3.5.3 Dynamical probing of pairing

We now return to the two-anyon-Hubbard model (3.25). We discuss how an expansion experiment may reveal the unconventional pairing properties of the two-anyon-Hubbard model in the (pseudo) boson limit. For the case of a pseudo-anyon Hubbard model (single component, soft-core anyons) similar ideas have been discussed in Ref. [89].

#### Bound pairs in the two-anyon-Hubbard model

Contrary to the hardcore anyon-Hubbard model, the phase diagram of model (3.25) depends strongly on the statistical angle $\phi$. Indeed, as a function of $\phi$ and the filling, a plethora of ground-state phases may be found. This includes the emergence of the PP phase and a paired singlet-superconducting-phase even for vanishing interactions $\tilde{U} = 0$.

Both PP and SS phases can be understood from the unconventional emergence of paired states in the spectrum of the model. Following our analysis and similar calculations for the soft-core anyon-Hubbard model [96], one observes that for a finite $\phi > 0$ bound states may form in the two-particle spectrum even for vanishing on-site interactions $\tilde{U} = 0$. For the two-anyon-Hubbard model with vanishing on-site

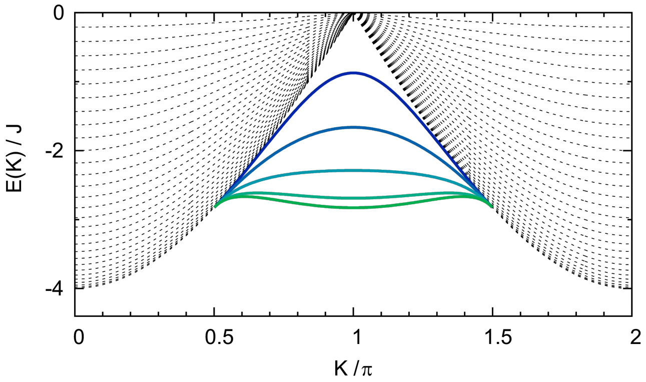

FIGURE 3.13: Unconventional bound states in the two-particle spectrum of Model (3.25), with vanishing on-site interactions $\tilde{U} = 0$ as a function of the total momentum $K$ of two particles. Dashed lines depict the two-particle scattering continuum. Solid lines show the bound states for $\phi/\pi = [0.1, 0.2, ..., 0.5]$ (top to bottom).

interaction term $\tilde{U} = 0$, we find two-body bound states with a dispersion relation

$$E_K = \pm 2\sqrt{2}t \frac{\cos(K)\cos(2\phi) + 1}{\sqrt{\cos(K)(2\cos(2\phi) - 1) + 1}} \tag{3.34}$$

Here $K$ is the total momentum of the two-particle solution and $\pi/2 < K < 3\pi/3$. For $\phi > \pi/3$ the bound state spectrum $E_K$ has a local minimum at $\pi$. Due to a quasi-condensation of bound pairs in this point PP and SS phases can form as the fractional statistics also induces an effective interaction between the anyons. Several examples of the two-particle spectrum are shown in Figure 3.13.

### Expansion dynamics

The formation of unconventional bound states resulting from the anyonic exchange statistics may be revealed by the characteristic expansion of a cloud of particles (now with balanced spin and open boundary conditions) into an empty lattice, as in Figure 3.9 (b). We consider the particles initially with opposite spin on two adjacent sites in the centre of an empty lattice.

In Figure 3.14-I we show the time evolution of the real space density $n_0(x) + n_1(x)$, and in Figure 3.14-II the spin $n_0(x) - n_1(x)$ for several values of $\phi$. All examples show a light-cone like ballistic expansion of the density with constant velocity independent of the statistical angle $\phi$, corresponding to single unbound particles moving into the empty lattice. Contrary to the case of soft-core anyons [89], the light cone is symmetric for all $\phi$.

As soon as bound states can be found in the two-particle spectrum for a finite $\phi > 0$ we observe a second light cone, most evident in Figure 3.14-I (b). As this feature is absent in the spin-density picture (see Figure 3.14-I) we conclude that it corresponds to bound pairs of particles. The pairs exhibit a larger effective mass due to the flatness of the bound state band (see Figure 3.13) and hence the second inner light cone is much steeper. Interestingly, for our choice of the initial state, the expansion of the bound-state fraction almost stops for $\phi = \pi/2$, as one can see in Figure 3.13 (c).

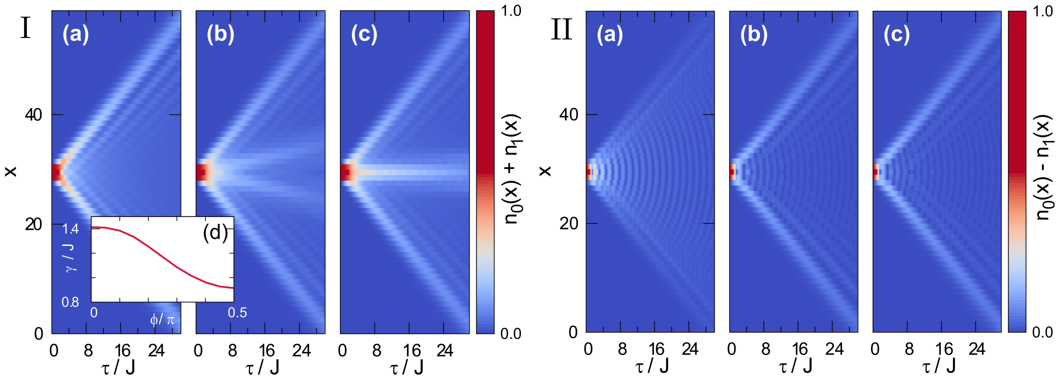

FIGURE 3.14: I - Expansion dynamics of the total density $n_0 + n_1(x)$ of the 2AHM with (a) $\phi = 0$, (b) $\phi = 0.4\pi$ and (c) $\phi = \pi/2$ initially prepared as a fully localized state of two particles on the two adjacent central sites of a $L = 60$ long chain, $\tilde{U} = 0$. Panel (d) depicts the calculated expansion rate $\gamma/J$ as a function of the statistical angle $\phi$. II - Expansion dynamics of the spin density $|n_0 - n_1|(x)$ of the 2AHM.

To further quantify this expansion dynamics we monitor the evolution of the average expansion of the cloud,

$$\Delta j(\tau) = \sqrt{\langle n_j (j - L/2)^2 \rangle (\tau)}, \tag{3.35}$$

which after some initial time becomes of the form $\Delta j(\tau) \sim \gamma\tau$. This expansion rate $\gamma$ is shown in Figure 3.14-I (d) and depends monotonously on the statistical angle $\phi$. As expected, for free fermions ($\phi = 0$, $U = 0$) we find $\gamma = \sqrt{2}$. For finite statistical angles the expansion rate is reduced due to the enhanced tendency to form bound pairs.

## 3.6 Conclusions

In this Chapter, we have proposed a versatile experimental scheme for analogue quantum simulations using Fermi gases on a one-dimensional optical lattice, which allows for a flexible separate manipulation of

- (a) correlated hopping, controlled by the modulation amplitudes $\delta V_s$
- (b) occupation-dependent gauge fields, given by the phase shift
- (c) effective on-site interactions needless of Feshbach resonance, provided by the detuning $U$
- (d) NN interactions, that depend on $J0/\Delta$ and $J0/|\Delta U|$

The method is experimentally straightforward and allows for the engineering of a very broad class of lattice models, including Hubbard Hamiltonians with correlated hopping and extended models. Moreover, it permits to create a two-particles anyon-Hubbard model whose spectrum exhibits a non-trivial dependence on the statistical phase. Expansion experiments employed for the two-component anyon-Hubbard model may reveal properties of the unconventional quantum phases of the model. In particular, a clear tendency of forming bound pairs may be observed in the pseudo-boson limit, revealing the underlying mechanism of the formation of the PP phase.

For a spin-dependent tilting the same scheme realizes a model in which for open boundary conditions the effect of the phase may be gauged out and, hence, has no influence on the dynamics or statics of the model if one focuses on observables such as local densities. The situation changes drastically if one allows for Raman-assisted spin-flips at the system boundaries. This scenario may be mapped to a single-component hardcore anyon model in a synthetic ring. We have shown how fractional quantum statistics may be monitored by means of a simple interferometer scheme. The density of a cloud of expanding particles and the total spin polarization may be used to clearly reveal the exchange statistics.

# Chapter 4

# Quantum simulation of Abelian Quantum Link Models

Lattice gauge theories play a central role in physics, ranging from the high-energy context to models for solid state and condensed matter physics. In the realm of quantum field theories, lattice gauge theories (LGTs) are the main tool we dispose of to investigate phenomena in the strong-coupling regime yet inaccessible in high-energy experiments. Quantum link models are a particular class of LGTs, that has been the subject of rising interest in recent years. The quantum link model (QLM) has three crucial features that differentiates it from Wilson's original formulation of LGTs and makes it appealing for numerical analysis and from a quantum simulation perspective:

- whilst usually LGTs are formulated in the Lagrangian language, QLMs have a Hamiltonian form;
- the gauge field that drives the interactions among the particles lives on a finite, discrete Hilbert space;
- despite the simplification, the QLM crucially maintains all the symmetry properties of the inherent gauge theory.

In this Chapter we will introduce the Abelian Quantum Link Model associated to compact quantum electrodynamics, focussing on the case with spin $S = \frac{1}{2}$ on the links. We will present the main findings of the abundant research carried out in recent years regarding the Quantum Link Model and its implementation on analogue quantum simulators.

## 4.1 Quantum field theories

**The standard model** Our best understanding of how elementary particles and three of the fundamental forces intertwine to each other is enclosed in the Standard Model. The Standard Model is a gauge invariant quantum field theory based on the symmetry group $\mathrm{SU}(3) \times \mathrm{SU}(2) \times \mathrm{U}(1)$, where the $\mathrm{SU}(3)$ colour group accounts for the strong force and the $\mathrm{SU}(2) \times \mathrm{U}(1)$ for the electroweak force. Non-Abelian relativistic fields are best described in terms of Yang-Mills theories, which are interacting, classical, massless, local gauge theories [126, 127]:

Fundamental particles are not all massless. In the electroweak force, the Higgs mechanism explains how massive gauge bosons are generated through the addition of a field to the relative Yang-Mills theory and a spontaneous symmetry breaking process. The same mechanism does not help explaining the mass gap in the strong force. Quantum Chromo Dynamics (QCD), the SU(3) Yang-Mills theory of the strong force, has the *asymptotic freedom* property, assessing free-field ultraviolet asymptotic behaviour [128, 129]. Roughly, this tells us that at short distances the effective coupling between quarks decreases and the quantum field displays a classical behaviour. Conversely, by the same token, as one considers smaller and smaller momentum scales, the effective coupling should become larger and larger, which would explain why isolated quarks are not observed. This property is called *confinement*; the fact that Yang-Mills theories support confinement is yet to prove (also, it is a Millennium Prize Problem). Other crucial questions concern establishing whether Yang-Mills theories account for and justify the *mass gap* and the *chiral symmetry breaking*.

The asymptotic freedom implies that the large momentum limit is a perturbative regime. In a perturbative regime it is possible to define the QCD Lagrangian, there exists techniques to quantize the otherwise classical Yang-Mills theory and the Lagrangian can be fruitfully analysed, with techniques proper of the perturbation theory. On the other hand, if the small momenta regime is strongly coupled, no perturbative approach can ultimately yield thorough answers. In fact, in the continuum, a dimensional regularization and renormalization applied to the QCD Lagrangian is not even defined at a non-perturbative level [130].

**Confinement and strong coupling regime** The concept of confinement refers to the absence of color charged asymptotic particle states [131]. For the sake of simplification, the strong force pushes inwards (confines) the quarks composing a hadron, analogously to the classical elastic force exerted from a spring on two massive bodies. By reason of that, color charged particles such as quarks and gluons can not be isolated from their hadronic cluster and therefore are not directly observable. The strong interaction linear potential does not rise indefinitely. The theory predicts that the potential flattens out due to a process known as *string breaking*. Two quarks in a hadron are connected by a string of potential energy, which increases as the quarks are pulled apart. At sufficiently high energies, the generation of two quarks out of the vacuum becomes energetically favourable, since they combine to form a new hadron (hadronization) and relax the string excitation onto two shorter strings.

Elucidations on the exact dynamics of string breaking and all problems involving real-time evolution as well as the physics at high baryon density are highly desirable [132]. Likewise, it is still to assess whether the hadronic spectrum is complete or whether states built by self-coupled gluons exist and if QCD accounts for the spontaneous breakdown of the chiral symmetry [133]. The answers to these questions do or may reside in the strong-coupling regime, intractable with perturbative approaches.

**Wilson's lattice gauge theory** The only non-perturbative formulation of QCD so far known is the lattice gauge theory, first worked out by Wilson in 1974 [134]. Whilst Wilson introduced LGTs in the Lagrangian formulation, which is the canonical form in the continuum for it is the argument of the Action, Kogut and Susskind elaborated in 1975 a LGTs in a Hamiltonian formalism [135]:

$$\hat{H}_{\mathrm{QCD}} = \sum_{\mathbf{i}} \mu_{\mathbf{i}} \hat{n}_{\mathbf{i}} + \sum_{\mathbf{i},u} J_u \left( \hat{\psi}^\dagger_{\mathbf{i}} \hat{U}_{\mathbf{i}u} \hat{\psi}_{\mathbf{i}+\mathbf{u}} + \hat{\psi}^\dagger_{\mathbf{i}+\mathbf{u}} \hat{U}^\dagger_{\mathbf{i}u} \hat{\psi}_{\mathbf{i}} \right) + \frac{g^2}{2} \sum_{\mathbf{i},u} (\hat{L}^2_{\mathbf{i}u} + \hat{R}^2_{\mathbf{i}u})$$
$$- \frac{1}{4g^2} \sum_{\square} \mathrm{Tr} \left( \hat{U}_\square + \hat{U}^\dagger_\square \right). \tag{4.1}$$

For the notation adopted in this thesis about the LGT Hamiltonian operators, see Sec. 4.2. In LGTs, the coefficient of the gauge plaquette term in the Lagrangian is the inverse square of the coupling constant $g$, whereas in the continuum formulation it is quadratic in $g$ [136]. This makes the expansion in the non-perturbative strong-coupling regime the natural one in LGTs. Because of the discrete spatial geometry, LGTs are particularly suitable for numerical methods à la Monte Carlo [137], which has led to significant and remarkable results [138]. However, due to the notorious sign problem affecting Monte Carlo algorithms, some problems remain intractable, such as the deep interior of neutron stars which may contain color superconducting quark matter [132].

**Simulation of quantum field theories** Owing to the Hamiltonian formulation, LGTs with a truncated gauge Hilbert space can be investigated with tensor network methods, which do not suffer the restrictions given by the sign problem. Also, the Hamiltonian language is the natural one in the context of atomic and optical physics. Although in principle the roadmap towards the analogue quantum simulation of non-Abelian lattice gauge theories is outlined, in practice it is a hard and long way to walk. Guidelines offered by leading researchers in this field suggest to put off the purse of the continuum limit and consider the more realistic and still extremely interesting strong coupling lattice dynamics per se [132]. Moreover, a quantum simulator may well start off with truncated LGTs and focus on phenomena of a qualitative nature, such as the presence or absence of specific phases: confinement is a preeminent example.

Non-Abelian gauge theories such as SU(3) QCD are particularly hard to tackle, because of the presence of self-interactions of the gauge bosons. However, phenomena like confinement, string breaking and chiral symmetry breaking are present also in Abelian compact gauge theories [138]. The U(1) gauge group acquires compactness when regularized on lattice [131], and consequentially so does QED too. In fact, compact Quantum Electro-Dynamics (cQED) is often studied as a model system for these physical phenomena [139] and it is a good starting point on the road towards the analogue quantum simulation of QFTs.

## 4.2 The Kogut-Susskind Hamiltonian

In this Section, we introduce the Abelian U(1) Quantum Link Model (QLM) [140], a Hamiltonian formulation of lattice gauge theories well-suited for quantum simulations with ultracold gases and for numerical analysis with Tensor Network algorithms. Owing to the focus of this work, we can start out directly from the Hamiltonian formulation of Quantum Electrodynamics on a lattice, as proposed by Kogut and Susskind [135]. The reader can refer to Wilson's original article [134] or to this volume of the Lecture Notes in Physics [141] for a detailed account of how a Lagrangian in the continuum is regularized on a lattice.

**Fermionic field operators** What are the ingredients for a Hamiltonian gauge theory of interacting matter in discrete coordinates? We need particle creation and annihilation operators $\hat{\psi}_\mathrm{i}^\dagger$ and $\hat{\psi}_\mathrm{i}$, obeying canonical anti-commutation relations

$$\left\{\hat{\psi}_\mathrm{i}^\dagger, \hat{\psi}_\mathrm{j}\right\} = \delta_{ij}, \qquad \left\{\hat{\psi}_\mathrm{i}^\dagger, \hat{\psi}_\mathrm{j}^\dagger\right\} = \{\hat{\psi}_\mathrm{i}, \hat{\psi}_\mathrm{j}\} = 0, \tag{4.2}$$

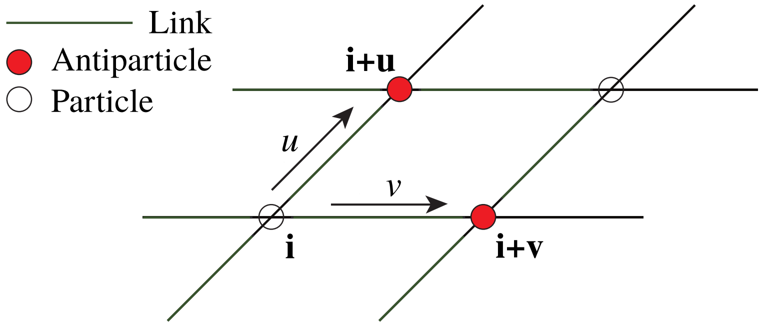

FIGURE 4.1: Graphical representation of the (2+1)-d cQED Quantum Link Model. The mass field is bipartite in particles and antiparticles. On the edges between two particles lie the links, hosting a truncated representation of the U(1) group.

acting on the vertices of a $d$-dimensional spatial lattice labelled by the multidimensional index $\mathbf{i} \in \mathbb{Z}^d$, as in Figure 4.1. The particles have staggered mass $\mu_{\mathbf{i}}$ and can hop within nearest-neighbouring sites,

$$\hat{H}_{\text{mass}} = \sum_{\mathbf{i}} \mu_{\mathbf{i}} \hat{\psi}_{\mathbf{i}}^{\dagger} \hat{\psi}_{\mathbf{i}} + \sum_{\mathbf{i},u} J_u \left( \hat{\psi}_{\mathbf{i}}^{\dagger} \hat{\psi}_{\mathbf{i}+\mathbf{u}} + \text{h.c.} \right),$$

where $\mathbf{u}$ is a unit vector in the $u \in \{1, \dots, d\}$ direction.

The reason for the staggered matter field lies in the fermion doubling phenomenon, posed by the Nielsen-Ninomiya no-go theorem [142]. The doubling problem is the emergence of $2^d$ fermion species from a $d$-dimensional lattice regularization under the assumptions of hermiticity, locality and translational invariance. Under these assumptions, the doubling problem can not be solved without breaking the chiral symmetry for vanishing fermion mass. One solution, presented by Wilson, requires to explicit breaking of the chiral symmetry by adding a proper term to the action. Another solution, introduced by Kaplan, considers domain wall fermions. We opt for the staggered fermions approach, which violates one Nielsen-Ninomiya requirement: the translational invariance. Via a process known as spin diagonalization, first suggested by Susskind [143], the "ghost" fermionic degrees of freedom are reduced and partly reinterpreted as fermion flavors [132]. In this sense, one can define $m_{\mathbf{i}} = m\mathbf{i}$ and $J_u = Ju$ and interpret $\mathbf{i}$ and $u$ as spin sign-factors; $\mathbf{i}$ represents a staggered chemical potential, $u$ a fixed $\mathbb{Z}(2)$ background gauge field with a $\pi$-flux on each plaquette. The spin-like interpretation brings the Quantum Link Model closer to more familiar and already implemented spin and Hubbard models.

**Gauge field operators** Let us now come to the effect of a background electromagnetic field on the staggered fermions propagation. The U(1) group operators are the *parallel transporters* of the gauge theory (also known as *connections* in the context of differential geometry or *comparators* [144]). The electromagnetic gauge field is a continuum vector potential; in its lattice version, the vector must stretch at least over two neighbouring sites. Therefore, we consider as a gauge field its integral in the continuum over the region between two vertices, named *link*. The parallel transporter reads

$$\hat{U}_{\mathbf{i}u} = \exp\left( \mathrm{i}e \int_{\mathbf{i}u} d\mathbf{r} A(\mathbf{r}) \right) = \exp\left(\mathrm{i}\hat{\phi}_{\mathbf{i}u}\right) \tag{4.3}$$

and acts on the $\mathbf{i}u$-link Hilbert space - see Figure 4.1. Notably, the parallel transporters remains invariant under the gauge transformation $A'(\mathbf{r}) = A(\mathbf{r}) - \partial\alpha$, since they transform as

$$\hat{U}_{\mathbf{i}u}[A'(\mathbf{r})] = V_{\mathbf{i}}\hat{U}_{\mathbf{i}u}[A(\mathbf{r})]V^{\dagger}_{\mathbf{i}+\mathbf{u}}$$

via $\hat{V}_{\mathbf{i}} \in \mathrm{U}(1)$ transformations. Conjugate momenta operators can be defined from the group parameter $\hat{\phi}_{\mathbf{i}u}$. The differential representation of the conjugate momentum is

$$\hat{E}_{\mathbf{i}u} = -\mathrm{i}\frac{\partial}{\partial\hat{\phi}_{\mathbf{i}u}}, \tag{4.4}$$

and the canonical commutation relation reads

$$\left[\hat{\phi}_{\mathbf{i}u}, \hat{E}_{\mathbf{i}u}\right] = \mathrm{i}. \tag{4.5}$$

Then, as $\hat{\phi}_{\mathbf{i}u}$ is the generator of infinitesimal rotations, it follows that

$$\left[\hat{E}_{\mathbf{i}u}, \hat{U}_{\mathbf{j}v}\right] = \delta_{\mathbf{i}\mathbf{j}}\delta_{uv}\hat{U}_{\mathbf{j}v}, \qquad \left[\hat{E}_{\mathbf{i}u}, \hat{U}^{\dagger}_{\mathbf{j}v}\right] = -\delta_{\mathbf{i}\mathbf{j}}\delta_{uv}\hat{U}^{\dagger}_{\mathbf{j}v}, \tag{4.6}$$

which identifies $\hat{E}_{\mathbf{i}u}$ as the electric field operator. The dynamic part of the gauge field is a term proportional to the square of the conjugate momentum, whose coefficient can be determined by taking the continuum limit [138]:

$$\hat{H}_{\mathrm{elec}} = \frac{e^2}{2}\sum_{\mathbf{i},u}\hat{E}^2_{\mathbf{i}u}. \tag{4.7}$$

This term is identifiable as the classical electric field energy, or electric stiffness [145].

**The Gauss' law** Insofar, the scalar potential $\Phi$ has not appeared. In the Lagrangian formulation, used in Feynman's path integral quantization, $\Phi$ plays the role of a Lagrange multiplier enforcing the Gauss' law. In the Hamiltonian formulation, Gauss' law can not be implemented as an operator identity, meaning that nothing constrains the divergence of the electric field to be null in the absence of charges [132].

Let us see how the Gauss' law enters lattice cQED. The operator $\hat{\psi}^{\dagger}_{\mathbf{i}}$ is a spinor of the U(1) group $\mathbb{G}$. Under the action of a group transformation $V \in \mathbb{G}$,

$$\hat{\psi}_{\mathbf{i}} \to \hat{V}_{\mathbf{i}}\hat{\psi}_{\mathbf{i}}, \qquad \hat{\psi}^{\dagger}_{\mathbf{i}} \to \hat{\psi}^{\dagger}_{\mathbf{i}}\hat{V}^{\dagger}_{\mathbf{i}}, \qquad \hat{U}_{\mathbf{i}u} \to \hat{V}_{\mathbf{i}}\hat{U}_{\mathbf{i}u}\hat{V}^{\dagger}_{\mathbf{i}+\mathbf{u}}, \tag{4.8}$$

the gauge symmetry of the Hamiltonian is maintained. Due to the gauge symmetry, the Hamiltonian has to commute with the generators $\hat{G}_{\mathbf{i}}$ of the local Lie group. The eigenvalues, or *charges*, of $\hat{G}_{\mathbf{i}}$ define gauge invariant sectors of the Hilbert space. The local gauge transformation generator [135] is the sum of the particle density on a vertex and the divergence of the electric fields on the links attached to that vertex:

$$\hat{G}_{\mathbf{i}} = \hat{n}_{\mathbf{i}} - \nabla_{\mathbf{i}}\hat{E}_{\mathbf{i}u} = \hat{n}_{\mathbf{i}} - \sum_{u\in *}\mathrm{sign(u)}\hat{\mathrm{E}}_{\mathrm{iu}}. \tag{4.9}$$

A general local gauge transformation is thus represented by the operator

$$\hat{V}_{\mathbf{i}} = \exp\left(\mathrm{i}e\alpha_{\mathbf{i}}\hat{G}_{\mathbf{i}}\right). \tag{4.10}$$

However, while the Hamiltonian commutes with $\hat{G}_\mathbf{i}$ for any $\mathbf{i}$, hence it is gauge invariant, most of the states do not. We can identify the kernel of $\hat{G}_\mathbf{i}$,

$$\hat{G}_\mathbf{i} \left|\psi\right\rangle_{\text{phys}} = 0, \tag{4.11}$$

as the subset of physical states, while its orthogonal complement includes the unphysical states, that must not be populated in an analogue quantum simulator.

### Lattice QED Hamiltonians

Now we can build a gauge field self-interaction term. An operator changing the conjugate momentum $\hat{E}_{\mathbf{i}u}$ must involve at least two links of one vertex, in order to compensate the variation and keep the gauge-invariance on the site. Thus, the minimal configuration maintaining the state in the same gauge-invariant charge sector leads to plaquette raising and lowering operators, acting on unit squares of the lattice,

$$\hat{U}_\square = \hat{U}_{\mathbf{i}u} \hat{U}_{\mathbf{i}+\mathbf{u},v} \hat{U}^\dagger_{\mathbf{i}+\mathbf{u}+\mathbf{v},-u} \hat{U}^\dagger_{\mathbf{i}+\mathbf{v},-v} \tag{4.12}$$

as in Fig. 4.1. This term represents the magnetic field energy. Obviously, in 1-D there are no plaquettes nor magnetic field. Analogously to the electric field energy, the coefficient can be derived by taking the continuum limit:

$$\hat{H}_{\text{plaq}} = -\frac{1}{4e^2} \sum_\square \left( \hat{U}_\square + \hat{U}^\dagger_\square \right). \tag{4.13}$$

This Hamiltonian term is also known as *plaquette* or *ring-exchange* operator, and we return to it in Sec. 4.2.1. Notice that, $\hat{H}_{\text{plaq}}$ and $\hat{H}_{\text{elec}}$ are the "potential" and "kinetic" energies of the Kogut-Susskind model (KS), both of which can be diagonalized respectively in the "position" and in the "conjugate momentum" basis [146]. In conclusion, the Kogut-Susskind Hamiltonian for compact QED takes the following form:

$$\hat{H}_{\text{KS}} = \sum_\mathbf{i} \mu_\mathbf{i} \hat{n}_\mathbf{i} + \sum_{\mathbf{i},u} J_u \left( \hat{\psi}^\dagger_\mathbf{i} \hat{U}_{\mathbf{i}u} \hat{\psi}_{\mathbf{i}+\mathbf{u}} + \text{h.c.} \right) + \frac{e^2}{2} \sum_{\mathbf{i},u} \hat{E}^2_{\mathbf{i}u} - \frac{1}{4e^2} \sum_\square \left( \hat{U}_\square + \hat{U}^\dagger_\square \right). \tag{4.14}$$

Notice that the Kogut-Susskind Hamiltonian is formally identical for both cQED and QCD lattice gauge theories, as one can see comparing with Eq. (4.1); the Hamiltonian formulation presented by the authors in [135] was indeed generic. We can establish a connection between the coupling parameter $g$ in QCD and $e$ and thus define weak- and strong-coupling regimes also in lattice QED. Although in lower spatial dimensions cQED is confining at any coupling, hence in principle dynamical phenomena such as string-breaking always occur, it is important to mind the coupling regime at which we set the analogue simulator. This is because, in order to obtain results that be congruous with QCD, the system should be in the strong-coupling regime, which is the limit in which these phenomena are expected in QCD: hence, small coefficient in front of $\hat{H}_{\text{plaq}}$ and large coefficient for $\hat{H}_{\text{elec}}$.

In what follows, we will also refer to the model Hamiltonian of Eq. (4.14) *truncated* KS (tKS); in that case, we refer to the Quantum Link Model representation of the Kogut-Susskind Hamiltonian, which has a finite (truncated) gauge field Hilbert space. The Hamiltonian (4.14) in 1-D is also known as the Schwinger model:

$$\hat{H}_{\text{Schw}} = \sum_{\mathbf{i}} \mu_{\mathbf{i}} \hat{n}_{\mathbf{i}} + \sum_{\mathbf{i},u} J_u \left( \hat{\psi}^{\dagger}_{\mathbf{i}} \hat{U}_{\mathbf{i}u} \hat{\psi}_{\mathbf{i}+\mathbf{u}} + \text{h.c.} \right) + \frac{g^2}{2} \sum_{\mathbf{i},u} \hat{E}^2_{\mathbf{i}u}. \tag{4.15}$$

The pure gauge Hamiltonian, without particles, is an interesting subject on its own, since such family of lattice gauge theories are believed to have a non-trivial phase structure:

$$\hat{H}_{\text{gauge}} = \frac{g^2}{2} \sum_{\mathbf{i},u} \hat{E}^2_{\mathbf{i}u} - \frac{1}{2g^2} \sum_{\square} \left( \hat{U}_{\square} + \hat{U}^{\dagger}_{\square} \right). \tag{4.16}$$

Compact QED has magnetic monopoles interacting with photons and these excitations are responsible for the confinement of electric charge [147]. In (3+1)-dimensions, the compact QED pure gauge theory is conjectured to have a Coulomb phase at weak coupling $g$ [148] and to be confining at strong coupling, while the two regions are separated by a first order phase transition [131, 132]. In (2+1)-dimensions, the electromagnetic potential between point charges scales as $\ln(r)^{-1}$ instead of $r^{-1}$; because of associated non-perturbative effects, the confinement property is found at all lattice couplings [138, 149]. In particular, the confinement mechanism in (2+1)-dimensional cQED is more related to the confinement of quarks in QCD as both of them are topological effects. Confinement at any coupling strength is also the case for (1+1)-dimensions, in which the model is exactly solvable and has no dependence on the coupling constant $g$ [138]. This was shown in the continuum by Schwinger (for the massless case), and by Banks, Susskind and Kogut in the lattice compact case (see [138] and references therein); numerically, this was confirmed more recently through simulations with Tensor Networks [150–153]. Therefore, a first objective could be the observation of electric flux tubes stretching between two confined charges and their dynamics, in both one- and two-dimensions.

### 4.2.1 Truncated Kogut-Susskind Hamiltonian

The limitation faced by the Kogut-Susskind Hamiltonian regarding quantum simulation resides in the gauge field. Since the U(1) group space is a continuous manifold, in both Wilson and Kogut-Susskind LGTs the local link Hilbert space is infinite-dimensional. This poses a severe challenge towards quantum simulation, since only a discrete and finite number $d_{\text{gf}}$ of atomic states is available to encode quantum information.

#### Quantum Link Model and Schwinger-Weyl QED

Two approaches are possible to reconcile the manifolds mismatch. The one approach, proper of the Quantum Link Model, is nailed on a minimal coupling prescription preserving the U(1) invariance of local transformations [140]. This means, in QLMs one demands the commutation relations in Eq. (4.6) between $\hat{E}_{\mathbf{i}u}$ and $\hat{U}_{\mathbf{j}v}$ or $\hat{U}^{\dagger}_{\mathbf{j}v}$ to be satisfied [148]. In finite dimensions, this comes at the cost of sacrificing the unitarity of the parallel transporter $\hat{U}_{\mathbf{i}u}$:

$$[\hat{U}_{\mathbf{i}u}, \hat{U}^{\dagger}_{\mathbf{i}u}] \neq 0. \tag{4.17}$$

Although the absence of a unitary gauge operator impacts on the structure of the hopping term, it does not compromise the gauge invariance of the Hamiltonian, for which the commutation relations in Eq. (4.6) are the necessary and sufficient condition.

The other approach is based on the discrete Schwinger–Weyl group [154], in which the unitarity of the operator $\hat{U}_{\mathbf{i}u}$ is guaranteed by the cyclic permutation property:

$$\hat{U}_{\mathbf{i}u} \left|\phi_n\right\rangle = \left|\phi_1\right\rangle . \tag{4.18}$$

The conjugate operator $\hat{E}_{\mathbf{i}u}$ possesses the cyclic property too in the gauge operator eigenbasis. The sets of operators

$$\{\hat{U}^k_{\mathbf{i}u}\}_{1\leq k\leq n}, \qquad \{\hat{E}^k_{\mathbf{i}u}\}_{1\leq k\leq n}, \tag{4.19}$$

are unitary representations of the group $\mathbb{Z}_n$. Like the QLM, a discrete LGT based on a $\mathbb{Z}_n$ gauge is relevant for its relation to the problem of confinement in QCD, it presents qualitative indications on phenomena like the electric flux string breaking and for large $d_{\mathrm{gf}}$ it tends asymptotically to the continuous theory. We will not adopt the Schwinger–Weyl theory in our work.

### Quantum Rotor Model and Spin-Gauge Hamiltonian

There exist different ways to realize in a lab a finite-dimensional parallel transporter $\hat{U}_{\mathbf{i}u}$ and a conjugate momentum $\hat{E}_{\mathbf{i}u}$ satisfying Eq. (4.6).

One way involves Bose-Einstein condensates in the limit $\hat{\delta}_N/N_0 \ll 1$ of small fluctuations over the mean number of atoms. In this limit it is valid the approximation to the quantum rotor model [155], under which the particle number operator can be expressed as the sum of a scalar and the fluctuation operator:

$$\hat{N} = N_0 + \hat{\delta}_N. \tag{4.20}$$

Associating the gauge vector with the BEC phase, $\hat{\phi}_{\mathbf{i}u} := \hat{\theta}$ and the electric field with the particle fluctuation, one can identify the phase-number relation of the condensates, $[\hat{N}, \hat{\theta}] = \mathrm{i}$, with the commutation rule of Eq. (4.5). The thermodynamic limit allows for the expansion of the creation and annihilation operators $\hat{b}^{(\dagger)}_{\mathbf{i}u}$, that gives:

$$\hat{U}_{\mathbf{i}u} := \hat{b}_{\mathbf{i}u} \simeq \sqrt{N_0} e^{\mathrm{i}\hat{\phi}_{\mathbf{i}u}}, \qquad \hat{E}_{\mathbf{i}u} := \hat{\delta}_N. \tag{4.21}$$

Because of the quantum rotor approximation, this method is suitable for the strong-coupling limit and slight deviations from that, but precludes the access to the weak-coupling regime. This first track was explored in early publications on the subject and was the hinge of a few experimental proposals [156, 157].

Another option is to represent the gauge operators with a SU(2) group algebra, supported by the set of quantum angular momentum (or spin) operators:

$$\hat{U}_{\mathbf{i}u} := \hat{L}^x_{\mathbf{i}u} + \mathrm{i}\hat{L}^y_{\mathbf{i}u} = \hat{L}^+_{\mathbf{i}u}, \qquad \hat{U}^\dagger_{\mathbf{i}u} := \hat{L}^-_{\mathbf{i}u}, \qquad \hat{E}_{\mathbf{i}u} := \hat{L}^z_{\mathbf{i}u}. \tag{4.22}$$

There are two drawbacks in using the SU(2) algebra. First, as mentioned above, while the local invariance is protected by the commutation relations (4.6), the unitary structure of the parallel transporter is lost

$$[\hat{U}_{\mathbf{i}u}, \hat{U}^\dagger_{\mathbf{i}u}] = 2\hat{E}_{\mathbf{i}u} \neq 0. \tag{4.23}$$

Second, the parallel transporters are represented by the raising and lowering ladder operators, accompanied by inhomogeneous state-dependent coefficients,

$$\hat{L}^{\pm}_{\mathbf{i}u} \, |l, m\rangle = \sqrt{l(l+1) - m(m \pm 1)} \, |l, m \pm 1\rangle \,, \tag{4.24}$$

which should be identical instead: $\mathrm{e}^{\pm \mathrm{i}\hat{\varphi}_{\mathbf{i}u}} \, |m\rangle = |m \pm 1\rangle$. Owing to this, the encoding through angular momenta does not exactly generate a QLM of the Kogut-Susskind model; rather, it realizes a model which has the same truncated Hilbert space dimension $d_{\mathrm{gf}}$, an equidistant spectrum of the electric field operator but an inhomogeneous parallel transporter operator. However, as remarked in [148], in the limit $l \gg 1$, the spectrum of the parallel transporter tends to be equally spaced in the range $|m| \ll l$ and the commutation relation (4.17) tends to 0, thus regaining the Kogut-Susskind Hamiltonian. On a side note, though asymptotically unitary, $\hat{U}_{\mathbf{i}u}$ in QLMs remains distinct from the unitary operator of the Schwinger–Weyl $\mathbb{Z}_n$ theory, characterized by the cyclic property of Eq. (4.18).

This second route based on the SU(2) algebra has taken hold in the community, where it is generally preferred over the quantum rotor model scheme and is at the root of a number of experimental proposals [158–161]. Most of these proposals, especially those focusing on the large-$d_{\mathrm{gf}}$ limit, do not actually consider fundamental angular momentum atomic states, since that does not offer a large enough Hilbert space. Concretely, to accomplish the SU(2) representation, one rather turns to a Schwinger boson representation, which is virtually capped only by the number of atoms that the experimentalists can load on a lattice link. The Schwinger bosons allow for an exact map between the creation and annihilation operators of a two-species ($a$ and $b$) Bose gas and the set of angular momentum operators:

$$\hat{L}^{+}_{\mathrm{Sb}} := \hat{a}^{\dagger}\hat{b}, \qquad \hat{L}^{z}_{\mathrm{Sb}} := \frac{1}{2}\left(\hat{n}_a - \hat{n}_b\right), \qquad l = \frac{1}{2}\left(\hat{n}_a + \hat{n}_b\right). \tag{4.25}$$

These mapped operators correctly reproduce the ladder operator coefficients and thus suffer from the same associated issues. Note that, in the limit $l \gg 1$, corresponding to $N_0 \gg 1$, the Schwinger bosons tend to form a BEC. Thus, one can approximate

$$\hat{n}_a \approx \sqrt{\frac{N_0}{2}} e^{\mathrm{i}\hat{\theta}}, \qquad \frac{1}{\sqrt{l(l+1)}} \hat{\psi}^{\dagger}_{\mathbf{i}} \hat{a}^{\dagger}_{\mathbf{i}u} \hat{b}_{\mathbf{i}u} \hat{\psi}_{\mathbf{i}+\mathbf{u}} \approx \hat{\psi}^{\dagger}_{\mathbf{i}} e^{\mathrm{i}\hat{\theta}} \hat{\psi}_{\mathbf{i}+\mathbf{u}}, \tag{4.26}$$

and regain the approximation to the quantum rotor model, Eq. (4.21).

Let us consider now the massless, pure gauge Hamiltonian $\hat{H}_{\mathrm{gauge}}$ of Eq. (4.16), which represents a simpler starting point than the Kogut-Susskind model. In the gauge model the masses are pinpointed and their distribution is reflected on the charges of the Gauss' law. Imaging to introduce two particles apart from one another, one can observe confinement in the form of tube fluxes connecting these charges. Due to the inhomogeneity of the coefficients in Eq. (4.24), the pare-gauge Hamiltonian $\hat{H}_{\mathrm{gauge}}$ is distinct from its truncated QLM counterpart, which takes the name of *spin-gauge* model. The two models are exactly reconciled at $d_{\mathrm{gf}}$=2 (total spin $S$=½) which is of interest on itself for its relevance in the context of condensed matter physics (see the next Section 4.2.1). Because the electric field in this limit can only take two values, such models are unable to manifest the presence of electric flux tubes but rather of different type of oriented strings. For the flux tubes, one has to upgrade at least to spin-1, which is an approximation of the pure gauge model with

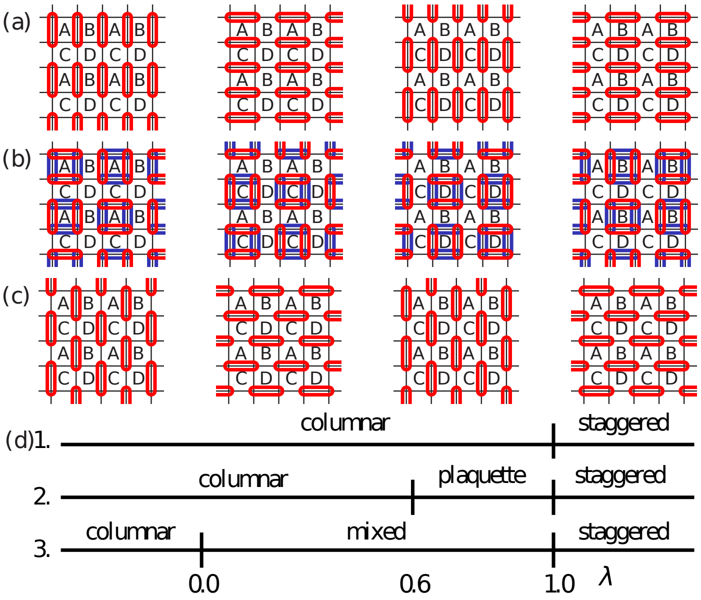

FIGURE 4.2: Columnar, plaquette and staggered order. In (d), results with different numerical methods and lattice sizes show competing scenarios, (d)1 being the latest and most accurate clue available. Figure from Banerjee *et al.* [162].

accuracy to first order (see Supplemental Material of [158]).

### Spin-½ QLM in condensed matter physics

The QLM belongs to the class of lattice models with a gauge symmetry. The notion of lattice gauge theories extends and finds application beyond the context of high-energy physics. Solid state materials naturally have discrete spatial coordinates and their properties may depend on inherent symmetry transformations. Abelian U(1) lattice gauge theories are used to describe different condensed matter systems. The intrinsic $\mathbb{Z}_2$ lattice gauge theory of Kitaev's toric code is relevant in quantum information theory.

The minimal dimension of the link space in QLMs is $d_{\text{gf}}$=2, with total spin $S$=½. This model may seem unnatural from a particle physics perspective, as it maximally constrains the gauge field Hilbert space and does not allow for a null electric field. However, in (1+1)-d it resembles the Schwinger model with non-zero vacuum angle [163]. In (2+1)-d, the model has been proposed as an effective theory for the pseudogap phase of high-temperature superconductors [139], for its analogy to spin ½ frustrated magnets [145]. When $S$=½, the plaquette term (4.13) reduces to the so-called *ring-exchange* operator $\hat{U}_{\text{RE}}$, which inverts the chirality of flippable plaquettes (those in which all spins are aligned either clock- or counterclock-wise) and annihilates the others,

$$\hat{U}_{\text{RE}} := \hat{U}_{\square} + \hat{U}^{\dagger}_{\square}. \tag{4.27}$$

The ring-exchange operator applied twice is known as *Rokhsar-Kivelson* (RK) term and represents a density operator for flippable plaquettes [164]:

$$\hat{U}_{\text{RK}} := (\hat{U}_{\square} + \hat{U}^{\dagger}_{\square})^2. \tag{4.28}$$

**Square Ice and Quantum Dimer models** The massless (2+1)-d U(1) QLM composed of a ring-exchange and the Rokhsar-Kivelson term,

$$\hat{H}_{\mathrm{RK}} = -J \sum_{\square} \left[ \hat{U}_{\square} + \hat{U}_{\square}^{\dagger} - \lambda \left( \hat{U}_{\square} + \hat{U}_{\square}^{\dagger} \right)^2 \right] . \tag{4.29}$$

has been investigated in the context of quantum spin liquids, where it is known as the Square Ice model (SIM).

The first terms act on flippable plaquettes $\square_F$ inverting their chirality and annihilating the non-flippable ones. The other term is a chemical potential, which determines the amount of flippable plaquettes $\square_F$ as a function of the parameter $\lambda$. For large $\lambda < 0$, the presence of $\square_F$ is favoured. The spins take a Neél-like order: neighbouring spins tend to counter-align in on order to maximize the number of adjacent plaquettes with opposite vorticity. For large $\lambda > 0$, columns of aligned spins are favoured which minimizes the RK chemical potential: in the limit of all spins aligned in one direction, on each axis, no flippable plaquette exists. The charges in the square ice model are fixed but can span the set $\{0, \pm 1, \pm 2\}$, whereas in cQED QLM the charges are dynamical but the physical states can only have charges $\{0, \pm 1\}$. The two regions are separated by a Resonating Valence Bond Solid phase [165], which spans from a critical (negative) $\lambda_c$ and runs up to the RK-point $\lambda_{RK} = 1$.

The Quantum Dimer Model (QDM) on a frustrated pyrochlore lattice [162, 166–168] results from the ½ QLM by setting a staggered charge pattern ±1 [132]. For $\lambda > 1$, the dimers are arranged in a staggered configuration. For $\lambda < 1$, the QDM has a confining phase. A columnar valence bond solid phase spans the whole region of negative $\lambda$. The details of the central region are unclear. It has been long discusses whether in the region $0 < \lambda < 1$ the phase shares characteristics of both the columnar and the plaquette phases - see Fig. 4.2 - or rather there is a clear boundary between the two. A recently devised, efficient Monte Carlo algorithm for the QDM has instead showed the predominance of a columnar phase all the way until the RK-point [162]. In any case, the two phases in the large $\lambda$ limit are similar in the SIM and the QDM. We will see in the next Chapter how they relate to the cQED QLM.

All these arguments make the spin-½ cQED Quantum Link Model fascinating and important. The investigation of this model is particularly relevant since it returns transferable theoretical knowledge as well as technical and general know-how concerning the analogue quantum simulation of such a class of model Hamiltonians. A direct experimental realization could be relevant to many areas of both condensed-matter and high-energy physics.

## 4.3 QLMs numerical analysis and quantum simulation

The past decade has seen a thrive of research on Abelian and non-Abelian QLMs, with the prospect of quantum simulation.

Numerical analyses anticipated the experimental realizations by studying the ground state properties and real time dynamics of lower-dimensional QLMs. From this point of view, one can roughly categorize the literature under two main areas based on the dimension of the Hilbert space on the gauge field. At $d_{\mathrm{gf}} \sim \mathcal{O}(1)$, MPS algorithms are suitable; using those, it was shown that, in (1+1)-d, QLMs with small $d_{\mathrm{gf}}$ converge quickly to the KS model, yielding thorough results regarding the ground state properties and a good qualitative picture of the dynamics. Arguably, in order to properly capture the real-time dynamics, it is necessary to explore the opposite limit, $d_{\mathrm{gf}} \to \infty$. For Hilbert space dimensions at which MPS algorithms inevitably fail, Functional Integrals represents a viable and fruitful alternative. Both methods are capable of solving the Kogut-Susskind Hamiltonian.

Various methods have been proposed to realize lattice gauge theories using ultracold gases, most of which are hinged on a few basic technical solutions. The simulation of plaquette terms in 2-D systems constitutes a crucial challenge. The difficulties towards the realization of a plaquette coupling, involving four distinct links and comprising the burden of the gauge-invariance character, makes of this a whole major topic on itself which we do not deal with in this work. We will rather focus and report on advances concerning the Schwinger model and 2-D systems not involving magnetic fields.

### 4.3.1 Experimental proposals

In order to implement the Schwinger model of Eq. (4.15) in cold gases, one mainly needs to achieve three goals:

- enforce the Gauss' law, either as a low-energy effective constraint or as a fundamental symmetry of the atomic and optical interactions;
- be equipped with a set of operators satisfying the commutation relations in Eq. (4.6) between $\hat{U}_{\mathbf{i}u}$ and $\hat{E}_{\mathbf{i}u}$;
- engineer a conjugate mass-gauge field dynamic term $\hat{\psi}^{\dagger}_{\mathbf{i}}\hat{U}_{\mathbf{i}u}\hat{\psi}_{\mathbf{i}+\mathbf{u}}$.

Generally, this is accomplished having at disposal particle creation and annihilation operators; there are different ways do that, either in the QLMs or in the context of $\mathbb{Z}_N$ gauges, both potentially connecting to the continuous limit U(1) for large $d_{\mathrm{gf}}$. We recap them in this Section.

#### Gauge invariance in the low-energy sector

A seminal proposal by Zohar et al. [158] envisaged the realization of a spin-gauge Hamiltonian using interacting single atoms with three internal levels, which play the role of the angular momentum multiplet. The work is a generalization of another method [169], in which a spin-1 model was encoded in the occupation number of a Bose gas. The Hamiltonian consists of a main term $H_G$ that sets the largest energy scale in the system and two smaller ones $H_E$ and $H_R$. $H_G$ enforces the Gauss' law in its ground sector: non-gauge invariant states do not belong in the kernel of $H_G$ and have very large energy, so they are not populated over the time scale of the experiment. The other terms realize the spin-gauge Hamiltonian to different orders of perturbation. The generalization to spin larger than one is also discussed, which requires some technical modifications. The group calculated the ground-state energy on a single elementary plaquette with two opposite charges, for which the exact result as a function of the coupling $g$ is known. The main numerical result shows the rapid convergence of the spin-gauge and the tKS model for $g < 1$ to the exact solution, with fairly small $d_{\mathrm{gf}}$.

A follow-up proposal by the same group extends the previous work to include dynamical Dirac fermions [159]. The scheme involves two fermionic species with different hyperfine levels, arranged to serve for specific angular momentum transfer; the gauge operators are realized with a SU(2) Schwinger algebra. The Gauss' law constraint is again implemented by a Hamiltonian term with the highest energy scale. The coupled hopping requires a fine-tuning of Feshbach resonances in order to eliminate unwanted quadratic contributions.

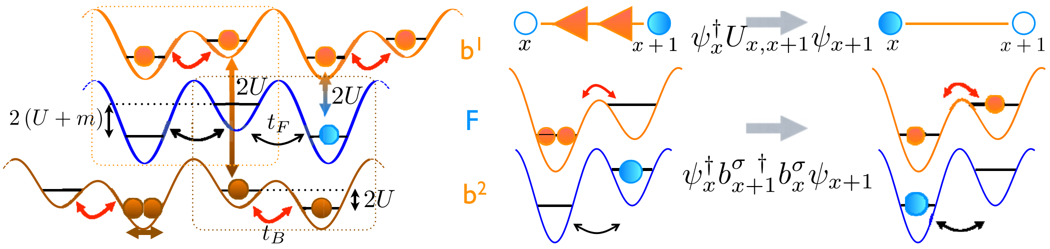
$b^1$
F
$b^2$
$2(U+m)$
$2U$
$2U$
$2U$
$t_F$
$t_B$
$x$
$x+1$
$\psi_x^\dagger U_{x,x+1}\psi_{x+1}$
$x$
$x+1$
$\psi_x^\dagger b^{\sigma\,\dagger}_{x+1} b^\sigma_x \psi_{x+1}$

FIGURE 4.3: Spin-1 cQED QLM. Left side: sketch of the optical super-lattices for one fermionic and two bosonic species. Bosons are bound to hop between two neighbouring sites. A fermion hopping to the left picks up the energy offset 2U from a boson, which simultaneously tunnels to the right. Right side: a correlated hopping between the fermions and the Schwinger bosons. Figure from Banerjee *et al.* [163].

Banerjee and collaborators [163] presented an implementation of the 1-D cQED QLM with an analogous scheme: gauge invariance imposed with a Gauss term in low-energy sector and SU(2) Schwinger algebra. Their focus was rather on the limit $d_{\mathrm{gf}} \sim \mathcal{O}(1)$, with spin-½ and spin-1. A two-species Bose gas is arranged on a stack of staggered super-lattices that presents isolated double wells, as in Figure 4.3; each pair is associated to one gauge link and each lattice host different species. The gauge-invariance can be easily enforced on the initial state, by starting out with a deep Mott pure state. The super-lattice energy offset prevents direct hopping. The gauge-invariant dynamics is driven by energy conservation and determined by second-order virtual hopping process, analogously to the super-exchange interactions [170]. The locality of the combined hopping processes, restrained by the wave-functions overlap, prevents unwanted processes to occur and break the gauge symmetry. The construction works in principle also in higher dimensions, although it lacks the ring-exchange, the magnetic term - or, as one may argue, the model describes the strong-coupling limit in which the amplitude of the magnetic term vanishes.

In general, these schemes are tortuous and ill-fated by the undesirable low-energy gauge invariance, which requires to devise the model Hamiltonian as a higher-order perturbation and may entail very weak effective interactions and eventual loss of invariance.

### Gauss law as a fundamental constraint

A conceptually more solid method, again by Zohar and co-workers [157], introduced an element of novelty regarding the enforcement of the Gauss' law. Two species of bosons $a$ and $b$ with different hyperfine angular momenta, separated by $\delta m_F$, are loaded on the links. The bosons realize a SU(2) algebra as described in Eq. (4.25); the number of bosons per link is conserved, since the deep lattice for the Bose gases tightens the Wannier functions and prevents overlaps between neighbouring links, as illustrated in Figure 4.4 (a). Two bipartite super-lattices with a large offset host the mass field. Each super-lattice traps one of the two fermionic species, $c$ and $d$, which have different hyperfine states Zeeman-tuned to match $\delta m_F$. The super-lattices are such that the deep minima of $c$ correspond to the shallow minima of $d$, which energetically forbids uncorrelated hopping processes over the time scales of the experiment. Assuming that the initial state obeys the Gauss' law, spin-changing collisions protect the U(1) symmetry by driving the hopping through gauge-invariant channels: a fermion $c$ tunnels to a neighbouring site and changes hyperfine state

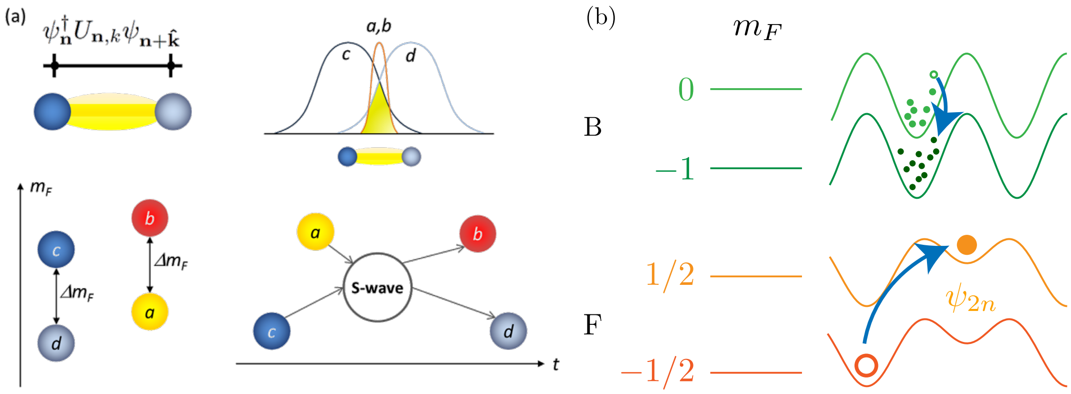

FIGURE 4.4: Gauge invariance enforced by angular momentum conservation. Starting with a symmetric state and taking advantage of angular momentum conservation, the dynamics is selectively driven to explore exclusively gauge-invariant states. Description in the text, Panel (a) from Zohar *et al.* [138], Panel (b) from Kasper *et al.* [161].

to $d$ while the angular momentum is conserved as a boson $a$ switches to $b$. Therefore, the angular momentum conservation plays the role of a gauge-invariance constraint, given by the fundamental atomic rules. Furthermore, the parallel transporter emerges naturally with an inverse dependence on the total angular momentum $l$,

$$\hat{U}_{\mathbf{i}u} = \frac{L^{\pm}}{\sqrt{l(l+1)}}_{\mathbf{i}u} \tag{4.30}$$

which normalizes the coefficients of the ladder operator and reconciles with the Kogut-Susskind Hamiltonian in the limit of large $l$:

$$\frac{L^{\pm}}{\sqrt{l(l+1)}}_{\mathbf{i}u} |l,m\rangle = \sqrt{1 - \frac{m(m \pm 1)}{l(l+1)}}\, |l, m \pm 1\rangle \underset{l \to \infty}{\to} |l, m \pm 1\rangle \tag{4.31}$$

Analogous proposals are based on the principle of gauge-invariant spin-collisions. The recent one by Kasper *et al.* [160, 161], illustrated in Figure 4.4 (b), differs in the addition of the energy conservation constraint on the allowed hopping processes. If in [157] the tunnelling of a fermion without spin-exchange was prevented by the super-lattice energy offset, here the quantum of energy is provided by a boson that, changing hyperfine state, hops to a Zeeman-tuned level with lower energy.

A scheme for $\mathbb{Z}_n$ discrete LGTs [154] has been proposed too: it requires the realization of a ring-shaped optical trap for the gauge fields, which would attain cyclic permutations of the state in real space.

### 4.3.2 Numerical studies

#### QLM with $d_{\mathrm{gf}} \gg 1$, Functional Integral

In 1-D, the Kogut-Susskind Hamiltonian can be studied with Functional Integral techniques, which allow to investigate the real-time dynamics of pair production and string-breaking (see [160] and References therein). Kasper *et al.* [160] used FI to study the Schwinger model and the corresponding QLM in the regime of large $d_{\mathrm{gf}}$, which is numerically inaccessible with tensor network methods. The work is

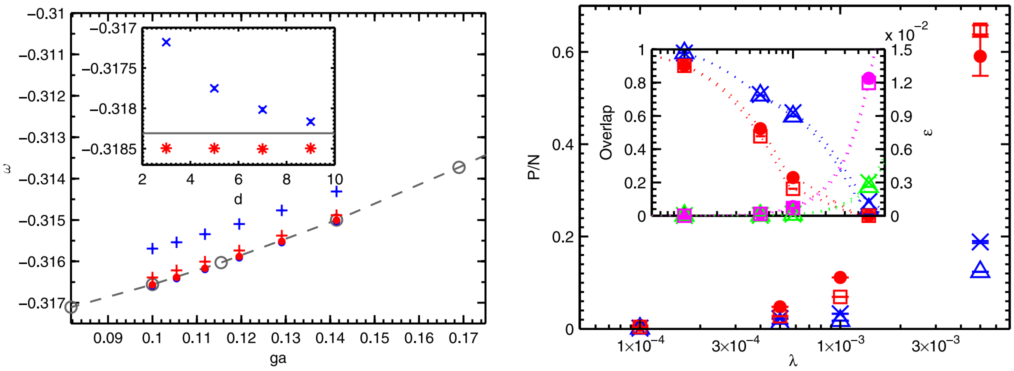

FIGURE 4.5: 1-D cQED QLM. Left panel: energy density for various values of $x = 1/(ga)^2$, Crosses show the values for $d_{\text{gf}}$=3 (blue) and $d_{\text{gf}}$=9 (red). Circles show the values for the $\mathbb{Z}_2$ model. Values obtained for the Schwinger model are shown in gray. Inset: extrapolation for $x \to \infty$, QLM (blue) and $\mathbb{Z}_2$ (red). Right panel: penalty energy at the end of the noisy adiabatic preparation as a function of the noise strength, for different chain length and $d_{\text{gf}}$. Inset: overlap and relative error in energy with respect to the noise-free exact ground state. Figures from Kühn *et al.* [151].

a benchmark for quantum simulation experiments, as it estimates the physical parameters required to capture essential features of strong-field QED and to describe the cQED phenomenon of pair production in a cold atoms simulator, thus setting a lower edge on $d_{\text{gf}}$. The pair production can be revealed by observing the time evolution of the correlations in the mass field; for a chain of length $L = 512$, whilst at $d_{\text{gf}} = 2500$ the two curves considerably deviate, at $d_{\text{gf}} = 5000$ the gap becomes small.

### QLM with $d_{\text{gf}} \sim \mathcal{O}(1)$, Tensor Networks

Using the Jordan-Wigner transformation, the Kogut-Susskind Hamiltonian can be mapped to a spin Hamiltonian [171]. The transformation associates particle creation operators to spin operators and the remaining gauge degrees of freedom are eliminated by the Gauss' law. In this form, the model is suitable for investigation with MPS algorithms. Adopting this approach, Bañuls *et al.* [150, 152] determined the ground state of the KS model and demonstrated the suitability of tensor network techniques for describing the thermal ground state and evolution of lattice gauge theories. Knowing the ground state in the KS limit allows to measure the accuracy of the cQED quantum link model. Kühn *et al.* examined the problem, comparing cQED QLMs (and $\mathbb{Z}_2$ theories as well) with different gauge space dimensions, from $d_{\text{gf}}$=3 to $d_{\text{gf}}$=9. As one can see on the left panel of Figure 4.5, the convergence to the KS limit is quite rapid ($\mathbb{Z}_2$ yields accurate results for any $d_{\text{gf}}$), and in the worst case ($d_{\text{gf}}$=3) the energy density has an error below 1%. This convergence backs and encourages the research towards experimental realizations with even limited link space dimension, since it suffices to attain quantitative results concerning the ground state properties (not the dynamics) of cQED. The adiabatic preparation of a gauge-invariant state with finite coupling was also simulated, with time dependent MPS methods. The evolution starts from the ground state at strong coupling, $x = 1/(ga)^2 = 0$ and brings the system to some finite final coupling $x_F$. To include possible sources of noise that cause deviation from the gauge invariant manifold, a perturbation of the gauge field $\lambda(\hat{L}^{+}_{\mathbf{i}u} + \hat{L}^{-}_{\mathbf{i}u})$ is included. Although the drastic violation of the Gauss law occurs already at small levels of noise, as in the right panel in Figure 4.5, the relative error in the energy stays below 2%; this means that quite accurate predictions for some ground-state observables can be attained despite the gauge invariance breaking.

Along this line, Rico and collaborators characterized the thermodynamical properties and phase diagram of the 1-D QLM with MPS methods, focussing on the spin-½ and the spin-1 links [172]. Interestingly, the model with half-integer link representation has the same physical properties as the model with integer link representation in a classical background electric $\hat{E}_{\mathbf{i}u} = \frac{1}{2}$.

The dynamics of the KS Hamiltonian and of the QLM has also been explored with tensor networks, with a spotlight on the process of string breaking, which also arises in QCD. In [163], the evolution of a S=1 QLM short chain initially in a fully-polarized $\langle \hat{E}_{\mathbf{i}u} \rangle = -1$ state was studied with exact diagonalization. For sufficiently small fermion mass, the string energy is converted into the mass of a dynamically created charge-anti-charge pair. In this process, the large negative electric flux $\langle \hat{E}_{\mathbf{i}u} \rangle$ of the string quickly relaxes to its vacuum value, illustrating the string breaking phenomenon. As one would expect by analogy with QCD, the large negative electric flux initially stored in the string quickly approaches its vacuum value. The non-equilibrium dynamics induced by a strong uniform electric field on the ground state was also studied by Buyens and coworkers [173] using TDVP and TEBD methods. More recently, Pichler *et al.* highlighted in a similar context the relation between string-breaking dynamics and the entanglement spreading in the system [153].

## 4.4 Conclusions

In this Chapter we have presented lattice gauge theories and their formulation with truncated gauge Hilbert spaces, focussing on QED. We outlined the main results of the theoretical research done in recent years, concerning the analogue quantum simulation and the numerical investigation of the model Hamiltonians.

A clear experimental routine, ready-to-go for the labs, has not been attained yet. On the large $d_{\mathrm{gf}}$ limit, the perspectives seem at the moment pretty bound to the employment of Bose gases. The opposite limit is perhaps a more convenient hunting ground. Numerical analyses with Tensor Network methods showed that the ground-state properties of the (1+1)-d cQED are well captured even by minimal link dimensions and that the real-time dynamics shows qualitatively correct behaviours. The (2+1)-dimensional QLM presents a wealth of intriguing physics. The confinement mechanism is intimately related to the confinement of quarks in QCD as both of them are topological effects. The spin-½ QLM is peculiar for it shares the same Hamiltonian with condensed matter systems such as the Square Ice and the Quantum Dimer Model.

A perspective on the numerical studies, from the point of view of Matrix Product States techniques, tells us that much has been done in (1+1)-d, both concerning the ground-state properties and the dynamics. These findings constitute a solid ground for successive developments, first in the direction of (1+1)-d non-Abelian LGTs but also towards the (2+1)-d Abelian cQED. In (2+1)-d LGTs, the numerical benchmarks are so far set by Monte Carlo sampling techniques; PEPS algorithms do not suffer from the sign problem and represent a promising candidate to outperform Monte Carlo methods, at least on the dynamics if not on variational searches yet. Although 2-D Tensor Network algorithms are not quite yet as full-fledged as DMRG is in one dimension, quasi-two-dimensional geometries - ladders or cylinders - are already well within reach of MPS methods. This is the direction of research that we pursued and led to the results that we illustrate in the next Chapter.

## Chapter 5

# Quantum link model on a ladder geometry

Motivated by the growing interest seen in recent years on Quantum Link Models, so far mostly studied in 1-D, we investigated the spin-½ compact QED QLM on the most elementary extension towards 2-D, i.e. on a ladder geometry. In two dimensions, the QLM with spin-½ presents analogies with solid state physics models. After analysing the two-leg ladder in open boundary conditions, we extended our study to multi-leg ladder, setting periodic boundary conditions on the long side to enquiry the system ground-state properties in the thermodynamic limit. In this chapter, we present our findings.

## 5.1 Introduction to the model

### 5.1.1 The Quantum Link Ladder model

We consider a quantum link model with spin-1/2 links on a ladder-type lattice (see Figures 5.1, 5.3). We call the model *Quantum Link Ladder* (QLL):

$$\begin{aligned}\hat{H}_{\mathrm{QLL}} =&\mu \sum_{i,j} (-1)^{i+j} n_{i,j} \\ &- J_x \sum_{i,j} \left( \Psi^{\dagger}_{i,j} \tilde{S}^{+}_{i,j;i+1,j} \Psi_{i+1,j} + \mathrm{H.c.} \right) \\ &- J_y \sum_{i} \left( \Psi^{\dagger}_{i,1} \tilde{S}^{+}_{i,0;i,1} \Psi_{i,0} + \mathrm{H.c.} \right) . \end{aligned} \tag{5.1}$$

Here, $\Psi_{i,j}$ are staggered fermionic operators at rung $i$ of leg $j = 0$ (upper) and $j = 1$ (lower), and $J_x$ ($J_y$) is the hopping along the legs (rungs) [135]. We define the A (B) sites as those with even (odd) $i + j$, which have positive (negative) mass $\mu$, such that one may interpret filled A sites as particles and empty B sites as anti-particles. The gauge field characterizing the bond between nearest-neighbouring sites, is represented for the Abelian case by a spin-$S$ operator [132]. We assume the simplest spin configuration on the links, $S = 1/2$; hence the field is described by spin-1/2 operators $\tilde{S}^{\pm}$. We consider the subset of physical states, namely those satisfying the Gauss' law. In terms of numerical computation, imposing the Gauss' law comes as a blessing, since the projection onto a subspace of the full Hilbert space considerably reduces the computational costs.

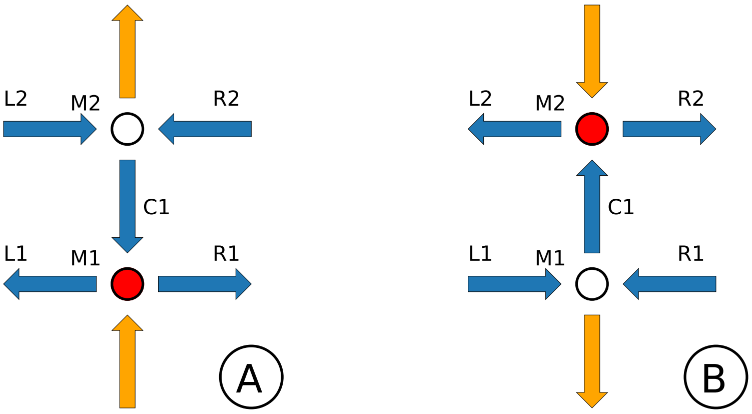

FIGURE 5.1: Legend of the graphical representation of a rung state. The masses are in the vacuum configuration (filled Dirac sea); the Gauss' law has $\epsilon_{M1\in A} = 0$ and $\epsilon_{M2\in A} = 1$ on Ⓐ, the opposite on Ⓑ. On the links, we denote ↓ (↑) and → (←) as spin +½ (-½). Orange arrows indicate the boundary conditions. See also Fig. 6.6.

### 5.1.2 Analysis of the one-dimensional QLM

In order to highlight the crucial differences between the QLM on a chain and on a ladder, we first review the best understood case of a 1-D QLM; for a detailed discussion of the 1-D QLM we invite the reader to follow Ref. [172]. We consider only states that obey a local gauge symmetry (Gauss' law),

$$\tilde{S}^z_{i,i+1} - \tilde{S}^z_{i-1,i} = n_i - \epsilon_i,$$

with $\epsilon_{i\in A} = 0$ and $\epsilon_{i\in B} = 1$. We can define the quantity $q_i = n_i - \epsilon_i$ the charge of the Gauss' law. In the cQED QLM, the vacuum state has charge $q_i =$. Positive charges $q_i = +1$ correspond to particles with positive mass; negative charges $q_i = -1$ represent positve-mass holes in the Dirac sea and is created destroying a particle in the negative-mass bipartition of the fermionic lattice. Particles-holes are always created in pairs, thus keeping the total amount of charges unvaried. In the large mass limit, $|\mu| \gg J_x$, we integrate out the particle motion, working for $\mu \to -\infty$ in the manifold in which the $A$ ($B$) sublattice is fully occupied (empty). In the 1-D QLM, the ground-state is uniquely determined by the Gauss' law, being a zero net flux (Z) phase, in which filled $A$ (empty $B$) sites are accompanied by outgoing (incoming) spins,

$$|0\rangle_A \equiv |\leftarrow 1 \rightarrow\rangle$$
$$|0\rangle_B \equiv |\rightarrow 0 \leftarrow\rangle$$

where we employ the spin notation introduced in Figure 5.1. For finite $\mu/J_x$, the Z phase presents defects:

$$\begin{aligned}
|+'\rangle_B &= |\leftarrow 1 \leftarrow\rangle \\
|-'\rangle_B &= |\rightarrow 1 \rightarrow\rangle \\
|-'\rangle_A &= |\leftarrow 0 \leftarrow\rangle \\
|+'\rangle_A &= |\rightarrow 0 \rightarrow\rangle.
\end{aligned}$$

The notation introduced here describes the local Hilbert space configurations, analogue to a rishon formulation of the quantum link model [167, 174]. We define the magnetization for a site $i$ as

$$S_i^z = (-1)^i (\tilde{S}^z_{i-1,i} + \tilde{S}^z_{i,i+1}), \tag{5.2}$$

and evaluate the parity order

$$\mathcal{O}_P^2 = \lim_{|k-j|\to\infty} e^{i\pi \sum_{k<l<j} S_l^z}, \tag{5.3}$$

and string order

$$\mathcal{O}_S^2 = \lim_{|k-j|\to\infty} S_k^z e^{i\pi \sum_{k<l<j} S_l^z} S_j^z. \tag{5.4}$$

Notice that the parity and the string order have a natural definition only in 1-D. On a finite ladder, there is a finite but large set of strings on which one could calculate these quantities. We consider the action of these operators on individual legs, without considering those patterns that cross over the rungs. On both of the two legs, plotting these parameters as a function of $J_y$ yield the same curves. The same occurs on the external legs of three- and four-leg ladders, whereas on the bulk legs we will see different behaviours. The Gauss' law breaks the $\mathbb{Z}_2$ chiral symmetry [172], and hence the defects on top of the Z phase are strictly formed in $|-', +'\rangle_{i,i+1}$ unsplittable pairs. This selective pair creation induces $\mathcal{O}_P^2 \neq 0$ and $\mathcal{O}_S^2 \neq 0$ for any $\mu$ [62], precluding a Haldane-like phase which would have $\mathcal{O}_P^2 = 0$ and $\mathcal{O}_S^2 \neq 0$. At $\mu/J_x \simeq 0.45$ there is an Ising-like phase transition into the non-zero flux phase [172]. This phase, which for $\mu \to \infty$ is a Néel-like state of $|\pm'\rangle$ defects, also presents $\mathcal{O}_P^2, \mathcal{O}_S^2 \neq 0$.

Figure 5.2 depicts $\mathcal{O}_P^2$ and $\mathcal{O}_S^2$ evaluated using infinite time evolving block decimation (iTEBD) simulations [106]. At $\mu/J_x \simeq 0.45$ a phase transition separates the Z and the NZ phase. The NZ phase exhibits at any $\mu$ a finite magnetization $S_L = \frac{1}{L}\sum_i |\langle S^z_{i,i+1}\rangle|$. In both phases $\mathcal{O}_P^2$, $\mathcal{O}_S^2 \neq 0$ due to the explicitly broken chiral symmetry.

## 5.2 Analysis of the quantum link ladder model

As for the 1-D QLM, in the QLL we are only interested in states that obey Gauss' law:

$$\tilde{S}^z_{i,j;i+1,j} - \tilde{S}^z_{i-1,j;i,j} + \tilde{S}^z_{i,j;i,j+1} - \tilde{S}^z_{i,j-1;i,j} = n_{i,j} - \epsilon_{i,j}, \tag{5.5}$$

with $\epsilon_{i,j\in A} = 0$ and $\epsilon_{i,j\in B} = 1$. Note that, the orientation of the virtual spins placed outside the ladder (in orange in Figs. 5.3) remains fixed, resulting in boundary conditions for the possible physical QLL states. We consider below $\mu < 0$, but, contrary to 1-D, the spatial mirror symmetry of the ladder-like lattice results in an identical ground-state phase diagram for $\mu > 0$.

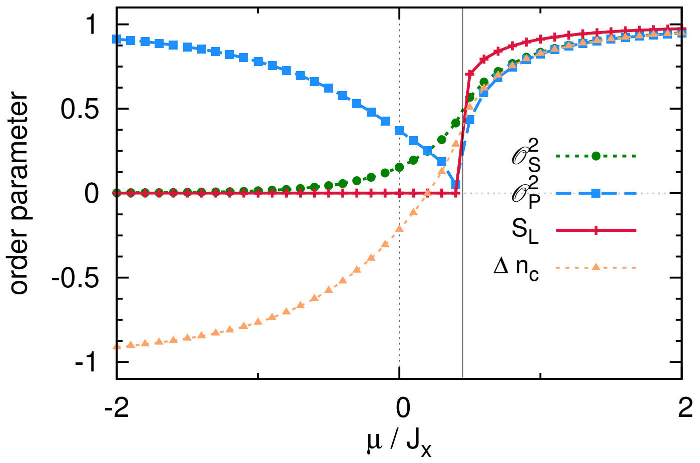

FIGURE 5.2: Ground-state order parameters for the 1-D QLM as a function of $\mu/J_x$. The results were obtained using iTEBD with 100 states. The solid vertical line marks the phase transition from the Z ($\mu < \mu_c \sim 0.45 J_x$) to the NZ phase ($\mu > \mu_c$).

### Large mass limit

Albeit in the 1-D quantum link model the Gauss' law fixes a unique ground-state for large $|\mu|$, this is not the case in the quantum ladder model. For concreteness, in the following we consider the limit $\mu \to -\infty$. In this limit, the particles are pinned at $A$ sites. The complete degeneracy of the space of spin configurations is lifted due to virtual fluctuations of the particles to adjacent lattice sites. We assume that for all virtual processes, Gauss' law is conserved exactly. We introduce a set of local states of spin configurations on the ladder legs, for $A$ sites:

$$\begin{aligned}
|0\rangle_A &\equiv |\leftarrow 1 \rightarrow\rangle, \\
|+\rangle_A &\equiv |\leftarrow 1 \leftarrow\rangle, \\
|-\rangle_A &\equiv |\rightarrow 1 \rightarrow\rangle.
\end{aligned}$$

Note that, due to the Gauss' law and the boundary conditions, the rung spin is fixed once the left and right spins are chosen. Similarly only three $B$ states are possible:

$$\begin{aligned}
|0\rangle_B &\equiv |\rightarrow 0 \leftarrow\rangle, \\
|+\rangle_B &\equiv |\rightarrow 0 \rightarrow\rangle, \\
|-\rangle_B &\equiv |\leftarrow 0 \leftarrow\rangle.
\end{aligned}$$

Analogously to the so-called rishon formulation of the QLM [167] we redundantly keep left and right spins, such that left and right spins of adjacent sites have to coincide in order to form a physical state. Due to the choice of staggered boundary conditions on a given rung, the only allowed configurations are

$$|\phi_0\rangle = \left| \begin{array}{c} 0 \\ 0 \end{array} \right\rangle, \qquad |\phi_+\rangle = \left| \begin{array}{c} + \\ + \end{array} \right\rangle, \qquad |\phi_-\rangle = \left| \begin{array}{c} - \\ - \end{array} \right\rangle.$$

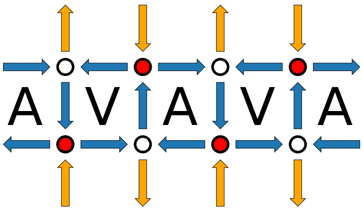

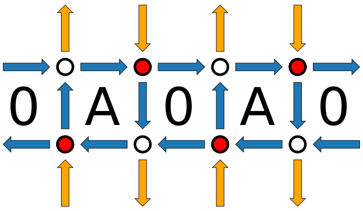

FIGURE 5.3: Ground state of the QLL for large mass $\mu \gg J_y/J_x$ with (a) $J_y/J_x = 0.2$ (VA phase) and (b) 1.8 (degenerate V0/A0 phase). The matter field is in the vacuum configuration: the particles occupy the bipartition corresponding to a filled Dirac see without charges. V (A) denote (anti)vortex-like spin configurations. In the SPT phase (not shown) the local spin expectations vanish and the fermions are evenly distributed.

and

$$|\phi_\pm\rangle = \left| \begin{matrix} + \\ - \end{matrix} \right\rangle , \qquad |\phi_\mp\rangle = \left| \begin{matrix} - \\ + \end{matrix} \right\rangle .$$

For a graphical representation of the spin-like states, see Fig. 5.4 (a). Hereafter we neglect the A and B indices. Obviously not all sequences of rung states $|\cdots \phi_\nu, \phi_{\nu'} \cdots\rangle$ are possible, as the spin orientations of adjacent states must coincide. The only allowed states are of the form $\{|\cdots \phi_\nu, \phi_{\nu'} \cdots\rangle\}$ with $\nu, \nu' \in \{0, +, -\}$ and

$$\begin{aligned} \text{if } \nu = 0 &\Rightarrow \nu' = 0 \text{ or } + , \\ \text{if } \nu = + &\Rightarrow \nu' = - , \\ \text{if } \nu = - &\Rightarrow \nu' = 0 \text{ or } + . \end{aligned}$$

In addition to this manifold of states one has the two states

$$|\cdots \phi_\pm, \phi_\pm \cdots\rangle$$

and

$$|\cdots \phi_\mp, \phi_\mp \cdots\rangle .$$

In the lowest order $J_x^2/2|\mu|$ and $J_y^2/2|\mu|$ particles virtually tunnel from A sites to the neighboring B sites and back as indicated in Fig. 5.4 (a). Hence, we find an energy $-2J_x^2/2|\mu|$ for each $|\phi_0\rangle$ and $-(J_x^2 + J_y^2)/2|\mu|$ for all other states. Here we already see, that a small $J_y < J_x$ energetically favours the VA state as a ground state, which corresponds to the trivial state $|\cdots \phi_0, \phi_0, \phi_0 \cdots\rangle$. The degeneracy between the $|\phi_\pm\rangle$, $|\phi_\mp\rangle$ and the $|\phi_+\rangle$, $|\phi_-\rangle$ states is lifted within fourth order due to the ring-exchange process. As shown in Fig. 5.4 (b), this process goes with $J_x^2 J_y^2/(4|\mu|^3)$ and acts on the rung basis as

$$|\cdots \phi_+, \phi_- \cdots\rangle \leftrightarrow |\cdots \phi_0, \phi_0 \cdots\rangle .$$

If we restrict the description to the manifold of states which is connected through this ring-exchange process, we result in the following effective spin-1 Hamiltonian,

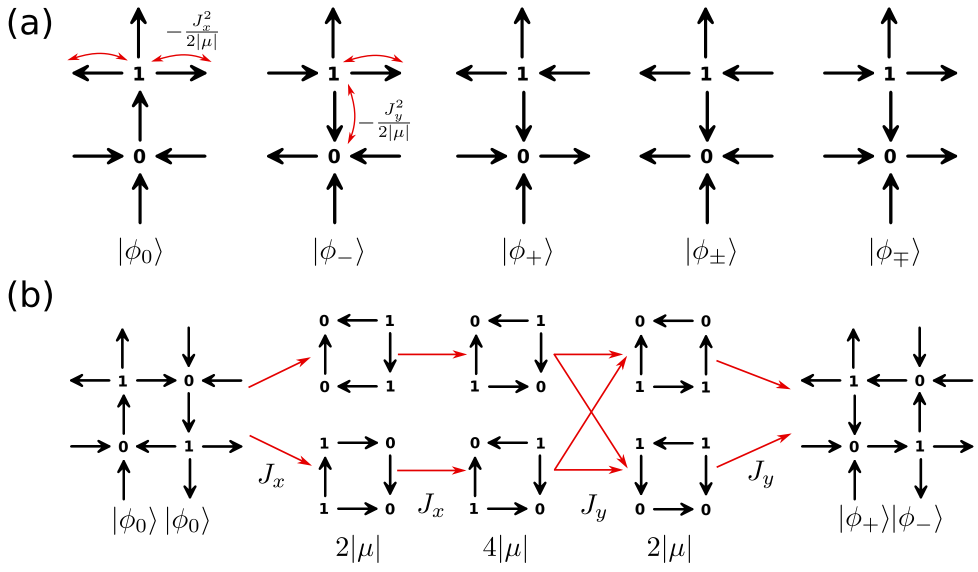

FIGURE 5.4: (a) The configurations of the local $\mu \to -\infty$ basis states $|\phi_0\rangle$,$|\phi_+\rangle$,$|\phi_-\rangle$,$|\phi_\pm\rangle$ and $|\phi_\mp\rangle$ on the even rungs. The configurations of the states on odd rungs are mirror symmetric to the given ones. The red arrows depict virtual second-order particle hopping processes along the legs and the rungs. (b) Fourth-order ring-exchange processes.

which determines the model up to order $J_{x,y}^4/\mu^3$:

$$H_{LM} = \sum_i \left\{ D(R_i^z)^2 + K\left[\left(R_i^+ R_{i+1}^-\right)\left(R_i^z R_{i+1}^z\right) + \text{H.c.}\right]\right\}. \tag{5.6}$$

Here we defined in rung $i$ the spin-1 operators $R_i^{\pm,z}$ in the basis $\{|\phi_0\rangle, |\phi_\pm\rangle\}$, with $D = (J_x^2 - J_y^2)/2\hbar^2|\mu|$, and $K = J_y^2 J_x^2/4\hbar^4|\mu|^3$ results from ring-exchange processes. For sufficiently large $D/K > 0$ (corresponding $J_y/J_x < 1$), the phase in which all rungs are in $|\phi_0\rangle$ is favored. This recalls the large-$D$ phase of spin-1 systems [175], or the Mott phase in Hubbard models. This phase corresponds to the vortex-antivortex (VA) configuration depicted in Figure 5.3(a). On the contrary, for large $D/K < 0$, a double-degenerate Néel-like phase $|\ldots\phi_+, \phi_-, \phi_+, \phi_- \ldots\rangle$ characterized by vortices separated by a plaquette without vorticity (V0) is the ground-state (Figure 5.3(b)), analogously to the density-wave phase found in extended Hubbard models. Crucially, the ring-exchange does not lead to a regular XY spin-exchange in Eq. (5.6), since due to the Gauss' law only processes $|\phi_0, \phi_0\rangle_{i,i+1} \leftrightarrow |\phi_-, \phi_+\rangle_{i,i+1}$ are allowed. As a result, whereas in the proximity of $D \simeq 0$ a Haldane phase is expected for the spin-1 XY model with single-ion anisotropy [175], we just observe for large $\mu$ a single second-order phase transition between the VA and the V0. As for the 1-D QLM we introduce for each leg the site magnetization

$$S_{i,j}^z = (-1)^{i+j}(\tilde{S}_{i-1,j;i,j}^z + \tilde{S}_{i,j;i+1,j}^z).$$

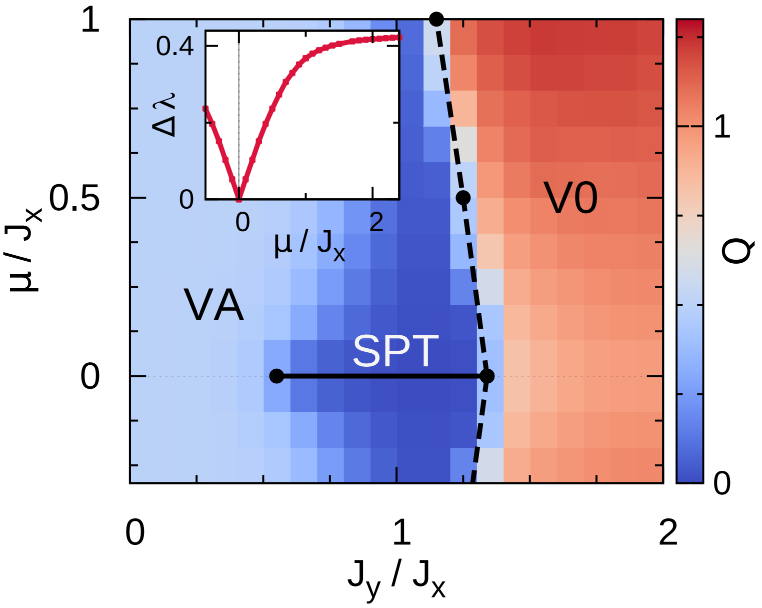

FIGURE 5.5: Phase diagram of the QLL as a function of $\mu/J_x$ and $J_y/J_x$ obtained with DMRG [112, 176] with up to 80 matrix states. The mirror symmetry of the ladder results in the same phase diagram for $\mu > 0$ and $\mu < 0$. For $\mu = 0$ a SPT phase is realized. The phase transition points (indicated by solid circles) are obtained keeping up to 800 Schmidt states. The inset shows the entanglement gap $\Delta\lambda$ as a function of $\mu/J_x$ for $J_y = J_x$.

Figure 5.5 depicts $Q = S_L + S_R$, where

$$S_L = \frac{1}{L}\sum_i |\langle S^z_{i,j}\rangle|$$

$$S_R = \frac{1}{L}\sum_i |\langle \tilde{S}^z_{i,0;i,1}\rangle|$$

characterizes respectively the leg and the rung spins and $L$ is the number of rungs. Note that, $Q = 1/2$ in the defect-free VA phase, whereas $Q = 3/2$ in the defect-free V0 phase. Hence the VA-V0 transition (dashed line) in the large-$\mu$ limit is characterized by an abrupt jump of $Q$.

### Finite mass region

For finite $\mu$, $Q$ significantly decreases within the VA phase when approaching the transition (deep blue region). This decrease is connected to the appearance of defects in the VA phase

$$|0'\rangle_A \equiv |\rightarrow 0 \leftarrow\rangle_A, \quad |0'\rangle_B \equiv |\leftarrow 1 \rightarrow\rangle_B, \quad |\pm'\rangle_A, \quad |\pm'\rangle_B. \tag{5.7}$$

From $S^z_{i,j}$, we evaluate the $\mathcal{O}^2_P$ and $\mathcal{O}^2_S$ along one of the two legs. Gauss' law induces $\mathcal{O}^2_S \neq 0$ for any $\mu$ and $J_y/J_x$. Contrary to 1-D, the ladder geometry permits the breaking along the leg of defect pairs created on top of the VA phase, and hence $\mathcal{O}^2_P$ may in principle vanish. However, we observe that $\mathcal{O}^2_P \neq 0$ for any $|\mu| > 0$. Hence, the VA (and V0) phase evolves adiabatically down to zero mass, undergoing

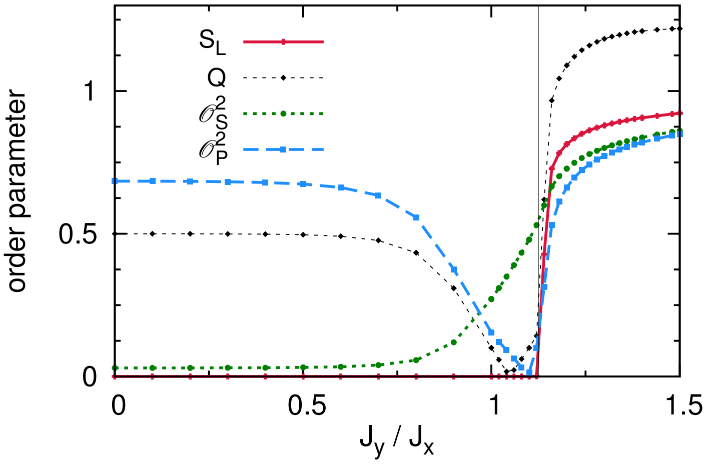

FIGURE 5.6: Cut for $\mu/J_x = 1$ of the phase diagram Fig. 5.5 as a function of $J_y/J_x$ (DMRG simulations with 100 states).

no phase transition. Figure 5.6 depicts the order parameters for a cut through the phase diagram of Fig. 5.5. We only observe one VA-to-V0 phase transition, marked by the abrupt growth of the leg magnetization $S_L$.

### Zero mass limit

The situation changes at zero mass where several local order parameters vanish, as shown in Figure 5.7. Examples are the local particle density imbalance between the sub-lattices $A$ and $B$

$$\Delta n_c = \sum_i (-1)^i \langle |\Psi_{i,0}^\dagger \Psi_{i,0} - \Psi_{i,1}^\dagger \Psi_{i,1}|\rangle,$$

and the entanglement gap

$$\Delta\lambda = \sum_i (-1)^i \lambda_i, \tag{5.8}$$

where $\lambda_i$ is the ordered sequence of Schmidt eigenvalues. Note that, the fact that $\Delta n_c \neq 0$ in the VA phase implies a spontaneous symmetry breaking of the sub-lattice inversion symmetry.

For $\mu = 0$ the parity order parameter $\mathcal{O}_P^2$ vanishes too, whereas $\mathcal{O}_S^2$ remains finite and only vanishes in the very limit of $|\mu| \to \infty$. This combined behaviour of $\mathcal{O}_P^2$ and $\mathcal{O}_S^2$ extends in an intermediate region at zero mass, around $J_y/J_x = 1$, where also all local order parameters that characterize the VA and V0 phases vanish, as shown in Figure 5.8 (a). This marks the onset of a symmetry-protected topological (SPT) phase. A confirmation of the topological character is provided by the doubly-degenerate entanglement spectrum in Figure 5.8 (b) [177, 178], occurring exclusively for $\mu = 0$. The inset of Figure 5.5 depicts the entanglement gap $\Delta\lambda$ as a function of $\mu/J_x$.

**Combined symmetry operations** A solid confirmation of the presence of a SPT phase can be obtained by identifying the symmetric transformations that protect the phase and verify numerically whether such rotations leave the state unaltered. As

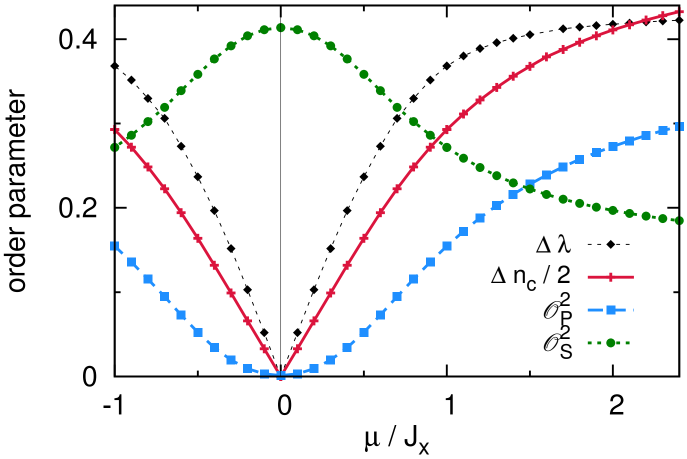

---

FIGURE 5.7: Cut through phase diagram Fig. 5.5 of the main text for $J_y = J_x$ as a function of the mass $\mu$. The ground state was obtained using DMRG, with $\chi = 100$ states. Only for $\mu = 0$ a SPT phase is realized and $\mathcal{O}_P^2$ vanishes while $\mathcal{O}_S^2$ remains finite. The mirror symmetry of the ladder results in a symmetry $\mu \leftrightarrow -\mu$ for the QLL.

in the spin-1 Heisenberg model, the SPT phase is protected by a $\mathbb{Z}_2 \times \mathbb{Z}_2$ symmetry given by the combined set of two orthogonal rotations [177–179]. We choose two transformations that leave $H_{\text{QLL}}$ invariant:

- ($\mathcal{C}$) particle-hole inversion at all sites, $\Psi_{i,j} \leftrightarrow \Psi^\dagger_{i,j}$ accompanied by a spin rotation $\sigma^x$ in all bonds, with $\sigma^{x,y,z}$ the Pauli matrices;
- ($\mathcal{R}$) $\Psi_{i,j} \to -\Psi_{i,j}$ for $(i,j) \in A$, and a rotation $\sigma^z$ in all bonds.

**Topological order parameter** We obtain the generalized topological order parameter $\mathcal{O}_T$ following the procedure of Ref. [179]. We used the DMRG method to obtain an infinite matrix-product state (iMPS) representation of the ground state of $H_{\text{QLL}}$ in canonical form:

$$|\Psi\rangle_{\alpha\beta} = \sum_{\sigma} \Gamma^{\sigma}_{\alpha\beta} \Lambda_{\beta\beta} |\sigma\rangle. \tag{5.9}$$

With that, we evaluate the eigenvalue $\eta_{\mathcal{C}}$ of the generalized transfer matrix

$$T^{\mathcal{C}}_{\alpha\alpha';\beta\beta'} = \sum_{\sigma} \sum_{\sigma'} \Sigma^{\mathcal{C}}_{\sigma\sigma'} \Gamma^{\sigma'}_{\alpha\beta} \left( \Gamma^{\sigma}_{\alpha'\beta'} \right)^* \Lambda_{\beta\beta} \Lambda_{\beta'\beta'}, \tag{5.10}$$

where $\Sigma^{\mathcal{C}}$ is the unitary matrix associated to the $\mathcal{C}$-symmetry, and likewise we do for the $\mathcal{R}$-symmetry. From the corresponding eigenstates we obtain the projective matrix representation of the symmetries, $\mathcal{U}_{\mathcal{C}}$ and $\mathcal{U}_{\mathcal{R}}$. The generalized topological order parameter is given by Eq. (5.11). As pointed out in Ref. [179], the iTEBD algorithm provides a ground-state representation composed of a double-tensor unit block $(\Gamma\Lambda)^A(\Gamma\Lambda)^B$, where neither of the two tensors $(\Gamma\Lambda)^{A,B}$ are in the translationally invariant canonical form. In this case, the transfer matrix may be equivalently constructed using the double-tensor unit cell.

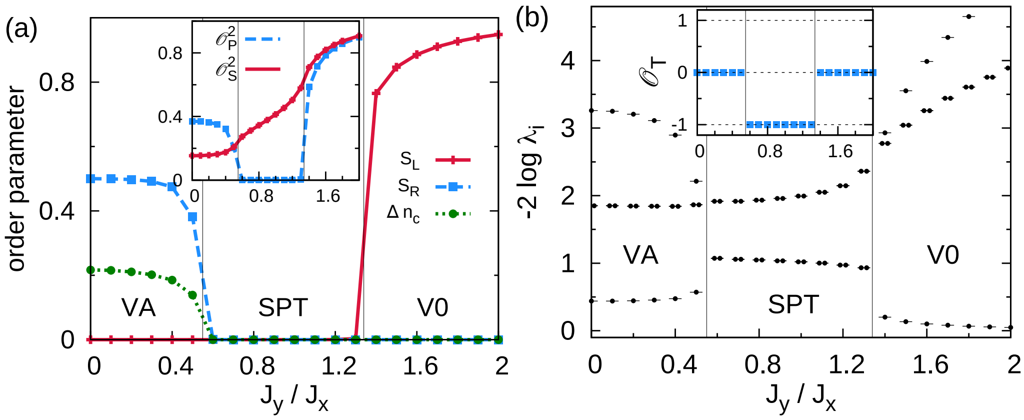

FIGURE 5.8: (a) $S_L$, $S_R$ and $\Delta n_c$ for $\mu = 0$. The inset shows $\mathcal{O}_P^2$ (blue dashed line) and $\mathcal{O}_S^2$ (red solid line) for the same parameters. (b) Largest values of the entanglement spectrum $\lambda_i$ for $\mu = 0$. In the SPT phase the spectrum is doubly degenerate. The inset shows the generalized topological order parameter $\mathcal{O}_T$.

From the dominant eigenvalue $\eta_{\mathcal{C},\mathcal{R}}$ and eigenvector of the generalized transfer matrix $T^{\mathcal{C},\mathcal{R}}$, with respect to the symmetries $\mathcal{C}$ and $\mathcal{R}$, we obtain the projective matrix representation of the symmetries, $\mathcal{U}_{\mathcal{C},\mathcal{R}}$. With this, we define

$$\mathcal{O}_T = \begin{cases} 0 & \text{if } |\eta_{\mathcal{C}}| < 1 \text{ or } |\eta_{\mathcal{R}}| < 1 \\ \frac{1}{\chi}\,\mathrm{tr}\left(\mathcal{U}_{\mathcal{C}}\mathcal{U}_{\mathcal{R}}\mathcal{U}_{\mathcal{C}}^{\dagger}\mathcal{U}_{\mathcal{R}}^{\dagger}\right) & \text{if } |\eta_{\mathcal{C}}| = |\eta_{\mathcal{R}}| = 1, \end{cases} \tag{5.11}$$

shown in the inset of Figure 5.8 (b) as a function of $J_y/J_x$. When $\mathcal{O}_T = 0$ the phase is non topological, while $\mathcal{O}_T = -1$ marks the presence of a topologically non-trivial SPT phase. Contrary to the large-$D$ phase of spin-1 chains, the VA phase does not show any $\mathcal{O}_T = +1$ topologically trivial phase, due to the mentioned spontaneous symmetry breaking of the sub-lattice symmetry.

**Fidelity susceptibility** In order to further characterize the phase transitions, we analyse by means of DMRG calculations the fidelity susceptibility [180]

$$\chi_{FS}(U) = \lim_{\delta U \to 0} \frac{-2\ln|\langle\Psi_0(U)|\Psi_0(U+\delta U)\rangle|}{(\delta U)^2}, \tag{5.12}$$

with $|\Psi_0\rangle$ being the ground-state wave function. Marked peaks reveal the presence of two phase transitions for $\mu = 0$, and a single one for $\mu \neq 0$. In particular, Figure 5.9 (b) shows a second-order phase transition for a cut through the phase diagram across the VA and V0 regions, hinted by the abrupt growth of the leg magnetization $S_L$, as in Figure 5.6. Figure 5.9 (b) confirm the presence of phase transitions at both edges of the SPT phase region, as suggested in Figure 5.8 (a) by the abrupt growth of local order parameters, associated to a spontaneous symmetry breaking. The scaling of the peak max$\chi_{FS}(\phi)$ with the system size is consistent with a second-order Ising-like character for all transitions.

Lastly, note that, in order to facilitate the open boundary DMRG simulations of the SPT phase we fix the edge spin configurations in a staggered way. This is analogous to adding an edge magnetic field or an additional spin in the context of

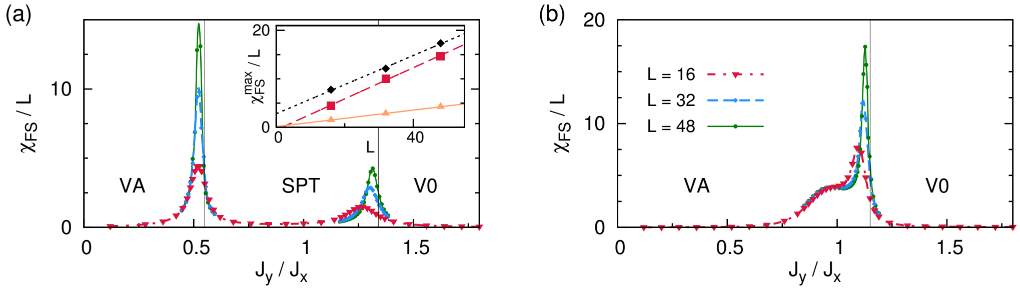

FIGURE 5.9: Scaling of the fidelity susceptibility $\chi_{FS}/L$ for the QLL as a function of $J_y/J_x$, for (a) $\mu/J_x = 0$ and (b) $\mu/J_x = 1$. The results are obtained from DMRG-simulations keeping up to 800 states. The inset of (a) shows a linear scaling of the peak of the $\chi_{FS}/L$-curve with the number of rungs $L$, proving the Ising character of the quantum phase transitions (from bottom to top) between SPT to V0 ($\mu = 0$), VA to SPT ($\mu = 0$) and VA to V0 ($\mu = J_x$).

simulations of the Haldane phase in spin-1 chains [181, 182]: in this way we lift the edge-state degeneracy.

## 5.3 Experimental realization with cold gases

In this Section, we introduce a simple scheme, which allows for the dynamical realization of the spin-1/2 U(1) quantum link model and in one- and two-dimensional lattices.

**Experimental scheme** The scheme is represented in Figure 5.10: we consider a single-component (spinless) Fermi gas in a $s$-$p$ lattice formed by deep (C) and shallow (A,B) sites similar to that realized in Ref. [44]. The lowest state of all C sites, which may be considered as fully pinned, remains filled at any time. We assume two non-degenerate $p$-orbitals, $\alpha = 1, 2$, in the C sites; the energy splitting $\Delta'$ between both orbitals may be achieved using elliptical sites (the third $p$ orbital is assumed to have a much larger energy and can be neglected). Due to the superlattice modulation shallow sites A and B have an energy difference $\Delta$. The Hamiltonian of the physical model is

$$\begin{aligned} H = & -t \sum_{k \in \mathrm{A,B}} \sum_{\alpha} \left( \Psi_k^\dagger \Phi_{k+1,\alpha} + \Psi_k^\dagger \Phi_{k-1,\alpha} + \mathrm{H.c.} \right) \\ & + \Delta \sum_{k \in \mathrm{B}} n_k + \sum_{k \in \mathrm{C}} \left( \sum_{\alpha} E_\alpha N_{k,\alpha} + U_{12} N_{k,1} N_{k,2} \right) \end{aligned} \tag{5.13}$$

where the operator $\Psi$ acts on the shallow sites $A$ or $B$, the operator $\Phi_\alpha$ acts on the $p$-orbitals of the deep sites C and finally $n_k = \Psi_k^\dagger \Psi_k$ and $N_{k,\alpha} = \Phi_{k,\alpha}^\dagger \Phi_{k,\alpha}$ are the respective particle density operators. The hopping rate between the A (B) sites and the $p$-orbitals is denoted by $t$, $E_\alpha$ is a chemical potential on the deep sites defined as

$$E_\alpha = E_0 + \frac{\Delta + (-1)^\alpha \Delta'}{2} + U,$$

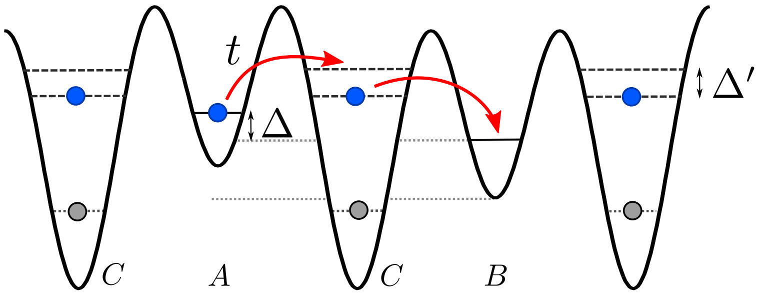

FIGURE 5.10: Sketch of the $s$-$p$ super-lattice scheme proposed for the realization of a spin-½ QLM - see text.

$U$ is the interaction energy between particles sitting on one of the $p$-orbitals and on the lowest $s$-orbital of the C sites, $U_{12}$ is the interaction between $p$ orbitals, and $E_0$ is an energy off-set, which can be neglected without loss of generality.

**Mapping to the QLM** We assume $t \sim |\Delta - \Delta'| \ll U, \Delta, \Delta'$. Within this time interval we can be confident that the gauge invariance is preserved within second-order processes because of energy conservation, while beyond $t$ contributions from higher-order corrections significantly populate non-physical states and leads to symmetry violation. We will probe the robustness of the model against deviations from the Hilbert subspace of physical states by simulating real time evolutions after a quench. The system is initially prepared with a single particle in the $p$ orbitals. Due to energy conservation, we may limit ourselves to the manifold in which at a given C site either the $p$-orbital $\alpha = 1$ or the $\alpha = 2$ is occupied. We may hence associate the two orbital occupation configurations to the two spin ½ link states, attributing

$$\tilde{S}^z_k = \epsilon(N_{k,2} - N_{k,1})/2,$$

where $\epsilon = 1$ $(-1)$ for C sites at the right (left) of A sites. The system then reduces to the one dimensional QLM with mass $\mu = (\Delta - \Delta')/2$, and $J_x = t^2 U_{12}/U(U + U_{12})$.

An identical scheme may be applied in the $y$ direction to get a two dimensional QLM, where a possibly different hopping constant results in $J_y$. The ladder configuration can be experimentally realized by decoupling the legs from the rest of the lattice using sufficiently large energy barriers [52]. We stress that within this setup the actual ground-state is generally not gauge invariant. However, once prepared the gauge-invariant manifold cannot be left within second-order processes due to energy conservation. This allows for the dynamical quasi-adiabatic preparation of QLM and QLL states, which we illustrate for the particularly relevant case of the SPT phase of the QLL.

**Adiabatic preparation of the SPT phase** The defect free VA phase is a product state that may be prepared by filling all B sites, keeping A sites empty, and filling the deepest and $\alpha = 1$ state of C sites. The preparation of this initial state fixes the boundary conditions of the QLL. Starting at large $\mu \gg J_{x,y}$, non-trivial quantum many-body states may be prepared by a quasi-adiabatic decrease of the mass $\mu$. Note in this sense that neither for the 1-D nor for the ladder case a phase transition is encountered, and hence $\mu = 0$ states may be prepared in a finite time without crossing a quantum critical point. Note also that, contrary to the small mass case, due to higher order contributions, the dynamics in the large mass limit cannot be

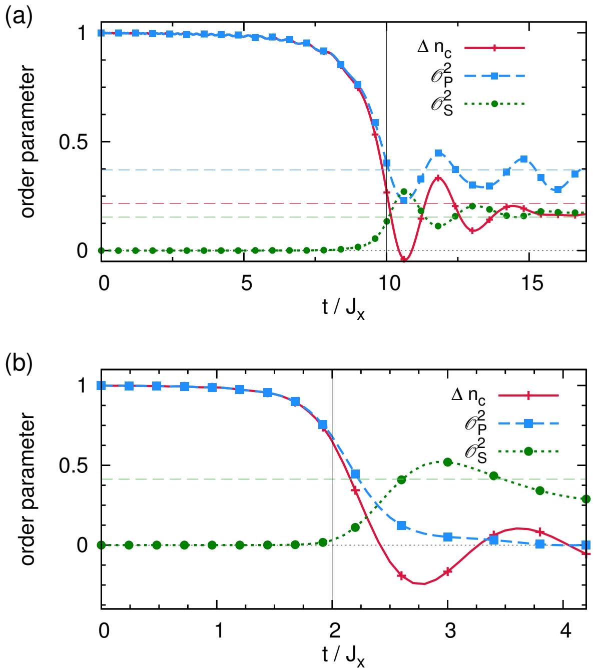

FIGURE 5.11: Quasi-adiabatic preparation. The mass is ramped from $\mu = 100J_x$ down to $\mu = 0$ as $\mu \sim (t - t_R)^{1/4}$. Figures (a) and (b) show the time evolution of $\mathcal{O}_P^2$, $\mathcal{O}_S^2$, and $\Delta n_c$ for, respectively, a 1-D QLM with $J_x t_R = 10$, and a QLL with $J_x t_R = 2$. The results have been obtained using iTEBD with up to 800 matrix states. Dashed horizontal lines indicate the expected values of the order parameters in the ground-state with $\mu = 0$.

efficiently simulated within the scenario of Eq. (5.13). In Figure 5.11(b) we show for the case $J_x = J_y$ that a short ramping sequence ($t_R \sim J_x$) is sufficient to prepare quantum states at $\mu = 0$ with properties very similar to the SPT state. Although due to the finite ramp the expectation values oscillate, these values are close to the ground-state expectation (dashed lines) showing $\mathcal{O}_P^2 \simeq 0$ but $\mathcal{O}_S^2 > 0$ as expected for the SPT phase. In contrast, a similar preparation for the 1-D QLM results as expected in $\mathcal{O}_P^2, \mathcal{O}_S^2 \neq 0$, as in Figure 5.11(a).

**Quench dynamics** In Fig. 5.12 we analyse the case of a sudden quench of $\mu$ for the 1-D QLM and the comparison to the time evolution of the $s$-$p$ Model (5.13). Interestingly, already the sudden quench situation exhibits a finite $\mathcal{O}_S^2, \mathcal{O}_P^2 > 0$. Both the time evolution of the effective QLM and of Model (5.13) agree accurately (note that due to numerical limitations we only follow the time evolution of the $s$-$p$ model for a shorter time). In order to quantify to which degree of accuracy Model (5.13) realizes an effective QLM, we study the deviation from Gauss' law [163]. The parameter

$$\Delta_n = \frac{1}{L} \sum_{k \in A,B} |N_{k-1,1} + n_k + N_{k+1,2} - 2| \tag{5.14}$$

measures the deviation of the occupation of particles on neighboring sites ($\Delta_n = 0$ for a perfect QLM realization). We furthermore analyse whether the $p$-orbitals form

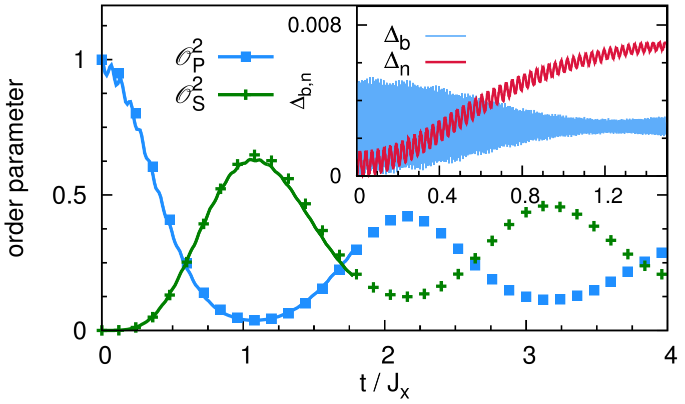

FIGURE 5.12: Emergence of $\mathcal{O}^2_S$ after a sudden quench. We compare the time evolution of $\mathcal{O}^2_S$ and $\mathcal{O}^2_P$ for the effective 1-D QLM and for Model (5.13) of the main text with $\Delta = 4\tilde{J}$ and $U = U_{12} = 40\tilde{J}$. For the full model only the total average particle number per unit cell is fixed. The inset shows the deviation of Model (5.13) $\Delta_n$ and $\Delta_b$ (see text). The iTEBD simulations are terminated after a limit of 800 matrix states is reached.

a spin ½, i.e. if precisely one $p$-orbital is occupied. To this aim we introduce

$$\Delta_b = \frac{1}{L}\sum_{k\in C} |N_{k,1} + N_{k,2} - 1| , \tag{5.15}$$

which is zero for a perfect QLM realization. For the parameters of Fig. 5.12 both $\Delta_n$ and $\Delta_b < 10^{-2}$ (inset of Fig. 5.12). Hence, with the system initialized as a gauge invariant product state, Gauss' law can be fulfilled for a sufficiently long time evolution that allows for the observation of nontrivial $\mathcal{O}^2_P$ and $\mathcal{O}^2_S$ correlations.

## 5.4 Multi-leg ladders

Encouraged by our findings on the two-leg ladder QLM, we extended our investigation to more general two-dimensional lattices. The main motivation of this part of the work was to understand the fate of the intermediate phase at $\mu_\mathrm{i} = 0$. Four-leg ladders can host a non-trivial number of coupled plaquettes; this allows to reveal local correlations and translation symmetry breaking in the thermodynamic limit, by imposing periodic boundary conditions (PBC) along the $y$-direction. PBCs yields a cylinder geometry that frees the system from potential boundary effects on the long edges.

The addition of legs requires some care concerning the numerics, given the considerable scaling of the Hilbert space - see Chapter 6 on this regard. The cylinder geometry has a larger local Hilbert space than its open boundary conditions (OBC) counterpart; in both cases, we could work out ladders with up to four legs with our DMRG algorithm. In order to avoid redundancy, we introduce the notation 2LL to refer to the two-leg ladder, and 3LL and 4LL for the three- and four-leg ladders. The ladders with three or four legs yielded the same qualitative results, hence we will focus the discussion hereafter on the largest system.

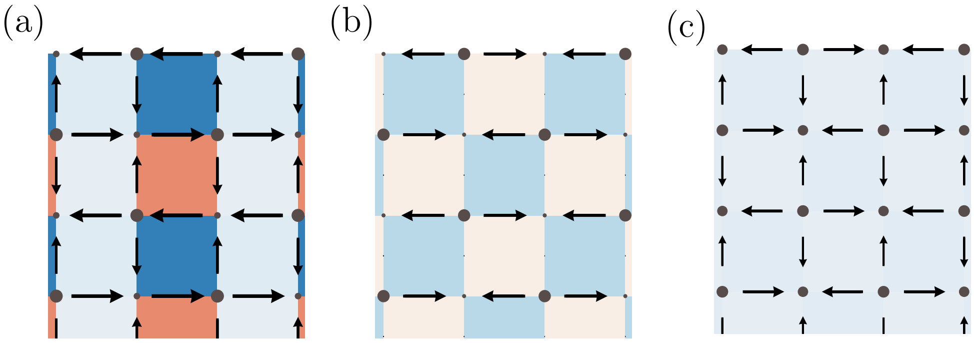

FIGURE 5.13: Illustration of the striped columnar and disordered phases, for a four-leg cylinder with PBCs along the vertical axis, mass $\mu = 0.8$. The color code depicts the vorticity $\langle Q_{\mathbf{r}} \rangle$. (a) Marked Sy striped columns $J_y = 2.4 J_x$; (b) no columnar pattern along $x$ appears from $\langle Q_{\mathbf{r}} \rangle$ at $J_y = 0.2 J_x$ due to the $y$ translation symmetry; the Sx striped phase is revealed by (next-)-nearest-neighbouring plaquette correlations; (c) disordered phase (D). The asymmetry inherent in the gauge invariant states distribution determines a slight imbalance in the bipartite mass and gauge fields expectation values.

### Large mass limit

A first comment regards the sets of gauge-invariant rung states which, we recall, are constituted by particles and blue links as in Figure 5.1, whereas the orange links are fixed. As we commented in Figure 5.5, the 2LL has a mirror symmetry over the mass $\mu$. In the very large and positive mass limit, the mass field is in the vacuum mass configuration (a filled Dirac sea) made of particles occupying the sites with negative mass; the total charge of the rung state is the sum of two null charges. Vice-versa, in the large and negative mass limit the particles are in the anti-vacuum configuration; the total charge of the rung states is $q = -1 + 1 = 0$, again null. The number of rung states is the same, five, in both limits and participate to the set of symmetries encountered in the OBC 2LL. In fact, that is the only, peculiar, case in which the two sets are balanced in number. In all other OBC and PBC (including 2LL PBC) cases, there always exists an imbalance in the number of spin configurations, with a larger set associated to the positive mass limit. This asymmetry at large masses, inherent in the Gauss' law, is visible in ground-state phase diagrams, which lack the mirror symmetry evidenced in the 2LL.

**Striped phases** In order to characterize the phases at large mass, we investigated the plaquette correlations. Reminding the definition given in Eq. (4.12), we introduce the ring-exchange operator in the language of a QLM with SU(2) algebra on the links:

$$\hat{U}_{\square} \rightarrow R^{+}_{\mathbf{r}} = S^{+}_{x,y;x+1,y} S^{+}_{x,y;x,y+1} S^{-}_{x,y+1;x+1,y+1} S^{-}_{x+1,y;x+1,y+1} \tag{5.16}$$

where $\mathbf{r} = (x, y)$ and we generalized the notation introduced in Eq. (5.1) for the operators indices. To quantify the imbalance between plaquettes with opposite vorticity, we define the operator

$$Q_{\mathbf{r}} = (R^{+}_{\mathbf{r}} R^{-}_{\mathbf{r}} - R^{-}_{\mathbf{r}} R^{+}_{\mathbf{r}}). \tag{5.17}$$

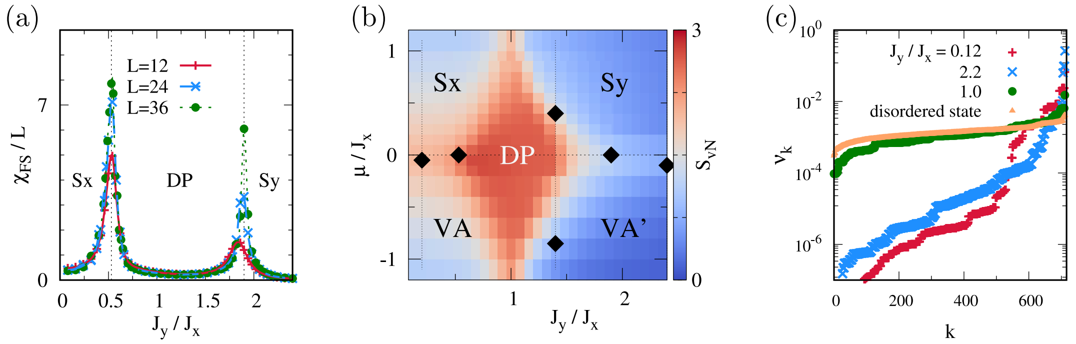

FIGURE 5.14: Phase diagrams of the four-leg QLM cylinder. (a) Finite-size scaling of the fidelity susceptibility at zero mass; (b) von-Neumann entropy $S_{vN}$ of the central rung density matrix $\rho_c$; (c) distribution of the central rung Fock states coefficients $\nu_k$.

Its square $Q^2_{\mathbf{r}}$ quantifies the amount of flippable plaquettes. In the limit $\mu \gg |J_{x,y}|$ of large positive mass, for $J_x < J_y$ we observe an ordered phase, favoured by fourth-order exchange terms, of alternate $y$-oriented columns of flippable plaquettes alongside columns of non-flippable plaquettes, as sketched in Figure 5.13(a). The spins pattern resembles the columnar phase of the Quantum Dimer Model at zero temperature and at large Rokhsar-Kivelson (RK)-coupling $\lambda$ [166]. For $J_x > J_y$, the symmetric behaviour that one would expect in 2-D systems is not perfectly realized, owing to the cylindrical geometry that breaks the symmetry along the $x$-direction, Figure 5.13(b). However, we can reveal the striped phase using two correlation operators: while nearest-columns correlations $\left\langle Q^2_{\mathbf{r}} Q^2_{\mathbf{r+y}} \right\rangle$ vanish, the correlations between nearest stripes $\left\langle Q^2_{\mathbf{r}} Q^2_{\mathbf{r+2y}} \right\rangle$ remain indeed finite.

As we mentioned, the system has no mirror symmetry across $\mu = 0$. Thus, on the opposite limit $\mu \ll |J_{x,y}|$ it presents a vortex-antivortex checkerboard pattern, different from the striped phases and reminiscent of the Neél-like order of the Square Ice model in the limit of large negative $\lambda$ parameter [165].

### Zero mass limit

**Emerging disordered phase** At low mass $\mu$, particle fluctuations become relevant and lead to intriguing physics. For $\mu \sim 0$ we observe three distinct phases as a function of $J_y/J_x$. As can be seen in Fig. 5.14 (a), by doing a finite-size scaling of the four-leg cylinder length one can observe two distinct diverging peaks occurring in the fidelity susceptibility $\chi_{FS}$. We observe a similar behaviour for three- and four-leg ladders (OBC).

Whereas for $\mu = 0^+$, at $J_y \ll J_x$ and $J_y \gg J_x$ the system is in a region that connects smoothly to the Sx and Sy phases, for $J_x \sim J_y$ an intermediate gapped phase occurs. The latter is characterized by vanishing $\langle Q_{\mathbf{r}} \rangle$ and $\langle Q^2_{\mathbf{r}} \rangle$ but a large expectation value of the ring-exchange $\langle R^+_{\mathbf{r}} \rangle$. A crucial insight on the physics of the intermediate phase is provided by the analysis of the reduced density matrix for the central rung $\rho_c$,

$$\rho_c = \operatorname{tr} |\Psi_0\rangle\langle\Psi_0|. \tag{5.18}$$

To calculate $\rho_c$, one can consider the Fock states $\phi_k$ in the space generated by tensor products of the eigenbasis of $\hat{S}^z_{\mathbf{i}u}$ and $\hat{n}_{\mathbf{i}}$. The trace of $\rho_c$ runs over all other rungs.

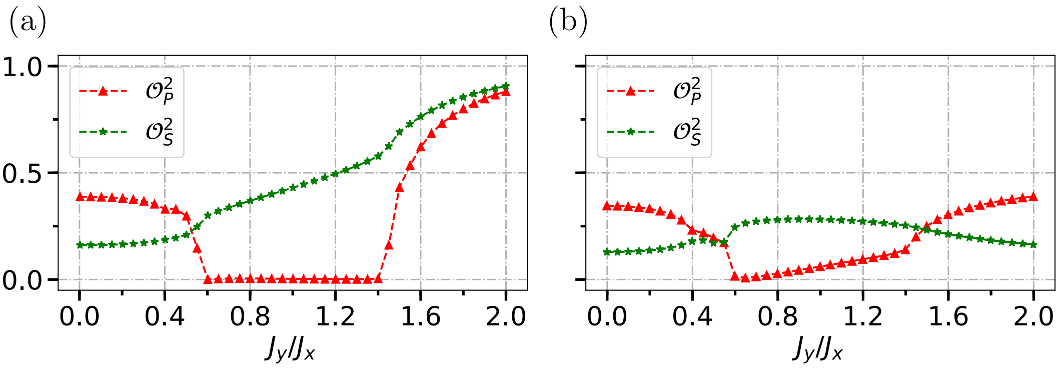

FIGURE 5.15: Parity and string order operators on an external leg (a) and on an inner leg (b) for the four-leg ladder, open boundary conditions.

In Fig. 5.14 (b) we show its diagonal elements $\nu_k = \langle\phi_k|\rho_c|\phi_k\rangle$: an effective local Hilbert space distribution, sorted by amplitude, for the case of a four-leg cylinder. The Sx and Sy phases are strongly localized in Fock space, i.e. $\nu_k$ has most weight for few basis states. The intermediate phase, however, exhibits a drastically different, much flatter distribution, where many local Fock states contribute with similar weight. The disordered character of the intermediate phase is also witnessed by the entanglement entropy $S_{vN} = -\operatorname{tr}(\rho_c \ln \rho_c)$, which we depict in Fig. 5.14(b).

The intermediate phase thus closely resembles the Rokhsar-Kivelson point, which contains an equal superposition of all dynamically connected states. We also show in Fig. 5.14 (c) the corresponding distribution of $\nu_k$ for a classical RK state, which compares well to the ground state obtained by the DMRG simulation. We obtain the same $\rho_c$ distribution for the classical RK state using a Metropolis algorithm and estimate the overlap between the two states to be 0.97. We hence characterize the intermediate gapped phase as a disordered (D) phase. Note that, due to the different Gauss' law on A and B sites, this phase still exhibits a slight particle imbalance between A and B sites, as well as finite link-variable expectation values, as shown in Fig. 5.13 (c).

**Boundary and bulk legs** As a first enquiry on the persistence of the SPT phase in the 4LL, we looked at the string and parity order operators $\mathcal{O}_S^2$ and $\mathcal{O}_P^2$. On the boundary legs, Figure 5.15(a), they are consistent with the behaviour observed in the 2LL (inset of Figure 5.8 (a)), namely a finite $\mathcal{O}_S^2$ accompanies a vanishing $\mathcal{O}_P^2$ in the central D phase. This relation disappears on the inner legs, as shown in Figure 5.15(b).

In fact, the string-parity order emerges a consequence of the open boundary conditions and only for the staggered set of spins indicated for the 2LL. Fixing one of the links reduces the set of available physical states and turns the leg into an effective 1-D chain coupled to an external bath. The addition of a leg in the bulk does not affect the external legs, in this sense. The physics of the external leg can be well understood from a mean-field-like strongly simplified 1-D model, in which the lower spins - connecting the edge with the bulk - fluctuate with an amplitude $J_y$. Six local

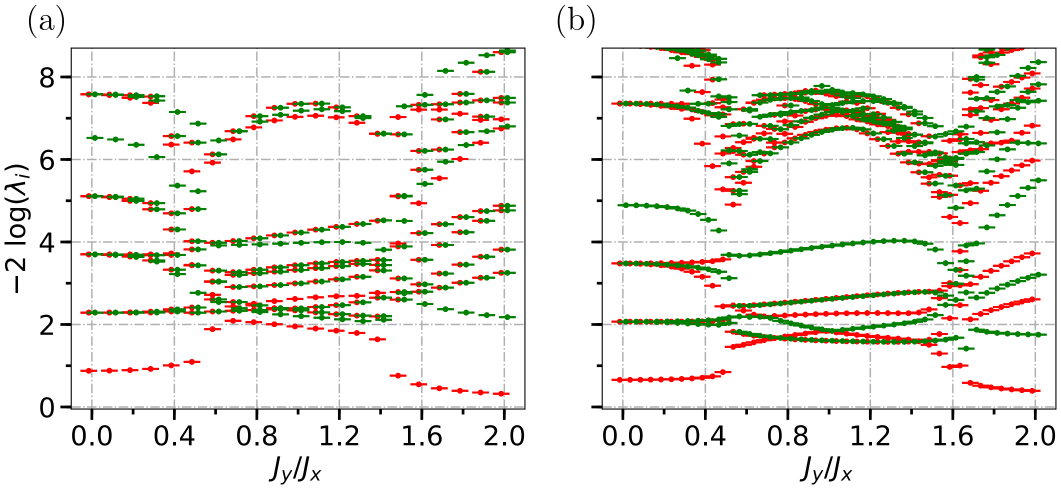

FIGURE 5.16: Entanglement spectrum of the (a) four- and (b) three-leg ladders, showing the ten largest Schmidt eigenvalues. The ground states were obtained with MPS DMRG, L=100, bond dimensions $\chi_4 = 100$, $\chi_3 = 200$. The perfect double degeneracy of the 2LL is lifted in the disordered phase of multi-leg ladders.

states are possible:

$$\begin{aligned}
|0_\pm\rangle &= \frac{\left|\underset{\uparrow}{\leftarrow\circ\leftarrow}\right\rangle \pm \left|\underset{\downarrow}{\leftarrow\bullet\leftarrow}\right\rangle}{\sqrt{2}}, \\
|\tilde{0}_\pm\rangle &= \frac{\left|\underset{\uparrow}{\rightarrow\circ\rightarrow}\right\rangle \pm \left|\underset{\downarrow}{\rightarrow\bullet\rightarrow}\right\rangle}{\sqrt{2}}, \\
|\alpha\rangle &= \left|\underset{\downarrow}{\rightarrow\circ\leftarrow}\right\rangle, \\
|\beta\rangle &= \left|\underset{\uparrow}{\leftarrow\bullet\rightarrow}\right\rangle . \qquad (5.19)
\end{aligned}$$

The Gauss' law imposes further restrictions on the allowed sequence of these local states: for instance, $0_\pm$ may be followed on its right by $0_\pm$ or $\beta$ ($0_\pm \to 0_\pm, \beta$), and so on with all the possible combinations:

$$\begin{aligned}
0_\pm &\to 0_\pm, \beta, \\
\tilde{0}_\pm &\to \tilde{0}_\pm, \alpha, \\
\alpha &\to \beta, 0_\pm, \\
\beta &\to \alpha, \tilde{0}_\pm . \qquad (5.20)
\end{aligned}$$

By construction, Gauss' law enforces a Neél-like order of $\alpha$ and $\beta$ states diluted by an arbitrary number of intermediate 0 or $\tilde{0}$ states. The model Hamiltonian at zero mass, given by

$$\hat{H}_{1D} = -J_x \sum_x \psi_x^\dagger S^+_{x,x+1} \psi_x - J_y \sum_x \psi_x^\dagger S_x^+ + \text{H.c.}, \qquad (5.21)$$

exhibits three ground-state phases. For $J_y \ll J_x$ the ground state is an infinite chain whose unit cell reads

$$\cdots |\alpha\rangle|\beta\rangle|\alpha\rangle|\beta\rangle \cdots \qquad (5.22)$$

whereas for $J_y \gg J_x$ the states

$$\cdots |0_-\rangle |0_-\rangle \cdots , \qquad \cdots |\tilde{0}_-\rangle |\tilde{0}_-\rangle \cdots \tag{5.23}$$

have the lowest energy. Interestingly, for $J_x \sim J_y$ an intermediate phase with Haldane-like diluted Neél order emerges, that resembles the SPT phase. We may describe this intermediate phase by a minimal AKLT-like [183] state with a two-fold degenerate entanglement spectrum and a non-vanishing string order

$$\mathcal{O}_S^2 = (-1)^{i-j} \frac{\cos^4 \phi}{4}, \tag{5.24}$$

while the parity order is exponentially suppressed. Although this is a drastically simplified description, it captures the essential ingredients of a ladder QLMs. In particular, fixing in a ladder the boundary spins to a staggered configuration enforces the dilute Neél order on the boundary leg. However, since for $L_y > 2$ the parity order remains finite in the D phase if measured on the inner legs, Figure 5.15(b), the phase is not topological. Ultimately, the Haldane physics revealed in the spin-½ cQED QLM is the hallmark of a peculiar 2-D geometry in specific staggered boundary conditions.

The absence of a SPT phase is confirmed by the entanglement spectrum, which is no longer strictly two-fold degenerate - see Figure 5.16. Interestingly, however, we observe a robust gap in the entanglement spectrum of the D phase between a low-lying manifold and the rest.

## 5.5 Conclusions

In this Chapter we presented the outcome of a thorough study on the compact QED Quantum Link Model with spin-½ on a multi-leg ladder and cylinder.

First, we showed that the two-leg QLM presents an interesting ground-state phase diagram and we unveiled the presence of a symmetry-protected topological phase. The SPT was revealed by looking at the non-local spin string and parity order parameters along the ladder legs. The topological character of the phase was confirmed by the doubly-degenerate entanglement spectrum and by testing with MPS methods the invariance of the state under symmetric transformations. We moved then to larger ladders, to scrutiny the fate of the intermediate phase at zero mass on authentic two-dimensional space. We clarified the coexistence of AKLT-like states on the external legs with the absence of SPT phases in multi-leg ladders.

As mentioned in Chapter 4, the spin-½ (2+1)-d cQED Quantum Link Model presents analogies to spin models studied in condensed matter physics, such as the Quantum Dimer Model and the Square Ice Model. Motivated by these analogies, we studied the QLM on a semi-infinite cylinder geometry to assess whether elements of the spin solids subsist in the presence of a dynamical gauge field. Whereas in the large mass limit we observe Neél-like vortex-antivortex and striped crystalline phases, for small masses there is a transition from the striped phases into a disordered phase, whose properties reminds those at the Rokhsar-Kivelson point of the quantum dimer model. As a main result, we have found an emergent disordered phase for $\mu \sim 0$ and $J_x \sim J_y$, which closely resembles an RK phase. On finite ladder systems with staggered boundary spins, this phase exhibits Haldane-like ordering at the edge legs.

# Chapter 6

# Numerical methods

"This new formulation appears extremely powerful and versatile, and we believe it will become the leading numerical method for 1-D systems, and eventually will become useful for higher dimensions as well." [176]. Thirty years later, it is safe to say that Steven White's prophecy was right.

In this chapter we discuss the numerical methods utilized in this research work. We used tensor network algorithms based on Matrix Product States to find the ground state of one-dimensional and ladder-like systems in the thermodynamic limit and to analyse the real time evolution of finite-size chains.

## 6.1 Tensor networks

### 6.1.1 Density Matrix Renormalization Group

It is known that numerical calculations on many-body systems are hindered by the exponentially growing Hilbert space dimension. A successful line of attack of problems in one-dimensional systems is the renormalization group (RG) in real space coordinates. The solution of the Kondo problem obtained by Wilson [184] was the first remarkable success of RG in the context of quantum chains. Following that dramatic breakthrough, Hames that the same approach could extend to a variety of non-trivial quantum lattice problems arose and soon got dashed, after that several different applications of the method had little success for anything but impurity problems.

Steven White [185] examined why the method fails so spectacularly even in simple models, such as the lattice version of the one-dimensional particle in a box. The standard real space RG approach consists of clustering a group of sites, the $AA$ block in Figure 6.1 (a), and diagonalizing the effective Hamiltonian relative to the cluster. One can then truncate the set of eigenstates, keeping only the $m$ states with the lowest energies and constructs with those a renormalized Hamiltonian for a new, larger block $A'$. Since the cluster Hamiltonian does not include any connection to the surrounding $AA$ blocks, its eigenstates have inappropriate features at the edges of a block; in fact, that it is equivalent to imposing hard wall boundary conditions, hence all the eigenstates of the $AA$ block have to vanish at the edges. That implies that the Hilbert space $A'A'$ at the following renormalization step will be orthogonal to a set of states which have finite amplitude in the centre, including the lowest energy mode with no nodes.

In a follow-up paper [176], White proposed a workaround based on the diagonalization of a large cluster of sites, named superblock, and the subsequent definition of a chunk of the superblock $S$ as the new, renormalized unit cell $A'$. Let us assume to diagonalize the Hamiltonian relative to a four-sites superblock $S$, depicted as $A \bullet \bullet A$ in Figure 6.1 (b). If we take a bipartition of $S$ and consider the states of the block $A\bullet$,

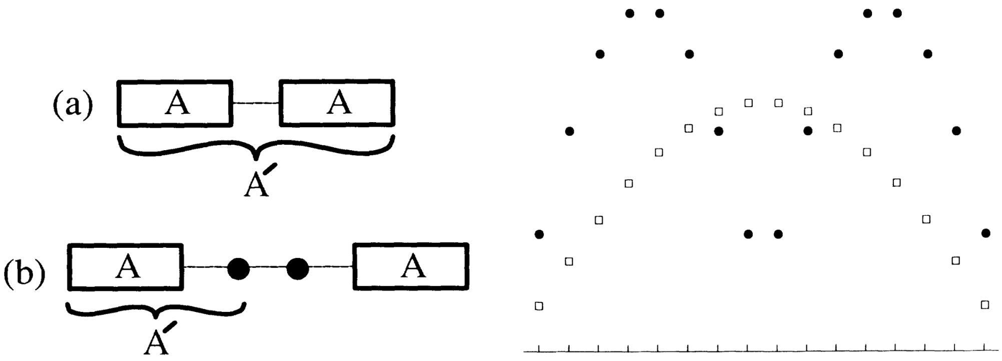

Figure 6.1: Left panel: (a) original Wilson's approach, real-space renormalization group of a 1-D system; (b) White's infinite DMRG, renormalizing a minimal super-block with one spare site. Right panel: discrepancy between the ground state of a free particle in a 1-D box with discrete coordinates (16 sites, white squares) and the ground state obtained through real-space renormalization of two blocks of 8 sites (black squares). Figures from White [176, 185].

which is our new block $A'$, we are guaranteed that such renormalized states will span a correct spectrum of boundary conditions (in the centre, between • and •), not limited by any hard boundary constraint. The projection onto $A'$ is not uniquely defined. The recipe proposed by White prescribes to compute the superblock density matrix and to trace out the environment of $A'$, e.g. the other half of the bipartition. It can be demonstrated that the eigenvectors of the reduced density matrix with the largest eigenvalues are the optimal states to keep. The routine is flexible in the size of the superblock and the renormalized block, but the minimal version designed in Figure 6.1 (b) is the optimal configuration, as the diagonalization of a superblock Hamiltonian rapidly becomes a hindrance with increasing size. Briefly, this is the core concept of Density Matrix Renormalization Group (DMRG), arguably the work-horse for numerical simulation of strongly correlated quantum chains. The method demonstrated to yield flawless results quite independently from the nature of the Hamiltonian, even for modest computational resources. The outstanding empirical success of DMRG hinted the presence of a physical origin for such stunning performances.

In what follows, we introduce the modern understanding of DMRG, based on arguments from quantum information theory. Comprehensive reviews linking the classical with the MPS formulation of DMRG can be found in [112, 186]. We will discuss the area law, which gives to DMRG a firm footing, and introduce the notion of Matrix Product States, upon which a variety of algorithms are based: to mention a few, (i)DMRG, (i)TEBD in real and imaginary time, TDVP.

### 6.1.2 Matrix Product States

The quantum state of a spin-½ chain of length $L$ can generically be described by a linear combination of the $d^L$ states ($d = 2$) of the full Hilbert space:

$$|\Psi\rangle = \sum_{\sigma_1,\dots,\sigma_L} c_{\sigma_1,\dots,\sigma_L} |\sigma_1,\dots,\sigma_L\rangle\,. \tag{6.1}$$

An alternative, convenient way to keep track of and deal with the coefficients $c_{\sigma_1,\dots,\sigma_L}$ is the following. By means of a series of consecutive Singular Value Decomposition operations, one can define a matrix $A^{\sigma_i}$ for each local spin $\sigma_i$ such that the coefficient $c_{\sigma_1,\ldots,\sigma_L}$ can be reconstructed by multiplying all those matrices,

$$c_{\sigma_1,\ldots,\sigma_L} = A_1^{\sigma_1} A_2^{\sigma_2} \ldots A_{L-1}^{\sigma_{L-1}} A_L^{\sigma_L}, \tag{6.2}$$

whence the name Matrix Product State (MPS). The $A_i$ objects are rank-three tensors, with one physical leg identified by the index $\sigma_i$ and two *virtual* legs. The laborious procedure to construct the $A^{\sigma_1}$ matrices in Eq. (6.2) is well clarified in the review paper by Schollwöck [112]. A beautiful pedagogical example of a matrix product diagram can be found in [187] II.B, with a graphical representation of a spin-½ chain with four sites. An exact representation of the quantum state requires central matrices of large ($d^{L/2}$) size:

$$(1 \times d), (d \times d^2), \ldots, (d^{L/2-1} \times d^{L/2}), (d^{L/2} \times d^{L/2-1}), \ldots, (d^2 \times d), (d \times 1). \tag{6.3}$$

A restricted class of matrix product states is defined by setting the matrix dimensions to a finite integer $\chi < d^{L/2}$, named *bond dimension*. The truncation of the bond dimension is necessary to make the numerical algorithms efficient. The ground state of a certain Hamiltonian in the $\chi$-MPS manifold is an approximation of the true ground state, recovered in the limit of $\chi \to d^{d/2}$. Algorithms performing ground-state search by minimizing the effective Hamiltonian on a double-tensor cell (as DMRG and TEBD) generally do an optimal truncation of the bond dimension by discarding the smallest Schmidt eigenvalues obtained through Singular Value Decomposition (SVD).

The MPS are fully equivalent to the old-fashioned states obtained in DMRG through diagonalization of the reduced density matrix. However, the description of quantum states in terms of the MPS manifold allows to work with a beautiful and simple formalism that renders clear the properties of tensor networks and essentially enforces correctness.

**Maximally entangled states** An alternative way of looking at MPS is through the concept of maximally entangled valence-bond states [188]. Though more abstract, this approach has some advantages. For instance, it is suitable for the description and interpretation of some paradigmatic 1-D models, as the AKLT [183, 189] or the Majumdar–Ghosh [190]. Also, it eases the generalization of MPS to two-dimensional systems, where they take the form of Projected Entangled Paired States (PEPS).

To illustrate the notion of maximally entangled states, let us consider a spin-1 quantum chain, with local Hilbert space dimension $d_p = 3$. Then, let us assume that each local spin is composed of two virtual elements, spin-½, with local space dimension $\chi$. Let us also assume that each virtual element is coupled to the virtual element of a neighbouring site, to form a maximally entangled superposition of product states, as in Figure 6.2,

$$|\phi_{i,i+1}) = \sum_{k=1}^{\chi} |r_i = k, l_{i+1} = k). \tag{6.4}$$

One can define an on-site linear map $\mathcal{M}$ from the Hilbert space of the virtual particles to the Hilbert space of the corresponding physical particle. The map $\mathcal{M}$ can be

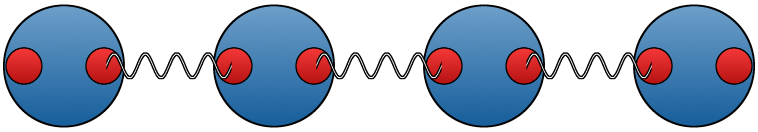

FIGURE 6.2: Maximally entangled states. The blue circles are spin-1 states, which can be expressed in the (rotated) basis of the direct sum of two spin-½ $S^z$ operators. The red circles host $\chi$ spin-½ virtual states, bijectively coupled to realize maximally entangled superpositions product states. Rank-three tensors $A^{\sigma_i}$ map the tensor product of virtual elements of the same site $i$ onto spin-1 states.

expressed in terms of a rank-3 tensor

$$\mathcal{M}_i = \sum_{\sigma_i=1}^{d_p} \sum_{l,r=1}^{\chi} A^{\sigma_i}_{lr} \left|\sigma_i\right\rangle \left(l,r\right|. \tag{6.5}$$

By applying the map $\mathcal{M}$ on all the sites of the chain, one obtains

$$\begin{aligned} \left|\Psi\right\rangle = & \left(\bigotimes_{j=1}^{L} \mathcal{M}_j\right) \left(\bigotimes_{i=1}^{L-1} \left|\phi_{i,i+1}\right)\right) \\ = & A^{\sigma_1} A^{\sigma_2} \dots A^{\sigma_{L-1}} A^{\sigma_L} \left|\sigma_1, \dots, \sigma_L\right\rangle , \end{aligned} \tag{6.6}$$

thus verifying the substantial equivalence between the notion of maximally entangled pairs and the previous construction of the MPS ansatz, Eq. (6.2).

**Area law for the entanglement entropy** A faithful approximate representation of a ground state can be attained if the low-energy sector of the Hilbert space scales conveniently with the system size. Naively, one would guess that the entropy of a region of space possesses an extensive character, meaning that it grows with the size of the region. Such a behaviour is referred to as a *volume scaling* and is observed for instance with thermal states [191]. However, it is not obvious a priori whether nature fully explores the vast territories of the entire Hilbert space. In fact, an edge in this sense is set by the fact that interactions always seem to happen locally and only between a few bodies. Arguments developed in the context of quantum information theory [192] suggest that there is an exponentially growing lower bound on the time it takes a pure state to overlap with a random one when exclusively driven by local interactions. This suggests already that all physical states live on a limited subspace.

**Entanglement entropy** Entanglement is a key concept in quantum mechanics [193]. The amount of entanglement helps determining whether a quantum computation can be efficiently simulated on a classical computer [194]. The key question is then: how much entanglement is present in the ground state of strongly correlated quantum many-body systems? A measure of the entanglement is the entanglement entropy, in the form given by Rényi

$$S_R(\rho, \alpha) = \frac{1}{1-\alpha} \ln(\mathrm{tr}(\rho^{\alpha})), \tag{6.7}$$

which is known as the von Neumann entropy in the limit $\alpha \to 1$:

$$S_{\mathrm{vN}}(\rho) = -\operatorname{tr}(\rho \ln(\rho)). \tag{6.8}$$

Here, $\rho$ is the reduced density matrix or, equivalently, the squared Schmidt eigenvalues of a bipartite state [195]. The problem of the entanglement scaling was first addressed in the context of black-hole entropy [196]. The investigation of the subject at the interface between quantum field theory and quantum information theory flourished [114, 197] and gave universal results that extend to condensed matter physics. Considering the generic case of a quantum spin system on a $n$-dimensional infinite lattice and a finite block of radius $L$, it has been shown that entanglement entropy does not have a volume law but rather scales as the boundary of the block, whence the name of *area law* [113]:

$$S(\rho_L) \propto cL^{n-1}. \tag{6.9}$$

In one dimension, the area law means that the entanglement entropy eventually saturates to a constant value $c$.

**Gapped Hamiltonians** A qualitative argument shows how gapped Hamiltonians with local interactions in 1-D generally satisfy the area law [192]. It is proven [198] that all connected correlation functions between two blocks of a gapped system decay exponentially as a function of the distance between the blocks. If the decay is exponential, tracing out a block of size larger than the correlation length yields a state that is to a good approximation a tensor product state. Iterating the fragmentation and then applying a disentangling operation on all blocks in parallel leads to a product state of many parts; in other words, this routines leads to the preparation of a MPS-like representation of the state, which is faithful up to exponentially small corrections. Matrix Product States define a manifold which satisfies the area law by construction, as they enforce an upper bound on the entanglement entropy corresponding to the maximally entangled states:

$$S = -\sum_{i=1}^{\chi} \frac{1}{\chi} \ln\left(\frac{1}{\chi}\right) = \ln(\chi). \tag{6.10}$$

This guarantees that MPS states are faithful approximations of the ground states of gapped Hamiltonian. Rigorous analys of this matter go beyond the scope of this work and can be retrieved in review papers [191, 192]. Violations of the area law in 1-D occur. For critical (gapless) lattice models, the entropy $S_L$ diverges logarithmically [113]. Using conformal field theory arguments, it can be shown that

$$S = \frac{c}{k} \log(L) + C, \tag{6.11}$$

where $c$ is the conformal charge, $k$ depends no the boundary conditions ($k = 3$ in PBC, $k = 6$ in OBC) and $C$ a non-universal constant. In quenched, out-of-equilibrium systems the entanglement entropy grows up to linearly in time [199]. In conclusion, considering that the number of relevant states in 1-D systems relates exponentially [200, 201] to the entanglement entropy,

$$\chi \propto \exp(S), \tag{6.12}$$

we can summarize the computational costs of 1-D tensor network simulations as follows:

- gapped system, OBC: $\chi = \text{const}$,
- gapped system, PBC: $\chi = \text{const}^2$,
- critical systems: $\chi \propto L^\alpha$.

### 6.1.3 The DMRG algorithm with MPS

Let us consider a finite-sized chain of length $L$. We have seen how the state of the chain can be represented as the contraction of the bond legs of $L$ rank-three tensors $A_j$. The Hamiltonian acting on the chain is a large operator with $2L$ physical legs, which can be conveniently built through contraction of small blocks named Matrix Product Operators (MPOs), described in Sec. 6.1.3. The (i)DMRG algorithm performs a variational ground state search on the MPS; the minimization is executed locally, usually on a single- or double-tensor $\mathcal{T}_{\text{var}}$ (the opaque tensors in Figure 6.3, see also Figure 6.5). We will consider hereafter a double-tensor minimization, on sites *j*, *j+1*. The contraction of the other chain tensors defines the tensor $\mathcal{T}_{\text{env}}^{[j,j+1]}$, which represents the environment of $\mathcal{T}_{\text{var}}^{[j,j+1]}$. The contraction of $\mathcal{T}_{\text{env}}^{[j,j+1]}$ with the MPO Hamiltonian yields the effective Hamiltonian $\hat{H}_{\text{eff}}^{[j,j+i]}$:

$$\hat{H}_{\text{eff}}^{[j,j+i]} = \left\langle \mathcal{T}_{\text{env}}^{[j,j+1]} \middle| \hat{H} \middle| \mathcal{T}_{\text{env}}^{[j,j+1]} \right\rangle . \tag{6.13}$$

The energy of the tensor network, graphically illustrated in Figure 6.3, reads

$$E = \langle \Psi | \hat{H} | \Psi \rangle = \langle \mathcal{T}_{\text{var}} | \, \langle \mathcal{T}_{\text{env}} | \hat{H} | \mathcal{T}_{\text{env}} \rangle | \mathcal{T}_{\text{var}} \rangle = \langle \mathcal{T}_{\text{var}} | \hat{H}_{\text{eff}} | \mathcal{T}_{\text{var}} \rangle , \tag{6.14}$$

where $|\Psi\rangle$ is the representation of the many-body state in the MPS manifold with bond dimension $\chi$. The effective Hamiltonian is a large matrix, of dimension $(d\chi)^2$, whose lowest eigenvector can be found by means of iterative methods à la Lanczos. In double-tensor DMRG, the updated $\mathcal{T}_{\text{var}}$ is reshaped onto a $d\chi$-dimensional matrix; an SVD with subsequent truncation returns the updated rank-three tensors $A$ and $A_{j+1}$. The algorithms proceeds then by iterating the local minimization on the neighbouring pair of sites. In classical DMRG language this is known as the *sweep* routine. The MPS may be initialized to a random list of $A$ tensors in the $\chi$-manifold. An educated guess can be obtained through what is classically known as the *warm-up* routine, or infinite DMRG (iDMRG). In iDMRG, an initial double-tensor pure state is minimized; a copy of the tensors $A_1$ and $A_2$ is then plugged in reversed order at the centre of the chain, which is thus two units longer. The iteration is repeated, until a chain of the desired length is obtained.

Attaining the ground state of finite size chains is crucial for the study of edge effects on the physics of the bulk and for the investigation on real time evolutions. In the next paragraph we examine the relations between MPS, iDMRG and the thermodynamic limit.

#### The thermodynamic limit

In studying a model Hamiltonian, one usually investigates the ground-state properties in the thermodynamic limit. The MPS ground-state in the $\chi$-manifold is a translation invariant uniform MPS (uMPS [202]), represented by an infinite chain of

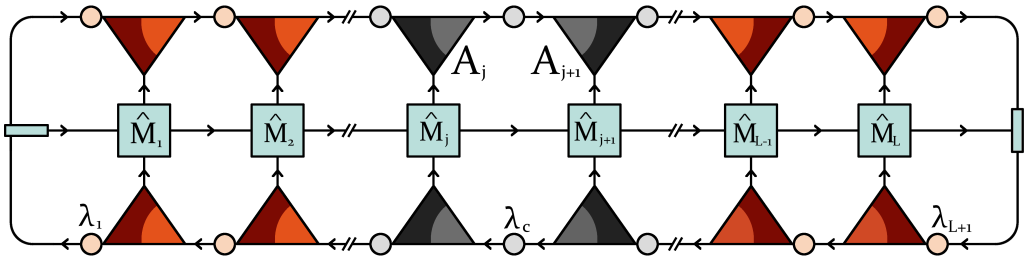

FIGURE 6.3: Illustration of a Tensor Network for DMRG. In gray scale, the variational double-tensor $\mathcal{T}_{\text{var}}$ and its Hermitian conjugate; the color network is the effective Hamiltonian $\hat{H}_{\text{eff}}^{[j,j+i]}$.

identical tensors $A_{\text{gs}}$. If the Hamiltonian has translational periodicity $m$, the thermodynamic MPS is built through the repetition of a unit cell of tensors. The notion of state and Hilbert space in the thermodynamic limit is subtle. Rigorous definitions exist [203] but we can evade the controversy by interpreting the infinite state as the uniform bulk of a large but finite MPS. The adjective *infinite* in the acronym iDMRG may be misleading. In fact, an iDMRG run with $N$ iterations returns a MPS of a chain of length $L = 2N$, which is subsequently improved by a few DMRG sweeps. The connection between iDMRG and the thermodynamic limit is established by assuming that the innermost tensor $A_{\text{c}}$ tends to $A_{\text{gs}}$ for long enough chains. This claim is solidly backed by the area law scaling of the entanglement entropy and the exponential decay of connected correlation on gapped systems.

A fundamental limitation of (i)DMRG is rooted in the locality of the variational update, which inevitably breaks the translation invariance of the tensors, including $A_{\text{c}}$. Variational methods such as TDVP or VUMPS work on a single tensor $A$, thus eluding by definition edge effects and enforcing translation invariance. The concept behind these algorithms is more elegant and adequate to the thermodynamic limit than it is iDMRG. Also, in numerous test cases, VUMPS demonstrated to dramatically outperform iDMRG or iTEBD, reaching convergence orders of magnitude faster, especially for critical systems [204]. However, (i)DMRG summons on a single platform the workhorse for finite-size systems and a satisfactory algorithm for the thermodynamic limit.

### Abelian symmetries in MPS

A gauge symmetry in quantum mechanics is described by a group $\mathcal{G}$ of transformations for which the unitary representation $U(g)$ of any group element $g$ commutes with the Hamiltonian. Consequently, there exists an irreducible representation (irrep) of the group labelled by a good quantum number $N$ (also called *charge*), associated to a conserved physical quantity (Noether's theorem). The U(1) continuous rotations group is a common case of Abelian global gauge symmetry. For instance, the conservation of the total number of particles, summed over all sites $j$ of a Hubbard chain, is a U(1) symmetry. In this case, the group infinitesimal generator is $\hat{N} = \sum_j \hat{n}_i$, the representations take the form

$$U(g) = e^{\mathrm{i}g\hat{N}} = \bigotimes_j e^{\mathrm{i}g\hat{n}_j}, \qquad g \in [0, 2\pi), \tag{6.15}$$

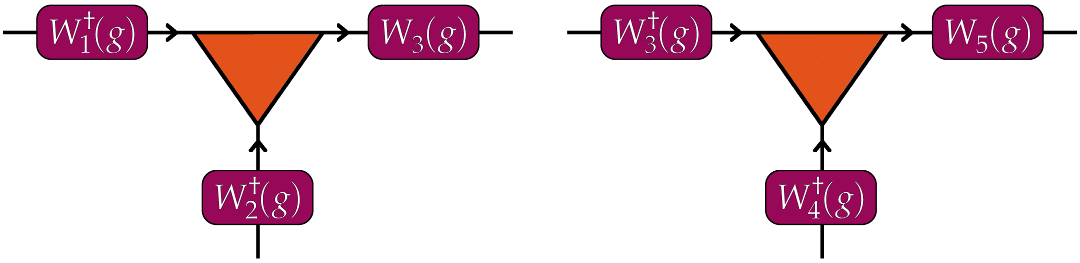

FIGURE 6.4: Local representations $W_j$ of a pointwise symmetry group acting on different MPS tensors. The unitary matrices $W_3$ and $W_3^\dagger$ are gauged out when the two tensors contract leg *j*=3.

the irreps are complex phases $e^{igN}$ and the Hamiltonian takes a block-diagonal form. The Hamiltonian blocks act on proper subspaces of the full Hilbert space, also referred to as *sectors* [205].

In the presence of a gauge symmetry, the use of an unconstrained algorithm for the variational ground-state search is perhaps a cheap choice but certainly not an optimal one. The symmetry-invariant dynamics does not guarantee the permanence in the same charge sector as that of the initial state; eventually, it leads to error accumulation, to the exploration of other charge sectors and ultimately it pushes the variational search towards the absolute ground state. A simple workaround consists in imposing fine-tuned chemical potentials; the solution is however inefficient since the algorithm still works in the grand-canonical full Hilbert space. Hard-coding charge conservation improves the performances of the algorithm in terms of speed and memory. The advantage consists in the possibility to reshape the matrices involved in the contractions onto a block-diagonal form; thereby, one stores less matrix entries and does the matmul of smaller matrix blocks (even in parallel, if convenient).

Imposing charge selection is not trivial, even in the simplest case of Abelian symmetries. Following the comprehensive review [205], we outline in the next paragraph the key concepts regarding pointwise symmetries in Tensor Networks.

### Pointwise symmetries

Global Abelian symmetries befitting an implementation on Tensor Networks are those for which the transformations of the symmetry group act on all the degrees of freedom of the network as linear operators. Equivalently, the representations of the group elements of these global symmetries are separable and can be expressed as the product of local representations $W_j(g)$ acting on single sites (points), as in Equation (6.15):

$$U(g) = \bigotimes_j W_j(g); \tag{6.16}$$

these are called global *pointwise* symmetries. The local representations may depend explicitly on *j*, as for instance in the case of non-homogeneously translation invariant systems. To promote a tensor $A$ to be symmetric we associate with each tensor leg $j$ a local unitary representation $W_j(g)$ of the pointwise symmetry group. In U(1) symmetries, these representations are diagonal matrices of complex phases acting on the tensor through contraction with their relative tensor leg, as in Figure 6.4. Each index $l_j$ of the $j$-th leg is thus equipped with a corresponding irrep of the group,

$$W_j^{(l)}(g) = e^{\mathrm{i}gn_j^{(l)}}, \tag{6.17}$$

labelled by the quantum number $n_j^{(l)}$. The simultaneous action of the local representation on all the tensor legs,

$$T(g) := W_1^\dagger(g) \otimes W_2^\dagger(g) \otimes W_3(g), \tag{6.18}$$

is a map from the $(d_1 \times d_2 \times d_3)$-dimensional vector space of the tensor indices to the unit circle in $\mathbb{C}$:

$$T(g)A_{l_1,l_2,l_3} = e^{\mathrm{i}g\left[-n_1^{(l_1)}-n_2^{(l_2)}+n_3^{(l_3)}\right]}A_{l_1,l_2,l_3}. \tag{6.19}$$

A tensor is symmetric if $T(g)$ acts on it as an identity transformation; as a consequence, the only non-zero entries of $A$ belong in the kernel of $T(g)$:

$$A_{l_1,l_2,l_3} = \begin{cases} 0, & \sum_j \mathrm{sign}(j)n_j^{(l_j)} \neq 0, \\ a \in \mathbb{C}, & \sum_j \mathrm{sign}(j)n_j^{(l_j)} = 0. \end{cases} \tag{6.20}$$

The tensor resulting from the contraction of two symmetric networks must be unaffected by the presence of $W_j$ operators on both fronts of the contracted leg. That means, if $W_j(g)$ acts on one leg, $W_j^\dagger(g)$ must act on the corresponding leg on the other tensor, so that the compound transformation is the identity operator (see Figure 6.4). This constraint introduces an orientation on the tensors legs, setting the sign in front of the affixed arrays of quantum numbers. We describe in the following two paragraphs how the charges are assigned in the MPO and bond legs. Figure 6.3 shows the gauge we chose for the charges flux.

### Matrix Product Operators

Consider the Fermi-Hubbard model of a single species spinless Fermi gas, with a translation invariant chemical potential:

$$\hat{H}_{\mathrm{FH}} = -J\sum_{<i,j>}\left(\hat{c}_i^\dagger\hat{c}_j + \hat{c}_j^\dagger\hat{c}_i\right) + \mu\sum_i \hat{n}_i. \tag{6.21}$$

The associated Matrix Product Operator (MPO) acting on site $j$ reads

$$\hat{\mathrm{M}}_j = \begin{array}{cc} \begin{array}{cccc} \phantom{\mathbb{1}_j} & \hat{c}^\dagger_{j+1} & \hat{c}_{j+1} & \phantom{\mu\hat{n}_j} \end{array} & \\ \begin{pmatrix} \mathbb{1}_j & \hat{c}_j & \hat{c}_j^\dagger & \mu\hat{n}_j \\ 0 & 0 & 0 & -J\hat{c}_j^\dagger \\ 0 & 0 & 0 & -J\hat{c}_j \\ 0 & 0 & 0 & \mathbb{1}_j \end{pmatrix} & \begin{array}{c} \\ \hat{c}_{j-1} \\ \hat{c}^\dagger_{j-1} \\ \\ \end{array} \end{array} \tag{6.22}$$

and it is easy to verify that the ordered matrix product $\prod_{j=1}^{L}\hat{\mathrm{M}}_j$ yields the Hamiltonian (6.21) on the top-right entry of the resulting matrix. The Hamiltonian is finally extracted by multiplying the matrix by a row- and a column-vector, embedded in the transfer matrices (see Figure 6.4):

$$\hat{\mathrm{v}}_L = \begin{pmatrix} \mathbb{1}_0 & 0 & 0 & 0 \end{pmatrix}, \qquad \hat{\mathrm{v}}_R = \begin{pmatrix} 0 & 0 & 0 & \mathbb{1}_{L+1} \end{pmatrix}^\dagger \tag{6.23}$$

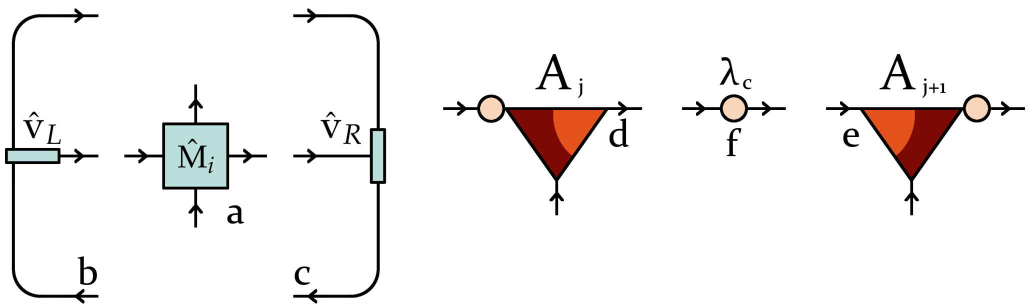

FIGURE 6.5: Basic elements of a Tensor Network for (i)DMRG algorithms. a) Hamiltonian MPO; b), c) transfer matrices embedding the Hamiltonian MPO; d), e) left- and right-canonical rank-three MPS tensors; f) truncated Schmidt eigenvalues spectrum, diagonal matrix; elements d) e) and f) contracted together give the double-tensor $\mathcal{T}_{\text{var}}$.

The formalism of complex weighted finite state automata wonderfully finds correspondence in the real of matrix product states, thus providing operational instructions to easily build the MPO of any Hamiltonian, no matter how baroque; for literature on the subject, see [186, 187, 206–208].

In broad terms, the architecture of the Hamiltonian MPO is as follows. The top-left and bottom-right corners host the identity matrix. On the top-right corner is the sum of the on-site operators. The other operators pair up with their complementaries on the previous or following site, as indicated by the adjacent operators in blue. The array of charges affixed to the (outgoing) MPO virtual legs - the horizontal legs, in Figure 6.5(a) - reads $\{0, -1, +1, 0\}$ and can be intuitively understood by looking at the first row of the matrix. The first and last entry do not modify the number of particles at site $j$ (remind that the generator of the local symmetry is $\hat{n}_j$), hence the relative quantum number is 0. The operator $\hat{c}_j$ destroys one particle, which is recovered on the next site by $\hat{c}_{j+1}$; this causes a negative imbalance on the total charge at site $j$, marked by a -1. Analogously, the third entry in the charges array is a +1. Note that the charges array depends on the chosen orientation of the MPO legs, that we arbitrarily set to flow left to right, as in Figure 6.3. If the flow was reversed, we would plug a minus sign in front the charges arrays, or equivalently infer the MPO virtual leg charges by looking at the operators on the MPO last column.

### SVD and Isometry

The Singular Value Decomposition is an orthogonal bisection method. In (i)DMRG it is used to obtain the rank-three tensors $A$ from the double-tensor $\mathcal{T}_{\text{var}}$, usually after the ground search routine is completed. To do this, $\mathcal{T}_{\text{var}}$ is reshaped onto a matrix with a virtual and a physical leg per side. The SVD returns three matrices, usually named $U$, $S$ and $V^\dagger$. The matrix $S$ is diagonal and contains the set of non-negative, real valued Schmidt eigenvalues; after discarding the lowest eigenvalues and consequently truncating the matrices, $U$ and $V^\dagger$ become *semi-unitary* (or *isometric*), respectively left- and right-canonical:

$$U^\dagger U = \mathbb{1}, \qquad V^\dagger V = \mathbb{1}. \tag{6.24}$$

We illustrate this property graphically in Figure 6.5 by marking the unitary region of tensor $A$ with a darker color. In (i)DMRG, a MPS is usually canonized in left- and right-canonical segments around a central pivot $\lambda_c$, as in Figure 6.3.

The quantum numbers are affixed to the bond legs of $A$ as follows. The external bond legs in a MPS, corresponding to $\lambda_1$ and $\lambda_{L+1}$, have size 1. According to our arrows orientation gauge, $\lambda_1$ has charge 0 while the quantum number of $\lambda_{L+1}$ must sum up to $N$, the irrep of the global symmetry, since it collects the MPS charges flux. If the system size $L$ is an integer multiple of $N$, it is convenient to offset the local symmetry generator,

$$\hat{n}_j \to \hat{n}_j - \frac{N}{L}\mathbb{1}, \tag{6.25}$$

so that the global irrep becomes 0. Assuming to know the charges of the bond legs of $\mathcal{T}_{\text{var}}$, the variational tensor can be reshaped onto a block-diagonal matrix in which each block is associated to a unique charge and can be decomposed individually through SVD. This allows to assign a charges set to the resulting internal bond leg. Applying this routine in iDMRG leads to the full knowledge of the charges on the finite MPS bond legs. Alternatively, one can choose a Fock state as initial MPS for a DMRG sweep [205]; in this case all bond legs have size 1 and the charges are known.

**Transfer matrices** We have seen that the MPO transfer matrix embeds the Hamiltonian expectation value on the MPS environment; these transfer matrices need to be built contracting leg after leg. The state transfer matrices (TM) are associated to the optimal contraction of the MPS norm (in [35], the rules for the efficient contraction of a Tensor Network). The TMs embed information on the state environment. The leftmost left transfer matrix $T_L^{[1]}$ is an identity matrix. The next element $T_L^{[2]}$ embeds $A_1$ and $A_1^\dagger$. Considering that $A_1$ is unitary on the contracted legs, the resulting transfer matrix is again the identity matrix; the series continues until $\lambda_c$ (analogously for the right transfer matrix). This is a powerful property of Tensor Networks. For instance, to calculate the expectation value of an operator acting on site $k$, left to the pivot, one should in principle contract the entire MPS state. In practice, the contraction of the left-canonical block yields the identity matrix $\mathbb{1}$, whence one can close the left bond legs of $A_k$ on themselves.

## 6.2 MPSs for the Quantum Link Model

Matrix Product States are able to describe the quantum state of not only 1-D systems but also cylindrical and ladder geometries, up to a limited number of legs. In order to achieve this, two main strategies are adopted. The one approach cuts and stretches the ladder back to a 1-D system, generating virtual Hamiltonians with potentially very long-range interactions associated to the inter-rung couplings. The other approach consists instead in setting the whole rung as a site of the chain. The trade-off is between the bond dimension $\chi$ and the local Hilbert space dimension $d$. In the first approach, the long-range interactions might get filtered out if $\chi$ is too small. In the second one, nearest-rungs couplings become nearest-neighbours interactions and intra-rung couplings are absorbed as on-site operators, but the Hilbert space dimension scales up as $\sim d^n$, where $n$ is the number of legs. For the Quantum Link Model we opted for the second strategy, since the Gauss' law constraint makes the local Hilbert space scale much more moderately than $d^n$, as one can see on Table 6.1. Let us analyse the local Hilbert space of the largest system that we studied, a ladder with four legs, illustrated in Figure 6.6. We define the local full Hilbert space as the tensor product of the 4 particles located on a rung and the thirteen links connected to them. Immediately, one notices that each of the links along the ladder legs (or $x$-links) are shared by two adjacent rungs. The redundancy costs a higher Hilbert

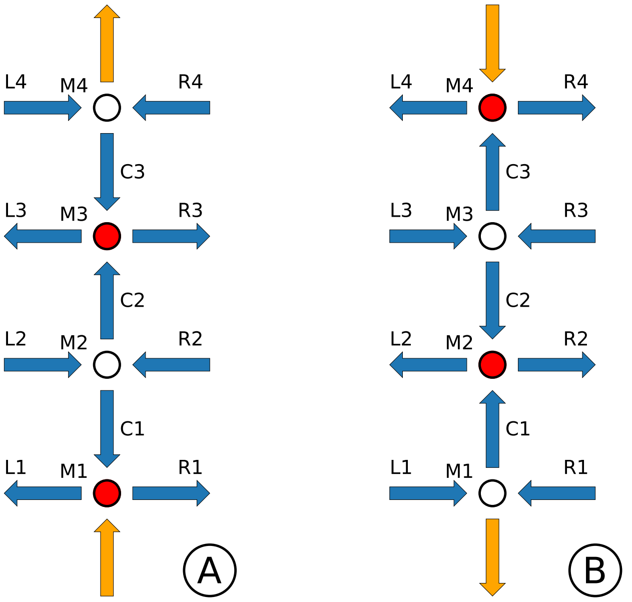

FIGURE 6.6: Two bipartite gauge invariant rung states for the four-leg QLM; the orange links are fixed in OBC and identical in PBC. The matter field is in the Dirac vacuum configuration, with mass $\mu > 0$: on the lowest site of the Ⓐ rung is an antiparticle. The links along the legs shared by different rungs must align.

space dimension but is necessary to define gauge-invariant states on a rung. Moreover, the overlap between shared sets of links is successively exploited as a pointwise global symmetry which enforces the alignment between those sets, besides bringing the computational advantages discussed in Section 6.1.3. As a consequence, inter-rung interaction or hopping terms are built in such a way that the on-site operators on both fronts have to include the same non-trivial operator acting on the links involved in the two-sites coupling. To make an example, let us consider the hopping of a particle on the lowest matter field from rung Ⓐ to rung Ⓑ. We define the annihilation operator $\hat{C}_{1R}$, Eq. (6.26a), as the tensor product of an annihilation operator $\hat{c}_{M1}$ acting on the matter field *M1*, a spin flip $\hat{S}^{-}_{R1}$ from right to left acting on the gauge field *R1* and identity operators on acting the other fields of the rung Ⓐ. Analogously, we define the operator $\hat{C}^{\dagger}_{1L}$ on the rung Ⓑ, Eq. (6.26b), including the creation operator $\hat{c}^{\dagger}_{M1}$ and minding to repeat the spin flip on the gauge field involved in the hopping process, carried out by the $\hat{S}^{-}_{L1}$ operator. Both operators are defined in the gigantic full Hilbert space and then projected onto the reduced, gauge-invariant Hilbert space.

$$\hat{C}_{1R} = \overbrace{\bigotimes_{i=1}^{4} \hat{\mathbb{1}}_{Li}}^{\text{Left links}} \; \underbrace{\bigotimes_{i=1}^{3} \hat{\mathbb{1}}_{Ci}}_{\text{Central links}} \; \overbrace{\bigotimes_{i=2}^{4} \hat{\mathbb{1}}_{Ri}}^{\text{Right links}} \; \underbrace{\bigotimes_{i=2}^{4} \hat{\mathbb{1}}_{Mi}}_{\text{Particles}} \otimes \hat{S}^{-}_{R1} \otimes \hat{c}_{M1} \tag{6.26a}$$

$$\hat{C}^\dagger_{1L} = \overbrace{\bigotimes_{i=2}^{4}\hat{\mathbb{1}}_{Li}}^{\text{Left links}} \quad \underbrace{\bigotimes_{i=1}^{3}\hat{\mathbb{1}}_{Ci}}_{\text{Central links}} \quad \overbrace{\bigotimes_{i=1}^{4}\hat{\mathbb{1}}_{Ri}}^{\text{Right links}} \quad \underbrace{\bigotimes_{i=2}^{4}\hat{\mathbb{1}}_{Mi}}_{\text{Particles}} \otimes \hat{S}^-_{L1} \otimes \hat{c}^\dagger_{M1} \tag{6.26b}$$

We have studied both open and periodic boundary conditions on the external links aligned along the rungs (or $y$-links), while the external $x$-links were usually fixed to an alternate configuration as in Figure 6.6. In the full Hilbert space, we define four Gauss' law diagonal operators $\mathbb{G}_i$, one for each particle. We set to 0 the eigenvalue of gauge-invariant state, and to 1 all the others. The sum of these operators $\mathbb{G} = \sum_{i=1}^{4}\mathbb{G}_i$ allows to identify the set of gauge-invariant rung states as the kernel of $\mathbb{G}$. At this stage we can opt for open or periodic boundary conditions, by imposing an additional constraint on the external $y$-links. In order to have periodic boundary conditions we simply impose the alignment between the top and the bottom links. For open boundary conditions we fix the links as in Figure 6.6 (with the top links flipped for the three-leg ladder); in fact, we explored all the possible combinations of open boundary conditions, unveiling the intriguing behaviours (first and foremost the SPT phase) discussed in Chapter 5 only for this links configuration.

Recently, Tschirsich *et al.* investigated a U(1) Quantum Link Model with fixed matter fields, also known as Square Ice Model, on a cylindrical geometry [165]. The system Hamiltonian acts on the system links via ring-exchange and Rokhsar-Kivelson terms. The matter field distribution, which in the Ice Model includes also the charges $\{\pm 2\}$, sets the gauge-invariant spin configurations. The strategy adopted to map the state onto a MPS representation coincides with our choice to group the links of a rung and encode them onto a single-site gauge-invariant state. The lack of dynamical matter fields allows to investigate ladders in PBC with a larger number of legs, up to 10. To find the ground state, the authors used a canonical TEBD algorithm in imaginary time for systems with up to 6 legs. For larger number of legs, some tailoring of the algorithm was introduced in order to keep the matrices size and the computational costs manageable. In particular, the evolution operators, which are expanded to first order in the time step $\tau$, are efficiently represented in terms of two three-indexed tensors, thus avoiding the full four-indexed $d^4$-tensor of standard TEBD.

In this Section we presented how we have dealt with Lattice Gauge Tensor Networs on a down-to-earth fashion and basing our narration on a specific example. For a rigorous and comprehensive review on the subject, we recommend to the reader the article by Silvi *et al.* [209].

TABLE 6.1: Column $D$ shows the dimension of the full Hilbert space of a $n$-leg rung, tensor product of $n$ matter fields and ~$3n$ spin-½ gauge fields: $3n$-1 in OBC, $3n$ in PBC (see Figure 6.6). Column $d$ shows the dimension of the gauge-invariant local Hilbert space, consisting of all the states satisfying the Gauss' law.

OBC

| **Legs** | $d$ | $D$ |
|---|---|---|
| 2 | 18 | 128 |
| 3 | 90 | 2048 |
| 4 | 468 | 32768 |

PBC

| **Legs** | $d$ | $D$ |
|---|---|---|
| 2 | 28 | 256 |
| 3 | 132 | 4096 |
| 4 | 712 | 65536 |

### LGT Tensor Networks with Python

A basic implementation of DMRG with Python makes use the *tensordot* routine from the *numpy* library to perform tensors contraction. Under the hood, *tensordot* performs a series of operations analogous to the transposition of the legs order with the function *transpose*, the reshaping of the tensors onto a matrix form with *reshape* and a matrix-matrix multiplication (matmul) with *dot*. The matmul operation takes a large portion of the required computational time, since it is a relatively costly operation, repeated multiple times within a Lanczos-type iterative matrix diagonalization. In *numpy*, linear algebra functions as *dot* are efficient as they rely on low level implementations with BLAS and LAPACK, properly wrapped in OpenBLAS, MKL or ATLAS libraries.

In Tensor Networks language, the tensor legs transposition and reshape are more properly called Links Permutation and Links Fusion [205]. Programming tensor networks algorithms that include Abelian symmetries requires the definition of subroutines dedicated to the direct control on each of these operations, which should be optimally coded in order to fully take advantage of the symmetry. We limit ourselves to a few comments on this, without entering into the detail of our implementation with Python. Our approach consists in storing all and only the entries of the symmetric sectors of a tensor on a 1-D *numpy* array, along with another array keeping track of tensor leg indices of the entries. It is worth reminding that the tensors are extremely sparse, as the symmetry constrains the system to a single irrep of the global group while formally the tensor network spans the grand-canonical ensemble. The symmetric local sectors are instead dense. The links permutation and fusion reduces to a series of operations performed on the array of the indices, relying on optimized *numpy* functions as *divmod*, *argsort* or slicing. Since this mapping become costly as the bond dimension grows the mapped indices are stored, thus the mapping is only performed on tensors with a new set of charges: in iDMRG, this normally saturates little after the bond dimension in the centre reaches $\chi$. No efficient built-in *numpy* function was found to load the sectors of the block-diagonal matrices with the entries of the storage array. An efficient solution consisted in defining dedicate functions with Cython, the C-Extension for Python.

In conclusion, during the doctorate a code for (i)DMRG and (i)TEBD in MPS language was developed from scratch. The satisfactory results obtained on the QLM confirmed once again the force and versatility of MPS algorithms. Moreover, it showed that newcomers on the matter can relatively quickly familiarize with such a powerful and flexible tool and make it to the development of a high-performing DMRG code using non-orthodox, user-friendly programming languages.

# Chapter 7

# Conclusions and Outlook

In this Thesis we have reported our theoretical results on density-dependent and dynamical gauge fields. We studied the ground-state physics and dynamics using MPS algorithms and interpreted the rich phase diagrams unveiled. Both for density-dependent gauge fields and quantum link models, we tried to keep a down-to-earth approach, proposing relatively simple experimental realizations.

Concerning density-dependent gauge fields, we have proposed a versatile experimental scheme based on the multi-color modulation of the depth of an optical lattice, that offers flexible and separate control on a trapped Fermi gas. The method is experimentally straightforward and allows for the engineering of Hubbard Hamiltonians with correlated hopping. One example is the two-component anyon-Hubbard model, whose spectrum exhibits a non-trivial dependence on the statistical phase. We have shown how fractional quantum statistics may be monitored by means of a simple interferometer scheme. The density of a cloud of expanding particles and the total spin polarization may be used to clearly reveal the exchange statistics. Further insights on the unconventional quantum phases of the model could also be attained with expansion experiments. The multi-color modulation permits several further interesting extensions, including the control of three-body interactions. In combination with Raman-induced coupling of several spin components, one may study density dependent magnetic fields. Further interesting experimental possibilities of our proposal for the realization of periodic boundary conditions could include an additional phase factor $\phi_1$ to the modulations, which would allow one to create a ring model penetrated by a finite flux. It is important to note that our proposal is not limited to 1-D lattices, although only for this case the interpretation in terms of an anyon model is valid. By adding an extended lattice in a second real-space direction one may create a 2-D or cylinder-like system with unconventional correlated hoppings and fluxes.

In the second part of the Thesis we studied the Quantum Link Model, a lattice gauge theory particularly suitable for quantum simulations, by virtue of the truncated gauge field Hilbert space. Starting from the rich literature on 1-D compact QED QLMs, we investigated the spin-½ QLM in ladder-type geometries. The promotion to a quasi 2-D space unveiled a rich ground-state phase diagram, featuring a symmetry-protected topological phase at zero mass. We revealed and assessed the presence of such a phase by looking at the entanglement spectrum and by probing non-local and topological order parameters, which can be conveniently extracted using Tensor Network methods. The evidence of topological properties is an element of novelty within systems with mediated interactions. The relation between lattice quantum field theories and topology is still a vastly unexplored and very intriguing subject, which has just recently begun to attract interest [210, 211]. Motivated by the appealing perspectives offered by the (2+1)-d cQED QLM, we extended the investigation on this model to three and four legs as well, both on ladder and on cylinder geometries. We found that the SPT phase is absent in any other system than the two-leg ladder. However, a Haldane-type physics is solidly present on the boundary legs of the ladders, a property which has found justification in the spin-fixing on the edges. We studied the model on the cylinder to explore the effects on the phase diagram of a semi-infinite geometry, with an emphasis on the relation between the QLM and solid-state models such as the Quantum Dimer or the Square Ice models. We observed that, despite the absence of plaquette terms, the quasi-two-dimensional QLMs are characterized by a highly non-trivial physics. In the large mass limit, the gauge spins are arranged in aligned or counter-aligned patterns that remind the columnar phase of the QDM or the Neél phase of the SIM. At vanishing masses, we found a disordered phase in the region where the two-leg ladder hosts the SPT phase. The phase, which resembles the RK point of the QDM, presents edge Haldane-like ordering in ladders. While being limited to a small number of legs, our observations are robust over two-, three- and four-leg ladders and four-leg cylinders, strongly hinting that the intermediate disordered phase may survive in more general 2-D lattices, which might inspire further numerical efforts in this direction.

Concerning the experimental realization, we have discussed a simplified dynamical method that permits the (quasi-)adiabatic creation of the states of the quantum-link models and, in particular, the topological phase in the two-leg ladder. The simple scheme for the realization of spin-1/2 U(1) QLMs is based on single-component fermions loaded in an optical lattice with $s$ and $p$ bands. However, instead of higher orbitals, one could equivalently realize the scheme through hyper-fine or spatial degrees of freedom, providing more flexibility for quantum simulation.

Many open questions are still to be answered, which regard the properties of QLMs and LGTs in two-dimensions. It would be interesting, for instance, to attain the ground state phase diagram and to understand the fate and the nature of the intermediate phase in the thermodynamic limit. Moreover, very recent results, which have not been discussed in this Thesis, show that whereas striped phases are confining, the intermediate disordered phase is deconfining (i.e. the string tension between gauge charges does not grow with the inter-charge distance). This opens exciting perspectives for the study not only of spin-liquid-like phases in the absence of explicit plaquette terms, but also the possibility to analyse confinement/deconfinement transitions.

Major open challenges comprise the engineering of plaquette terms (ring-exchange and RK) terms, which would be a sound breakthrough in the context of analogue quantum simulation of dynamical gauge models. However, as our results have shown, this issue could be sidestepped in the regimes in which QDM-like physics can be attained through the sole dynamics of the coupled mass-gauge fields in 2-D QLMs, for which feasible experimental schemes, including the minimalistic method discussed in this Thesis, have been proposed.

# Appendix A

# Derivation of the effective model via Magnus expansion

For the simplified case of a time periodic Hamiltonian, i.e. assuming that the frequencies $\omega_1 = \Delta$ and $\omega_2 = \Delta + U$ are integer multiples of $\omega = |\Delta - U|$ ($\omega_1 = m_1\omega$, $\omega_2 = m_2\omega$), we may obtain the same effective Hamiltonian of Eqs. (3.12) and (3.14) employing a formal Magnus expansion [63, 212–214] or Floquet analysis [100]. Following the presentation of Ref. [214] we may express the effective Hamiltonian as a series in $1/\omega$ as $\hat{H}_{\text{eff}} = H^{(0)} + H^{(1)}_{ME} + \mathcal{O}\left(\frac{1}{\omega^2}\right)$, ultimately resulting from an integral over time on period $T = 2\pi/\omega$. The lowest order term

$$H^{(0)} = \frac{1}{T}\int_0^T dt_1 H(t_1) \tag{A.1}$$

provides Eq. (3). The first order correction in $1/\omega$ may be expressed as [212]

$$H^{(1)}_{ME} = \frac{-\mathrm{i}}{2T}\int_0^T dt_2 \int_0^{t_2} dt_1 [H(t_2), H(t_1)]. \tag{A.2}$$

If the time periodic Hamiltonian is given by a Fourier series $H(t) = \hat{H}_0 + \sum_n V^{(n)}\mathrm{e}^{in\omega t}$, then

$$H^{(1)}_{ME} = \frac{1}{\omega}\sum_n \frac{1}{n}\Big([V^{(n)}, V^{(-n)}] - [V^{(n)}, \hat{H}_0] + [V^{(-n)}, \hat{H}_0]\Big). \tag{A.3}$$

In our case, the Fourier series is restricted to the following three terms:

$$\begin{aligned} V^{(\pm 1)} &= -\frac{\delta J_3}{2} H_{hop}, \\ V^{(\pm m_1)} &= -e^{\pm \mathrm{i}\phi}\frac{\delta J_1}{2} H_{hop}, \\ V^{(\pm m_2)} &= -e^{\pm \mathrm{i}\phi}\frac{\delta J_2}{2} H_{hop}, \end{aligned} \tag{A.4}$$

where $H_{hop} = \sum_{j,\sigma} \hat{c}^{\dagger}_{j+1,\sigma}\hat{c}_{j,\sigma}$. Equation (2) can be recovered by expanding the exponential term $\mathrm{e}^{\pm \mathrm{i}tUn_{j\sigma}} = 1 + (\mathrm{e}^{\pm \mathrm{i}tU} - 1)n_{j\sigma}$. Then

$$\tilde{\mathcal{H}}(t) = (J_0 + \delta J(t))\left(\mathrm{e}^{\mathrm{i}t[\Delta - U]}\bar{V}^{(1)} + \mathrm{e}^{\mathrm{i}t\Delta}\bar{V}^{(2)} + \mathrm{e}^{\mathrm{i}t[\Delta+U]}\bar{V}^{(3)} + \text{H.c.}\right) \tag{A.5}$$

with

$$\begin{aligned}
\bar{V}^{(1)} &= \sum_{j,\sigma} d^{\dagger}_{j,\sigma}\hat{c}_{j+1,\sigma} - d^{\dagger}_{j,\sigma}d_{j+1,\sigma}\,, \\
\bar{V}^{(2)} &= \sum_{j,\sigma} \left(d^{\dagger}_{j,\sigma} - \hat{c}_{j,\sigma}\right)\left(d^{\dagger}_{j+1,\sigma} - \hat{c}_{j+1,\sigma}\right)\,, \\
\bar{V}^{(3)} &= \sum_{j,\sigma} \hat{c}^{\dagger}_{j,\sigma}d_{j+1,\sigma} - d^{\dagger}_{j,\sigma}d_{j+1,\sigma},
\end{aligned}$$

where we employ the correlated annihilation operator $d_{j,\sigma} \equiv n_{j,\bar{\sigma}}\hat{c}_{j,\sigma}$. Neglecting terms of order $J_0\delta J$ and $\delta J^2$ we may write

$$H^{(1)}_{ME} = \frac{J_0^2}{\Delta - U}\left[\bar{V}^{(1)}, \bar{V}^{(1)\dagger}\right] + \frac{J_0^2}{\Delta}\left[\bar{V}^{(2)}, \bar{V}^{(2)\dagger}\right] + \frac{J_0^2}{\Delta + U}\left[\bar{V}^{(3)}, \bar{V}^{(3)\dagger}\right] + \mathcal{O}\left(\delta J\right)\,, \tag{A.6}$$

which after some algebra yields Eq. (4).

# Appendix B

# Multi-component phase

## Two-particle model

We assume for simplicity $\beta = 1$, hence we consider the model described in Eq.(3.19). We are interested in the two-particle problem, with one ↑ particle and one ↓ particle. Let $|D(j)\rangle$ be a doubly occupied site, and $|S(j, j+l)\rangle$ a singlet state placed in sites $j$ and $j+l$. Then:

$$\begin{aligned}
\hat{H}_{\text{eff}}|D(j)\rangle &= -\frac{\delta J_1}{\sqrt{2}}\left[e^{\text{i}\phi}|S(j,j+1)\rangle + e^{-\text{i}\phi}|S(j-1,j)\rangle\right] + \tilde{U}|D(j)\rangle, \\
\hat{H}_{\text{eff}}|S(j,j+1)\rangle &= -\frac{\delta J_1}{\sqrt{2}}\left[e^{\text{i}\phi}|D(j+1)\rangle + e^{-\text{i}\phi}|D(j)\rangle\right] \\
&\quad -\frac{\delta J_1}{2}\left[|S(j-1,j+1)\rangle + |S(j,j+2)\rangle\right], \\
\hat{H}_{\text{eff}}|S(j,j+l)\rangle &\overset{l\geq 1}{=} -\frac{\delta J_1}{2}\Big[|S(j-1,j+l)\rangle + |S(j+1,j+l)\rangle \\
&\quad + |S(j,j+l-1)\rangle + |S(j,j+l+1)\rangle\Big].
\end{aligned}$$

Let us define

$$|D(k)\rangle = \frac{1}{\sqrt{L}}\sum_l e^{\text{i}kl}|D(l)\rangle \tag{B.1}$$

$$|S(j,k)\rangle = \frac{1}{\sqrt{L}}\sum_l e^{\text{i}k(l+j/2)}|S(l,l+j)\rangle \tag{B.2}$$

with $k$ the center-of-mass momentum of the pair, and $L$ the number of sites. Then $\hat{H}_{\text{eff}} = \sum_k \hat{H}_{\text{eff}}(k)$, with $\hat{H}_{\text{eff}}(k) = \hat{H}_0(k) + H_1(k)$, where:

$$\begin{aligned}
\hat{H}_0(k) &= \tilde{U}|D(k)\rangle\langle D(k)| - A(k)\left[|S(1,k)\rangle\langle D(k)| + H.c.\right], \\
H_1(k) &= -B(k)\sum_{j\geq 1}\left[|S(j,k)\rangle\langle S(j+1,k)| + H.c.\right],
\end{aligned} \tag{B.3}$$

with $A(k) = \sqrt{2}\delta J_1\cos(k/2-\phi)$ and $B(k) = \delta J_1\cos(k/2)$. We may diagonalize $\hat{H}_0$:

$$\hat{H}_0(k) = E_+(k)|\tilde{P}(k)\rangle\langle\tilde{P}(k)| + E_-(k)|P(k)\rangle\langle P(k)|, \tag{B.4}$$

where the eigenenergies are

$$E_\pm(k) = \frac{\tilde{U}}{2} \pm \sqrt{\left(\frac{\tilde{U}}{2}\right)^2 + A(k)^2}, \tag{B.5}$$

and the corresponding eigenstates are

$$\begin{aligned}|\tilde{P}(k)\rangle &= \cos\theta(k)|D(k)\rangle + \sin\theta(k)|S(1,k)\rangle,\\ |P(k)\rangle &= -\sin\theta(k)|D(k)\rangle + \cos\theta(k)|S(1,k)\rangle,\end{aligned} \tag{B.6}$$

with $\tan\theta(k) = \frac{\tilde{U}/2 - E_-(k)}{A(k)}$. The Hamiltonian $\hat{H}_0$ characterizes deeply-bound pairs. We may then split $H_1(k) = H_c(k) + H_u(k)$, where

$$H_u(k) = -B(k)\sum_{j\geq 2}\left[|S(j,k)\rangle\langle S(j+1,k)| + H.c.\right] \tag{B.7}$$

determines the physics of broken pairs, where the dynamics of the relative coordinate $j$ is given by the hopping rate $B(k)$, and

$$H_c(k) = -\,B(k)\left(\sin\theta(k)|P(k)\rangle + \cos\theta(k)|\tilde{P}(k)\rangle\right)\langle S(2,k)| + H.c, \tag{B.8}$$

characterizes the coupling between deeply-bound and unbound pairs. Note that such a coupling is also given by $B(k)$.

Let us consider $\phi = \frac{\pi}{2}$. In that case,

$$E_\pm(k) = \frac{\tilde{U}}{2} \pm \sqrt{\left(\frac{\tilde{U}}{2}\right)^2 + 2\delta J_1^2\sin^2(k/2)}. \tag{B.9}$$

The minimal energy is clearly for $k = \pi$, $E_P \equiv E_-(\pi) = \frac{\tilde{U}}{2} \pm \sqrt{\left(\frac{\tilde{U}}{2}\right)^2 + 2\delta J_1^2}$. If existing, bound pairs will quasi-condense in $|P\rangle \equiv |P(\pi)\rangle$. Crucially, $B(\pi) = 0$, and hence $H_c = 0$. As a result, $|P\rangle$ remains a deeply-bound two-particle eigenstate, fully decoupled from the unbound pairs, irrespective of the value of $\tilde{U}/\delta J_1$. On the contrary for $\phi = 0$, i.e. without occupation-dependent gauge (occupation-dependent gauge), the bound pairs are fully connected with the rest and cannot be formed unless $\tilde{U} < 0$ dominates. For $\phi$ in the vicinity of $\pi/2$ the coupling $H_c$ may be considered perturbative, and deeply-bound pairs due to the occupation-dependent gauge still exist even if $\phi$ is not exactly $\pi/2$.

The existence of these pairs that are deeply-bound by the occupation-dependent gauge rather than by attractive interactions is crucial to understand the nature of the MC phase. The metallic phase is stable if $E_P/2 > E_F$, with $E_F$ the Fermi energy of the metal. However, for decreasing $\tilde{U} > 0$, $E_F < E_P/2$, and hence it is energetically favorable to pair part of the Fermi sea into $|P\rangle$ pairs, until reaching an equilibrium at a new Fermi energy $E_F' = E_P/2$. This partial pairing, and the corresponding coexistence of a two-component metal and a superconductor explains the MC phase, and its $c = 3$ central charge. For $E_-(\pi) < -2\delta J_1$ (which occurs at $\tilde{U}/\delta J_1 \simeq -1$) the Fermi sea is completely depleted, and the system enters the fully-paired (SS) phase.

## Momentum distribution

The momentum distribution of the ↑ component in the $|P\rangle$ state is

$$n_\uparrow^{(P)}(k) = \sum_{i,j} e^{\mathrm{i}k(i-j)}\langle P|\hat{c}_{i,\uparrow}^\dagger \hat{c}_{j,\uparrow}|P\rangle,$$

where

$$\langle P|\hat{c}^{\dagger}_{l,\uparrow}\hat{c}_{l,\uparrow}|P\rangle = \frac{1}{L}, \tag{B.10}$$

$$\langle P|\hat{c}^{\dagger}_{l+1,\uparrow}\hat{c}_{l,\uparrow}|P\rangle = \langle P|\hat{c}^{\dagger}_{l-1,\uparrow}\hat{c}_{l,\uparrow}|P\rangle^{*} = \frac{-\sin(2\theta(\pi))}{L\sqrt{2}}e^{\mathrm{i}\pi/2}, \tag{B.11}$$

$$\langle P|\hat{c}^{\dagger}_{l+2,\uparrow}\hat{c}_{l,\uparrow}|P\rangle = \langle P|\hat{c}^{\dagger}_{l-2,\uparrow}\hat{c}_{l,\uparrow}|P\rangle = \frac{-\sin^{2}(\theta(\pi))}{2L}, \tag{B.12}$$

and other correlations are zero. After normalizing:

$$\begin{aligned} n^{(P)}_{\uparrow}(k) = \frac{1}{2\pi}\Big[&1-\sqrt{2}\sin(2\theta(\pi))\sin(k/2) \\ &-\sin^{2}\theta(\pi)\cos(2k)\Big] \end{aligned} \tag{B.13}$$

with $\theta(\pi) = \arctan\left[\chi + \sqrt{\chi^{2}+1}\right]$, with $\chi = \frac{\tilde{U}}{2\sqrt{2}\delta J_1}$. For the ↓ component the expression is identical. This expression is in excellent agreement with the blurred momentum distribution that is found in our numerics in the MC phase (Figure 3(c)) in addition to the partially-depleted slab-like Fermi sea.

# List of Figures

1.1 Superfluid to Mott phase transition . . . . . 8
1.2 Phase diagram of the Fermi-Hubbard model . . . . . 9
1.3 Lattice shaking . . . . . 10
1.4 Amplitude modulation spectroscopy of an optical lattice . . . . . 11
1.5 Superlattice with $p$-band population . . . . . 12

2.1 Scheme of the Raman-assisted tunnelling . . . . . 18
2.2 Artificial gauge with Raman-assisted tunnelling . . . . . 19
2.3 Decoupled ladders permeated by magnetic field . . . . . 20
2.4 Excitations in periodically driven lattices . . . . . 25
2.5 Artificial gauge with lattice shaking . . . . . 26
2.6 Illustration of particles exchange in three dimensions . . . . . 28
2.7 Drawing of the Jordan-Wigner transformation for 1-D anyons . . . . . 30
2.8 Density-dependent artificial gauge field . . . . . 31

3.1 Scheme of the three-color modulation . . . . . 36
3.2 Time-evolution of the average double occupancy . . . . . 40
3.3 Three-colors modulation, ground-state phase diagram . . . . . 42
3.4 Momentum distribution vs Peierls phase . . . . . 43
3.5 Effective model with nearest-neighbour interaction . . . . . 44
3.6 Mott to density-wave phase transition with NN-interaction . . . . . 45
3.7 Equivalence between the time-independent and the anyon model . . . 46
3.8 Scheme for anyons interferometry . . . . . 47
3.9 Experimental protocol for anyons interferometry . . . . . 48
3.10 Local density time evolution . . . . . 49
3.11 Central sites density diffusion and retrieval . . . . . 50
3.12 Spin polarization vs statistical angle . . . . . 51
3.13 Two-particles bound states . . . . . 52
3.14 Expansion dynamics of the total density and spin density . . . . . 53

4.1 Illustration of the (2+1)-d QED Quantum Link Model . . . . . 58
4.2 Quantum dimer model ground state phases . . . . . 64
4.3 Quantum simulation of the spin-1 QLM . . . . . 67
4.4 Exact gauge invariance with angular momentum conservation . . . . . 68
4.5 QLM to Kogut-Susskind convergence . . . . . 69

5.1 Illustration of two QLL rung states . . . . . 74
5.2 1-D QLM ground-state order parameters . . . . . 76
5.3 Illustration of two QLL states at large negative mass . . . . . 77
5.4 Spin configurations and ring-exchange processes at large mass . . . . . 78
5.5 Phase diagram of the QLL . . . . . 79
5.6 Order parameters vs rung tunnelling amplitude at finite mass . . . . . 80
5.7 Order parameters for vanishing mass . . . . . 81

5.8 Topological order parameters at zero mass . . . . . . . . . . . . . . . . 82
5.9 Fidelity susceptibility analysis . . . . . . . . . . . . . . . . . . . . . . . . 83
5.10 Spin-½ QLM on cold gases via *s*-*p* orbitals . . . . . . . . . . . . . . . . . 84
5.11 Quasi-adiabatic preparation of the SPT phase . . . . . . . . . . . . . . . 85
5.12 Quench dynamics on a 1-D QLM . . . . . . . . . . . . . . . . . . . . . . 86
5.13 Sketches of the striped columnar and disordered phases . . . . . . . . 87
5.14 Phase diagrams of the four-leg QLM cylinder . . . . . . . . . . . . . . . 88
5.15 String-parity order parameters on edges and bulk . . . . . . . . . . . . 89
5.16 Entanglement spectrum of the three- and four-leg ladders . . . . . . . 90

6.1 Real-space renormalization group, standard approach limitations . . . 94
6.2 Illustration of maximally entangled states . . . . . . . . . . . . . . . . . 96
6.3 Illustration of a DMRG Tensor Network . . . . . . . . . . . . . . . . . . 99
6.4 Pointwise symmetric tensors . . . . . . . . . . . . . . . . . . . . . . . . . 100
6.5 Elements of a Tensor Network for (i)DMRG . . . . . . . . . . . . . . . . 102
6.6 Gauge invariant rung states . . . . . . . . . . . . . . . . . . . . . . . . . 104

# List of Tables

6.1 Hilbert space dimension for full and gauge-invariant rung states . . . 105

# Bibliography

[1] A. A. Houck, H. E. Türeci, and J. Koch. "On-chip quantum simulation with superconducting circuits". In: *Nature Physics* 8.4 (Apr. 2012), pp. 292–299. DOI: 10.1038/nphys2251.

[2] R. P. Feynman. "Simulating physics with computers". In: *International Journal of Theoretical Physics* 21.6-7 (June 1982), pp. 467–488. DOI: 10.1007/bf02650179.

[3] S. Lloyd. "Universal Quantum Simulators". In: *Science* 273.5278 (Aug. 1996), pp. 1073–1078. DOI: 10.1126/science.273.5278.1073.

[4] L. Lamata et al. "Digital-analogue quantum simulations with superconducting circuits". In: *Advances in Physics: X* 3.1 (Jan. 2018), p. 1457981. DOI: 10.1080/23746149.2018.1457981.

[5] K. R. Brown, J. Kim, and C. Monroe. "Co-designing a scalable quantum computer with trapped atomic ions". In: *npj Quantum Information* 2.1 (Nov. 2016). DOI: 10.1038/npjqi.2016.34.

[6] R. Blatt and C. F. Roos. "Quantum simulations with trapped ions". In: *Nature Physics* 8.4 (Apr. 2012), pp. 277–284. DOI: 10.1038/nphys2252.

[7] J. S. Pedernales et al. "Quantum Rabi Model with Trapped Ions". In: *Scientific Reports* 5.1 (Oct. 2015). DOI: 10.1038/srep15472.

[8] R. Puebla, M.-J. Hwang, and M. B. Plenio. "Excited-state quantum phase transition in the Rabi model". In: *Physical Review A* 94.2 (Aug. 2016). DOI: 10.1103/physreva.94.023835.

[9] S. Korenblit et al. "Quantum simulation of spin models on an arbitrary lattice with trapped ions". In: *New Journal of Physics* 14.9 (Sept. 2012), p. 095024. DOI: 10.1088/1367-2630/14/9/095024.

[10] URL: https://ucan.physics.utoronto.ca/research-groups/.

[11] URL: https://quantumoptics.at/en/links.html.

[12] A. Ashkin. "Atomic-Beam Deflection by Resonance-Radiation Pressure". In: *Physical Review Letters* 25.19 (Nov. 1970), pp. 1321–1324. DOI: 10.1103/physrevlett.25.1321.

[13] T. W. Hänsch and A. L. Schawlow. "Cooling of gases by laser radiation". In: *Optics Communications* 13.1 (Jan. 1975), pp. 68–69. DOI: 10.1016/0030-4018(75)90159-5.

[14] K. G. Wilson. "Confinement of quarks". In: *Physical Review D* 20.4 (1975), pp. 637–637.

[15] W. D. Phillips. "Nobel Lecture: Laser cooling and trapping of neutral atoms". In: *Reviews of Modern Physics* 70.3 (July 1998), pp. 721–741. DOI: 10.1103/revmodphys.70.721.

[16] *Alkali D Line Data*. https://steck.us/alkalidata/. Accessed: 2019-07-08.

[17] P. D. Lett et al. "Observation of Atoms Laser Cooled below the Doppler Limit". In: *Physical Review Letters* 61.2 (July 1988), pp. 169–172. DOI: `10.1103/physrevlett.61.169`.

[18] P. L. Gould, P. D. Lett, and W. D. Phillips. *New Measurements with Optical Molasses*. Springer Berlin Heidelberg, 1987, pp. 64–67. DOI: `10.1007/978-3-540-47973-4_16`.

[19] J. Dalibard and C. Cohen-Tannoudji. "Laser cooling below the Doppler limit by polarization gradients: simple theoretical models". In: *J. Opt. Soc. Am. B* 6.11 (Nov. 1989), pp. 2023–2045. DOI: `10.1364/JOSAB.6.002023`.

[20] R. Grimm, M. Weidemüller, and Y. B. Ovchinnikov. *Optical Dipole Traps for Neutral Atoms*. Elsevier, 2000, pp. 95–170. DOI: `10.1016/s1049-250x(08)60186-x`.

[21] D. M. Stamper-Kurn et al. "Optical Confinement of a Bose-Einstein Condensate". In: *Physical Review Letters* 80.10 (Mar. 1998), pp. 2027–2030. DOI: `10.1103/physrevlett.80.2027`.

[22] M. H. Anderson et al. "Observation of Bose-Einstein Condensation in a Dilute Atomic Vapor". In: *Science* 269.5221 (July 1995), pp. 198–201. DOI: `10.1126/science.269.5221.198`.

[23] K. B. Davis et al. "Bose-Einstein Condensation in a Gas of Sodium Atoms". In: *Physical Review Letters* 75.22 (Nov. 1995), pp. 3969–3973. DOI: `10.1103/physrevlett.75.3969`.

[24] S. Burger et al. "Dark Solitons in Bose-Einstein Condensates". In: *Physical Review Letters* 83.25 (Dec. 1999), pp. 5198–5201. DOI: `10.1103/physrevlett.83.5198`.

[25] K. W. Madison et al. "Vortex Formation in a Stirred Bose-Einstein Condensate". In: *Physical Review Letters* 84.5 (Jan. 2000), pp. 806–809. DOI: `10.1103/physrevlett.84.806`.

[26] M. W. Zwierlein et al. "Vortices and superfluidity in a strongly interacting Fermi gas". In: *Nature* 435.7045 (June 2005), pp. 1047–1051. DOI: `10.1038/nature03858`.

[27] G. Lamporesi et al. "Spontaneous creation of Kibble–Zurek solitons in a Bose–Einstein condensate". In: *Nature Physics* 9.10 (Sept. 2013), pp. 656–660. DOI: `10.1038/nphys2734`.

[28] L. Tanzi et al. "Observation of a Dipolar Quantum Gas with Metastable Supersolid Properties". In: *Physical Review Letters* 122.13 (Apr. 2019). DOI: `10.1103/physrevlett.122.130405`.

[29] M. Greiner et al. "Quantum phase transition from a superfluid to a Mott insulator in a gas of ultracold atoms". In: *Nature* 415.6867 (Jan. 2002), pp. 39–44. DOI: `10.1038/415039a`.

[30] ISBN: 9780444538574. DOI: `10.1016/b978-0-444-53857-4.00005-2`.

[31] A. Georges and T. Giamarchi. *Many-Body Physics with Ultracold Gases*. Ed. by Christophe Salomon, Georgy V. Shlyapnikov, and Leticia F. Cugliandolo. Lecture Notes of the Les Houches Summer School. Oxford University Press, 2012. Chap. 1. DOI: `10.1093/acprof:oso/9780199661886.001.0001`.

[32] B. DeMarco and D. S. Jin. "Exploring a quantum degenerate gas of fermionic atoms". In: *Physical Review A* 58.6 (Dec. 1998), R4267–R4270. DOI: `10.1103/physreva.58.r4267`.

[33] L. Tarruell and L. Sanchez-Palencia. "Quantum simulation of the Hubbard model with ultracold fermions in optical lattices". In: *Comptes Rendus Physique* 19.6 (Sept. 2018), pp. 365–393. DOI: `10.1016/j.crhy.2018.10.013`.

[34] M. Troyer and U.-J. Wiese. "Computational Complexity and Fundamental Limitations to Fermionic Quantum Monte Carlo Simulations". In: *Physical Review Letters* 94.17 (May 2005). DOI: `10.1103/physrevlett.94.170201`.

[35] R. Orús. "A practical introduction to tensor networks: Matrix product states and projected entangled pair states". In: *Annals of Physics* 349 (Oct. 2014), pp. 117–158. DOI: `10.1016/j.aop.2014.06.013`.

[36] P. W. Anderson. "The Resonating Valence Bond State in La2CuO4 and Superconductivity". In: *Science* 235.4793 (Mar. 1987), pp. 1196–1198. DOI: `10.1126/science.235.4793.1196`.

[37] P. A. Lee, N. Nagaosa, and X.-G. Wen. "Doping a Mott insulator: Physics of high-temperature superconductivity". In: *Reviews of Modern Physics* 78.1 (Jan. 2006), pp. 17–85. DOI: `10.1103/revmodphys.78.17`.

[38] K. Le Hur and T. M. Rice. "Superconductivity close to the Mott state: From condensed-matter systems to superfluidity in optical lattices". In: *Annals of Physics* 324.7 (July 2009), pp. 1452–1515. DOI: `10.1016/j.aop.2009.02.004`.

[39] M. Holthaus. "Collapse of minibands in far-infrared irradiated superlattices". In: *Physical Review Letters* 69.2 (July 1992), pp. 351–354. DOI: `10.1103/physrevlett.69.351`.

[40] A. Eckardt, C. Weiss, and M. Holthaus. "Superfluid-Insulator Transition in a Periodically Driven Optical Lattice". In: *Physical Review Letters* 95.26 (Dec. 2005). DOI: `10.1103/physrevlett.95.260404`.

[41] H. Lignier et al. "Dynamical Control of Matter-Wave Tunneling in Periodic Potentials". In: *Physical Review Letters* 99.22 (Nov. 2007). DOI: `10.1103/physrevlett.99.220403`.

[42] A. Zenesini et al. "Coherent Control of Dressed Matter Waves". In: *Physical Review Letters* 102.10 (Mar. 2009). DOI: `10.1103/physrevlett.102.100403`.

[43] R. Ma et al. "Photon-Assisted Tunneling in a Biased Strongly Correlated Bose Gas". In: *Physical Review Letters* 107.9 (Aug. 2011). DOI: `10.1103/physrevlett.107.095301`.

[44] G. Wirth, M. Ölschläger, and A. Hemmerich. "Evidence for orbital superfluidity in the P-band of a bipartite optical square lattice". In: *Nature Physics* 7.2 (Dec. 2010), pp. 147–153. DOI: `10.1038/nphys1857`.

[45] O. Dutta et al. "Non-standard Hubbard models in optical lattices: a review". In: *Reports on Progress in Physics* 78.6 (May 2015), p. 066001. DOI: `10.1088/0034-4885/78/6/066001`.

[46] P. Soltan-Panahi et al. "Quantum phase transition to unconventional multi-orbital superfluidity in optical lattices". In: *Nature Physics* 8.1 (Oct. 2011), pp. 71–75. DOI: `10.1038/nphys2128`.

[47] D. Xiao, M.-C. Chang, and Q. Niu. "Berry phase effects on electronic properties". In: *Reviews of Modern Physics* 82.3 (July 2010), pp. 1959–2007. DOI: `10.1103/revmodphys.82.1959`.

[48] D. Jaksch and P. Zoller. "Creation of effective magnetic fields in optical lattices: the Hofstadter butterfly for cold neutral atoms". In: *New Journal of Physics* 5 (2003), pp. 56–56. DOI: `10.1088/1367-2630/5/1/356`.

[49] J. Dalibard et al. "Colloquium: Artificial gauge potentials for neutral atoms". In: *Reviews of Modern Physics* 83.4 (Nov. 2011), pp. 1523–1543. DOI: 10.1103/revmodphys.83.1523.

[50] H. Miyake et al. "Realizing the Harper Hamiltonian with Laser-Assisted Tunneling in Optical Lattices". In: *Physical Review Letters* 111.18 (2013). DOI: 10.1103/physrevlett.111.185302.

[51] M. Aidelsburger et al. "Realization of the Hofstadter Hamiltonian with Ultracold Atoms in Optical Lattices". In: *Physical Review Letters* 111.18 (2013). DOI: 10.1103/physrevlett.111.185301.

[52] M. Atala et al. "Observation of chiral currents with ultracold atoms in bosonic ladders". In: *Nature Physics* 10.8 (July 2014), pp. 588–593. DOI: 10.1038/nphys2998.

[53] A. Celi et al. "Synthetic Gauge Fields in Synthetic Dimensions". In: *Physical Review Letters* 112.4 (Jan. 2014). DOI: 10.1103/physrevlett.112.043001.

[54] M. Mancini et al. "Observation of chiral edge states with neutral fermions in synthetic Hall ribbons". In: *Science* 349.6255 (Sept. 2015), pp. 1510–1513. DOI: 10.1126/science.aaa8736.

[55] B. K. Stuhl et al. "Visualizing edge states with an atomic Bose gas in the quantum Hall regime". In: *Science* 349.6255 (Sept. 2015), pp. 1514–1518. DOI: 10.1126/science.aaa8515.

[56] A. Eckardt. "Colloquium: Atomic quantum gases in periodically driven optical lattices". In: *Reviews of Modern Physics* 89.1 (Mar. 2017). DOI: 10.1103/revmodphys.89.011004.

[57] J. Struck et al. "Tunable Gauge Potential for Neutral and Spinless Particles in Driven Optical Lattices". In: *Physical Review Letters* 108.22 (May 2012). DOI: 10.1103/physrevlett.108.225304.

[58] J. Gong, L. Morales-Molina, and P. Hänggi. "Many-Body Coherent Destruction of Tunneling". In: *Physical Review Letters* 103.13 (Sept. 2009). DOI: 10.1103/physrevlett.103.133002.

[59] F. K. Abdullaev, P. G. Kevrekidis, and M. Salerno. "Compactons in Nonlinear Schrödinger Lattices with Strong Nonlinearity Management". In: *Physical Review Letters* 105.11 (Sept. 2010). DOI: 10.1103/physrevlett.105.113901.

[60] M. Di Liberto et al. "Quantum simulation of correlated-hopping models with fermions in optical lattices". In: *Physical Review A* 89.1 (Jan. 2014). DOI: 10.1103/physreva.89.013624.

[61] Á. Rapp, X. Deng, and L. Santos. "Ultracold Lattice Gases with Periodically Modulated Interactions". In: *Physical Review Letters* 109.20 (Nov. 2012). DOI: 10.1103/physrevlett.109.203005.

[62] S. Greschner, L. Santos, and D. Poletti. "Exploring Unconventional Hubbard Models with Doubly Modulated Lattice Gases". In: *Physical Review Letters* 113.18 (Oct. 2014). DOI: 10.1103/physrevlett.113.183002.

[63] G. Jotzu et al. "Experimental realization of the topological Haldane model with ultracold fermions". In: *Nature* 515.7526 (Nov. 2014), pp. 237–240. DOI: 10.1038/nature13915.

[64] J. M. Leinaas and J. Myrheim. "On the theory of identical particles". In: *Il Nuovo Cimento B Series 11* 37.1 (Jan. 1977), pp. 1–23. DOI: 10.1007/bf02727953.

[65] F. Wilczek. “Magnetic Flux, Angular Momentum, and Statistics”. In: *Physical Review Letters* 48.17 (Apr. 1982), pp. 1144–1146. DOI: 10.1103/physrevlett.48.1144.

[66] F. Wilczek. “Quantum Mechanics of Fractional-Spin Particles”. In: *Physical Review Letters* 49.14 (Oct. 1982), pp. 957–959. DOI: 10.1103/physrevlett.49.957.

[67] F. D. M. Haldane. “"Fractional statistics" in arbitrary dimensions: A generalization of the Pauli principle”. In: *Physical Review Letters* 67.8 (Aug. 1991), pp. 937–940. DOI: 10.1103/physrevlett.67.937.

[68] Y.-S. Wu. “Statistical Distribution for Generalized Ideal Gas of Fractional-Statistics Particles”. In: *Physical Review Letters* 73.7 (Aug. 1994), pp. 922–925. DOI: 10.1103/physrevlett.73.922.

[69] G. S. Canright and S. M. Girvin. “Fractional Statistics: Quantum Possibilities in Two Dimensions”. In: *Science* 247.4947 (Mar. 1990), pp. 1197–1205. DOI: 10.1126/science.247.4947.1197.

[70] F. E. Camino, W. Zhou, and V. J. Goldman. “Realization of a Laughlin quasiparticle interferometer: Observation of fractional statistics”. In: *Physical Review B* 72.7 (Aug. 2005). DOI: 10.1103/physrevb.72.075342.

[71] L. Jiang et al. “Anyonic interferometry and protected memories in atomic spin lattices”. In: *Nature Physics* 4.6 (Apr. 2008), pp. 482–488. DOI: 10.1038/nphys943.

[72] P. Bonderson, K. Shtengel, and J. K. Slingerland. “Interferometry of non-Abelian anyons”. In: *Annals of Physics* 323.11 (Nov. 2008), pp. 2709–2755. DOI: 10.1016/j.aop.2008.01.012.

[73] Z. N. C. Ha. “Exact Dynamical Correlation Functions of Calogero-Sutherland Model and One-Dimensional Fractional Statistics”. In: *Physical Review Letters* 73.12 (Sept. 1994), pp. 1574–1577. DOI: 10.1103/physrevlett.73.1574.

[74] M. V. N. Murthy and R. Shankar. “Thermodynamics of a One-Dimensional Ideal Gas with Fractional Exclusion Statistics”. In: *Physical Review Letters* 73.25 (Dec. 1994), pp. 3331–3334. DOI: 10.1103/physrevlett.73.3331.

[75] Y.-S. Wu and Y. Yu. “Bosonization of One-Dimensional Exclusons and Characterization of Luttinger Liquids”. In: *Physical Review Letters* 75.5 (July 1995), pp. 890–893. DOI: 10.1103/physrevlett.75.890.

[76] J.-X. Zhu and Z. D. Wang. “Topological effects associated with fractional statistics in one-dimensional mesoscopic rings”. In: *Physical Review A* 53.1 (Jan. 1996), pp. 600–603. DOI: 10.1103/physreva.53.600.

[77] L. Amico, A. Osterloh, and U. Eckern. “One-dimensionalXXZmodel for particles obeying fractional statistics”. In: *Physical Review B* 58.4 (July 1998), R1703–R1706. DOI: 10.1103/physrevb.58.r1703.

[78] A. Kundu. “Exact Solution of Double$\delta$Function Bose Gas through an Interacting Anyon Gas”. In: *Physical Review Letters* 83.7 (Aug. 1999), pp. 1275–1278. DOI: 10.1103/physrevlett.83.1275.

[79] M. T. Batchelor, X.-W. Guan, and N. Oelkers. “One-Dimensional Interacting Anyon Gas: Low-Energy Properties and Haldane Exclusion Statistics”. In: *Physical Review Letters* 96.21 (June 2006). DOI: 10.1103/physrevlett.96.210402.

[80] M. D. Girardeau. “Anyon-Fermion Mapping and Applications to Ultracold Gases in Tight Waveguides”. In: *Physical Review Letters* 97.10 (Sept. 2006). DOI: `10.1103/physrevlett.97.100402`.

[81] P. Calabrese and M. Mintchev. “Correlation functions of one-dimensional anyonic fluids”. In: *Physical Review B* 75.23 (June 2007). DOI: `10.1103/physrevb.75.233104`.

[82] O. I. Pâţu, V. E. Korepin, and D. V. Averin. “Correlation functions of one-dimensional Lieb–Liniger anyons”. In: *Journal of Physics A: Mathematical and Theoretical* 40.50 (Nov. 2007), pp. 14963–14984. DOI: `10.1088/1751-8113/40/50/004`.

[83] Y. Hao, Y. Zhang, and S. Chen. “Ground-state properties of one-dimensional anyon gases”. In: *Physical Review A* 78.2 (Aug. 2008). DOI: `10.1103/physreva.78.023631`.

[84] Y. Hao, Y. Zhang, and S. Chen. “Ground-state properties of hard-core anyons in one-dimensional optical lattices”. In: *Physical Review A* 79.4 (Apr. 2009). DOI: `10.1103/physreva.79.043633`.

[85] P. Calabrese and R. Santachiara. “Off-diagonal correlations in one-dimensional anyonic models: a replica approach”. In: *Journal of Statistical Mechanics: Theory and Experiment* 2009.03 (Mar. 2009), P03002. DOI: `10.1088/1742-5468/2009/03/p03002`.

[86] G. Tang, S. Eggert, and A. Pelster. “Ground-state properties of anyons in a one-dimensional lattice”. In: *New Journal of Physics* 17.12 (Dec. 2015), p. 123016. DOI: `10.1088/1367-2630/17/12/123016`.

[87] A. del Campo. “Fermionization and bosonization of expanding one-dimensional anyonic fluids”. In: *Physical Review A* 78.4 (Oct. 2008). DOI: `10.1103/physreva.78.045602`.

[88] Y. Hao and S. Chen. “Dynamical properties of hard-core anyons in one-dimensional optical lattices”. In: *Physical Review A* 86.4 (Oct. 2012). DOI: `10.1103/physreva.86.043631`.

[89] L. Wang, L. Wang, and Y. Zhang. “Quantum walks of two interacting anyons in one-dimensional optical lattices”. In: *Physical Review A* 90.6 (Dec. 2014). DOI: `10.1103/physreva.90.063618`.

[90] R. Santachiara, F. Stauffer, and D. C Cabra. “Entanglement properties and momentum distributions of hard-core anyons on a ring”. In: *Journal of Statistical Mechanics: Theory and Experiment* 2007.05 (May 2007), pp. L05003–L05003. DOI: `10.1088/1742-5468/2007/05/l05003`.

[91] H. Guo, Y. Hao, and S. Chen. “Quantum entanglement of particles on a ring with fractional statistics”. In: *Physical Review A* 80.5 (Nov. 2009). DOI: `10.1103/physreva.80.052332`.

[92] G. Marmorini, M. Pepe, and P. Calabrese. “One-body reduced density matrix of trapped impenetrable anyons in one dimension”. In: *Journal of Statistical Mechanics: Theory and Experiment* 2016.7 (July 2016), p. 073106. DOI: `10.1088/1742-5468/2016/07/073106`.

[93] T. Keilmann et al. “Statistically induced phase transitions and anyons in 1D optical lattices”. In: *Nature Communications* 2.1 (June 2011). DOI: `10.1038/ncomms1353`.

[94] S. Greschner et al. "Spontaneous Increase of Magnetic Flux and Chiral-Current Reversal in Bosonic Ladders: Swimming against the Tide". In: *Physical Review Letters* 115.19 (Nov. 2015). DOI: 10.1103/physrevlett.115.190402.

[95] J. Arcila-Forero, R. Franco, and J. Silva-Valencia. "Critical points of the anyon-Hubbard model". In: *Physical Review A* 94.1 (July 2016). DOI: 10.1103/physreva.94.013611.

[96] W. Zhang et al. "Ground-state properties of the one-dimensional unconstrained pseudo-anyon Hubbard model". In: *Physical Review A* 95.5 (May 2017). DOI: 10.1103/physreva.95.053614.

[97] E. Fradkin. "Jordan-Wigner transformation for quantum-spin systems in two dimensions and fractional statistics". In: *Physical Review Letters* 63.3 (July 1989), pp. 322–325. DOI: 10.1103/physrevlett.63.322.

[98] S. Greschner and L. Santos. "Anyon Hubbard Model in One-Dimensional Optical Lattices". In: *Physical Review Letters* 115.5 (July 2015). DOI: 10.1103/physrevlett.115.053002.

[99] D. Jaksch et al. "Cold Bosonic Atoms in Optical Lattices". In: *Physical Review Letters* 81.15 (Oct. 1998), pp. 3108–3111. DOI: 10.1103/physrevlett.81.3108.

[100] C. Sträter, S. C. L. Srivastava, and A. Eckardt. "Floquet Realization and Signatures of One-Dimensional Anyons in an Optical Lattice". In: *Physical Review Letters* 117.20 (Nov. 2016). DOI: 10.1103/physrevlett.117.205303.

[101] F. Görg et al. "Realisation of density-dependent Peierls phases to couple dynamical gauge fields to matter". In: (Dec. 2018).

[102] L. W. Clark et al. "Observation of Density-Dependent Gauge Fields in a Bose-Einstein Condensate Based on Micromotion Control in a Shaken Two-Dimensional Lattice". In: *Physical Review Letters* 121.3 (July 2018). DOI: 10.1103/physrevlett.121.030402.

[103] Q. Xie et al. "The quantum Rabi model: solution and dynamics". In: *Journal of Physics A: Mathematical and Theoretical* 50.11 (Feb. 2017), p. 113001. DOI: 10.1088/1751-8121/aa5a65.

[104] M. A. Cazalilla and A. M. Rey. "Ultracold Fermi gases with emergent SU(N) symmetry". In: *Reports on Progress in Physics* 77.12 (Nov. 2014), p. 124401. DOI: 10.1088/0034-4885/77/12/124401.

[105] M. Höfer et al. "Observation of an Orbital Interaction-Induced Feshbach Resonance inYb173". In: *Physical Review Letters* 115.26 (Dec. 2015). DOI: 10.1103/physrevlett.115.265302.

[106] G. Vidal. "Classical Simulation of Infinite-Size Quantum Lattice Systems in One Spatial Dimension". In: *Physical Review Letters* 98.7 (Feb. 2007). DOI: 10.1103/physrevlett.98.070201.

[107] L. Arrachea and A. A. Aligia. "Exact Solution of a Hubbard Chain with Bond-Charge Interaction". In: *Physical Review Letters* 73.16 (Oct. 1994), pp. 2240–2243. DOI: 10.1103/physrevlett.73.2240.

[108] L. Arrachea, A. A. Aligia, and E. Gagliano. "Anomalous Flux Quantization in a Hubbard Ring with Correlated Hopping". In: *Physical Review Letters* 76.23 (June 1996), pp. 4396–4399. DOI: 10.1103/physrevlett.76.4396.

[109] L. Arrachea, E. R. Gagliano, and A. A. Aligia. “Ground-state phase diagram of an extended Hubbard chain with correlated hopping at half-filling”. In: *Physical Review B* 55.2 (Jan. 1997), pp. 1173–1184. DOI: `10.1103/physrevb.55.1173`.

[110] A. A. Aligia and L. Arrachea. “Triplet superconductivity in quasi-one-dimensional systems”. In: *Physical Review B* 60.22 (Dec. 1999), pp. 15332–15338. DOI: `10.1103/physrevb.60.15332`.

[111] A. A. Aligia et al. “Phase diagrams from topological transitions: The Hubbard chain with correlated hopping”. In: *Physical Review B* 61.12 (Mar. 2000), pp. 7883–7886. DOI: `10.1103/physrevb.61.7883`.

[112] U. Schollwöck. “The density-matrix renormalization group in the age of matrix product states”. In: *Annals of Physics* 326.1 (Jan. 2011), pp. 96–192. DOI: `10.1016/j.aop.2010.09.012`.

[113] G. Vidal et al. “Entanglement in Quantum Critical Phenomena”. In: *Physical Review Letters* 90.22 (June 2003). DOI: `10.1103/physrevlett.90.227902`.

[114] P. Calabrese and J. Cardy. “Entanglement entropy and quantum field theory”. In: *Journal of Statistical Mechanics: Theory and Experiment* 2004.06 (June 2004), P06002. DOI: `10.1088/1742-5468/2004/06/p06002`.

[115] F. H. L. Essler et al. *The One-Dimensional Hubbard Model*. Cambridge University Press, 2005. DOI: `10.1017/cbo9780511534843`.

[116] A. Moreno, A. Muramatsu, and S. R. Manmana. “Ground-state phase diagram of the one-dimensionalt-Jmodel”. In: *Physical Review B* 83.20 (May 2011). DOI: `10.1103/physrevb.83.205113`.

[117] S. Ejima and S. Nishimoto. “Phase Diagram of the One-Dimensional Half-Filled Extended Hubbard Model”. In: *Physical Review Letters* 99.21 (Nov. 2007). DOI: `10.1103/physrevlett.99.216403`.

[118] H. J. Schulz and B. Sriram Shastry. “A New Class of Exactly Solvable Interacting Fermion Models in One Dimension”. In: *Physical Review Letters* 80.9 (Mar. 1998), pp. 1924–1927. DOI: `10.1103/physrevlett.80.1924`.

[119] A. Osterloh, L. Amico, and U. Eckern. “Bethe Ansatz solution of a new class of Hubbard-type models”. In: *Journal of Physics A: Mathematical and General* 33.9 (Feb. 2000), pp. L87–L92. DOI: `10.1088/0305-4470/33/9/101`.

[120] O. Boada et al. “Quantum simulation of non-trivial topology”. In: *New Journal of Physics* 17.4 (Apr. 2015), p. 045007. DOI: `10.1088/1367-2630/17/4/045007`.

[121] W. S. Bakr et al. “A quantum gas microscope for detecting single atoms in a Hubbard-regime optical lattice”. In: *Nature* 462.7269 (Nov. 2009), pp. 74–77. DOI: `10.1038/nature08482`.

[122] J. F. Sherson et al. “Single-atom-resolved fluorescence imaging of an atomic Mott insulator”. In: *Nature* 467.7311 (Aug. 2010), pp. 68–72. DOI: `10.1038/nature09378`.

[123] M. Endres et al. “Observation of Correlated Particle-Hole Pairs and String Order in Low-Dimensional Mott Insulators”. In: *Science* 334.6053 (Oct. 2011), pp. 200–203. DOI: `10.1126/science.1209284`.

[124] M. Cheneau et al. “Light-cone-like spreading of correlations in a quantum many-body system”. In: *Nature* 481.7382 (Jan. 2012), pp. 484–487. DOI: `10.1038/nature10748`.

[125] M. E. Tai et al. “Microscopy of the interacting Harper–Hofstadter model in the two-body limit”. In: *Nature* 546.7659 (June 2017), pp. 519–523. DOI: 10.1038/nature22811.

[126] A. Pickering and J. T. Cushing. “Constructing Quarks: A Sociological History of Particle Physics”. In: *American Journal of Physics* 54.4 (Apr. 1986), pp. 381–383. DOI: 10.1119/1.14594.

[127] G. 't Hooft. “When was asymptotic freedom discovered? or The rehabilitation of quantum field theory”. In: *Nuclear Physics B - Proceedings Supplements* 74.1-3 (Mar. 1999), pp. 413–425. DOI: 10.1016/s0920-5632(99)00207-8.

[128] D. J. Gross and F. Wilczek. “Ultraviolet Behavior of Non-Abelian Gauge Theories”. In: *Physical Review Letters* 30.26 (June 1973), pp. 1343–1346. DOI: 10.1103/physrevlett.30.1343.

[129] H. D. Politzer. “Reliable Perturbative Results for Strong Interactions?” In: *Physical Review Letters* 30.26 (June 1973), pp. 1346–1349. DOI: 10.1103/physrevlett.30.1346.

[130] U.-J. Wiese. *An introduction to lattice field theory*. https://saalburg.aei.mpg.de/wp-content/uploads/sites/25/2017/03/wiese.pdf. Accessed: 2019-07-08. 2009.

[131] J. Greensite. *An Introduction to the Confinement Problem*. Springer Berlin Heidelberg, 2011. DOI: 10.1007/978-3-642-14382-3.

[132] U.-J. Wiese. “Ultracold quantum gases and lattice systems: quantum simulation of lattice gauge theories”. In: *Annalen der Physik* 525.10-11 (2013), pp. 777–796. DOI: 10.1002/andp.201300104.

[133] H. J. Rothe. *Lattice Gauge Theories*. World Scientific, Nov. 2011. DOI: 10.1142/8229.

[134] K. G. Wilson. “Confinement of quarks”. In: *Physical Review D* 10.8 (Oct. 1974), pp. 2445–2459. DOI: 10.1103/physrevd.10.2445.

[135] J. Kogut and L. Susskind. “Hamiltonian formulation of Wilson’s lattice gauge theories”. In: *Physical Review D* 11.2 (Jan. 1975), pp. 395–408. DOI: 10.1103/physrevd.11.395.

[136] K. G. Wilson. “The Origins of Lattice Gauge Theory”. In: *Nuclear Physics B - Proceedings Supplements* 140 (Mar. 2005), pp. 3–19. DOI: 10.1016/j.nuclphysbps.2004.11.271.

[137] M. Creutz. “Asymptotic-Freedom Scales”. In: *Physical Review Letters* 45.5 (Aug. 1980), pp. 313–316. DOI: 10.1103/physrevlett.45.313.

[138] E. Zohar, J. I. Cirac, and B. Reznik. “Quantum simulations of lattice gauge theories using ultracold atoms in optical lattices”. In: *Reports on Progress in Physics* 79.1 (2015), p. 014401. DOI: 10.1088/0034-4885/79/1/014401.

[139] E. Kapit and E. Mueller. “Optical-lattice Hamiltonians for relativistic quantum electrodynamics”. In: *Physical Review A* 83.3 (Mar. 2011). DOI: 10.1103/physreva.83.033625.

[140] S. Chandrasekharan and U.-J Wiese. “Quantum link models: A discrete approach to gauge theories”. In: *Nuclear Physics B* 492.1-2 (May 1997), pp. 455–471. DOI: 10.1016/s0550-3213(97)80041-7.

[141] C. Gattringer and C. B. Lang. *Quantum Chromodynamics on the Lattice*. Springer Berlin Heidelberg, 2010. DOI: 10.1007/978-3-642-01850-3.

[142] H. B. Nielsen and M. Ninomiya. “A no-go theorem for regularizing chiral fermions”. In: *Physics Letters B* 105.2-3 (Oct. 1981), pp. 219–223. DOI: `10.1016/0370-2693(81)91026-1`.

[143] L. Susskind. “Lattice fermions”. In: *Physical Review D* 16.10 (Nov. 1977), pp. 3031–3039. DOI: `10.1103/physrevd.16.3031`.

[144] M. E. Peskin and D. V. Schroeder. *An Introduction To Quantum Field Theory*. 1995. DOI: `10.1201/9780429503559`.

[145] M. Hermele, M. P. A. Fisher, and L. Balents. “Pyrochlore photons: TheU(1)spin liquid in aS=12three-dimensional frustrated magnet”. In: *Physical Review B* 69.6 (Feb. 2004). DOI: `10.1103/physrevb.69.064404`.

[146] A. Milsted and T. J. Osborne. “Quantum Yang-Mills theory: An overview of a program”. In: *Physical Review D* 98.1 (July 2018). DOI: `10.1103/physrevd.98.014505`.

[147] A.M. Polyakov. “Quark confinement and topology of gauge theories”. In: *Nuclear Physics B* 120.3 (Mar. 1977), pp. 429–458. DOI: `10.1016/0550-3213(77)90086-4`.

[148] S. Chandrasekharan. “Confinement, chiral symmetry breaking and continuum limits in quantum link models”. In: *Nuclear Physics B - Proceedings Supplements* 73.1-3 (Mar. 1999), pp. 739–741. DOI: `10.1016/s0920-5632(99)85189-5`.

[149] S. Ben-Menahem. “Confinement in compact QED for low couplings”. In: *Physical Review D* 20.8 (Oct. 1979), pp. 1923–1933. DOI: `10.1103/physrevd.20.1923`.

[150] M.C. Bañuls et al. “The mass spectrum of the Schwinger model with matrix product states”. In: *Journal of High Energy Physics* 2013.11 (Nov. 2013). DOI: `10.1007/jhep11(2013)158`.

[151] S. Kühn, J. I. Cirac, and M.-C. Bañuls. “Quantum simulation of the Schwinger model: A study of feasibility”. In: *Physical Review A* 90.4 (Oct. 2014). DOI: `10.1103/physreva.90.042305`.

[152] M. C. Bañuls et al. “Thermal evolution of the Schwinger model with matrix product operators”. In: *Physical Review D* 92.3 (Aug. 2015). DOI: `10.1103/physrevd.92.034519`.

[153] T. Pichler et al. “Real-Time Dynamics in U(1) Lattice Gauge Theories with Tensor Networks”. In: *Physical Review X* 6.1 (Mar. 2016). DOI: `10.1103/physrevx.6.011023`.

[154] S. Notarnicola et al. “Discrete Abelian gauge theories for quantum simulations of QED”. In: *Journal of Physics A: Mathematical and Theoretical* 48.30 (July 2015), 30FT01. DOI: `10.1088/1751-8113/48/30/30ft01`.

[155] J. J. Garcia-Ripoll et al. “Variational ansatz for the superfluid Mott-insulator transition in optical lattices”. In: *Optics Express* 12.1 (2004), p. 42. DOI: `10.1364/opex.12.000042`.

[156] E. Zohar and B. Reznik. “Confinement and Lattice Quantum-Electrodynamic Electric Flux Tubes Simulated with Ultracold Atoms”. In: *Physical Review Letters* 107.27 (Dec. 2011). DOI: `10.1103/physrevlett.107.275301`.

[157] E. Zohar, J. I. Cirac, and B. Reznik. “Quantum simulations of gauge theories with ultracold atoms: Local gauge invariance from angular-momentum conservation”. In: *Physical Review A* 88.2 (Aug. 2013). DOI: `10.1103/physreva.88.023617`.

[158] E. Zohar, J. I. Cirac, and B. Reznik. “Simulating Compact Quantum Electrodynamics with Ultracold Atoms: Probing Confinement and Nonperturbative Effects”. In: *Physical Review Letters* 109.12 (Sept. 2012). DOI: `10.1103/physrevlett.109.125302`.

[159] E. Zohar, J. I. Cirac, and B. Reznik. “Simulating (2+1)-Dimensional Lattice QED with Dynamical Matter Using Ultracold Atoms”. In: *Physical Review Letters* 110.5 (Jan. 2013). DOI: `10.1103/physrevlett.110.055302`.

[160] V. Kasper et al. “Schwinger pair production with ultracold atoms”. In: *Physics Letters B* 760 (Sept. 2016), pp. 742–746. DOI: `10.1016/j.physletb.2016.07.036`.

[161] V. Kasper et al. “Implementing quantum electrodynamics with ultracold atomic systems”. In: *New Journal of Physics* 19.2 (Feb. 2017), p. 023030. DOI: `10.1088/1367-2630/aa54e0`.

[162] D. Banerjee et al. “Interfaces, strings, and a soft mode in the square lattice quantum dimer model”. In: *Physical Review B* 90.24 (Dec. 2014). DOI: `10.1103/physrevb.90.245143`.

[163] D. Banerjee et al. “Atomic Quantum Simulation of Dynamical Gauge Fields Coupled to Fermionic Matter: From String Breaking to Evolution after a Quench”. In: *Physical Review Letters* 109.17 (Oct. 2012). DOI: `10.1103/physrevlett.109.175302`.

[164] D. S. Rokhsar and S. A. Kivelson. “Superconductivity and the Quantum Hard-Core Dimer Gas”. In: *Physical Review Letters* 61.20 (Nov. 1988), pp. 2376–2379. DOI: `10.1103/physrevlett.61.2376`.

[165] F. Tschirsich, S. Montangero, and M. Dalmonte. “Phase diagram and conformal string excitations of square ice using gauge invariant matrix product states”. In: *SciPost Physics* 6.3 (Mar. 2019). DOI: `10.21468/scipostphys.6.3.028`.

[166] R. Moessner and K. S. Raman. *Quantum dimer models*. 2008. eprint: `arXiv:0809.3051`.

[167] D. Banerjee et al. “The (2 + 1)-d U(1) quantum link model masquerading as deconfined criticality”. In: *Journal of Statistical Mechanics: Theory and Experiment* 2013.12 (Dec. 2013), P12010. DOI: `10.1088/1742-5468/2013/12/p12010`.

[168] D. Marcos et al. “Two-dimensional lattice gauge theories with superconducting quantum circuits”. In: *Annals of Physics* 351 (Dec. 2014), pp. 634–654. DOI: `10.1016/j.aop.2014.09.011`.

[169] L. Mazza et al. “Emerging bosons with three-body interactions from spin-1 atoms in optical lattices”. In: *Physical Review A* 82.4 (Oct. 2010). DOI: `10.1103/physreva.82.043629`.

[170] S. Trotzky et al. “Time-Resolved Observation and Control of Superexchange Interactions with Ultracold Atoms in Optical Lattices”. In: *Science* 319.5861 (Jan. 2008), pp. 295–299. DOI: `10.1126/science.1150841`.

[171] T. Banks, L. Susskind, and J. Kogut. “Strong-coupling calculations of lattice gauge theories: (1+1)-dimensional exercises”. In: *Physical Review D* 13.4 (Feb. 1976), pp. 1043–1053. DOI: 10.1103/physrevd.13.1043.

[172] E. Rico et al. “Tensor Networks for Lattice Gauge Theories and Atomic Quantum Simulation”. In: *Physical Review Letters* 112.20 (May 2014). DOI: 10.1103/physrevlett.112.201601.

[173] B. Buyens et al. “Matrix Product States for Gauge Field Theories”. In: *Physical Review Letters* 113.9 (Aug. 2014). DOI: 10.1103/physrevlett.113.091601.

[174] M. Dalmonte and S. Montangero. “Lattice gauge theory simulations in the quantum information era”. In: *Contemporary Physics* 57.3 (Mar. 2016), pp. 388–412. DOI: 10.1080/00107514.2016.1151199.

[175] W. Chen, K. Hida, and B. C. Sanctuary. “Ground-state phase diagram ofS=1XXZchains with uniaxial single-ion-type anisotropy”. In: *Physical Review B* 67.10 (Mar. 2003). DOI: 10.1103/physrevb.67.104401.

[176] S. R. White. “Density matrix formulation for quantum renormalization groups”. In: *Physical Review Letters* 69.19 (Nov. 1992), pp. 2863–2866. DOI: 10.1103/physrevlett.69.2863.

[177] F. Pollmann et al. “Entanglement spectrum of a topological phase in one dimension”. In: *Physical Review B* 81.6 (Feb. 2010). DOI: 10.1103/physrevb.81.064439.

[178] F. Pollmann et al. “Symmetry protection of topological phases in one-dimensional quantum spin systems”. In: *Physical Review B* 85.7 (Feb. 2012). DOI: 10.1103/physrevb.85.075125.

[179] F. Pollmann and A. M. Turner. “Detection of symmetry-protected topological phases in one dimension”. In: *Physical Review B* 86.12 (Sept. 2012). DOI: 10.1103/physrevb.86.125441.

[180] S.-J. Gu. “Fidelity approach to quantum phase transitions”. In: *International Journal of Modern Physics B* 24.23 (Sept. 2010), pp. 4371–4458. DOI: 10.1142/s0217979210056335.

[181] S. R. White and D. A. Huse. “Numerical renormalization-group study of low-lying eigenstates of the antiferromagneticS=1 Heisenberg chain”. In: *Physical Review B* 48.6 (Aug. 1993), pp. 3844–3852. DOI: 10.1103/physrevb.48.3844.

[182] E. G. Dalla Torre, E. Berg, and E. Altman. “Hidden Order in 1D Bose Insulators”. In: *Physical Review Letters* 97.26 (Dec. 2006). DOI: 10.1103/physrevlett.97.260401.

[183] I. Affleck et al. “Rigorous results on valence-bond ground states in antiferromagnets”. In: *Physical Review Letters* 59.7 (Aug. 1987), pp. 799–802. DOI: 10.1103/physrevlett.59.799.

[184] K. G. Wilson. “The renormalization group: Critical phenomena and the Kondo problem”. In: *Reviews of Modern Physics* 47.4 (Oct. 1975), pp. 773–840. DOI: 10.1103/revmodphys.47.773.

[185] S. R. White and R. M. Noack. “Real-space quantum renormalization groups”. In: *Physical Review Letters* 68.24 (June 1992), pp. 3487–3490. DOI: 10.1103/physrevlett.68.3487.

[186] I. P. McCulloch. “From density-matrix renormalization group to matrix product states”. In: *Journal of Statistical Mechanics: Theory and Experiment* 2007.10 (Oct. 2007), P10014–P10014. DOI: 10.1088/1742-5468/2007/10/p10014.

[187] G. M. Crosswhite and D. Bacon. "Finite automata for caching in matrix product algorithms". In: *Physical Review A* 78.1 (July 2008). DOI: `10.1103/physreva.78.012356`.

[188] J. Eisert. "Entanglement and tensor network states". In: (2013). eprint: `arXiv:1308.3318`.

[189] I. Affleck et al. "Valence bond ground states in isotropic quantum antiferromagnets". In: *Communications in Mathematical Physics* 115.3 (Sept. 1988), pp. 477–528. DOI: `10.1007/bf01218021`.

[190] C. K. Majumdar and D. K. Ghosh. "On Next-Nearest-Neighbor Interaction in Linear Chain. II". In: *Journal of Mathematical Physics* 10.8 (Aug. 1969), pp. 1399–1402. DOI: `10.1063/1.1664979`.

[191] J. Eisert, M. Cramer, and M. B. Plenio. "Colloquium: Area laws for the entanglement entropy". In: *Reviews of Modern Physics* 82.1 (Feb. 2010), pp. 277–306. DOI: `10.1103/revmodphys.82.277`.

[192] F. Verstraete, V. Murg, and J. I. Cirac. "Matrix product states, projected entangled pair states, and variational renormalization group methods for quantum spin systems". In: *Advances in Physics* 57.2 (Mar. 2008), pp. 143–224. DOI: `10.1080/14789940801912366`.

[193] M. A. Nielsen and I. L. Chuang. *Quantum Computation and Quantum Information*. Cambridge University Press, 2009. DOI: `10.1017/cbo9780511976667`.

[194] G. Vidal. "Efficient Classical Simulation of Slightly Entangled Quantum Computations". In: *Physical Review Letters* 91.14 (Oct. 2003). DOI: `10.1103/physrevlett.91.147902`.

[195] A. Hamma, R. Ionicioiu, and P. Zanardi. "Bipartite entanglement and entropic boundary law in lattice spin systems". In: *Physical Review A* 71.2 (Feb. 2005). DOI: `10.1103/physreva.71.022315`.

[196] L. Bombelli et al. "Quantum source of entropy for black holes". In: *Physical Review D* 34.2 (July 1986), pp. 373–383. DOI: `10.1103/physrevd.34.373`.

[197] M. B. Plenio et al. "Entropy, Entanglement, and Area: Analytical Results for Harmonic Lattice Systems". In: *Physical Review Letters* 94.6 (Feb. 2005). DOI: `10.1103/physrevlett.94.060503`.

[198] M. B. Hastings. "Locality in Quantum and Markov Dynamics on Lattices and Networks". In: *Physical Review Letters* 93.14 (Sept. 2004). DOI: `10.1103/physrevlett.93.140402`.

[199] P. Calabrese and J. Cardy. "Evolution of entanglement entropy in one-dimensional systems". In: *Journal of Statistical Mechanics: Theory and Experiment* 2005.04 (Apr. 2005), P04010. DOI: `10.1088/1742-5468/2005/04/p04010`.

[200] F. Verstraete and J. I. Cirac. "Matrix product states represent ground states faithfully". In: *Physical Review B* 73.9 (Mar. 2006). DOI: `10.1103/physrevb.73.094423`.

[201] F. Verstraete et al. "Criticality, the Area Law, and the Computational Power of Projected Entangled Pair States". In: *Physical Review Letters* 96.22 (June 2006). DOI: `10.1103/physrevlett.96.220601`.

[202] L. Vanderstraeten, J. Haegeman, and F. Verstraete. "Tangent-space methods for uniform matrix product states". In: *SciPost Physics Lecture Notes* (Jan. 2019). DOI: `10.21468/scipostphyslectnotes.7`.

[203] M. Fannes, B. Nachtergaele, and R. F. Werner. “Finitely correlated states on quantum spin chains”. In: *Communications in Mathematical Physics* 144.3 (Mar. 1992), pp. 443–490. DOI: `10.1007/bf02099178`.

[204] V. Zauner-Stauber et al. “Variational optimization algorithms for uniform matrix product states”. In: *Physical Review B* 97.4 (Jan. 2018). DOI: `10.1103/physrevb.97.045145`.

[205] P. Silvi et al. “The Tensor Networks Anthology: Simulation techniques for many-body quantum lattice systems”. In: *SciPost Physics Lecture Notes* (Mar. 2019). DOI: `10.21468/scipostphyslectnotes.8`.

[206] B. Pirvu et al. “Matrix product operator representations”. In: *New Journal of Physics* 12.2 (Feb. 2010), p. 025012. DOI: `10.1088/1367-2630/12/2/025012`.

[207] M. P. Zaletel et al. “Time-evolving a matrix product state with long-ranged interactions”. In: *Physical Review B* 91.16 (Apr. 2015). DOI: `10.1103/physrevb.91.165112`.

[208] J. Motruk et al. “Density matrix renormalization group on a cylinder in mixed real and momentum space”. In: *Physical Review B* 93.15 (Apr. 2016). DOI: `10.1103/physrevb.93.155139`.

[209] P. Silvi et al. “Lattice gauge tensor networks”. In: *New Journal of Physics* 16.10 (Oct. 2014), p. 103015. DOI: `10.1088/1367-2630/16/10/103015`.

[210] G. Magnifico et al. “Symmetry-protected topological phases in lattice gauge theories: Topological QED2”. In: *Physical Review D* 99.1 (Jan. 2019). DOI: `10.1103/physrevd.99.014503`.

[211] G. Magnifico et al. “$\mathbb{Z}_N$ gauge theories coupled to topological fermions: $QED_2$ with a quantum mechanical $\theta$ angle”. In: *Physical Review B* 100.11 (Sept. 2019). DOI: `10.1103/physrevb.100.115152`.

[212] M. Matti Maricq. “Application of average Hamiltonian theory to the NMR of solids”. In: *Physical Review B* 25.11 (June 1982), pp. 6622–6632. DOI: `10.1103/physrevb.25.6622`.

[213] N. Goldman et al. “Light-induced gauge fields for ultracold atoms”. In: *Reports on Progress in Physics* 77.12 (Nov. 2014), p. 126401. DOI: `10.1088/0034-4885/77/12/126401`.

[214] M. Aidelsburger et al. “Measuring the Chern number of Hofstadter bands with ultracold bosonic atoms”. In: *Nature Physics* 11.2 (Dec. 2014), pp. 162–166. DOI: `10.1038/nphys3171`.

# *Acknowledgements*

In a journey lasting longer than four years, many winds have to blow and for long before the boat finally reaches a safe harbour. In these few lines I want to express my deepest gratitude to all the people that have been part of my doctorate route.

First and foremost, I would like to thank Prof. Luis Santos for offering me the opportunity to pursue my doctoral studies under his supervision. I consider it a privilege to have received such a positive, supportive and proficient guidance in these years. Working very closely with you has given me the chance to learn what it takes to not only be a brilliant researcher but also a great group leader. It has been enriching, scientifically and personally.

A special thanks goes to Dr. Sebastian Greschner, with whom I am particularly indebted for the precious combination of moral and technical support I received during the time of our collaboration. Without your backing while my code was little more than a beta, and without your striking solutions and advices, most of my work would simply not have been possible. Again, a first-hand experience of what it means to be an excellence.

The daily life in the office would not have been so fun though, if it was only about physics. I will keep memories of the working (and sometimes no-working too) time spent together with all the friends at ITP - Vincent, Falk, Meghana, Tim and all the other present and past members of our group. Particular thanks in this sense goes to Prof. Hendrik Weimer, for the countless enjoyable conversations that we had during these years; be they about natural, social and economical sciences or simply about football, there was always something to learn.

I would like to express my gratitude to Prof. Matteo Rizzi, for the invaluable knowledge acquired during the pleasant visit I had at the JGU in Mainz; those have been among the clearest lessons that I have ever had the pleasure to attend.

I gratefully acknowledge financial support from the Deutsche Forschungsgemeinschaft through the Research Training Group 1729 "Fundamentals and applications of ultra-cold matter" and the Institut für Theoretische Physik Hannover, as well as the administrative personnel at the ITP for making our lives beautifully easier.

Being forgetful now about my time before moving to Hannover would be an unforgivable dismissal of the help that some wonderful persons gave me whilst in agitated waters. Among the many whom I had around during those days, I want to thank Georgios, Simos and Martina. Dr. Reza Bakhtiari deserves a special mention; I owe you much of the fortunate change that I made.

To conclude, I want to thank my parents and my sister Alessia for always being present with love. Without a solid ground, it would not be possible to spring high.

# Curriculum Vitae

Email : lorenzocarda@gmail.com

## Personal profile

| | | |
|---|---|---|
| Birth | : | June 1989, Macerata, Italy |
| Gender | : | Male |
| Nationality | : | Italian |
| Languages | : | Italian, English, French, German |

## Education

| | | |
|---|---|---|
| 2015 - 2019 | : | PhD, Leibniz Universität Hannover, Germany |
| 2015 - 2018 | : | Member of the Research Training Group 1729:<br>*Fundamentals and applications of ultracold matter* |
| 2008 - 2014 | : | Master of Science in Physics, University of Camerino, Italy |
| 2003 - 2008 | : | Secondary school studies, Sarnano, Italy |

# Publications

Part of the content of this thesis has appeared previously in the following publications.

- Lorenzo Cardarelli, Sebastian Greschner, and Luis Santos:
  "Engineering interactions and anyon statistics by multicolor lattice-depth modulations"
  *Physical Review A* **94**, 023615 (2016)
- Lorenzo Cardarelli, Sebastian Greschner, and Luis Santos:
  "Hidden order and symmetry protected topological states in quantum link ladders"
  *Physical Review Letters* **119**, 180402 (2017)
- Sebastian Greschner, Lorenzo Cardarelli, and Luis Santos:
  "Probing the exchange statistics of one-dimensional anyon models"
  *Physical Review A* **97**, 053605 (2018)